

# Electrically Excited Liquid Water

*Lessons from the Floating Water Bridge*

Adam D. Wexler

# Electrically Excited Liquid Water

## *Lessons from the Floating Water Bridge*

### **Thesis committee**

#### **Promotor**

Prof. Dr C.J.N. Buisman  
Professor of Biological Recovery and Re-use Technology  
Wageningen University, Netherlands

#### **Co-promoters**

Prof. Dr J. Woisetschläger  
Head of Metrology – Laser Optical Metrology  
Graz University of Technology, Austria

Dr. E.C. Fuchs  
Scientific Program Manager Applied Water Physics  
Wetsus – European Center of Excellence for Sustainable Water Technology, Leeuwarden

#### **Other members**

Prof. Dr H. van Amerongen, Wageningen University, Netherlands  
Prof. Dr M. Musso, University of Salzburg, Austria  
Prof. Dr L. Brecker, University of Vienna, Austria  
Dr. Hyok Yoo, University of Washington, United States of America

This research was conducted under the auspices of the Graduate School of Socio-Economic and Natural Sciences of the Environment (SENSE) and the Wageningen Institute for Environment and Climate Research (WIMEK)

**Adam D. Wexler**

Thesis  
submitted in fulfillment of the requirements for the degree of doctor  
at Wageningen University  
by the authority of the Rector Magnificus  
Prof. Dr A.P.J. Mol,  
in the presence of the  
Thesis Committee appointed by the Academic Board  
to be defended in public  
on Tuesday, 19 April 2016  
at 3:30 p.m. in De Kanselarij, Leeuwarden.



for Papa & Chelsea

Adam David Wexler

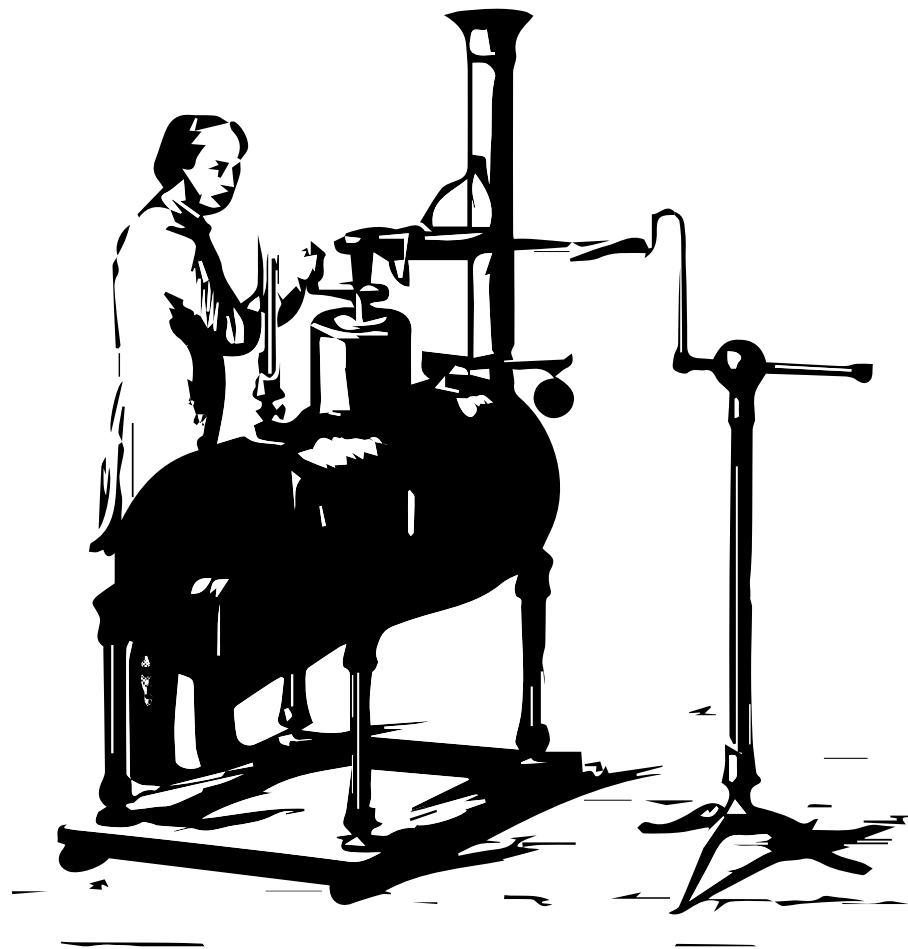
Electrically Excited Liquid Water – Lessons from the floating water bridge

240 pages.

PhD thesis, Wageningen University, Wageningen, NL (2016)

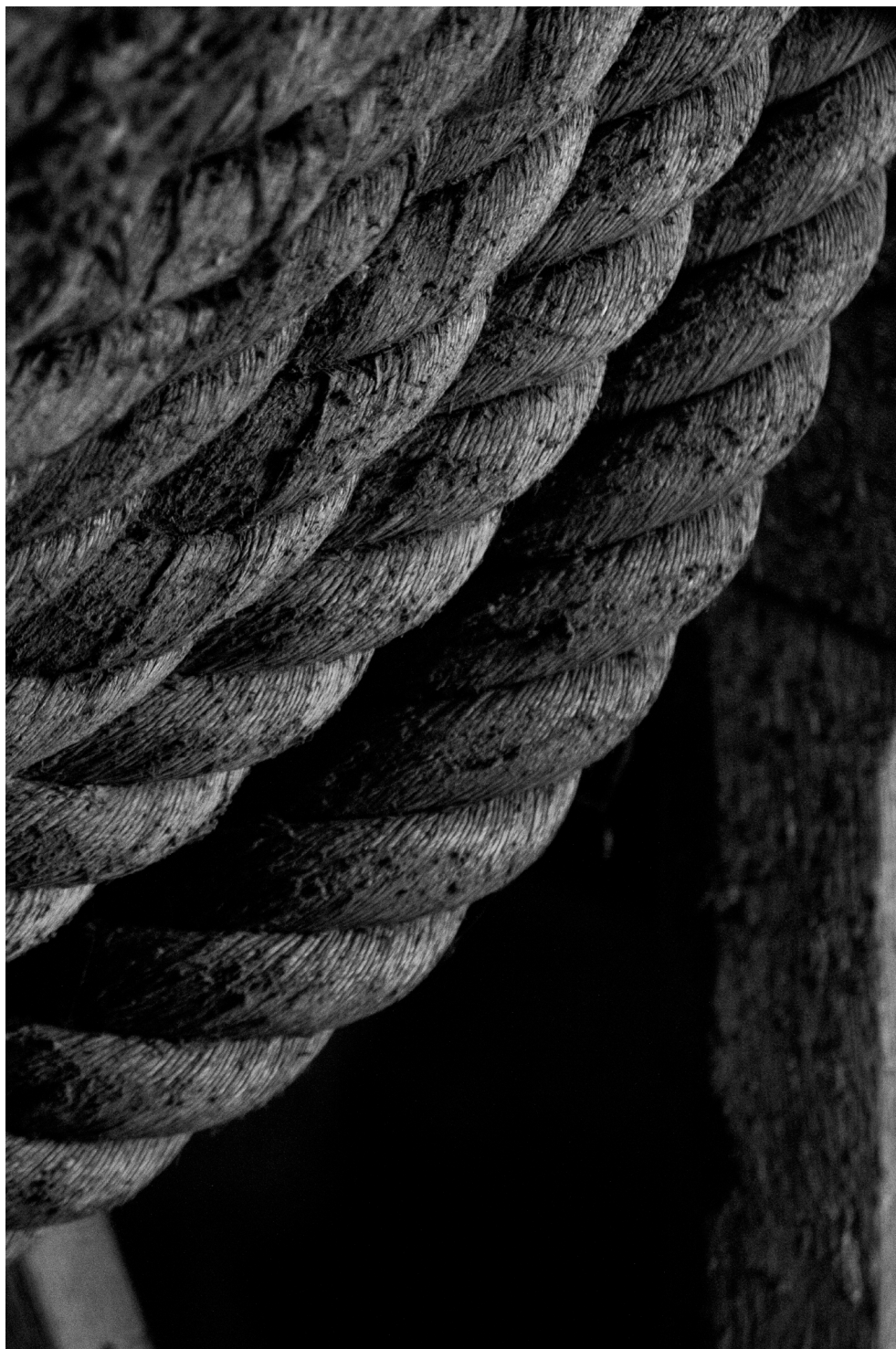
With references, with summary in English

ISBN 978-94-6257-703-9



Take the initiative. Go to work, and above all co-operate and don't hold back on one another or try to gain at the expense of another. Any success in such lopsidedness will be increasingly short-lived. These are the synergetic rules that evolution is employing and trying to make clear to us.

—R. Buckminster Fuller  
*Operating Manual for Spaceship Earth (1963)*



# Contents

|   |    |
|---|----|
| 1 Much Ado About Water .....  | 1  |
| 1.1 The Global Context .....  | 2  |
| 1.2 Water.....  | 2  |
| 1.2.1 Physical Properties.....  | 3  |
| 1.2.2 Anomalous Properties.....   | 4  |
| 1.3 Liquid Matter: Neither soft solid, nor dense gas .....                | 5  |
| 1.4 The mesoscale .....   | 6  |
| 1.5 Investigation of field gradient effects, hypothesis and mission ..... | 7  |
| 2 Electrohydrodynamic Bridges.....  | 13 |
| 2.1 A brief history of electrohydrodynamics .....                         | 14 |
| 2.1 EHD liquid bridges .....  | 16 |
| 2.2 Electrohydrodynamic Theory .....                                      | 22 |
| 2.3 The floating water bridge: stability against gravity .....            | 24 |
| 2.3 Bridges in other polar liquids .....                                  | 26 |
| 2.4 Is there a molecular basis to EHD phenomena? .....                    | 28 |
| 2.5 Concluding Remark .....   | 29 |
| Appendix A: Safe EHD Bridge Protocol.....                                 | 33 |
| A.1. General recommendations.....   | 33 |
| A.2. Experimental set-up .....  | 33 |
| A.3. Operation of Liquid Bridges .....                                    | 34 |

|   |           |
|---|-----------|
| <b>3 A Tour Of The Toolbox.....</b>   | <b>39</b> |
| 3.1 General Measurement Principles .....                                    | 40        |
| 3.1.1 Matter-Energy Interactions .....                                      | 40        |
| 3.1.2 Dielectric Relaxation and Polarization.....                           | 41        |
| 3.1.2.1 Leaking Charges.....  | 41        |
| 3.1.2.2 Relaxation Processes .....  | 42        |
| 3.1.3 Length Scales, and Interaction Fields .....                           | 42        |
| 3.1.4 Methodology .....   | 44        |
| 3.2 EHD bridges – experimental setup.....                                   | 44        |
| 3.3 Electrochemical Characterization .....                                  | 46        |
| 3.3.1 Hydrogen Detection .....  | 46        |
| 3.3.2 Gas Chromatography.....   | 47        |
| 3.3.3 Quantification of Dissolved Ions (Ca, K, Mg, Na, Zn, C and Pt).....   | 47        |
| 3.3.4 Conductivity Measurements.....  | 48        |
| 3.3.5 Colorimetric Analysis of pH Dye Solutions .....                       | 48        |
| 3.3.6 Optical Fiber pH Measurements .....                                   | 49        |
| 3.3.7 Electrochemical pH Measurements in Low Ionic Strength Solutions ..... | 49        |
| 3.3.8 Impedance Spectroscopy .....  | 49        |
| 3.4 Infrared emission .....   | 50        |
| 3.4.1 Infrared Measurement Principles .....                                 | 50        |
| 3.4.2 Infrared Emission Spectroscopy.....                                   | 51        |
| 3.4.3 Long-wave Infrared (LWIR) Imaging .....                               | 52        |
| 3.5 Elastic Radiation Scattering .....                                      | 53        |
| 3.5.1 Wide Angle X-ray Scattering (WAXS).....                               | 53        |
| 3.5.2 Temperature effect on total X-ray scattering and tetrahedrality.....  | 54        |
| 3.5.3 Small Angle Neutron Scattering (SANS) .....                           | 55        |
| 3.5.4 Anolyte and Catholyte Neutron Scattering Cross-section .....          | 58        |
| 3.5.5 Empirical potential structure refinement .....                        | 59        |
| 3.6 Quasi-Elastic Neutron Scattering (QENS) .....                           | 60        |
| 3.6.1 QENS Theory.....  | 60        |
| 3.6.2 General experimental considerations.....                              | 61        |
| 3.6.3 QENS Protocol .....   | 61        |
| 3.6.4 QENS Data Analysis .....  | 63        |

|  |           |
|--|-----------|
| 3.7 Nuclear Magnetic Resonance (NMR) .....   | 64        |
| 3.7.1 Magnetic resonance principles.....   | 64        |
| 3.7.2 EHD Bridges in high magnetic field environment.....  | 67        |
| 3.7.3 High Field NMR Spectroscopy.....   | 69        |
| 3.7.3.1 Sample preparation for nuclear magnetic resonance (NMR) spectroscopy.....                        | 69        |
| 3.7.3.2 Nuclear magnetic resonance (NMR) spectroscopy .....  | 69        |
| 3.7.4 Low Field NMR Spectroscopy.....  | 70        |
| 3.7.5 MRI sequences and protocols for isotope and flow analysis .....                                    | 70        |
| 3.7.6 Image analysis .....   | 71        |
| 3.7.7 MR Relaxation Mapping and Thermometry.....   | 73        |
| 3.7.7.1 Glycerol bridges .....   | 73        |
| 3.7.7.2 MR imaging of glycerol bridges .....   | 73        |
| 3.7.7.3 MR image analysis.....   | 75        |
| 3.7.7.4 Calibration of temperature behavior of relaxation times of glycerol .....                        | 77        |
| 3.9 Interferometry .....   | 80        |
| 3.9.1 Interferometry principles.....   | 80        |
| 3.9.2 Interferometry measurement .....   | 80        |
| 3.10 Raman Spectral Imaging.....   | 82        |
| 3.10.1 Raman Principles .....  | 82        |
| 3.10.2 Raman measurement details .....   | 83        |
| Appendix B Electromagnetic Radiation and Matter.....   | 90        |
| B.1 Electromagnetic Interactions with Matter.....  | 90        |
| B.2 Electromagnetic Wave Propagation .....   | 92        |
| B.3 Electromagnetic Emission .....   | 96        |
| <b>4 Water Speaks.....</b>   | <b>99</b> |
| 4.1 Unveiling hidden flow structures with proton imaging – The water bridge in a medical MR-scanner. 100 |           |
| 4.1.1 Flow in the bridge.....  | 100       |
| 4.2 The discovery of charged water – Proton Production & Charge Separation .....                         | 103       |
| 4.2.1 Electrochemistry .....   | 103       |
| 4.2.1.1 Conductivity .....   | 103       |
| 4.2.1.2 pH Change .....  | 104       |
| 4.2.1.3 The proton resistor .....  | 106       |
| 4.2.2 Impedance Spectroscopy.....  | 108       |

|   |     |
|---|-----|
| 4.3 Coupling Local Structures in an Electrically Stressed Polar Liquid .....        | 112 |
| 4.3.1 Total scattering of water under moderate electric field .....                 | 112 |
| 4.3.2 Structure refinement to extract site-site radial distribution functions ..... | 115 |
| 4.3.3 Analysis of the EPSR simulation .....   | 118 |
| 4.4 Excitation of Water by an Electric Field Gradient .....                         | 121 |
| 4.4.1 Interferometry .....  | 121 |
| 4.4.2 Thermographic Imaging of the Polarized Surface.....                           | 125 |
| 4.4.3 Mid-Infrared Raman Imaging Spectroscopy .....                                 | 125 |
| 4.4.4 Mid-Infrared Emission Imaging .....   | 131 |
| 4.4.4.1 Bulk water emission .....   | 134 |
| 4.4.4.2 Water bridge emission .....   | 136 |
| 4.5 Proton transport in water bridges – Quantification by QENS .....                | 138 |
| 4.6 Ultrafast relaxation revisited .....  | 143 |
| 4.7 Probing the Nuclear Environment for Coherent Spin Coupling.....                 | 146 |
| 4.5.1 MR Relaxation Mapping and Thermometry.....                                    | 146 |
| 4.5.2 Water – Glycerol Interaction .....  | 146 |
| 4.5.3 Low-field eNMR – The echo of free protons .....                               | 148 |
| Appendix C: Supplemental Results.....   | 155 |
| C.1 Supplemental MRI Results .....  | 155 |
| C.1.1 Electrical polarization, bridge ignition and noise .....                      | 155 |
| C.1.2 Mass transport and isotope mixing.....  | 155 |
| C.2 Electrochemistry .....  | 162 |
| C.2.1 Trace elements from the electrodes .....                                      | 162 |
| C.2.2 Other trace elements .....  | 162 |
| C.2.3 Carbon .....  | 162 |
| C.2.4 Hydrogen production and measurement .....                                     | 165 |
| C.2.5 EHD flow and microbubbles.....  | 166 |
| C.2.6 Direct gas solvation.....   | 167 |
| C.3 Vapour emission between 1300 and 2000cm <sup>-1</sup> .....                     | 167 |
| C.4 Diagnostic Values from EPSR simulation used for PSF recovery .....              | 170 |
| C.5 NMR spectroscopy of, and environmental effects on, dry glycerol.....            | 171 |

|   |     |
|---|-----|
| 5 Excited Liquid Water .....  | 177 |
| 5.1 Introduction .....  | 178 |
| 5.2 The discovery of charge imbalance in EHD bridges .....                                    | 178 |
| 5.2.1 Impedance spectroscopy of pure water .....  | 178 |
| 5.2.2 Conductivity shift of anolyte and catholyte .....                                       | 178 |
| 5.2.3 Anolyte .....   | 178 |
| 5.2.4 Catholyte .....   | 180 |
| 5.3 The emergence of proton channels.....   | 181 |
| 5.3.1 The infrared signature of Grotthuss librations .....                                    | 181 |
| 5.3.2 Two distinct proton populations.....  | 184 |
| 5.3.2.1 Comparison of results to confined water in an electric field .....                    | 184 |
| 5.3.2.2 Comparisons of results to electrohydrodynamic experiments .....                       | 184 |
| 5.3.2.3 Pre-ambles for a possible molecular interpretation of the experimental QENS data..... | 186 |
| 5.3.2.4 Proton jumps .....  | 186 |
| 5.3.2.5 Proton Channels .....   | 187 |
| 5.4 Approach to radiation scattering in electrically stressed liquid water .....              | 189 |
| 5.5 The effect of exciting a delocalized vibrational state .....                              | 190 |
| 5.6 Implications of an extended vibrational energy mode .....                                 | 193 |
| 5.7 Enhanced local field heterogeneity drives quantum chaos.....                              | 194 |
| 6 Much To Do About Water .....  | 203 |
| 6.1 Rethinking Water: A programmable material.....  | 204 |
| 6.2 A different approach to water technology .....  | 209 |
| 6.3 An era of new human technology .....  | 210 |
| 6.3.1 Materials and medicines .....   | 210 |
| 6.3.2 New lifeforms .....   | 211 |
| 6.3.3 Computational capabilities .....  | 211 |
| 6.3.4 Geoengineering .....  | 211 |
| Summary .....   | 215 |
| Acknowledgements .....  | 218 |
| About the Author .....  | 221 |
| Author's Publications .....   | 222 |



# 1

## Much Ado About Water

### *A brief Introduction*

*The primary topic of this thesis is concerned with water in the liquid state. The importance and unusual properties of water, along with the complexity of the liquid state, and a quick glance at the mesoscale follow.*

## 1.1 The Global Context

The material properties of water are simultaneously a great challenge to, and opportunity for, developing water technologies that improve human sustainability. The economic and environmental costs of processing water are significant. At present much engineering effort is being made to develop and optimize the recovery of energy and valuable resources (e.g. phosphate, volatile fatty acids, and ammonia) from waste water streams. Likewise, the production of drinking water and purified water for industrial processes face challenges related to rising operational costs and the environmental impact associated with current technologies such as tightening discharge limits [1], [2]. Every sector of human activity requires the processing of vast amounts of water and as our global population and wealth grows the demand for water related resources will grow and likely in a non-linear fashion. The importance of the global climate system for maintaining the biotic viability of the planet is well known and the impact of changes to this system are now becoming readily apparent. Extreme weather events, anomalous climatic phenomena, and the destabilization of global ice repositories promise to exacerbate human population stress on the environment. Furthermore, these two systems form a feedback loop whereby destabilization of human society can result from changes in how water is distributed over the planet. The failure of crops in arid regions, most recently in Syria, has been linked to the eruption of human conflict [3]. Thus the work of significantly improving the access of all people to clean useable water along with the efficient and local recovery of critical resources for food production becomes a matter of global security.

## 1.2 Water

Water, as a material, is most commonly quoted as having the chemical formula  $H_2O$ ; however, while stoichiometrically true, discrete singular molecules are only observable in the gas phase. Understanding the liquid and solid condensed phases is more complicated revealing myriad anomalous physical properties such as: high heat capacity, increased density upon melting, high thermal conductivity, and high surface tension [4]. There are extensive reviews on the material properties and general physics of water that go into much more detail than is practical here [5]–[9]. Many of the unique properties of water can be attributed to the extensive hydrogen bonding between water molecules. It is difficult to identify a single water molecule in the liquid because in the condensed phase water is a continuous material with poorly defined molecular motifs. Essentially, it is very difficult to say with certainty that a given hydrogen belongs to a specific oxygen. Liquid water can thus be considered a very large super-molecular system with no discernable difference between the near or far side of a given bulk volume, and this is the essence of the isotropic limit at the continuum level [10].

One of the current challenges is to describe how the extensive hydrogen bonded water network behaves under myriad conditions. The influence of mobile ions on the bulk properties of water hints at the sensitivity of the molecular network. It is common knowledge that the addition of some salts can raise the boiling point and affect bubble coalescence [11], [12]. There are also changes in the organization of the liquid at the molecular level revealed through infrared [13] and x-ray measurements [14]. In addition work on water at interfaces and confined geometries also reveals modulated dynamics which reveal the extreme mutability of water to its surroundings [15]. Water has been suggested to be a mixture of high and low density regions; whereby those regions with high tetrahedrality between the molecules have lower density than those regions dominated by reorienting and thus poorly coordinated molecules. However, others refute this claim and hold fast to the idea that water is a continuum material without any discernable local motifs [16]. The discussion continues [17] and there are other interpretations all together of the structure of liquid water especially at longer interaction scales [18], [19] some of more solid scientific basis than others – but regardless this should make it clear that the matter is far from settled regarding the extended structure of liquid water.

Dissolved substances and charge carriers such as electrons and protons not only traverse the network but also perturb the resonant dynamics. The time scale over which many of these processes occur is extremely short; femtoseconds for electron delocalization [20], and picoseconds for molecular reorientation [21]. Such high frequency fluctuations not only distribute energy but may also be able to store it particularly near interfaces [22]. Water forms multiple structural motifs depending on what is present. Even two fully miscible liquids such as water and ethanol establish nanoscale biphasic materials [23]. These structural heterogeneities are essential to various self-assembly [24] and colloidal phenomena [25].

### 1.2.1 Physical Properties

Water like all common matter can be found in three material phases, solid, liquid and gas. The shape of the phase transitions shown in Figure 1.1 obey the Clausius–Clayperon equation and the state equations of thermodynamics reasonably well. Recent work, however, on supercooled water [26], [27], water under negative pressures [28], and amorphous water ices [29], [30] have shown that in these peculiar regions the memory function used in mode-coupling theory may actually lead to hysteresis whereby the homogeneous state equation fails indicating that under some conditions water remains outside of thermodynamic equilibrium for very long times [31]. Furthermore, there appear to be discontinuities or “No-man’s lands” in the phase diagram under these extreme conditions which further raises uncertainty regarding the validity of statistically averaged methods for interpreting the molecular landscape of water. A critical question remains regarding the degree of molecular homogeneity in condensed water phases that are far from equilibrium.



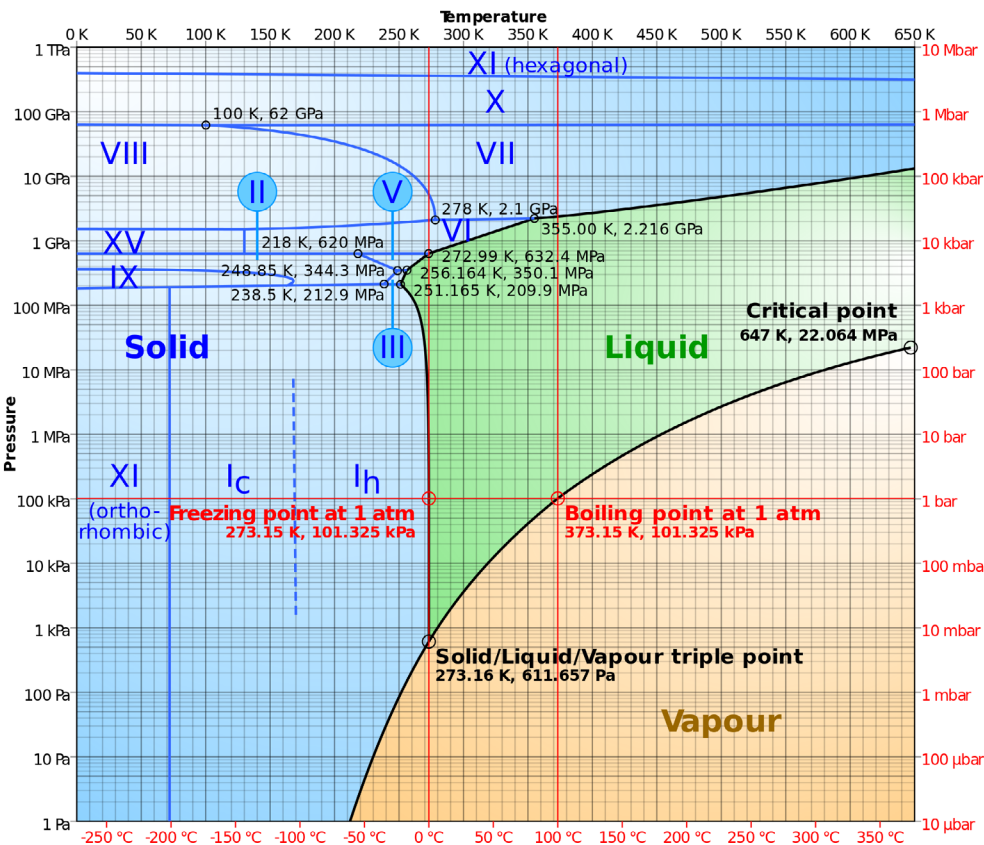


Figure 1.1: The barochoric phase diagram of water. [32]

1.2.2 Anomalous Properties

The anomalous properties of water can be split into five categories: phase, material, physical, density and thermodynamic; representative examples are given in Table 1.1. Many of these anomalies are thermodynamic such as the isothermal compressibility and the isobaric specific heat which hints at a complex energetic landscape at the molecular level. The prevailing consensus in the field is that nearly all the anomalous and unexplained properties of water arise from the strong hydrogen bonding between water molecules. The exact energetic stability of the H-bond is not well understood as the energy levels for water molecules in the liquid state are extrapolated from those measured in the gas and solid phases (Kuhne, 2007). Such extrapolations are problematic because they assume an equilibrium framework. Experimental evidence from deep inelastic neutron scattering hints that the energy barrier between the covalent and hydrogen bonds is much lower in supercooled water [33], [34]. Studies on the self-diffusion rate of hydrogen in water at STP find anomalously high rates

indicating that the possibility of quantum effects such as tunneling may not only be relegated to extremes of the phase diagram [35]. Indeed the contribution of nuclear quantum states has been found important to improving water models [36]. However, the molecular view of water escapes effective simulation because current models suffer from classical assumptions, sample size limitations, and problems of defining boundary conditions [37].

Table 1.1: Various examples of the anomalous characteristics of water. Nearly all physical parameters of water exhibit strong non-linearities and various minima and maxima arising from the mutable nature of the hydrogen bond network [4].

| Category of Anomaly | Examples  |
|---------------------|---|
| Phase               | High melting and boiling point, Mpemba effect, ease of superheating and supercooling but not a good glass former.       |
| Density             | Low thermal expansion, density increase on melting, low compressibility, speed of sound is nonlinear.                   |
| Material            | Non-Ideality, isotopic effect, high dielectric with a temperature maximum, non-linear non-polar gas solubility          |
| Physical            | High viscosity, high surface tension, large diffusion decrease with lower temperature, high proton self-diffusion rates |
| Thermodynamic       | High specific heat capacity with many non-linearities, high thermal conductivity, high heat of vaporization             |

1.3 Liquid Matter: Neither soft solid, nor dense gas

Liquids are a unique state of matter governed by both structure and dynamics. The interplay between these forces manifests differently as one moves across physical length scales. In a liquid the molecules are free to spatially translate and interact with the electromagnetic (EM) fields of neighboring molecules. The molecular composition of the liquid determines the basis for the interaction fields. The notion of structure in a liquid is tied to this interaction which prevents spatial overlap and governs the local trajectories. Each molecule at any given moment will have an energy which is dependent upon the total distribution of energy in the material as well as the history of that particular molecule. The flow of energy through a molecular fluid follows the simple path excitation, transport, and de-excitation. The pathways available for the specific process depend upon the excitation source energy as well as the state of the liquid. Thermal perturbation for example provides a continuous source of local energy fluctuations which depending on the degree of correlation between neighboring states will affect the spectral distribution of the energy modes. Depending on the conditions placed



upon the liquid the spectral density of states will change. This gives rise to changes in the thermodynamic response functions (such as density, dielectric permittivity, and viscosity). For a polar liquid such as water the dominant intermolecular coupling mode is the hydrogen bond (HB). The nature of the HB is partly electrostatic and partly covalent [38]. This means that not only will the electron density function be affected but the nuclear spin states can also be affected especially in the case of proton delocalization between neighboring molecules [39], [40]. Liquids are highly correlated materials, as the local repulsive and attractive forces are dynamically optimized by the shuttling of mass and energy within the bulk. Much of what we know regarding liquids has been learned through the study of samples at equilibrium, however, the most useful property of liquid matter is the ability to conform to the field surrounding it. This requires not only short range local modes, but also longer range collective modes [41].

## 1.4 The mesoscale

At the macroscale physics is familiar and we can readily describe events using classical physics which for fluid flow is certainly no simple task. While at the nanoscale physics is unfamiliar and downright strange – quantum mechanics rules. The observer and the observed cannot be kept separate – both participate in the measurement and smooth transitions give way to jumps in energy levels between neighboring bodies. There exists a middle ground or mesoscale which lies between the extremes of the nanoscale and continuum world. It can best be understood as a place where the very neat quantum mechanical description of matter becomes too messy and chaotic for even nature to keep up with and this gives rise to new behaviors that are only observable at this length scale but which underlie continuum mechanics. The mesoscale is defined by six criteria [42]:

1. Atomic granularity
2. Energy quantization
3. Collective behavior
4. Interacting degrees of freedom
5. Defects, fluctuations, and statistical variation
6. Heterogeneity of structure and dynamics

At this length scale we can observe the emergence of Anderson locality – which to quote the theories namesake “more is different” [43]. The fluctuations naturally present in the material are not smooth at this length scale, there are just too many individuals to have uniformity and yet the size is not so large that all possibilities are represented in the population at any given time. Very short range sub populations, fully disordered transients, and long range collective modes will be present, however the constraints on the system (e.g. atomic granularity and energy quantization) will mean that the instantaneous values of the system will fluctuate about the mean of the distribution but not settle into equilibrium. The

mesoscale is a length scale that reveals the non-equilibrium thermodynamics inherent to all materials [44]. The emergence of quantum chaos for such interactions will stabilize the non-equilibrium distribution within a stable attractor that is dependent on the superposition of the intrinsic and extrinsic (or applied) fields [45].

## 1.5 Investigation of field gradient effects, hypothesis and mission

Most if not all natural systems do not exist in thermal equilibrium and certainly not living systems [46], [47]. The hypothesis for this thesis is that liquid water can be excited from the ground state using an inhomogeneous electric field. The resulting excited state will exhibit not only unique physical properties, but also dynamic stability and local negative entropy. Furthermore, a dynamic heterogeneity will appear at the mesoscale in the electrically stressed liquid and this will reorganize the material by extending the coupling range beyond nearest neighbors. The liquid will also exhibit a type of coherence stabilized by chaos. Thus, the potential to study the non-equilibrium thermodynamics of liquid water and other polar liquids under electric field stress presents an opportunity to expand our fundamental understanding of natural systems was considered feasible. To this end an overlooked phenomenon was chosen as the model system of study – namely, the floating water bridge with the understanding that the system can be generalized to a number of polar liquids. Electrohydrodynamic liquid bridges were thus used to test whether the distribution of dynamic energies and structural conformations in polar liquids, such as water, can be shifted from the thermal equilibrium ground state to an excited state exhibiting the expected properties for a system far from thermal equilibrium.

## Bibliography

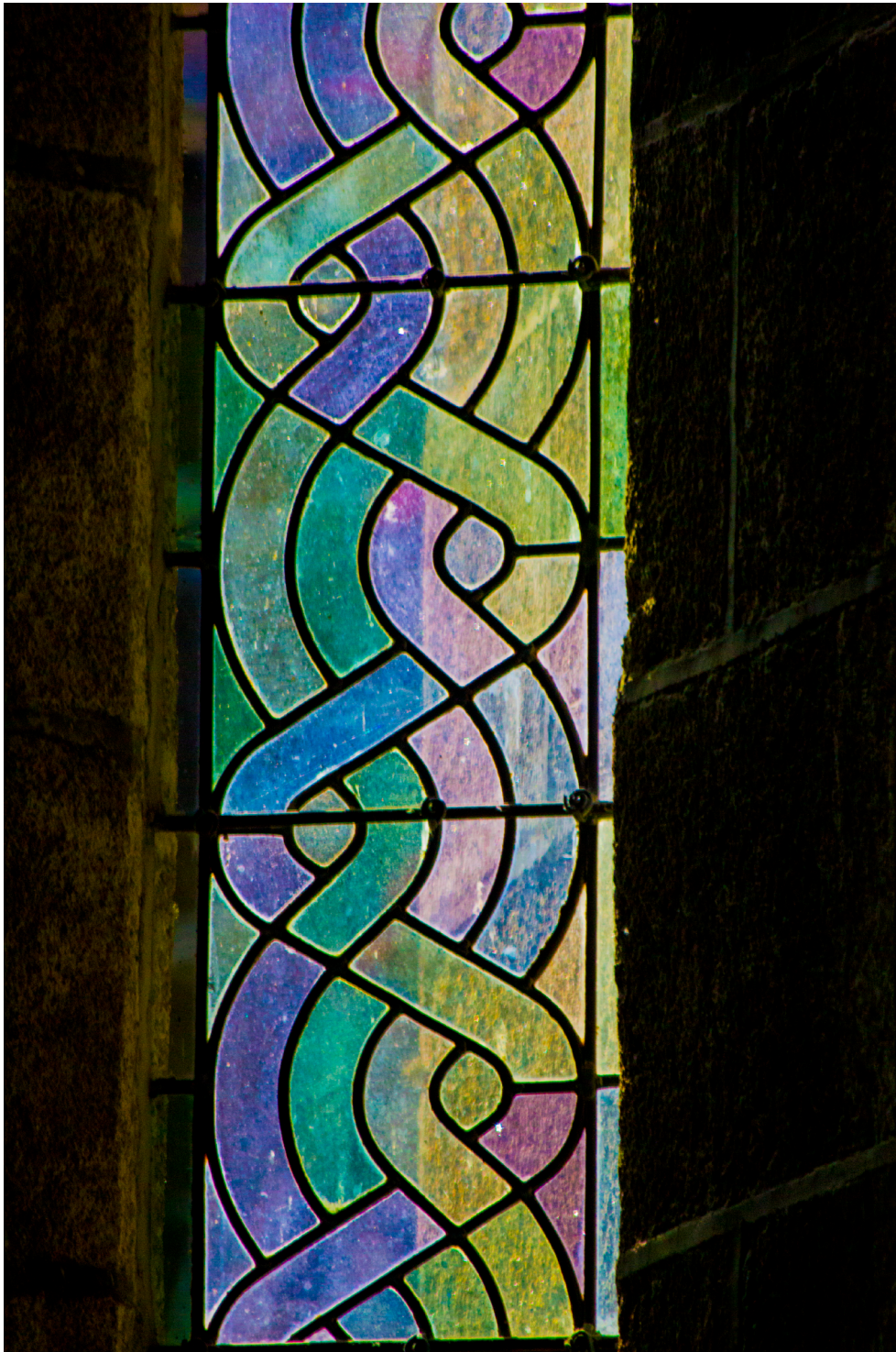
- [1] S.-H. You, D.-H. Tseng, and G.-L. Guo, "A case study on the wastewater reclamation and reuse in the semiconductor industry," *Resour. Conserv. Recycl.*, vol. 32, no. 1, pp. 73–81, 2001.
- [2] I. Muñoz and A. R. Fernández-Alba, "Reducing the environmental impacts of reverse osmosis desalination by using brackish groundwater resources," *Water Res.*, vol. 42, no. 3, pp. 801–811, 2008.
- [3] C. P. Kelley, S. Mohtadi, M. A. Cane, R. Seager, and Y. Kushnir, "Climate change in the Fertile Crescent and implications of the recent Syrian drought," *Proc. Natl. Acad. Sci.*, vol. 112, no. 11, pp. 3241–3246, 2015.
- [4] M. Chaplin, "Water's unexplained properties," *Water structure and science.*, 2015. [Online]. Available: <http://www.lsbu.ac.uk/water/strange.html>. [Accessed: 01-Oct-2015].
- [5] J. L. Finney, "Water? What's so special about it?," *Philos. Trans. R. Soc. Lond. B. Biol. Sci.*, vol. 359, no. 1448, pp. 1145–63; discussion 1163–5, 1323–8, Aug. 2004.
- [6] P. Ball, "Water as an active constituent in cell biology," *Chem. Rev.*, vol. 108, pp. 74–108, 2008.
- [7] A. Nilsson and L. G. M. Pettersson, "Perspective on the structure of liquid water," *Chem. Phys.*, vol. 389, no. 1–3, pp. 1–34, Nov. 2011.
- [8] A. K. Soper, "Recent water myths," *Pure Appl. Chem.*, vol. 82, no. 10, pp. 1855–1867, 2010.
- [9] G. N. I. Clark, C. D. Cappa, J. D. Smith, R. J. Saykally, and T. Head-Gordon, "The structure of ambient water," *Mol. Phys.*, vol. 108, no. 11, pp. 1415–1433, 2010.
- [10] J. Teixeira, A. Luzar, and S. Longeville, "Dynamics of hydrogen bonds: how to probe their role in the unusual properties of liquid water," *J. Phys. Condens. Matter*, vol. 18, pp. S2353–S2362, 2006.
- [11] C. Chen, C. Huang, I. Waluyo, T. Weiss, L. G. M. Pettersson, and A. Nilsson, "Long-range ion–water and ion–ion interactions in aqueous solutions," *Phys. Chem. Chem. Phys.*, 2015.
- [12] V. S. J. Craig, B. W. Ninham, and R. M. Pashley, "The Effect of Electrolytes on Bubble Coalescence in Water," no. type 2, pp. 10192–10197, 1993.
- [13] H. J. Bakker and J. L. Skinner, "Vibrational spectroscopy as a probe of structure and dynamics in liquid water," *Chem. Rev.*, vol. 110, no. 3, pp. 1498–1517, 2010.
- [14] C. Huang, K. T. Wikfeldt, T. Tokushima, D. Nordlund, Y. Harada, U. Bergmann, M. Niebuhr, T. M. Weiss, Y. Horikawa, M. Leetmaa, M. P. Ljungberg, O. Takahashi, A. Lenz, L. Ojamäe, A. P. Lyubartsev, S. Shin, L. G. M. Pettersson, and A. Nilsson, "The inhomogeneous structure of water at ambient conditions," *Proc. Natl. Acad. Sci. U. S. A.*, vol. 106, no. 36, pp. 15214–15218, 2009.
- [15] M. D. Fayer and N. E. Levinger, "Analysis of water in confined geometries and at interfaces," *Annu. Rev. Anal. Chem. (Palo Alto, Calif.)*, vol. 3, pp. 89–107, Jan. 2010.
- [16] A. K. Soper, J. Teixeira, and T. Head-Gordon, "Is ambient water inhomogeneous on the nanometer-length scale?," *Proc. Natl. Acad. Sci. U. S. A.*, vol. 107, no. 12, p. E44; author reply E45, 2010.
- [17] C. Huang, K. T. Wikfeldt, T. Tokushima, D. Nordlund, Y. Harada, U. Bergmann, M. Niebuhr, T. M. Weiss, Y. Horikawa, M. Leetmaa, M. P. Ljungberg, O. Takahashi, A. Lenz, L. Ojamäe, A. P. Lyubartsev, S. Shin, L. G. M. Pettersson, and A. Nilsson, "Reply to Soper et al.: Fluctuations in water around a bimodal distribution of local hydrogen-bonded structural motifs," vol. 107, no. 12, p. E45, 2010.
- [18] G. H. Pollack, *The Fourth Phase of Water: Beyond Solid, Liquid, and Vapor*. Ebner & Sons, 2013.
- [19] R. H. Hinchman and S. J. Cockram, "Water's non-tetrahedral side," *Faraday Discuss.*, vol. 167, p. 529, 2013.
- [20] D. Nordlund, H. Ogasawara, H. Bluhm, O. Takahashi, M. Odelius, M. Nagasono, L. Pettersson, and A. Nilsson, "Probing the Electron Delocalization in Liquid Water and Ice at Attosecond Time Scales," *Phys. Rev. Lett.*, vol. 99, no. 21, p. 217406, Nov. 2007.
- [21] E. Cornicchi, G. Onori, and A. Paciaroni, "Picosecond-time-scale fluctuations of proteins in glassy matrices: the role of viscosity," *Phys. Rev. Lett.*, vol. 95, no. 15, p. 158104, Oct. 2005.
- [22] A. G. Volkov, M. I. Gugeshashvili, and D. W. Deamer, "Energy conversion at liquid/liquid interfaces: Artificial photosynthetic systems," *Electrochim. Acta*, vol. 40, no. 18, pp. 2849–2868, Dec. 1995.
- [23] J.-H. Guo, Y. Luo, A. Augustsson, S. Kashtanov, J.-E. Rubensson, D. K. Shuh, H. Ågren, and J. Nordgren, "Molecular Structure of Alcohol-Water Mixtures," *Phys. Rev. Lett.*, vol. 91, no. 15, p. 157401, Oct. 2003.
- [24] N. Ise, "Like likes like: counterion-mediated attraction in macroionic and colloidal interaction," *Phys. Chem. Chem. Phys.*, vol. 12, no. 35, pp. 10279–87, Sep. 2010.
- [25] J. N. Israelachvili, *Intermolecular and Surface Forces: Revised Third Edition*. Academic Press, 2011.
- [26] F. Sciortino, P. Tartaglia, D. Fisica, I. Nazionale, and R. La, "Harmonic Dynamics in Supercooled Liquids :The Case of Water," pp. 2385–2388, 1997.
- [27] F. Sciortino, "Slow dynamics in supercooled water," *Chem. Phys.*, vol. 258, no. 2–3, pp. 307–314, Aug. 2000.
- [28] F. Caupin and E. Herbert, "Cavitation in water: a review," *Comptes Rendus Phys.*, vol. 7, no. 9–10, pp. 1000–1017, Nov. 2006.
- [29] R. Torre, P. Bartolini, and R. Righini, "Structural relaxation in supercooled water by time-resolved spectroscopy," vol. 428, no. March, pp. 587–590, 2004.
- [30] M. S. Skaf and M. T. Sonoda, "Optical Kerr effect in supercooled water," *Phys. Rev. Lett.*, vol. 94, no. April, pp. 1–4, 2005.
- [31] T. D. Wheeler and A. D. Stroock, "The transpiration of water at negative pressures in a synthetic tree," *Nature*, vol. 455, no. 7210, pp. 208–12, Sep. 2008.
- [32] CMG Lee, Phase diagram of water, licensed for reuse under CC-BY-SA-3.0, [https://commons.wikimedia.org/wiki/File:Phase\\_diagram\\_of\\_water.svg](https://commons.wikimedia.org/wiki/File:Phase_diagram_of_water.svg), retrieved 14 March 2016
- [33] A. Pietropaolo, R. Tor, D. Fisica, C. Nast, V. R. Scientifica, R. Senesi, C. Andreani, and J. Mayers, "Quantum Effects in Water : Proton Kinetic Energy Maxima in Stable and Supercooled Liquid," pp. 318–321, 2009.

- [34] A. Pietropaolo, R. Senesi, C. Andreani, A. Botti, M.A. Ricci, and F. Bruni, "Excess of proton mean kinetic energy in supercooled water.," *Phys. Rev. Lett.*, vol. 100, no. 12, p. 127802, Mar. 2008.
- [35] G. Stirnemann and D. Laage, "Communication: On the origin of the non-Arrhenius behavior in water reorientation dynamics.," *J. Chem. Phys.*, vol. 137, no. 3, p. 031101, Jul. 2012.
- [36] A. Zeidler, P. S. Salmon, H. E. Fischer, J. C. Neufeind, J. M. Simonson, and T. E. Markland, "Isotope effects in water as investigated by neutron diffraction and path integral molecular dynamics.," *J. Phys. Condens. Matter*, vol. 24, no. 28, p. 284126, Jul. 2012.
- [37] M. J. McGrath, J. I. Siepmann, I.-F.W. Kuo, C. J. Mundy, J. VandeVondele, M. Sprik, J. Hutter, F. Mohamed, M. Krack, and M. Parrinello, "Toward a Monte Carlo program for simulating vapor-liquid phase equilibria from first principles," *Comput. Phys. Commun.*, vol. 169, no. 1-3, pp. 289-294, Jul. 2005.
- [38] E. Arunan, G. R. Desiraju, R. A. Klein, J. Sadlej, S. Scheiner, I. Alkorta, D. C. Clary, R. H. Crabtree, J. J. Dannenberg, P. Hobza, H. G. Kjaergaard, A. C. Legon, B. Mennucci, and D. J. Nesbitt, "Definition of the hydrogen bond (IUPAC Recommendations 2011)," *Pure Appl. Chem.*, vol. 83, no. 8, pp. 1637-1641, 2011.
- [39] A. Giuliani, M.A. Ricci, and F. Bruni, "Water Proton Environment: A New Water Anomaly at Atomic Scale?," in *Liquid Polymorphism*, Vol. 152, H. E. Stanley, Ed. Hoboken, NJ, USA: John Wiley & Sons, Inc., 2013, pp. 175-187.
- [40] A. Hassanali, F. Giberti, J. Cuny, T. D. Kühne, and M. Parrinello, "Proton transfer through the water gossamer.," *Proc. Natl. Acad. Sci. U. S. A.*, vol. 110, no. 34, pp. 13723-8, 2013.
- [41] P. M. Chaikin and T. C. Lubensky, *Principles of Condensed Matter Physics*. Cambridge University Press, 2000.
- [42] J. Hemminger, G. Crabtree, and J. Sarrao, "From Quanta to the Continuum: Opportunities for Mesoscale Science," 2012.
- [43] P.W. Anderson, N. Series, and N. Aug, "More Is Different," vol. 177, no. 4047, pp. 393-396, 2006.
- [44] D. Kondepudi and I. Prigogine, *Modern Thermodynamics: From Heat Engines to Dissipative Structures*, vol. 5. Wiley, 2014.
- [45] K. Nakamura, *Quantum versus Chaos: Questions Emerging from Mesoscopic Cosmos*. Kluwer Academic Publishers, 2002.
- [46] T. Chou, K. Mallick, and R. K. P. Zia, "Non-equilibrium statistical mechanics: from a paradigmatic model to biological transport," *Reports Prog. Phys.*, vol. 74, no. 11, p. 116601, 2011.
- [47] M. Pitk, "Negentropy Maximization Principle," pp. 1-67, 2003.

Photo credit chapter 1 overleaf: *Orion Nebula*, NASA, ESA, M. Robberto (Space Telescope Science Institute/ESA) and the Hubble Space Telescope Orion Treasury Project Team - <http://hubblesite.org/newscenter/newsdesk/archive/releases/2006/01/> and is released to the public domain for copyright-free distribution.

Photo credit contents overleaf: *Rhode spool, Mont St. Michel Abbey*, ©A.D. Wexler, 2015





# 2

## Electrohydrodynamic Bridges

*Experimental access to gradient induced non-equilibrium states in liquids*

*A comprehensive review of EHD liquid bridges is given and forms the basis for the further exploration of the molecular response of a molecular liquid to electrical excitation.*



## 2.1 A brief history of electrohydrodynamics

The interaction between electric fields and liquid matter results in a number of forces evolving within the material bulk. In real liquid dielectric systems, the non-negligible field gradients and symmetry breaking geometries result in a number of seemingly peculiar effects. Hertz was one of the first to note the rotational motion in liquid-solid dielectric systems [1]. Quincke observed that the interfacial tension between two fluids was not only changed by the application of an external electric field but that this change resulted in the exertion of forces on the fluid body and could be used to induce rotational motion [2]. Armstrong discovered the floating water bridge (Fig. 2.1) in 1893 [3] which remained an enigmatic gimmick until recently when Fuchs and co-workers explored mass and charge transport mechanics [4], [5] and reopened serious scientific inquiry into the mechanisms by which these bridges form. Electric fields have the ability to lift liquids against the force of gravity as Pellat's work on dielectric liquid rise between parallel plate electrodes shows [6]. This lifting action shows a frequency dependence and ultimately can be described via the Maxwell stress tensor [7]. This is important when considering the liquid level rise associated with electrohydrodynamic (EHD) liquid bridges which under AC conditions also show a frequency dependence [8] similar to electrowetting on dielectric (EWOD) and dielectrophoretic (DEP) mass flow [9]. Furthermore, the application of high potential electric fields is important in controlling liquid jet break up and the interaction of the electric field with liquids is essential for understanding the industrially important process of electrospray atomization [10], [11].

An external electric field does not only influence the surface energy. Due to the action of polarization and shear stress, flow patterns can be established. One example is the circulation of liquids in the presence of inhomogeneous electric fields. Hereby electroconvective currents

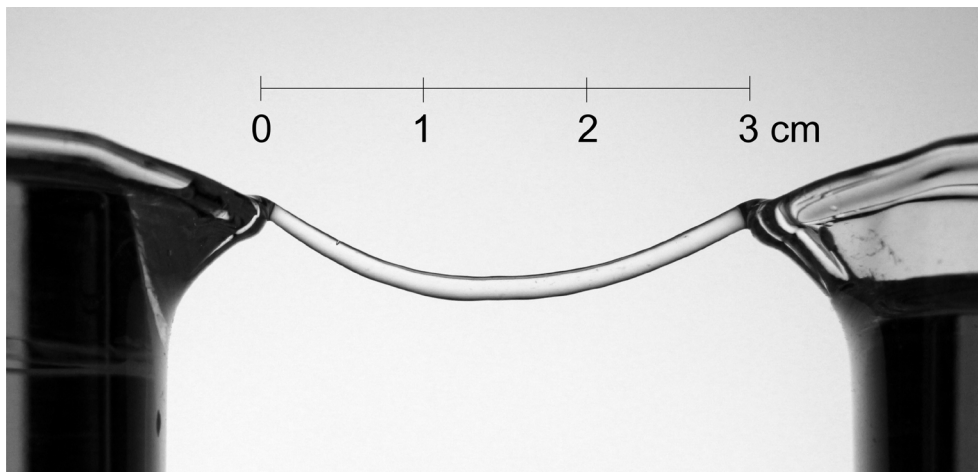


Figure 2.1 the floating water bridge near the limit of maximum extensibility. Catenary length is ~35mm, applied voltage 35 kV.

are established in the liquid bulk driven by shear stresses. Sumoto demonstrated that a fluid motor could be built using a glass rotor containing either a polar liquid or a metal rod immersed in a non-polar dielectric bath and placed within an inhomogeneous electric field [12]. Later analysis by Okano used a homogeneous field approximation [13] to solve the rotation problem which could only qualitatively match the experimental results and required the dielectric liquids to respond as a singular mass. Other researchers on the subject missed the point entirely as they erroneously reported and explored the Sumoto effect as a liquid level rise [14]–[16] in response to the electric field; work pioneered by Pellat [17] and repeated here with a twist. For this, two electrodes were immersed in glycerol – a polar dielectric liquid with high viscosity. The experiment then demonstrates the rise of this fluid between the electrodes when a high-voltage is applied, and is often used to discuss the effects of non-uniform electric

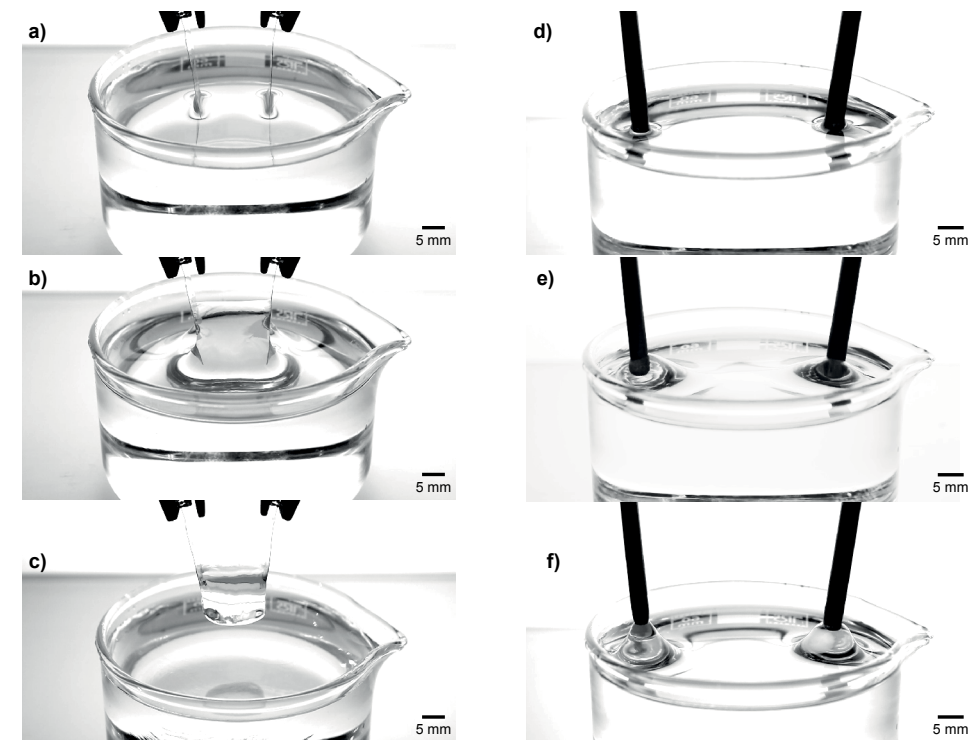


Figure 2.2 Dielectrophoresis and Electrowetting. The electromechanical response of glycerol to high potential electric fields. Two platinum electrodes immersed in anhydrous glycerol at 0 kV (a), and 19 kV (b) show how the liquid is strongly driven upwards. In a modification of Pellat's experiment the lifted volume is completely removed from the subtending reservoir yielding an EHD glycerol bridge held between the two electrodes (c). Likewise, in the case of rod shaped electrodes (d) the contact line advances up the electrode with application of 15 kV (e) raising the electrodes pulls the liquid body upwards to form conical frustum (f) showing the enhanced wetting generated by the strong fields.

fields on liquids [18], [19]. In figure 2.2 it is shown that when lifting the electrodes out of the liquid while under voltage, a horizontal bridge forms between the electrodes revealing all the properties previously discussed for a horizontal water bridge.

It must be mentioned that all EHD discussions of the horizontal liquid bridge experiments use previous literature on a phenomenon named 'liquid bridge', meaning a vertical column of liquid, pinned at each end between planar electrodes, and surrounded by a non-conducting, dielectric gas. These experiments were performed in AC and DC fields; the discussions led to a detailed analysis of this vertical liquid bridge and its stability [20]–[24]. These early experiments in vertical jets between charged electrodes also indicate that the longitudinal field along the jet axis has a stabilizing effect on the liquid – gas interface [25], which was later also discussed for vertical liquid bridges [26].

## 2.1 EHD liquid bridges

EHD liquid bridges are distinct from capillary liquid bridges by three properties: 1) flow, 2) extensibility, 3) thermal emission; a comparison is shown in figure 2.3. Prior to application of voltage small capillary bridges are often observable between the two vessels when the liquid level is even with the spouts in the horizontal configuration. They are unavoidable in the vertical configuration when the separation distance is less than a few millimeters. The applied electric field affects the extensibility of the liquid body. Measurements of the elastic (Young's) modulus in both water and DMSO bridges found that the electric field enhanced the elastic properties of the liquid in the bridge section [27]. It is also interesting to note that for fields on the order of 105 V/m the modulus of water was reported to be as high as 24 MPa, whereas for DMSO the values achieved (~63 kPa) were three orders of magnitude lower. A follow on study suggested that the change in elasticity and the appearance of slow relaxation oscillations of bridge diameter are caused by the production and migration of ions to the bridge surface [28].

Voltage can be applied either in a ramp or step function (see §A.4.2 in the appendix). Voltages below the threshold value ( $V_t$ ) will not produce an EHD bridge but can trigger several other phenomena such as liquid volume expansion (Fig 2.4), upward movement of the liquid electrode contact line (Fig 2.2), rotation and circulation of the liquid bulk (Fig 2.5), electrospraying and jet formation (Fig 2.6).  $V_t$  is a property of the dielectric liquid under investigation, the concentration and type of constituents present, as well as the shielding atmosphere used. The threshold for ignition is also a function of vessel separation. While bridge ignition is possible with separations of many millimeters the applied voltage must be higher and a longer quiescent period can be observed with more violent electrospraying before a stable liquid connection is formed. For example, with water filled reservoirs separated by 5 mm,  $V_t$  increases to 17–20 kV or higher. Once  $V_t$  has been exceeded a combination of arcing and spraying marks ignition (Fig. 2.7a, 2.8a) followed immediately by the formation of a thin bridge < 1 mm in diameter. Once the bridge is established current will flow followed

by swelling of the bridge (Fig 2.7b, 2.8b) to 3–5 mm diameter depending on the conditions. In many of the liquids studied thus far the time from bridge ignition to swelling is between 10–500 ms and is largely a function of the applied voltage, separation distance, and liquid viscosity [8], [30], [31].

In horizontal bridges flow direction is dependent on the specific liquid conditions. Typically the net flow runs from the anode towards the cathode when the high voltage polarity is positive. Upon extension (Fig. 8c) the diameter will fluctuate typically at low frequencies between 1–10 Hz. Higher frequency oscillations also occur and are visible as surface waves. Optically active density waves are visible in the bridge body when back illuminated with a binary fringe pattern. The specific response function of the system is dependent on both the liquid system as well as the power supply characteristics. Vertical bridges are similar in many respects to horizontal ones; however, these do not show evidence of strong mass flow and typically have an exaggerated amphora-like shape. Increasing the driving voltage results

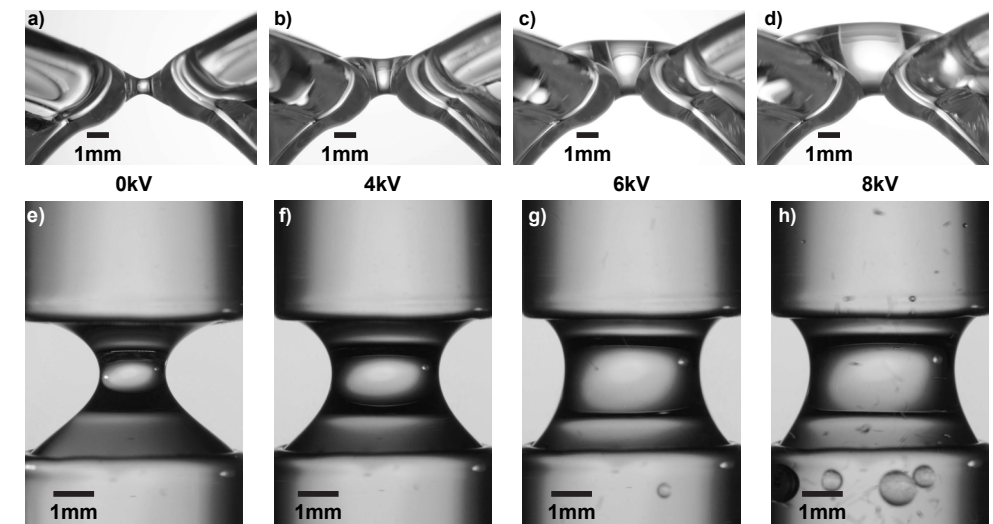


**Figure 2.3 Comparison of capillary and EHD water bridges. A horizontal capillary bridge can only span a small gap of 1.5mm (a) whereas, horizontal EHD bridges at three different voltages 4kV (b), 6kV (c), 8kV (d) easily pass the gap. Note that EHD bridges flow over the spouts whereas a capillary bridge is suspended between the spouts. Likewise the vertical capillary bridge (e) has a narrower waist (~1.5mm dia.) and can only be extended ~3.3mm unlike vertical EHD bridges which are extensible. Three EHD bridges driven at 4kV (f), 6kV (g), and 8kV (h) at the same separation distance as the capillary bridge are shown. Higher voltage increases bridge waist diameter, flow velocity and increased heating as a result of increased power dissipation in the bridge (Ohmic heating). An increase in bubble formation is also observed at higher voltages as gas solubility decreases with increasing temperature. The scale bar in all frames is 1mm.**

in a more cylindrical column of liquid and extensibility (Fig. 2.8c) is a little better than in horizontal bridges (e.g. 1.25 mm/kV for water). Like horizontal bridges vertical bridges can form without direct contact between the fluid bodies prior to voltage. In this case a Taylor cone is observed to form on the upper pendulous droplet. This spray will extend downwards forming a stable jet that quickly swells upon contact with the lower sessile droplet.

Bridge breakup can occur through a number of pathways. It will likely happen when the bridge is either extended too far for the operating voltage or when the applied voltage is lowered below the value necessary to maintain a bridge at a given length as predicted by the electrogravitational number. The breakup will usually proceed through the reduction of the diameter (Fig. 2.7d, 2.8d) until a critical value is reached and Plateau-Rayleigh instabilities disrupt the ligand-like bridge (Fig. 2.7e, 2.8e) into a string of droplets which will migrate in the electric field. Another mode of bridge disruption, typically only found in the horizontal configuration, occurs when the bridge diameter becomes too large resulting in high mass and a downward jet of water. This behavior can lead to oscillations of the bridge producing a “swinging” effect which may cause the bridge to again destabilize into droplets. Large diameter bridges can occur as a result of excess hydrostatic head pressure in one vessel due to unidirectional flow which results in an overflow condition; alternatively increasing the voltage to high values with only small separation will produce a very wide bridge or “water highway”. These large diameter bridges can also fail by collapsing into one large droplet which falls downwards under gravity.

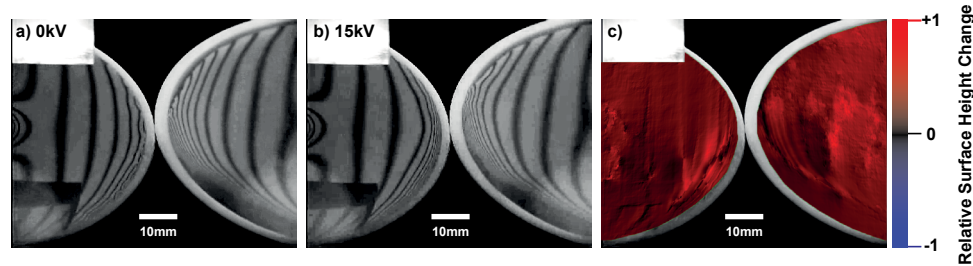


**Figure 2.4 Volume expansion.** The entire liquid surface of two vessels can be seen to rise in response to the applied electric field with the aid of a projected binary fringe pattern. Two Teflon beakers filled with water are imaged with a projected fringe pattern at two different applied voltages a)0kV and b)15kV. The change in the projected fringe (panel c) is analyzed using IDEA [29] software which uses a filtered Fourier transform to convert changes in the fringe modulation frequency to a relative height rise. The non-uniformity of the detected shift is due to the low spatial frequency of the projected fringe and artifacts due to the discrete cosine transform based phase unwrapping method.[30]

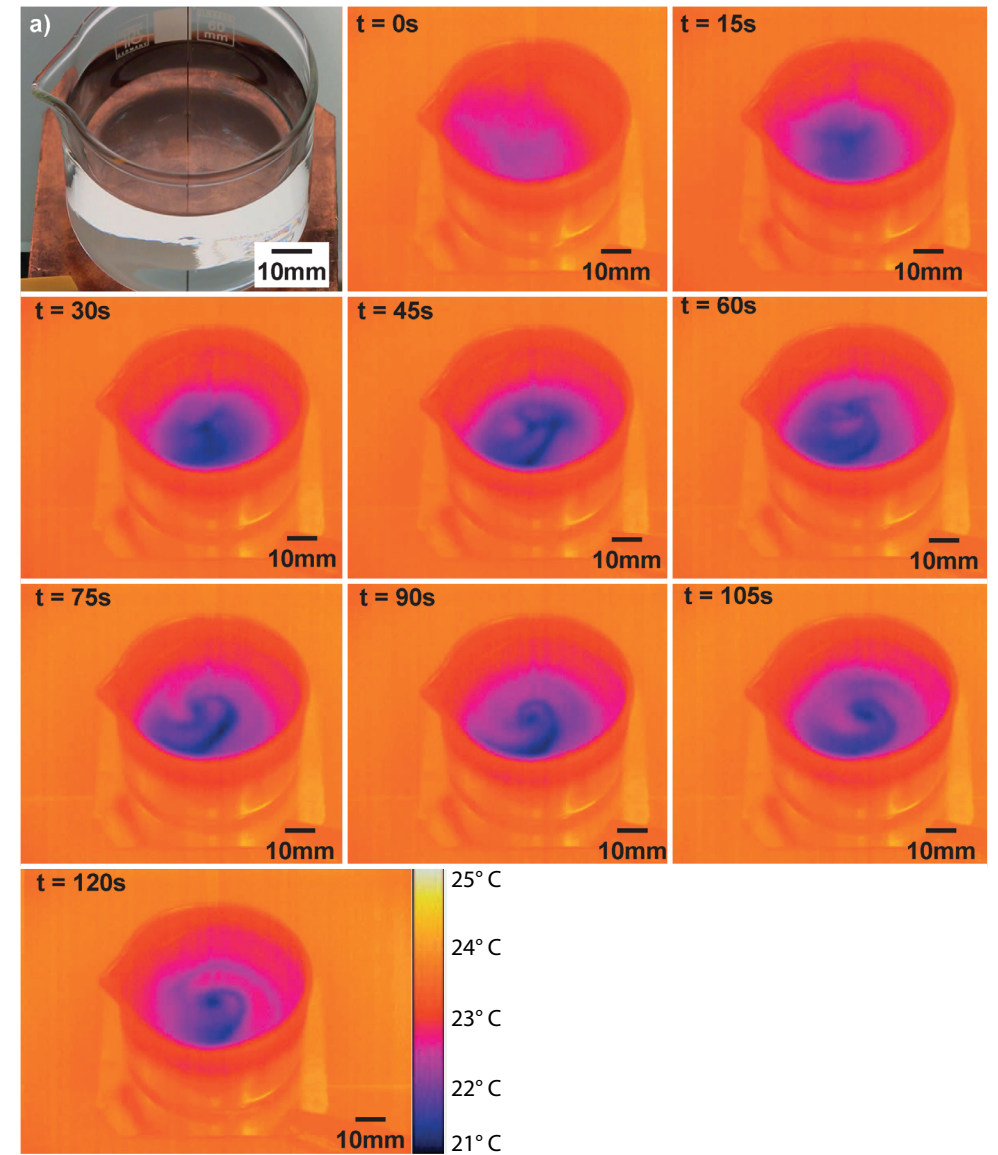


**Figure 2.5 Sumoto Effect visualized in the infrared.** Infrared image sequence of a single vessel of glycerol in an inhomogeneous electric field provided using a simple point plane electrode system shown in visible light in panel (a). Power (19 kVDC) is applied at  $t=0$  seconds. Local surface cooling occurs beneath the point electrode ( $t=15$  sec) This local cooling spreads across the surface and develops heterogeneities, the generation of a rotational force while immediate is initially small and requires approximately 75 seconds to become visible on the surface. Time between frames is 15 seconds. Scale bar is 10 mm.



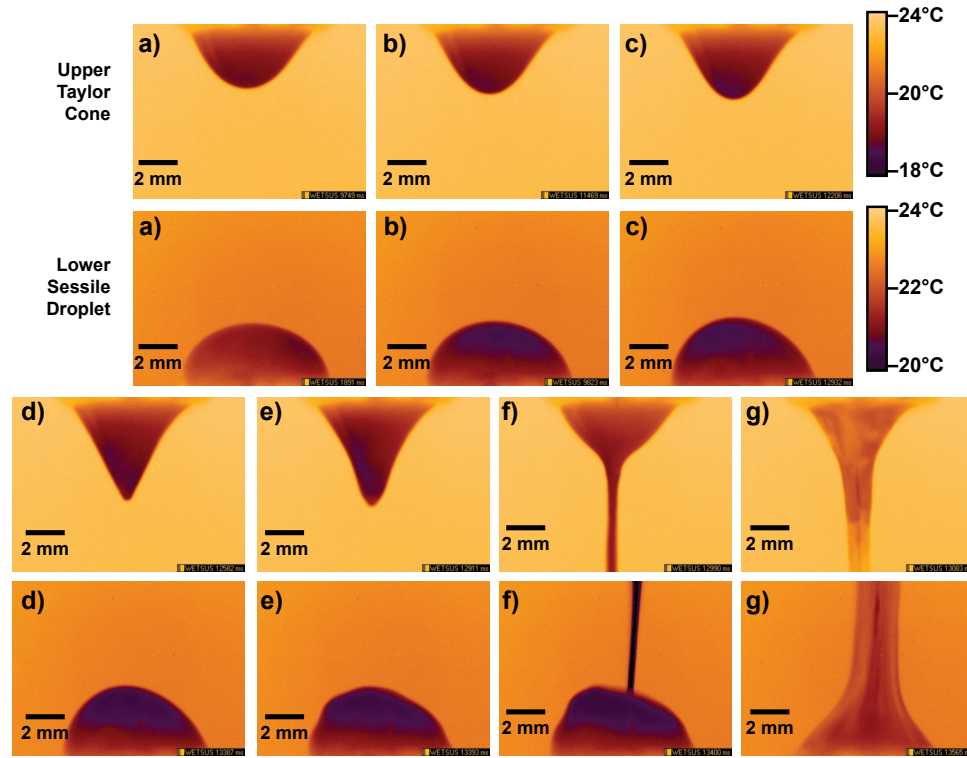


Figure 2.6 Pre-ignition cooling in a vertical bridge system with 10mm separation distance. The upper Taylor cone and lower sessile drop of a vertical water bridge set-up are shown in close-up during a voltage ramp. The images are in the long-wave infrared and represent the IR surface emission. With Planck law and emissivity, local temperatures can be derived. From the images there is a steady cooling and elongation (a-d) of both liquid surfaces as the applied voltage is increased both reaching a minimum temperature of 1-2°C below initial (a) just prior to the ejection of a jet (e) from the upper Taylor cone. The lower droplet recoils in advance of the charged jet but rapidly joins following contact (e-f), the emission quickly rises as a stable EHD liquid bridge is established (g). Temperature reduction was confirmed using a fiber optic thermo-probe. The lower sessile droplet is ~2°C warmer than the upper cone due to operation previously; typically the high voltage vessel will achieve a slightly higher temperature.

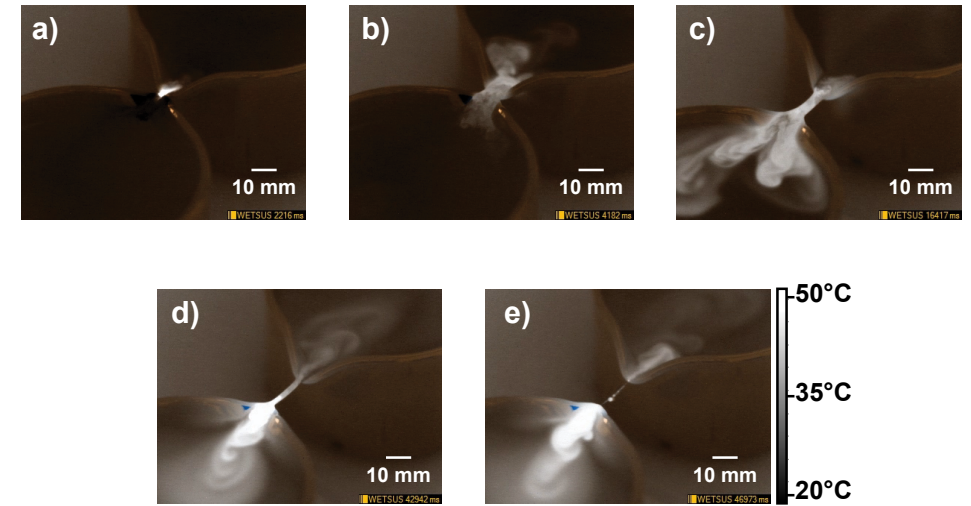


Figure 2.7 Thermographic images of a horizontal water bridge from ignition to extinction. Representative series of composite mid-wave (3.7-5.0  $\mu\text{m}$ ) and long-wave (8.0-9.4  $\mu\text{m}$ ) infrared images characterizing the operational stages for horizontal liquid bridges shown for water: (a) ignition, (b) expansion, (c) extension, (d) stabilization, (e) breakup. In this image sequence the bridge was extinguished by removing power to the system.

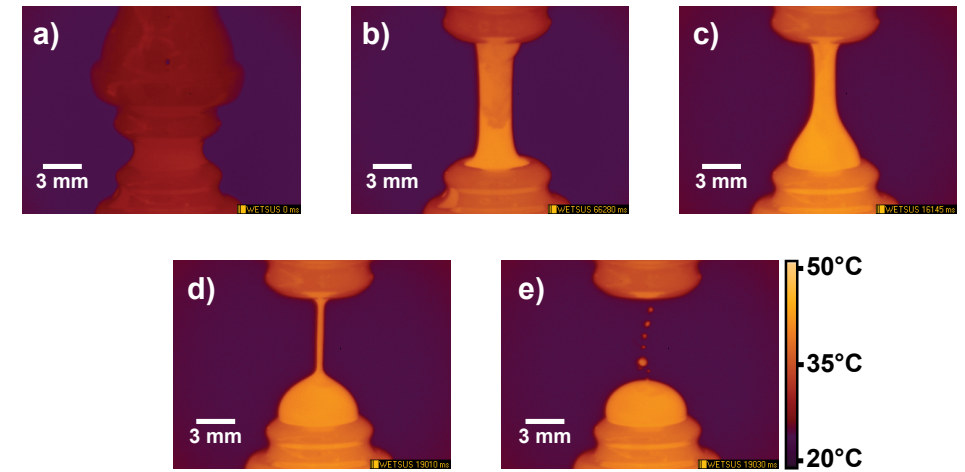


Figure 2.8 Thermographic images of a vertical water bridge from ignition to extinction. Representative series of long-wave infrared (7.5-9.0  $\mu\text{m}$ ) images characterizing the operational stages for vertical liquid bridges shown for water: (a) ignition, (b) expansion, (c) reduced voltage, (d) ligand formation, (e) breakup into droplets under the influence of Rayleigh-plateau instabilities. Elapsed time is shown in ms. The background contrast was adjusted in the last frames to enhance droplet visualization.



## 2.2 Electrohydrodynamic Theory

Understanding the influence of surface symmetry breaking on the process of localizing charge and generated shear stress [32] is essential to research on liquid EHD bridges. Melcher's treatise on continuum electromechanics [19] provides a complete theoretical basis for treating bulk liquids and simplifies free surfaces within the isotropic homogeneous limit. The importance of surfaces is nonetheless clear even from the continuum standpoint as the loss of symmetry results in shear stress that can generate bulk movement. Taken in the general case of discrete mobile fluid volumes which can be polarized and are subject to the resulting reactive force upon approach to the surface, the electric field interaction can be substituted into both the Navier-Stokes [33] and Bernoulli [7], [30], [34] relations to describe the multitude of EHD flow phenomena including liquid bridges.

The methods described in section §3.2 provide access to the formation of EHD liquid bridges which are found in polar liquids whose molecules possess a permanent dipole moment. The imposed inhomogeneous electric field results in a partial polarization of the dipole population yielding a local change of dielectric permittivity thus further reinforcing field gradients [32], [35], [36]. This polarization gives rise to a displacement force which depending on the relative intensity of the applied field will generate a number of different liquid responses (see Figs. 2.2, 2.4-2.6) eventually resulting in the formation of a bridge. The liquid will also develop a Taylor flow [30], [37] along the electrode surfaces especially in cases where there is a sharp edge present on the electrodes. The possibility of charge injection at sharp edges also exists and is consistent with the formation of heterocharge layers which generate electroconvective currents in the liquid bulk [30] thus linking the liquid bridge system with the Sumoto effect [12]. The governing EHD relationships for bridges are extensively covered elsewhere for water and other polar liquids [30], [31], [37], [38] and summarized here. These theoretical approaches suffer certain limitations which should be considered when approaching experimental data. The Maxwell stress tensor treatment [37] is insensitive to field heterogeneities as well as non-uniformities in the liquid bridge. Regardless of this limitation EHD phenomena can be understood through the gradients of the Maxwell pressure, which is part of the Maxwell stress tensor

$$T_{ij} = \epsilon_0 \epsilon_r E_i E_j - \frac{1}{2} \delta_{ij} \epsilon_0 \epsilon_r E_k E_k \quad (\text{Eq. 2.1})$$

with  $T_{ij}$  the stresses in the electric field,  $E_i$  the component of the electric field,  $\delta_{ij}$  the Kronecker delta function,  $\epsilon_0$  the vacuum permittivity ( $8.85 \cdot 10^{-12} \text{ A s V}^{-1} \text{ m}^{-1}$ ) and  $\epsilon_r$  the relative permittivity of the liquid as given in Table 2.1. With this approach the pressure in the Bernoulli flow of an adiabatic, incompressible liquid is given by [37]

$$p + \frac{1}{2} \rho v^2 + \rho gh - \frac{1}{2} \epsilon_0 (\epsilon_r - 1) E^2 = \text{const.} \quad (\text{Eq. 2.2})$$

with the pressure  $p$ , the fluid density  $\rho$ , the fluid velocity  $v$ , the height  $h$  of the level rise caused by the hydrostatic pressure  $\rho gh$ , and  $g$  the acceleration due to gravity ( $g = 9.80665 \text{ ms}^{-2}$ ). In equilibrium the hydrostatic pressure and the Maxwell pressure counteract, causing a rise of the liquid level as observed in Fig. 2.2b. Using the relation between force density and Maxwell pressure  $p_{\text{Maxwell}}$  we obtain the Kelvin force density

$$\vec{f}_{\text{Kelvin}} = -\nabla p_{\text{Maxwell}} = \frac{1}{2} \epsilon_0 (\epsilon_r - 1) \nabla (E^2) \quad (\text{Eq. 2.3})$$

Thus, the gradient of the Maxwell pressure gives the resulting force on a dielectric liquid in a varying electric field, directing upward into the region of higher field intensity. This relation is valid within a linear dielectric with constant permittivity. Therefore, glycerol is pushed into the electric field between the electrodes in Fig. 2.2b because of the force on individual dipoles in the fringing field between the tips of the electrodes.

When discussing the horizontal liquid bridges forming between two beakers in terms of the Maxwell pressure, these bridges have a high electric field due to the small cross-section and hence a negative pressure that tends to replenish the liquid within the bridge against drainage.

Table. 2.1 Liquids tested in a horizontal bridge (data at 298 K from Riddick and Bunger 1989 [39]; Wohlfarth 2008 [40]).

| Name              | Relative static permittivity | Conductivity [ $\mu\text{S cm}^{-1}$ ] | Dynamic viscosity [ $\text{mPa s}$ ] | Surface tension [ $\text{mN m}^{-1}$ ] | Density [ $\text{kg m}^{-3}$ ] |
|-------------------|------------------------------|--|--------------------------------------|--|--------------------------------|
| Cyclohexane       | 2.02                         | 0.05                                   | 0.883                                | 24.4                                   | 773.9                          |
| Tetrahydrofuran   | 7.36                         | 0.048                                  | 0.471                                | 27.04                                  | 881.9                          |
| Dichloromethane   | 8.51                         | 0.000043                               | 0.413                                | 27.2                                   | 1316.6                         |
| 2-Propanol        | 19.45                        | 0.058                                  | 2.039                                | 21.1                                   | 780.7                          |
| Acetone           | 20.59                        | 0.005                                  | 0.303                                | 22.7                                   | 784.3                          |
| 1-Propanol        | 20.73                        | 0.00917                                | 1.952                                | 23.1                                   | 798.9                          |
| Ethanol           | 24.35                        | 0.00135                                | 1.067                                | 22.3                                   | 784.9                          |
| Methanol          | 33.77                        | 0.0015                                 | 0.542                                | 22.1                                   | 768.3                          |
| Dimethylformamide | 37.65                        | 0.06                                   | 0.796                                | 36.3                                   | 943.8                          |
| Glycerol          | 42.49                        | 0.06                                   | 987.8                                | 63.0                                   | 1258.1                         |
| Dimethylsulfoxide | 47.13                        | 0.002                                  | 1.98                                 | 42.8                                   | 1095.4                         |
| Water, deionised  | 79.5                         | 0.05                                   | 0.89                                 | 72.01                                  | 997.1                          |
| Methylformamide   | 176.54                       | 0.8                                    | 1.65                                 | 39.58                                  | 966.6                          |

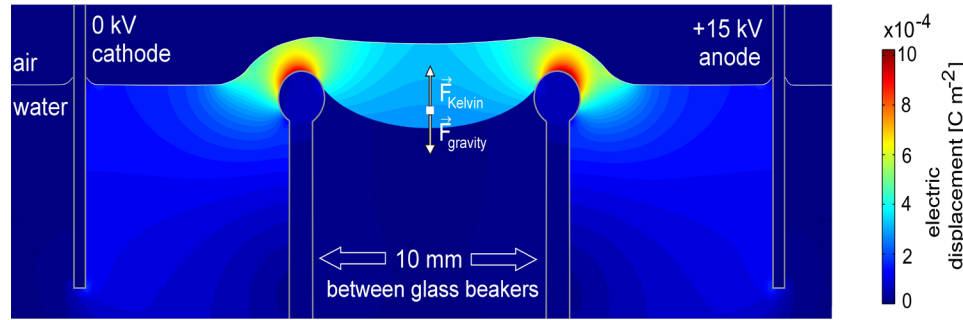


**Figure 2.9** finite numerical simulation of the electric field within the bridge using the electrostatic interface in the AC/DC module in Comsol 4.1 multiphysics software (Comsol Inc., Palo Alto, CA) based on Gauss' law, solving the elements grid with a quadratic interpolation. A 2-dimensional geometry was chosen, with two glass beakers 20 mm in width and 10 mm height (glass  $\epsilon_r = 4.2$ ), metal electrodes and a water bridge 10 mm long with 3 mm diameter at the beaker (water  $\epsilon_r = 80$ ), slightly sagging in the middle. Thus, for this simulation of the electric field inside the bridge the surface geometry was that for a stable bridge under equilibrium conditions. The infinite boundary for the mesh was set at a 50 mm radius away from the bridge centre.

Especially with long axial lengths horizontal bridges slightly sag under their weight, leading to distortions of the electric field lines inside the bridge. This is schematically plotted in figure 2.9, with the electric displacement field as number. Whenever a fluid element wants to drip from the bridge, the concomitant distortion in the electric field will counteract this motion and stabilize the bridge against gravity by the non-zero gradient of the Maxwell pressure (eq.2.3) and the resulting force density.

## 2.3 The floating water bridge: stability against gravity

The Maxwell stress equations derived above provide steady state definitions that can predict the mechanical properties and physical dimensions of the bridge (e.g. aspect ratio); however, the flow dynamics and important transient phenomena (e.g. bridge creation) are not predicted. Three dimensionless numbers are useful when analyzing the bridge's stability and are derived here as previously published by Marin & Lohse [31]. The electrocapillary number ( $Ca_E$ ) is which is defined as the ratio between electrical and capillary forces:

$$Ca_E = \frac{\epsilon_0 \epsilon_r E_t^2 D_m}{\gamma}; D_m = \sqrt{d_s d_l} \quad (\text{Eq 2.4})$$

Where  $\epsilon_0$  is the vacuum permittivity,  $\epsilon_r$  the relative dielectric permittivity of the liquid,  $E_t$  is the electric field across the bridge,  $\gamma$  is the surface tension,  $d_s$  and  $d_l$  are the vertical and horizontal projections of the diameter so as to yield the mean diameter  $D_m$ . The Bond number ( $Bo$ ) describes the balance between gravity and capillary forces:

$$Bo = \frac{\rho g V^{2/3}}{\gamma}; V = \frac{\pi}{4} d_s d_l l \quad (\text{Eq 2.5})$$

where  $g$  is the gravitational acceleration,  $l$  is the free bridge length, and  $V$  is the bridge volume. The relationship between gravitational, capillary, and electrical forces can be expressed in terms of the electrogravitational number  $G_E$ :

$$G_E = \frac{\rho g V^{1/3}}{\epsilon_0 \epsilon_r E^2} = \left( \frac{4}{\pi \beta} \right)^{1/3} \frac{Bo}{Ca_E}; \beta = \frac{l}{D_m} \quad (\text{Eq 2.6})$$

The maximum extensibility of a bridge is related to the applied voltage while the current flowing through the bridge is related to the cross sectional area and thus the diameter. These relationships are coupled, determine the bridge volume, and thus define the region of stability for any given operating liquid bridge. The characteristic curves for a water bridge are given in figure 2.10 which shows a lower threshold below which the applied field is too weak to overcome surface tension forces and an upper threshold above which the mass of the bridge is too great resulting in leaking which further disrupts the field and results in bridge rupture.

At the macroscale EHD phenomena arise simply because the necessary pressure terms which accompany electrostriction are only found at the liquid interface [34]. Furthermore, there is a relationship between the stability of EHD liquid bridges and the stability of the interfaces in the system. In the case of reduced gravity experiments [41] the expanding surface area results in a force which tears the bridge apart. Likewise if the surface is too confined or the subtending contact area small the bridge will likely develop instabilities. This can be illustrated in bridges which are fed by tubing or in the case of vertical bridges where one electrode is pulled upwards from the surface - the resulting bridges are less stable in long term operation as they lack the characteristic flow dynamics found in the situation where both reservoirs have a large free surface area. Bridges whose connections to the fluid reservoir are confined within tubing show increased thermal accumulation and falling surface tension. It is typical that an air interface will spontaneously form within the tubing. This condition limits both the maximum extensibility as well as the average lifetime of the bridge for confined liquid bridges. Open surface water bridges can be extended to 35 mm length at 35 kV (Fig. 2.1) whereas no bridge will persist at such an accelerating voltage in confinement as the liquid preferentially transitions into an electrospray mode. Likewise free surface water bridges have stability lifetimes approaching 10 hours under controlled conditions, whereas in tube fed systems the lifetime is typically less than 2 hours.

## Set of Characteristic Curves - The Floating Water Bridge

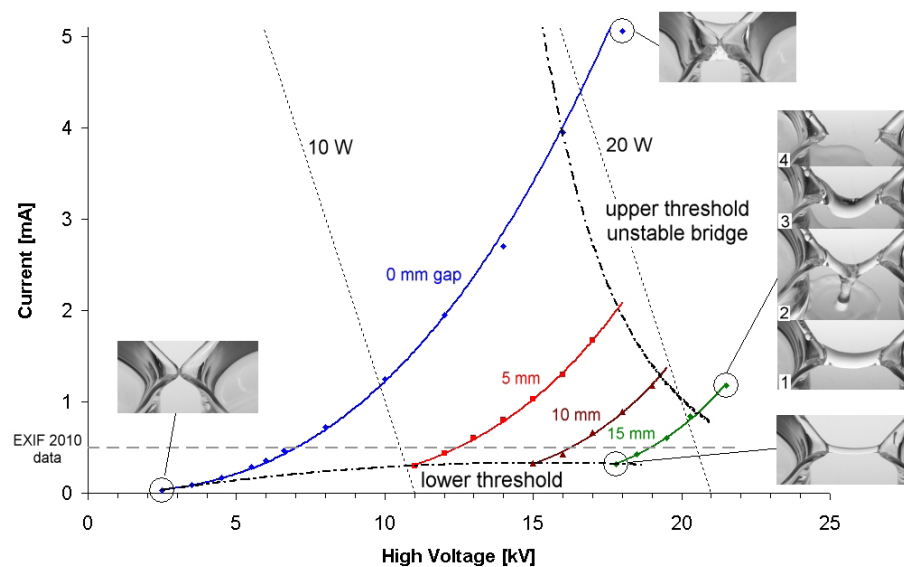


**Figure 2.10** Characteristic curves for a liquid water bridge. The current-voltage relationship for liquid water bridges at 0, 5, 10, 15 mm separation distance is plotted. A lower threshold below which no liquid bridge will form (see inset photo at lower left), and an upper threshold above which bridges are unstable (inset photos 1-4) bound the region of stability. For most bridges with some measureable extension (i.e.  $\geq 5$  mm) the total power dissipation lies between 10 and 20 watts. The rupture of a bridge beyond the upper threshold will often follow a sequence of events progressing from normal operation (inset 1), to leaking (inset 2), sagging (inset 3), and finally rupture (inset 4).

## 2.3 Bridges in other polar liquids

A number of polar liquids have been explored including water, the lower aliphatic alcohols (e.g. methanol), poly-alcohols (e.g. glycerol), dimethylsulfoxide (DMSO), and other polar organics (e.g. dimethylformamide). Figure 2.11 provides a visual comparison of EHD bridges produced from many liquids. Non-polar dielectric liquids (e.g. hexane) do not exhibit bridge formation. The dielectric liquids capable of supporting bridges thus far studied [8], [30], [31] lie within a well-defined group of physical parameters that establish a good starting point for further experimentation: low conductivity ( $\sigma < 5 \mu\text{S/cm}$ ), moderate static relative permittivity ( $\epsilon = 20$ -80), moderate to high surface tension ( $\gamma = 21$ -72 mN/m). Interestingly a wide range of viscosities ( $\eta = 0.3$ -987 mPa·s) work in such bridges. In liquids with sufficiently high viscosity

such as glycerol it is possible to pull a bridge directly from the liquid bulk (see Fig. 2.2) and is an important link between dielectrophoretic forces and liquid bridges. Ionic solutions (e.g.  $\text{NaCl}_{(\text{aq})}$ ) are highly disruptive to bridge formation and in previous studies [42] have been shown to increase the temperature of the bridge, decrease the length to applied voltage ratio, and to reduce extensibility. This behavior is largely attributed to the charge shielding effect of dissolved ions as well as increased current conduction which reduces the coupling between the fluid volume elements and the electric field.

The more general treatment of liquid bridges in polar solvents [19], [30] provides the combined pressure terms operating with the bridge to predict the forces governing flow dynamics in the context of a modified Bernoulli equation with electric displacement terms added to the pressure term. In addition the Onsager relationship for ion stability [43] is incorporated in agreement with experimental observations on equilibrium pumping direction and thermal emission. As a point of comparison figure 2.12 shows the thermal emission distribution in DMSO and glycerol.

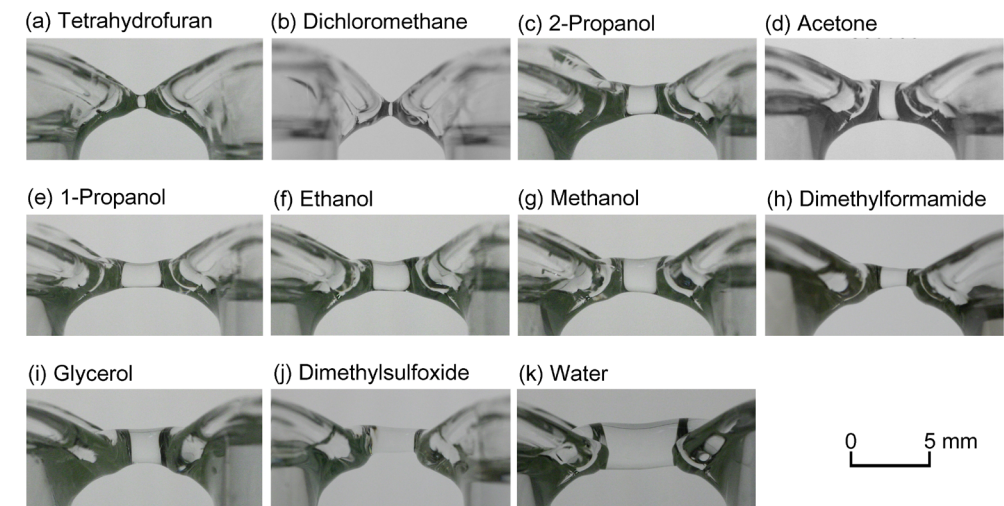


**Figure 2.11** (opposite) Horizontal bridges forming in different polar liquids under atmospheric conditions and DC voltage. (a) Tetrahydrofuran 16 kV, (b) dichloromethane 19 kV, (c) 2-propanol 8 kV, (d) acetone 10 kV, (e) 1-propanol 10 kV, (f) ethanol 9.5 kV, (g) methanol 9.5 kV, (h) dimethylformamide 12.5 kV, (i) glycerol 11.5 kV, (j) dimethylsulfoxide 12 kV, (k) water 12 kV.

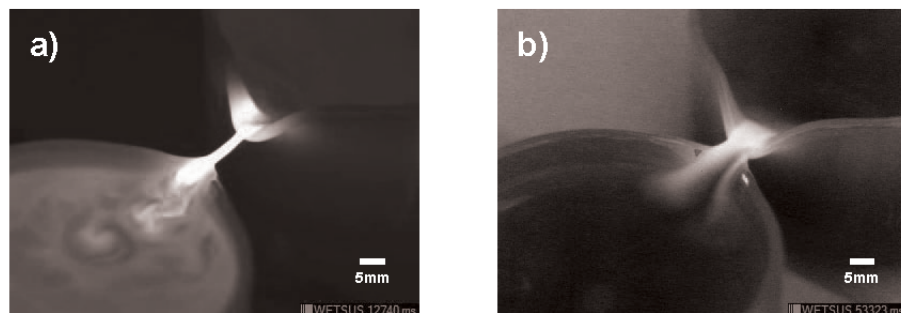


**Figure 2.12** Thermographic images of horizontal bridges in DMSO and glycerol. Dimethylsulfoxide (DMSO) (a), and glycerol (b) bridge emission in a composite of mid-wave ( $3.7\text{--}5.0\ \mu\text{m}$ ) and long-wave infrared ( $8.0\text{--}9.4\ \mu\text{m}$ ).

## 2.4 Is there a molecular basis to EHD phenomena?

EHD phenomena are typically considered only at the continuum level. A limited number of studies on the molecular basis of liquid bridges have been conducted. A Raman study [44] using vertical AC bridges investigated the inter-molecular OH-stretching band compared to bulk water. Some changes in the scattering profiles after application of the electric field are shown to have a structural origin. Using ultrafast mid-infrared pump probe spectroscopy on a floating water bridge [45] the vibrational lifetime of the OH stretch vibration of HDO molecules contained in an HDO:D<sub>2</sub>O water bridge was found to be shorter ( $630 \pm 50$  fs) than for HDO molecules in bulk HDO:D<sub>2</sub>O ( $740 \pm 40$  fs), whereas in contrast, the thermalization dynamics following the vibrational relaxation are much slower ( $1500 \pm 400$  fs) than in bulk HDO:D<sub>2</sub>O ( $250 \pm 90$  fs). These differences in energy relaxation dynamics strongly indicate that the water bridge and bulk water differ on a molecular scale and will be examined in both chapters 4 and 5. Another more recent Raman study reported that in DC water bridges there is a radial distribution in the spectra which is indicative of relative difference in the local pH between the core and outer shell of the bridge [46]. The radial distribution of physical characteristics within EHD liquid bridges is further supported by inelastic UV scattering experiments [46] which gives contradictory radial distributions in the temperature and density profiles and can be explained either by a gradient in molecular degrees of freedom or the presence of a secondary phase as nano-bubbles. The later concept is not supported by a small angle X-ray scattering study [48] while the concept of hindered rotation (i.e. librations) is supported from infrared emission spectra [49]. The preferential flow direction in EHD liquid bridges arises from changes in the auto-dissociation kinetics. In agreement with the

work of Onsager this finding holds promise for connecting molecular and continuum level phenomena [30]. Further evidence for a molecular basis to EHD phenomena is found in the observation that thermal emission from a dielectric droplet decreases locally in response to the increasing electric field and reaches a minimum just prior to the onset of a bridge (see Fig. 2.6).

## 2.5 Concluding Remark

EHD bridges are complex phenomena that depend on the balance between competing external forces such as gravity and the electric field moderated by the fluid properties. These phenomena present an opportunity to examine the interplay between forces at multiple length scales. These systems are far from thermal equilibrium and as such offer additional benefits when examining the dissipation of energy in molecular liquids. Such studies can help to clarify the relationships governing the emergence of long range order from short range correlated materials – liquids.



## Bibliography

- [1] H. R. Hertz, "Ueber die Vertheilung der Electricität auf der Oberfläche bewegter Leiter," *Ann. Phys.*, vol. 249, no. 6, pp. 266–275, 1881.
- [2] G. Quincke, "Electrische Untersuchungen," *Ann. Phys.*, vol. 255, no. 8, pp. 545–588, 1883.
- [3] W. Armstrong, "Account of the transactions of the Newsactle Literary and Philosophical Society," 1893.
- [4] E. C. Fuchs, J. Woisetschlager, K. Gatterer, E. Maier, R. Pecnik, G. Holler, and H. Eisenkölbl, "The floating water bridge," *J. Phys. D: Appl. Phys.*, vol. 40, no. 19, pp. 6112–6114, Oct. 2007.
- [5] E. C. Fuchs, K. Gatterer, G. Holler, and J. Woisetschlager, "Dynamics of the floating water bridge," *J. Phys. D: Appl. Phys.*, vol. 41, no. 18, p. 185502, Sep. 2008.
- [6] M. H. Pellat, "Mesure de la force agissant sur les diélectriques liquides non électrisés placés dans un champ électrique," *C R Acad Sci Paris*, vol. 123, pp. 691–696, 1896.
- [7] T. B. Jones, "An electromechanical interpretation of electrowetting," *J. Micromechanics Microengineering*, vol. 15, no. 6, pp. 1184–1187, Jun. 2005.
- [8] F. Saija, F. Aliotta, M. E. Fontanella, M. Pochylski, G. Salvato, C. Vasi, and R. C. Ponterio, "Communication: An extended model of liquid bridging," *J. Chem. Phys.*, vol. 133, no. 8, p. 081104, Aug. 2010.
- [9] T. B. Jones, K. Wang, and N. York, "Frequency-Dependent Electromechanics of Aqueous Liquids : Electrowetting and Dielectrophoresis," no. 7, pp. 7646–7651, 2004.
- [10] R. T. Collins, M. T. Harris, and O. A. Basaran, "Breakup of electrified jets," *J. Fluid Mech.*, vol. 588, pp. 75–129, 2007.
- [11] M. Cloupeau and B. Prunet-Foch, "Electrostatic spraying of liquids in cone-jet mode," *Journal of Electrostatics*, vol. 22, pp. 135–159, 1989.
- [12] I. Sumoto, "An Interesting Phenomenon Observed on Some Dielectrics," *J. Phys. Japan*, vol. 10, p. 494, 1955.
- [13] K. Okano, "On Rotary Motion of Dielectrics in Static Electric Fields," *Jpn. J. Appl. Phys.*, vol. 4, no. 4, p. 292–8, 1965.
- [14] W. F. Pickard, "An Explanation of the DC Sumoto Effect," *J. Appl. Phys.*, vol. 33, no. 3, pp. 941–942, 1962.
- [15] W. F. Pickard, "Electrical Force Effects in Dielectric Liquids," *Prog. Dielectr.*, vol. 6, pp. 1–39, 1965.
- [16] J. S. Mirza, C. W. Smith, and J. H. Calderwood, "Liquid motion and internal pressure in electrically stressed insulating liquids," *Journal of Physics D: Applied Physics*, vol. 3, p. 580, 1970.
- [17] M. H. Pellat, "Force agissant á la surface de séparation de deux diélectriques," *C.R. Seances Acad. Sci.*, vol. 119, pp. 675–678, 1894.
- [18] T. B. Jones, "On the relationship of dielectrophoresis and electrowetting," *Langmuir*, vol. 18, no. 2, pp. 4437–4443, 2002.
- [19] J. M. Melcher, "Electromechanical Flows," *Contin. Electromechanics*, 1981.
- [20] R. J. Raco, "Electrically Supported Column of Liquid," *Science (80-.)*, vol. 160, no. 3825, pp. 311–312, 1968.
- [21] C. L. Burcham and D. A. Saville, "Electrohydrodynamic stability: Taylor–Melcher theory for a liquid bridge suspended in a dielectric gas," *J. Fluid Mech.*, vol. 452, pp. 163–187, Feb. 2002.
- [22] C. L. Burcham and D. A. Saville, "The electrohydrodynamic stability of a liquid bridge: microgravity experiments on a bridge suspended in a dielectric gas," *J. Fluid Mech.*, vol. 405, pp. 37–56, 2000.
- [23] D. A. Saville, "ELECTROHYDRODYNAMICS: The Taylor-Melcher Leaky Dielectric Model," *Annu. Rev. Fluid Mech.*, vol. 29, no. 1962, pp. 27–64, 1997.
- [24] H. González, F. M. J. McCluskey, a. Castellanos, and a. Barrero, "Stabilization of dielectric liquid bridges by electric fields in the absence of gravity," *J. Fluid Mech.*, vol. 206, p. 545, 1989.
- [25] J. R. Melcher and E. P. Warren, "Electrohydrodynamics of a current-carrying semi-insulating jet," *J. Fluid Mech.*, vol. 47, pp. 127–143, 1971.
- [26] A. Ramos and A. Castellanos, "Bifurcation diagrams of axisymmetric liquid bridges of arbitrary volume in electric and gravitational axial fields," *J. Fluid Mech.*, vol. 249, pp. 207–225, 1993.
- [27] O. Teschke, D. Mendez Soares, and J. F. Valente Filho, "Floating liquid bridge tensile behavior: Electric-field-induced Young's modulus measurements," *Appl. Phys. Lett.*, vol. 103, no. 25, p. 251608, 2013.
- [28] O. Teschke, G. WE, J. Roberto de Castro, J. Filho, and S. DM, "Relaxation Oscillations in Floating Liquid Bridges," *Chem. Sci. J.*, vol. 6, no. 3, pp. 1–5, 2015.
- [29] M. Hipp, J. Woisetschlager, P. Reiterer, and T. Neger, "Digital evaluation of interferograms," *Measurement*, vol. 36, no. 1, pp. 53–66, Jul. 2004.
- [30] J. Woisetschlager, A. D. Wexler, G. Holler, M. Eisenhut, K. Gatterer, and E. C. Fuchs, "Horizontal bridges in polar dielectric liquids," *Exp. Fluids*, vol. 52, no. 1, pp. 193–205, 2012.
- [31] A. G. Marín and D. Lohse, "Building water bridges in air: Electrohydrodynamics of the floating water bridge," *Phys. Fluids*, vol. 22, no. 12, p. 122104, 2010.
- [32] J. R. Melcher and G. I. Taylor, "Electrohydrodynamics: A Review of the Role of Interfacial Shear Stresses," *Annu. Rev. Fluid Mech.*, vol. 1, no. 1, pp. 111–146, Jan. 1969.
- [33] C. L. Druzgalski, M. B. Andersen, and a. Mani, "Direct numerical simulation of electroconvective instability and hydrodynamic chaos near an ion-selective surface," *Phys. Fluids*, vol. 25, no. 11, p. 110804, 2013.
- [34] J. R. Melcher, *A tutorial on induced electrohydrodynamic forces*. Cambridge, MA: MIT Press, 1968.
- [35] R. P. Feynman, R. B. Leighton, and M. Sands, *The Feynman Lectures on Physics, Vol. II: The New Millennium Edition: Mainly Electromagnetism and Matter*, vol. 24. Basic Books, 2010.
- [36] X. Zhang and M. Zahn, "Kerr electro-optic field mapping study of the effect of charge injection on the impulse breakdown strength of transformer oil," *Appl. Phys. Lett.*, vol. 103, no. 16, p. 162906, Oct. 2013.

- [37] A. Widom, J. Swain, J. Silverberg, S. Sivasubramanian, and Y. Srivastava, "Theory of the Maxwell pressure tensor and the tension in a water bridge," *Phys. Rev. E*, vol. 80, no. 1, p. 016301, Jul. 2009.
- [38] K. Morawetz, "Theory of water and charged liquid bridges," *Phys. Rev. E - Stat. Nonlinear, Soft Matter Phys.*, vol. 86, no. 2, pp. 1–9, 2012.
- [39] J. A. Riddick and W. B. Bunger, *Organic Solvents: Physical properties and methods of purification*. New York: Wiley, 1989.
- [40] C. H. Wohlfarth, Ed., *Springer Materials -- The Landolt-Börnstein Database*. Berlin, Heidelberg: Springer, 2008.
- [41] E. C. Fuchs, L. L. F. Agostinho, A. Wexler, R. M. Wagterveld, J. Tuinstra, and J. Woisetschlager, "The behaviour of a floating water bridge under reduced gravity conditions," *J. Phys. D: Appl. Phys.*, vol. 44, no. 2, p. 025501, Jan. 2011.
- [42] H. Nishiumi and F. Honda, "Effects of Electrolyte on Floating Water Bridge," *Adv. Phys. Chem.*, vol. 2009, pp. 1–3, 2009.
- [43] S. B. Fuller, E. J. Wilhelm, and J. M. Jacobson, "Ink-jet printed nanoparticle microelectromechanical systems," *J. Microelectromechanical Syst.*, vol. 11, no. 1, pp. 54–60, 2002.
- [44] R. C. Ponterio, M. Pochylski, F. Aliotta, C. Vasi, M. E. Fontanella, and F. Saija, "Raman scattering measurements on a floating water bridge," *J. Phys. D: Appl. Phys.*, vol. 43, no. 17, p. 175405, May 2010.
- [45] L. Piatkowski, A. D. Wexler, E. C. Fuchs, H. Schoenmaker, and H. J. Bakker, "Ultrafast vibrational energy relaxation of the water bridge," *Phys. Chem. Chem. Phys.*, vol. 14, no. 18, pp. 6160–4, May 2012.
- [46] V. B. Oshurko, A. A. Ropyanoi, A. N. Fedorov, M. V. Fedosov, and N. A. Shelaeva, "Spectrum of OH-stretching vibrations of water in a 'floating' water bridge," *Tech. Phys.*, vol. 57, no. 11, pp. 1589–1592, Nov. 2012.
- [47] E. C. Fuchs, B. Bitschnau, S. Di Fonzo, A. Gessini, and J. Woisetschlager, "Inelastic UV Scattering in a Floating Water Bridge," vol. 1, pp. 135–147, 2011.
- [48] L. B. Skinner, C. J. Benmore, B. Shyam, J. K. R. Weber, and J. B. Parise, "Structure of the floating water bridge and water in an electric field," *Proc. Natl. Acad. Sci. U. S. A.*, vol. 109, no. 41, pp. 16463–8, Oct. 2012.
- [49] E. C. Fuchs, A. Cherukupally, A. H. Paulitsch-Fuchs, L. L. F. Agostinho, A. D. Wexler, J. Woisetschlager, and F. T. Freund, "Investigation of the mid-infrared emission of a floating water bridge," *J. Phys. D: Appl. Phys.*, vol. 45, no. 47, p. 475401, Nov. 2012.

Photo credit chapter 2 overleaf: *River Window, Mont St. Michel Abbey*, ©A.D. Wexler, 2015

## Appendix A: Safe EHD Bridge Protocol

### A.1. General recommendations

A1.1) Wear disposable, powder-free gloves throughout the set-up of the experiment to prevent contamination by sweat or oil from hands.

A1.2) Clean all glassware, electrodes and any other parts that contact the liquid under study, paying special attention to prevent the introduction of contaminants that can dissolve in the liquid phase.

A1.3) Using a conductivity meter, measure the electrical conductivity of the liquid that will be used in the experiment and confirm that it is  $\leq 1 \mu\text{S/cm}$ .

### A.2. Experimental set-up

#### A.2.1) Horizontal bridge system (Fig. 3.1a)

A.2.1.1) Place a pair of adjustable height platforms on a level non-conducting surface. Fix one platform in place and mount the other platform on a motorized linear translation stage that has a minimum travel of 25mm.

A.2.1.2) Secure insulating plates (Fig. 3.1a, part j) to the top surface of the adjustable platforms. Use insulating plates that are over-sized so that they overhang the platforms by at least 10 mm on all sides. Use common materials such as Teflon, acrylic, or window glass. Choose the thickness to prevent breakdown at the planned maximum voltage.

A.2.1.3) Connect the high voltage power supply (Fig. 3.1a, part m) according to manufacturer instructions.

A.2.1.4) Solder alligator clips to the end of both the high voltage and ground wires.

A.2.1.5) Clamp one end of a support arm constructed from rigid insulating material onto a ring stand with the insulating rod protruding horizontally over the insulating platforms.

A.2.1.6) Mount the ground and high voltage wires to the support arms using either several wraps of electrical tape, nylon wire ties, or other appropriate means so the alligator clips protrude downwards above the insulated platforms.

A.2.1.7) Clip one platinum electrode (Figure 3.1a, part k) into each of the two alligator clips.

A.2.1.8) Position the support arms so that the high voltage wire is above the fixed platform and the ground wire is above the moving platform.

**A.2.2) Vertical bridge system (Fig 3.1b)**

A.2.2.1) Attach a non-conductive clamp to a linear translation stage so that the clamp can travel a minimum of 25mm. Use this clamp to hold the vessel (Fig. 3.1b, part i) which will be connected to the ground wire.

A.2.2.2) Mount this assembly to a vertical rigid support structure.

A.2.2.3) Attach a similar non-conductive clamp in line and below the support on the linear translation stage. Use this clamp to hold the vessel which will be connected to the high voltage wire.

**A.2.3) Make a “dead-stick” (See Figure 3.1c for illustration)**

A.2.3.1) Obtain a piece of non-conductive rigid material such as a glass or plastic rod 30-40 cm long (Fig. 3.1c, part p).

A.2.3.2) Attach a piece of conductive metal 10-15 cm long (Fig. 3.1c, part q) to one end of the rod using several wraps of electrical tape (Fig. 3.1c, part r) applied in a crisscrossed manner or other fixing material.

A.2.3.3) Use the “dead-stick” to bridge the high voltage and ground electrodes with the metal end after the power supply is switched off to assure that the circuit is discharged prior to handling equipment.

**A.3. Operation of Liquid Bridges****A.3.1) Horizontal Liquid Bridges**

A.3.1.1) Fill each vessel (Fig. 3.1a, part i) with enough liquid to bring the surface to within 1-5 mm of the beaker spout or rim. For the vessels (diameter 60mm) used in this demonstration, use 67 g of liquid for water, 74 g for DMSO, or 84.4 g for glycerol.

A.3.1.2) Place the two vessels onto the insulating platform such that they physically contact each other at a single location such as the spouts but the straight wall rim will also work.

A.3.1.3) Adjust the platform heights so that the liquid will only contact the platinum electrode and not the alligator clip or wire. Pay attention to the vertical alignment so that the resulting bridge is horizontally level.

A.3.1.4) Position the platinum electrodes into the liquid filled vessels so that they are a minimum of 15 mm from the contact position where the bridge will form. Note: Typically the electrodes are placed between the center of the vessel and the wall furthest from where the two vessels make contact.

**A.3.2) Vertical Liquid Bridges**

A.3.2.1) Use two clean, closed vessels with one liquid port as shown in Figure 3.1b, part i.

A.3.2.2) Fill each vessel with the liquid under study so that there are no trapped air bubbles.

A.3.2.2) Insert an electrode (Fig. 3.1b, part k) into each vessel and close the cap to hold the liquid in place.

A.3.2.3) Mount the two closed vessels into the non-conductive clamps (see A.2.2) such that the openings point towards each other.

A.3.2.4) Add a few drops of liquid to the opening of the lower tube so that a curved liquid surface protrudes a few millimeters above the glass rim.

A.3.2.5) Bring the upper vessel down so that it just contacts the lower one forming a small capillary bridge.

A.3.2.6) Connect the high voltage output of the power supply (Fig. 3.1b, part m) to the lower vessel (stationary) electrode terminal and the ground to the upper (translating) vessel.

**A.3.3) High Voltage Operations****A.3.3.1) General Considerations**

A.3.3.1.1) Before proceeding further confirm that all surfaces are dry and that no liquid pools, films, or droplets are present on the insulating platforms.

A.3.3.1.2) **IMPORTANT HIGH VOLTAGE SAFETY!** Prior to applying power to the experiment confirm that there are no short circuits and that there are no ground paths present which can result in personnel or equipment coming into contact with energized surfaces. Be certain to follow all procedures and observe warnings issued by the high voltage power supply manufacturer. When in doubt seek advice from qualified electrical safety personnel.

A.3.3.1.3) Set the polarity of the power supply (if selectable) prior to applying power. Typically, use positive voltage polarity as this provides more stable bridges. Note: Negative polarity can also be used but tends to yield pronounced space charge effects which can significantly affect the physical properties of both the dielectric liquid and affects the local charge density in the experimental area due to the functional difference in sinking rather than sourcing electrons under high potentials as excess charge can be sprayed onto surrounding insulating support structures.

A.3.3.1.4) Open the current limit on the power supply so as to provide no more than 5-6 mA of current.

A.3.3.2) Choose one of the two voltage profiles that can be applied – ramp or step.

A.3.3.2.1) Use a voltage ramp when first starting and the performance characteristics of the liquid are not yet known.

A.3.3.2.1.1) Turn down the voltage limit on the power supply to provide 0 kV.

A.3.3.2.1.2) Enable the output on the power supply and slowly begin to increase the voltage limit at a rate of approximately 250 V/s.

A.3.3.2.1.3) Observe the voltage at which bridge ignition occurs, this is the approximate ignition threshold voltage ( $V_i$ ).

A.3.3.2.2) Use a voltage step to quickly apply voltage to the system.

A.3.3.2.2.1) Set the power supply voltage limit to the desired value above the ignition threshold which was determined by using a voltage ramp for the liquid system under study (see A.3.3.2.1.3).

A.3.3.2.2.2) Enable the output on the power supply. Note: A voltage step can result in arcing and the ejection of droplets and may require several seconds before a stable bridge forms. Arcing will produce ozone and peroxide resulting in increased liquid conductivity if allowed to persist for more than a few seconds. It is recommended to replace the liquid with fresh material if arcing is a problem.

A.3.3.3) Stabilize the bridge following ignition.

A.3.3.3.1) Confirm bridge ignition by observing a steady stream of liquid between the two vessels. Note: This will occur typically between 8-10 kV and will be accompanied by current conduction between 250-500  $\mu$ A depending on the liquid used.

A.3.3.3.2) Tune the bridge for extension by increasing the voltage to 10-15 kV with current consumption  $\sim$  1000  $\mu$ A. Note: the actual value will depend on the liquid used.

A.3.3.3.3) Extend the bridge to a distance of approximately 1 mm per 1 kV applied voltage, e.g. 15 mm for 15 kV. If necessary, tune the bridge further depending on the requirements of the experiment. Note: A stable bridge can exist for many hours.

#### A.3.4) Shutdown Procedures

A.3.4.1) Extinguish the bridge by disabling the output on the high voltage power supply. Wait several seconds for the power supply capacitors to discharge and the voltage readout to fall to zero.

A.3.4.2) Use the “dead-stick” constructed in section §A.1.3 to short the electrode holders prior to handling any previously energized parts.







# 3

## A Tour Of The Toolbox

### *Experimental methods*

*The interaction of radiation, both particle and electromagnetic, with matter is the basis for the experimental tools used in this thesis. The general principles and the complementarity of the techniques is discussed along with the procedural details for preparing and examining EHD bridges.*

## 3.1 General Measurement Principles

*The following section discusses the interaction between electromagnetic waves and matter with respect to field theory and methods from atomic physics. The basis for interaction over different length scales is established.*

### 3.1.1 Matter-Energy Interactions

The propagation of light through isotropic matter is explicitly derived in the appendix of this chapter. In the case of EHD bridges however, the applied electric field is expected to induce an anisotropic response. An anisotropic material will exhibit orientational heterogeneous dispersion because of the distortions in the binding forces between atomic or molecular elements. These distortions can be induced via structural asymmetries (e.g. calcite or liquid crystals) or in response to externally applied forces (e.g. strain in polymers). Birefringence and polarization will only occur over those wavelengths which can “see” the anisotropic features implying that the phase velocity of the incident wave is shifted with respect to the optical axis – that direction which does not exhibit dispersion as the wave passes through the material. The introduction of conductive elements into a dielectric material can also result in polarization, birefringence and in some cases higher order optical phenomena such as retroreflection [1].

Atomic or molecular oscillators can also be treated as individual antenna and in condensed matter it is incorrect to treat each element independently – rather one must consider an array of elements. The interaction between the incident radiation and the antenna array becomes dependent on the spacing, fundamental wavelength(s), phase, thermal state, and momentum of each antenna element. The critical separation distance which determines how many elements act collectively is known as the coherence length – and corresponds to the upper limit set by Heisenberg uncertainty. The theory of coherent molecular oscillators was pioneered by Dicke [2] who also developed the concept of aperture synthesis which is the foundation of modern radio-astronomy. When a photon becomes delocalized across an array of coherently oscillating atoms or molecules non-linear phenomena are observed; notably superradiance – a high intensity emission proportional to the square of the population  $N^2$  or subradiance – abnormally low emission due to photon trapping. These phenomena are fundamental to the field of cavity quantum electrodynamics and those theoretical treatments of the water bridge which aim to explain the phenomenon from the molecular level up [3]. There is a fundamental problem that must be addressed and this is the apparent dualistic classical-quantum nature of such processes. An examination of Heisenberg’s seminal work [4] by Li [5] reveals that all real systems have a coherent space-time. The coherence space is defined by the physical dimensions of an array as discussed above [2], [6] and further elaborated on by delGuidice [7] who uses the term Coherence Domains to describe such arrays. Within these coherent regions an interference pattern is sustained for a given characteristic time period

– the coherence time. Within the coherent time-space an interference pattern holds phase information, outside the domain this phase information is lost and the system again appears as a classical body. The mechanics of how these domains manifest and remain stable in matter is a topic of ongoing discussion. Thermally driven fluctuations are oft cited by opponents of long-term or long-range coherence in liquid systems; however, such processes being again dependent on dispersion have a wavelength dependence that may preclude thermal disruption of the phenomenon. In quantum mechanics the polariton quasi-particle is invoked in order to handle the interrelation of dispersion and harmonic oscillations in groups of electromagnetically active dipoles.

It must be noted that cavity quantum theory does not violate Planck’s radiation law because the process of statistically averaging a chaotic process at *thermal equilibrium* will result in a linear relationship between the number of radiators and the irradiance of the system. In other words, random motion with an energy level of  $k_b T$  reduces the coherence space-time of the system for those modes centered around  $\omega_{\max} = vT/b$  according to Wien’s law, where  $v$  is the phase speed,  $T$  the temperature in Kelvin, and  $b$  is Wien’s displacement constant ( $2.8977685 \times 10^{-3}$  m·K). Thus any radiation processes in this region will be largely non-coherent as long as there are no physical constraints on the system which allow the background thermal energy to “over-pump” the system and restoring superradiance. Collective processes in condensed phase matter remain largely obscured by various assumptions of molecular level dynamics. *Ab-initio* methods such as mode coupling theory (MCT) attempt to describe the effects of temporal and spatial length scale coherence decays in terms of real quantities like density. MCT derives its initial conditions from the structure factor found in glass forming liquids – water is arguably one such material – and searches for correlation between the position and momentum of the various oscillators in the modeled system. Indeed the method does find some degree of success in modeling relaxation dynamics and aging (non-equilibrium) effects in unstructured materials, however the method yields incorrect transitions from the ergodic liquid state to the non-ergodic glassy state, is only valid over small temperature steps, and ultimately fails in regards to collective relaxation processes – especially those which are non-Gaussian. The relevance of relaxation processes will now be discussed.

### 3.1.2 Dielectric Relaxation and Polarization

#### 3.1.2.1 Leaking Charges

A liquid which behaves as a perfect dielectric will become polarized in the presence of an externally applied electric field; however the electrical boundary condition at the air-liquid interface results in zero free surface charge. Conversely, in a leaky dielectric liquid whereby small islands of charge can become liberated from the bulk fluid and migrate to the surface [8]. This leads to two important surface constrained mechanisms which lead to bridge stability notably free charge convection and Ohmic surface conduction [9]. The situation becomes even more complex in the case of a freely dissociable material as is the case for

many polar solvents. The stability of the resulting ions is dependent not only on the molecular structure but also on the magnitude of the externally applied field [10]. Above a critical field strength the dissociation and recombination rates are no longer coupled and free ion species can accumulate in the system which leads to changes in the electrical response of the system [11]–[13].

### 3.1.2.2 Relaxation Processes

Any collection of oscillators will eventually transition from an excited state back to a ground state condition giving up excess energy and relaxing into a state of equilibrium with its surroundings. Depending on the type and frequency of the perturbation the characteristic relaxation time ( $\tau_0$ ) will vary. Typically these relaxation processes show a temperature dependence which is consistent with Dicke and cavity quantum electrodynamic theory. In glass forming systems two main relaxation dynamics are known: structurally correlated  $\alpha$ -relaxations coupled to viscosity and glass transition temperature; and secondary  $\beta$ -relaxations that arise from local heterogeneities. In simple polar liquids such as those studied here an additional Debye like relaxation has been measured but whose underlying mechanisms still remain unknown [14]. A hint comes when comparing the faster ( $10^{-14}$  to  $10^{-15}$  s)  $\tau_{0,\alpha}$  arising from molecular or quasi-lattice vibrations to the slower ( $10^{-11}$  s)  $\tau_{0,\text{Debye}}$  suggesting that the process is related to the collective motion of larger molecular assemblies that oscillate and thus relax in concert [15]. In water the temperature dependence of this  $\tau_{0,\text{Debye}}$  loses linearity and converges with  $\tau_{0,\alpha}$  above 310 K which also fits with the idea that thermal fluctuations decrease the size of coherently coupled oscillators.

There is one more relevant process: the Maxwell-Wagner interfacial polarization which essentially is the development of heterocharge layers at non-reflection symmetric boundary conditions. The most obvious cases of this would occur at the liquid-air and liquid-electrode interfaces, but can also occur between volume elements in the liquid itself as the result of shed heterocharge and density fluctuations which have long (i.e. seconds) relative lifetimes.

### 3.1.3 Length Scales, and Interaction Fields

The experimental methods used in this thesis cover a large portion of the electromagnetic spectrum from the extreme low frequencies ( $10^1$  Hz) to hard X-rays ( $10^{19}$  Hz). It is necessary to consider then how the wavelength of the probing radiation and the physical size of the sample volume influences the interpretation of the results. There are three cases that can be considered and in each case a different observable quantity is found to contribute to the polarization response of the sample [16].

**Sample size much smaller than probe wavelength.** Typical for the low frequencies between extremely low ( $10^1$  Hz) up to radio frequency ( $10^9$  Hz) where the wavelength is on the order of Mm – cm. The measurement principle used is the lumped impedance which includes the terms for capacitance and conductance of the liquid sample. Thus the low frequency complex

dielectric permittivity ( $\epsilon_{\text{low}}^*$ ) is defined as:

$$\epsilon_{\text{low}}^*(\omega) = \epsilon'(\omega) - i\epsilon''(\omega) = \frac{C^*(\omega)}{C_0} \quad (\text{Eq. 3.1})$$

The angular frequency of the probe,  $\omega$ , and  $C^*(\omega) = k_{\text{cell}}\epsilon^*(\omega)$  is the complex capacitance and  $C_0 = k_{\text{cell}}\epsilon_0$  is the capacitance of the empty electrode set-up, and  $k_{\text{cell}}$  a factor related to the electrode geometry. The signal is determined by the electrically driven motion of solvated charges (i.e. ions), locally constrained groups of molecules, and single molecular dipoles. These motions are primarily translational and rotational.

**Sample size comparable to probe wavelength.** The wavelengths considered now are in the microwave range between  $10^9$  Hz and  $10^{11}$  Hz. The interaction is dependent upon how well the sample volume can propagate the EM field relative to the transmission line (e.g. waveguide or free space) used to deliver the probe. Again molecular tumbling is seen as the dominant interaction quantity, which depends upon the spectral density of intermolecular coupling modes in the material. The mismatch between the complex impedance of the transmission line,  $Z_0$ , and sample,  $Z(\omega)$ , will cause part of the probe energy to be reflected. The mid-range complex impedance is related to the dielectric permittivity by:

$$\epsilon_{\text{mid}}^*(\omega) = \frac{1}{i\omega\epsilon_0 Z(\omega) C_0} \quad (\text{Eq. 3.2})$$

The ratio of the mismatch gives the reflection coefficient  $\rho^*(\omega)$ :

$$\rho^*(\omega) = \frac{Z(\omega) - Z_0}{Z(\omega) + Z_0} \quad (\text{Eq. 3.3})$$

**Sample size much larger than probe wavelength.** The wavelength of the probe radiation now crosses into the optical and X-ray frequencies ( $10^{10}$  Hz –  $10^{18}$  Hz). The principle quantities of interest are related to molecular vibrational and electronic transitions; namely the index of refraction,  $n$ , and absorption coefficient,  $\alpha$ , of the sample which combine to give the complex refractive index,  $n^*(\omega)$ :

$$\eta^*(\omega) = \eta(\omega) + i\alpha(\omega) \quad (\text{Eq. 3.4})$$

and equated to the complex dielectric constant by:

$$\epsilon_{\infty}^*(\omega) = [n^*(\omega)]^2 \quad (\text{Eq. 3.5})$$



For water (and other simple polar liquids) the dielectric response across these three cases can be combined into a single relationship [17]:

$$\epsilon_{total}^* = \epsilon_{\infty}^* + \frac{\epsilon_{low}^* - \epsilon_{mid}^*}{1 + i\omega\tau_{slow}} + \frac{\epsilon_{mid}^* - \epsilon_{\infty}^*}{1 + i\omega\tau_{fast}} \quad (\text{Eq. 3.6})$$

The coupling of the relaxation time constants  $\tau_{slow}$  and  $\tau_{fast}$  reflect the relaxation time dynamics of the probed population as discussed previously.

### 3.1.4 Methodology

For all methods used the instrument response is characterized so the particular observable quantities can be measured and correlated with various physical parameters (e.g. temperature). However, the contribution of additional physical responses of the material that are wavelength dependent will be convolved with the recovered signal of interest. Fortunately, methods have been developed to allow the deconvolution of the signal and subsequent processing to remove unwanted contributions. This works well when the system under study is at thermal equilibrium but poses problems when a non-equilibrium and dynamic sample is used, as the case is in this work. The principal reason for this is that underlying the deconvolution process are also some assumptions which may or may not hold under the given experimental circumstances. For example in neutron and x-ray scattering there are assumptions about the inelastic contributions and atomic form factors that rely upon how one assumes the nuclear and electronic fields to couple. Similar examples can be found in each of the methods used and thus the caveat is made that not all of the assumptions may hold upon which the data are interpreted. By comparing data from multiple experimental methods which probe overlapping time and length scales through differing means a cross-correlated data set emerges which is more robust than any single method alone.

## 3.2 EHD bridges – experimental setup

*The standard protocols to reliably and repeatably generate floating liquid bridges are briefly presented.*

Most of the EHD bridges used for the research presented in this thesis were run in accordance with the methods outlined in Wexler et al. [18] in a pair of single-spout, squat-shaped Pyrex beakers, 60 mm diameter, 35 mm height, a wall thickness of 1.5 mm and a 2.2 – 2.5 mm (diameter) lip around the upper edge. The beakers were filled with  $66.0 \pm 0.5$  g of the de-ionized room temperature water up to about 3 mm below the rim. The initial conductivity of the water was  $0.055 \mu\text{S}\cdot\text{cm}^{-1}$  as measured with a conductivity/TOC meter integrated in the Millipore A10 TOC type water supply system (Millipore Corp., Billerica, MA, USA). This conductivity increased to  $0.4 - 1.0 \mu\text{S}\cdot\text{cm}^{-1}$  depending on the atmospheric conditions [19] and storage time in a dark glass bottle. The pH value of the water was  $\sim 5.5$ , due to ambient  $\text{CO}_2$

saturation. In general the electrodes were either platinum plates (25 mm x 25 mm, 0.5 mm thick, 99.99%), platinum foil strip (5 mm x 50 mm, 0.25 mm thick, 99.999%) or platinum wire (0.5mm diameter 99.99% platinum) unless noted otherwise. Electrodes were typically placed towards the side of the beaker opposite the bridge (spouts) giving a separation distance of approximately 12 cm. Unless otherwise noted the anode (positive pole, high voltage) was on the left, the cathode (negative pole, ground) on the right. The two beakers were positioned so that the dry spouts of the two beakers touched each other.

The power was provided by a FUG HCP 350-20000 (FUG Elektronik GmbH, Rosenheim, Germany) variable DC supply capable of providing up to 6 mA and  $20 \pm 0.1$  kV, with a ripple less than 0.05%. The applied operating voltage varied between 5 kV to 20 kV, mostly between 10 and 15 kV, at currents typically on the order of 0.5 – 1.5 mA. Depending on the current, the bridge thickness varied between  $\sim 2$  mm (0.5 mA) and  $\sim 5$  mm (1.5 mA), for example. As soon as the bridge was formed, the beakers were pulled apart to a distance of  $(10 \pm 1)$  mm. The average time between the formation and final beaker position was  $\sim 10$  s. The bridge water

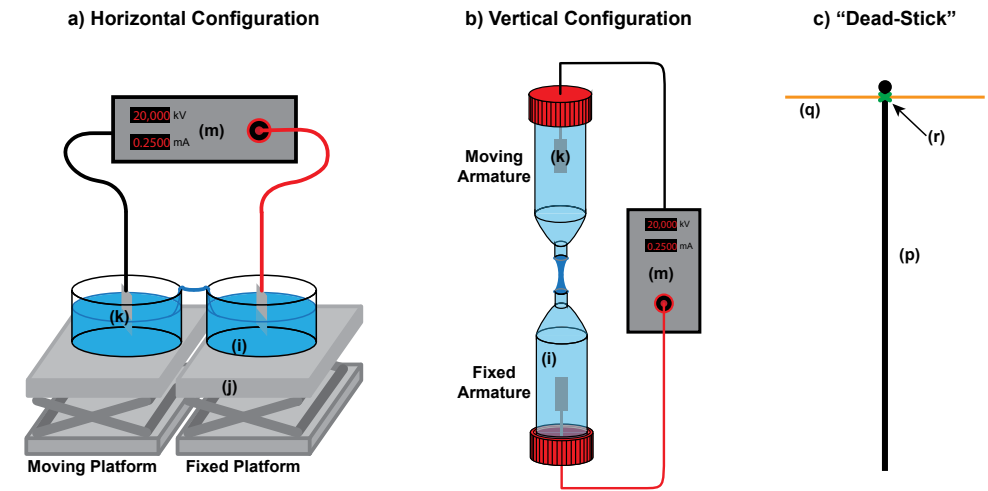


**Figure 3.1 Basic equipment for EHD liquid bridge experiments. Schematic representation of typical horizontal (a) and vertical (b) experimental system for the creation of EHD liquid bridges. Some mechanical details such as mounting straps and electrode supports are omitted for clarity. The essential components are liquid vessels (i), insulating platforms or mounts (j), electrodes (k), and a high voltage power supply (m). Linear translation stages are recommended for the safe separation of the two vessels once a bridge is established. The dead stick shown in panel (c) is assembled from a piece of non-conductive rigid material (p), a conductive metal rod (q), and several wraps of electrical tape applied in a crisscrossed manner or other fixing material (r). The metal end is used to form a short between the two electrodes after the conclusion of the experiments to assure that the circuit is discharged prior to handling equipment.**

was at room temperature in the beginning and slightly warmer after the end of the bridge runs [20]. The temperature of a water bridge is dependent on the current, its characteristics have been published [20], [18]. From the  $\sim 0.3$  mA measured we estimated its temperature to be  $\sim 45$  °C. Standard experimental configurations are shown in Figure 3.1.

### 3.3 Electrochemical Characterization

*This section reviews the methods used to estimate and characterize the influence of ionic charge transfer through the water bridge. Impedance spectroscopy provides proof that a protonic current is in operation in EHD water bridges.*

#### 3.3.1 Hydrogen Detection

Deionized water which had been stored in a glass bottle was used for the inductively coupled plasma (ICP) experiments for determination of species concentrations. Each floating water bridge was operated for 20–30 minutes (unless otherwise specified) at a current of 0.3 – 0.9 mA (1.9 – 3.8 mA when a pH dye was added), the voltage was kept constant at 14 kV. In all experiments the current rose to reach its maximum after 15–20 minutes and then started to drop again. For the ICP measurements three bridge experiments were run until shortly after the current maximum was reached. Electrodes and beakers were cleaned with diluted nitric acid and carefully rinsed with deionized water prior to water bridge experiments. For the hydrogen detection experiment, a special gas-tight set-up and fresh Milli-Q water were used (Fig. 3.2). Custom borosilicate beakers with a threaded stem centred in the bottom of each beaker allowed the insertion of the electrodes (0.5 mm 99.99% platinum wires) from below. The beakers rested on a 10 mm thick glass plate. A gas-tight glass dome was placed over the entire beaker set-up and was closed with a Duran screw septum cap (polybutylene

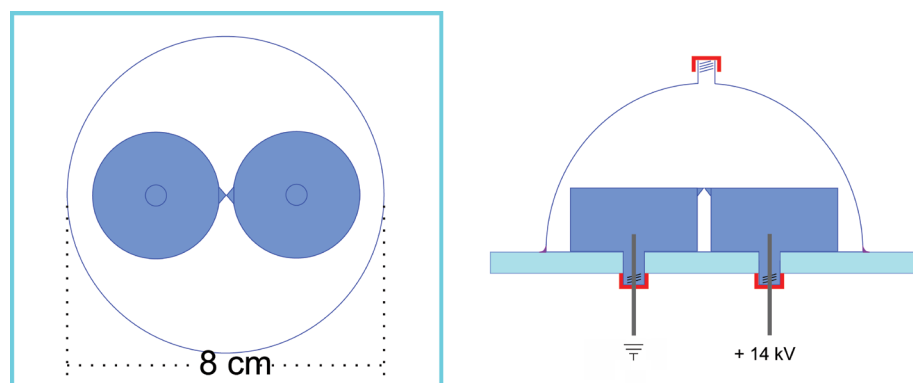


**Figure 3.2** Gas detection water bridge set-up, view from above (left) and front (right). Beakers, dome and ground plate are made of glass; the electrodes are 0.5 mm platinum wires (99.99%); and the red caps are polybutylene terephthalate with PTFE coated silicone septa inside (double septum on top opening).

terephthalate, GL14) enclosing a pair of PTFE coated silicone septa in order to minimize hydrogen leaking whilst still allowing gas sample extraction. All glass to glass connections were sealed with grease (glisseal®, Borer Chemie AG, Switzerland). In this experiment the currents were higher than in the experiments for the ICP analysis (1.3 mA) due to a shorter bridge length. Whereas water bridges with currents of  $\sim 0.5$  mA can be sustained for hours, bridges running at 1 mA and more are thicker, heavier and less stable. When operating such bridges occasional overflowing can occur, reducing the amount of water in the system and therefore also the lifetime of the experiment. Whenever such a spilling occurred, the voltage was increased to maintain the original current level.

#### 3.3.2 Gas Chromatography

The atmosphere above the water bridge was investigated with gas chromatography (GC) for hydrogen formed by electrolysis. Before initiating the water bridge in the set-up shown in Fig. 3.2 the dome was flushed with nitrogen for five minutes and a reference sample was taken from the atmosphere. Subsequently, the water bridge was run for another 100 minutes with the dome sealed. Afterwards, a sample of the atmosphere inside was taken with a syringe (1 mL) and analysed with a gas chromatograph (Varian  $\mu$ GC CP4900, Agilent Technologies Netherlands B.V.). This  $\mu$ GC analyser is equipped with two discrete channels, each fitted with a specific column and a Thermal Conductivity Detector (TCD). The sample was manually injected into channel 1 where hydrogen, nitrogen and oxygen were separated. This channel is equipped with a Mol Sieve 5 Å PLOT column (10 m x 0.53 mm, 30  $\mu$ m fused silica) which was operated at a column temperature of 80°C and a pressure of 150 kPa, using argon as the carrier gas. The  $\mu$ GC was routinely calibrated using 15 defined gas mixture standards obtained from Air Products B.V. (Utrecht, The Netherlands). The sample acquisition was performed using Galaxie Chromatography Software (Agilent Technologies, USA) which automatically integrated and normalized the chromatogram thereby providing actual gas concentrations.

#### 3.3.3 Quantification of Dissolved Ions (Ca, K, Mg, Na, Zn, C and Pt)

A simultaneous, axially viewed inductively coupled plasma optical emission spectrometer (ICP-OES; Ciro Vision EOP, Spectro, Germany) equipped with a cross-flow nebulizer, a Scott type PFA spray chamber and a standard ICP torch with 2.5 mm injector diameter was used for the quantification of Ca, K, Mg, Na, and Zn. The selected plasma conditions were 1350 W RF power, 12.5 L min<sup>-1</sup> outer gas flow, 0.6 L min<sup>-1</sup> intermediate gas flow and 0.83 L min<sup>-1</sup> nebulizer gas flow; and the following emission lines were used: Ca 396.847 nm, K 766.491 nm, Mg 280.270 nm, Na 589.592 nm, Zn 213.856 nm. Limits of quantitation (LOQ) for Ca was 1  $\mu$ g L<sup>-1</sup> and 2  $\mu$ g L<sup>-1</sup> for K, Mg, Na, and Zn. The LOQ's were calculated from the calibration function (4 concentration levels, 5 repetitions, 95% confidence level). Calibration standards in the range 0 – 100  $\mu$ g L<sup>-1</sup> were prepared from a multi element stock solution (100 mg L<sup>-1</sup> 28 element stock solution, Roth, Germany).

A calibration of the ICP-OES for the absolute carbon concentration is difficult: Carbon dioxide can be expected to be the dominant source of carbon in the investigated samples, since carbon dioxide is part of the atmosphere. When using an aqueous carbon calibration standard (e.g. potassium hydrogen phthalate) the behaviour of the calibrant and the analyte in the spray chamber will be significantly different resulting in a systematic error. Nevertheless, the carbon emission signal of the C 193.091 nm emission line was used to obtain relative values of the concentration distribution in the investigated solutions.

The Pt concentration was quantified using an inductively coupled plasma mass spectrometer (ICP-MS; Elan DRC+, Perkin Elmer, USA) equipped with a Meinhard Type A nebulizer, a quartz cyclonic spray chamber and Ni- cones. The selected plasma conditions were 1350 W RF power, 14 L min<sup>-1</sup> outer gas flow, 1 L min<sup>-1</sup> intermediate gas flow and 0.93 L min<sup>-1</sup> nebulizer gas flow. Using m/z 195 the LOQ of Pt calculated from the calibration function (4 concentration levels, 5 replications, 95% confidence level) was 0.02 µg L<sup>-1</sup>. Calibration standards in the range of 0 – 0.5 µg L<sup>-1</sup> were prepared from a Pt single element stock solution (1000 mg L<sup>-1</sup> Pt stock solution, Alfa Aesar, Germany).

### 3.3.4 Conductivity Measurements

Conductivity measurements were performed using an Impedance / Gain Phase Analyzer HP 4194A (Hewlett-Packard, California, U.S.A) which was connected via four BNC cables to a BDS 1200 connection head containing a BDS 1309 measurement cell (NOVOCONTROL Technologies, Germany). The BDS 1309 consists of two gold plated electrodes with a Teflon® isolation ring in between, the diameter of the electrodes was 11 mm and the distance between the electrodes was 6.1 mm. This sample cell is especially designed for the investigation of high permittivity liquids. The software WinDETA (NOVOCONTROL Technologies, Germany) was used to calibrate the system using the stray capacity of the cell (1.2 pF) and to measure the samples' conductivity. Each sample was measured three times.

### 3.3.5 Colorimetric Analysis of pH Dye Solutions

A liquid pH dye 3-10 (Riedel-de Haën GmbH, Seelze) was used to visualise differences in the pH between anolyte and catholyte. Twenty-one drops (1 mL) were added to anode and cathode beaker before, during and after bridge operation depending on the experiment. A Colorimetric analysis was performed to evaluate the colours of dyed solutions. All images for this analysis were recorded using the same camera system (Canon 300D) with the same settings (exposure, ISO, aperture), the same background and the same lighting. The original RGB colours of the images recorded were transformed into the CIE L\*a\*b\* colour space assuming a D65K white reference. This colour space is spanned by three axes: a\* from green to red, b\* from blue to yellow and L\* from black to white. It is perceptually uniform which means that the difference between two colours (as perceived by the human eye) is proportional to the Euclidian distance within the colour space [21], [22]. Since the reddening of the solution

is the point of interest in this evaluation the distances on the a\* axis were compared to the respective distance between pH 5 and 6 on the pH dye's legend.

### 3.3.6 Optical Fiber pH Measurements

Additionally, the pH was measured using a pre-calibrated fiber optic PreSens pH microsensor (Z8X pH-1) (Regensburg, Germany). The optical fiber probe was submerged a few mm into anolyte and catholyte, respectively, for 9 minutes and 33 seconds after the water bridge reached its thermal equilibrium (15 minutes after start). 565 data points per solution were recorded.

### 3.3.7 Electrochemical pH Measurements in Low Ionic Strength Solutions

For low ionic strength pH measurements a pH-meter Orion Star A211 was used in conjunction with the Orion PerpHecT ROSS combination pH micro electrode (Cat. No. 8220BNWP). Two point calibration was performed using Pure Water pH 6.97 buffer A, Cat. No. 700702 and Pure Water pH 4.10 buffer B, Cat. No. 700402 (Thermo Fisher Scientific Chelmsford, MA 01824 USA) according to manufacturer instructions. As temperature can affect ion-selective electrode potentials both the calibration buffers, ionic strength adjustor, and sample were maintained at the same temperature. All liquid handling was done using calibrated adjustable pipettes (Cat. No. 3120000070 and Cat. No. 3120000054, Eppendorf AG, Hamburg, Germany). The sample was prepared by mixing 3.5mL of anolyte or catholyte with 35 µL of the pHISA pH ionic strength adjustor (Cat. No. 700003 Thermo Fisher Scientific Chelmsford, MA 01824 USA) in a disposable 5mL polypropylene tube (Cat. No. 0030119401, Eppendorf AG, Hamburg, Germany). The pH electrode was then rinsed with additional sample and placed in the tube containing the mixture. After stabilization the pH value of the solution was recorded.

### 3.3.8 Impedance Spectroscopy

Horizontal EHD water bridges were created using a pair of 100 mL Teflon beakers or, alternatively, borosilicate beakers filled with de-ionized water in accordance with the procedures and methods described in §3.2.1 above. For the measurement of “fresh” milli-Q water (results shown in Fig. 4.11), this water was filled into the cell directly with minimal exposure to the atmosphere. The applied operating voltage varied between 5 kV to 20 kV, mostly between 10 and 15kV, at currents on the order of 0.5mA. The distance between the electrodes used for these measurements was about 7 cm. As soon as the bridge was formed, the beakers were pulled apart to a distance of (1.0 ± 0.1) cm. Impedance measurements were performed using an Impedance/Gain Phase Analyzer HP 4194A (Hewlett-Packard, California, U.S.A) which was connected via four BNC cables to a BDS 1200 connection head containing a BDS 1309 measurement cell (NOVOCONTROL Technologies, Germany) thereby applying

voltage and measuring current separately in a bipolar electrode configuration. The BDS 1309 consists of two gold electrodes with a Teflon® isolation ring in between, the diameter of the electrodes was 11 mm and the distance between the electrodes was 6.1 mm. This sample cell (volume 579 mm<sup>3</sup>) is especially designed for high permittivity liquids. The software WinDETA (NOVOCONTROL Technologies, Germany) was used to calibrate the system using the stray capacity of the cell (1.2 pF) and to perform the measurements. We measured the complex impedance in a frequency range from 100 Hz to 10 MHz. All measurements were performed at room temperature. The analyzer settings were chosen to provide 65 data points on a logarithmic scale from 100 Hz to 10 MHz with threefold internal averaging. Impedance spectra were fitted with “EIS Spectrum Analyser” software [23] using the Powell algorithm [24].

## 3.4 Infrared emission

*Infrared spectroscopy provides access to the vibrational and rotational motions of molecular oscillators. The methods employed in this work allow both spatially as well as energetically resolved measurements.*

### 3.4.1 Infrared Measurement Principles

Infrared imaging and emission spectroscopy are methods which measure the intensity of infrared light emitted from the region under study. The simple difference being that imaging systems have better spatial resolution and accept a broad spectral range, whereas the spectrometer can resolve spectral features at the cost of spatial information. Together they can provide useful information on the phenomenon under study. There are two primary physical processes that contribute to the infrared signature: 1) blackbody or thermal radiation, and 2) infrared active molecular processes. The blackbody radiation intensity obeys Planck's law and is directly proportional to temperature regardless of material composition.

$$M_{\lambda}(T) = \frac{2hc^2}{\lambda^5 \left( \exp \left[ \frac{hc}{\lambda k_B T} \right] - 1 \right)} \cdot 10^{-6} \left[ \frac{W}{m^2 \cdot \mu m} \right] \quad (\text{Eq. 3.7})$$

Blackbody emission covers a very broad spectral range and is a smooth distribution as it results from the total ensemble of allowed transitions for the material driven solely by thermal excitation. This is in contrast to molecular processes active in the infrared region, again for water these are vibrational, rotational, and translational motions described by the appropriate Hamiltonians. Depending on the molecular environment these spectral features will have a defined width that is much narrower than the thermal background. In the gas phase the transition probability distribution is very narrow and becomes inhomogeneously broadened as the liquid condenses due to the increased coupling between neighboring molecular oscillators. These two sources of infrared light (e.g. thermal and molecular) are convolved

along with the surface emissivity. This materially dependent quantity is defined as the ratio of intensity emitted from the real object versus that from an ideal blackbody at the same temperature:

$$\varepsilon = \frac{M_{\lambda}}{M_{\lambda}^0} \quad (\text{Eq. 3.8})$$

For pure liquid water and is not dependent upon the viewing angle as for solid surfaces.

### 3.4.2 Infrared Emission Spectroscopy

The water bridges used for these measurements were prepared using pyrex vessels, Type I HPLC grade water. The applied operating voltage varied between 5 kV to 20 kV at currents on the order of ~ 0.3 mA.

The IR emission spectra were recorded with a Bruker IR spectrometer VERTEX 70 using a liquid N<sub>2</sub>-cooled CdHgTe detector and an emission attachment that consisted of an articulated, internally gold-plated brass tube (length 120 cm, diameter 3.81 cm), which was continuously purged with dry N<sub>2</sub>. The open end of the tube was positioned at ~3 cm from the water bridge, its height being adjusted so that the bridge would be closest to the center of the tube. Thus, the area surrounding the water bridge was constantly flushed with nitrogen from the brass tube. Before each measurement, the instrument was interferometrically calibrated. A cylindrical IR mirror was placed directly behind the bridge at a distance of approx. 1 cm in order to collimate as much IR light as possible into the tube. A sketch of the set-up is shown in figure 3.3.

When recording the emission from bulk water, the open end of the emission attachment was placed above a beaker containing approx. 200 mL of water at a specified temperature. For background measurements a black body calibration source at 22°C was used. All water bridge spectra presented here are an average of 50 scans divided by 50 background scans, 25 of which were recorded before and 25 after the measurement. All water spectra presented here are an average of 50 scans divided by 100 background scans, 50 of which were recorded before and 50 after the measurement. In all cases the background spectra before and after the measurements were indistinguishable. The standard deviation of the bridge measurements was, depending on the wavenumber, between 0.1 and 1.5% (background), 0.2 and 1.4% (bridge) and 0.2 and 2.1% (resultant curve), respectively. For the water at 37°C measurements, the standard deviation was between 0.2 and 2.4% (background), 0.8 and 2.8% (water) and 0.9 and 3.0% (resultant curve); for the water at 47°C measurements, the standard deviation was between 0.2 and 2.7% (background), 1.2 and 4.7% (water) and 1.5 and 4.8% (resultant curve); respectively. Since this is, for all cases, hardly more than the thickness of the curve, it is not shown in the spectra.

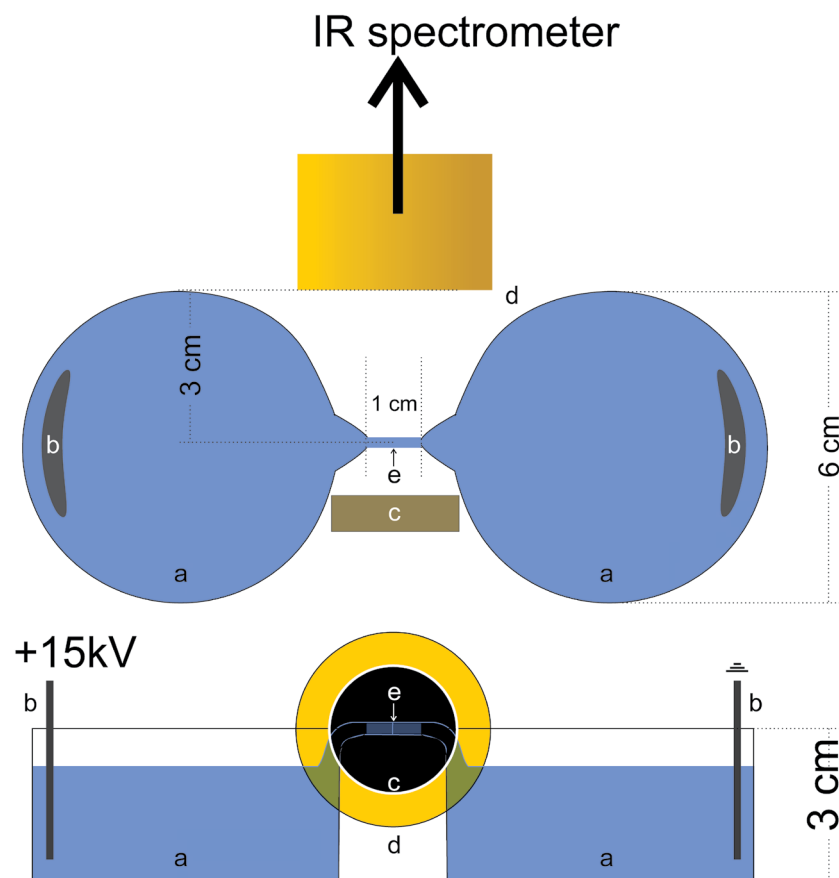


**Figure 3.3** Water bridge infrared emission measurement set-up, horizontal and vertical view.  
*a* - glass beakers, *b*-Pt electrodes, *c*- cylindrical mirror, *d*- gold plated brass tube (external input of spectrometer), *e*- floating water bridge

### 3.4.3 Long-wave Infrared (LWIR) Imaging

The bridge was imaged thermographically using several different LWIR cameras. For the data presented in §4.4.4 an Inframetrics camera (Model 760 Infrared Thermal Imager, Inframetrics, North Billerica, MA) was used. This dual band camera operated in two spectral windows: 3-5 $\mu$ m (2000 – 3333 cm<sup>-1</sup>) and 8-12 $\mu$ m (833 - 1250 cm<sup>-1</sup>). Both ranges were calibrated for the observed temperature range. For data presented in chapter 2 the IRCAM Taurus 110k L (7.7-9.4  $\mu$ m) and the Gemini 110k ML (3.7-5  $\mu$ m / 8-9.4  $\mu$ m) cameras were used.

## 3.5 Elastic Radiation Scattering

*The local structure of the liquid matter contained in the bridge can be elucidated through the methods discussed here. X-rays provide information on the electron density whereas neutrons reveal nuclear positions. Together with isotope substitution a complete picture of the motionally averaged local structure of the liquid in the bridge can be recovered.*

### 3.5.1 Wide Angle X-ray Scattering (WAXS)

X-ray powder diffraction measurements were conducted on the MS-X04SA beamline[25] at Paul-Scherrer Institute (Villingen PSI, Switzerland) using the 60000 element MYTHEN II strip detector[26] which collects up to 120° of scatter simultaneously. Radial translation of the detector removes small gaps of 0.17° between modules and acts to improve intensity normalization as different channels will collect the same scattering angle. For the measurements used here the detector assembly was translated to four radial positions allowing collection of scattering angles between 0.105° and 125.161° ( $10^{-3} \text{ \AA}^{-1} > q < 22.5 \text{ \AA}^{-1}$ ). The monochromator was set to a beam energy of 24.9882 keV ( $\lambda=0.496 \text{ \AA}$ ). The incident beam was focused into the center of the bridge and slitted down to cover a rectangular area 1.00 mm vertical by 4.00 mm horizontal. Type 1 ultrapure water (Cat No. ZMQSP0D01, Millipore Corp., MA, USA) was used throughout the X-ray experiments for both bridge and reference measurements. The bridge experiment was set-up in a similar fashion to that of the neutron experiments and is shown in figure 3.4.

The beakers were mounted onto an armature with two moveable platforms (Cat No. MTS25Z8, Thorlabs, USA) that allowed both bridge extension as well as centering the incident beam so it coincided with the center of the bridge. The armature was mounted to the two axis mechanical translation stage integrated into the beamline endstation; this allowed vertical translation of the bridge and alignment with the beam focal point. Platinum sheet electrodes (Cat. No. 7440-06-4, Alfa Aesar GmbH, Germany) delivered the positive 9-18 kV generated by the high voltage power supply (HCP 140-20000, FUG Elektronik GmbH, Germany). Typical current consumption was 400-1200  $\mu$ A for bridge diameters between 3-8 mm and lengths between 6-8mm. Bridges are known to undergo an initial stabilization period of approximately 15-20 minutes during which flow and thermal variations are maximal [27]. Measurements commenced 30 minutes after ignition once these inherent instabilities had subsided and continued for as long as the bridge remained stable – determined to be the period where the bridge diameter reduction remained less than 20% of the initial value. Reference scattering at 0 V was collected from a cylindrical jet of water gravity fed from a 20 L reservoir maintained at a range of constant ( $\pm 1.5 \text{ }^\circ\text{C}$ ) temperatures between 5  $^\circ\text{C}$  and 65  $^\circ\text{C}$ . The flow rate was regulated so the jet overfilled the beam aperture in the same fashion as the water bridges.



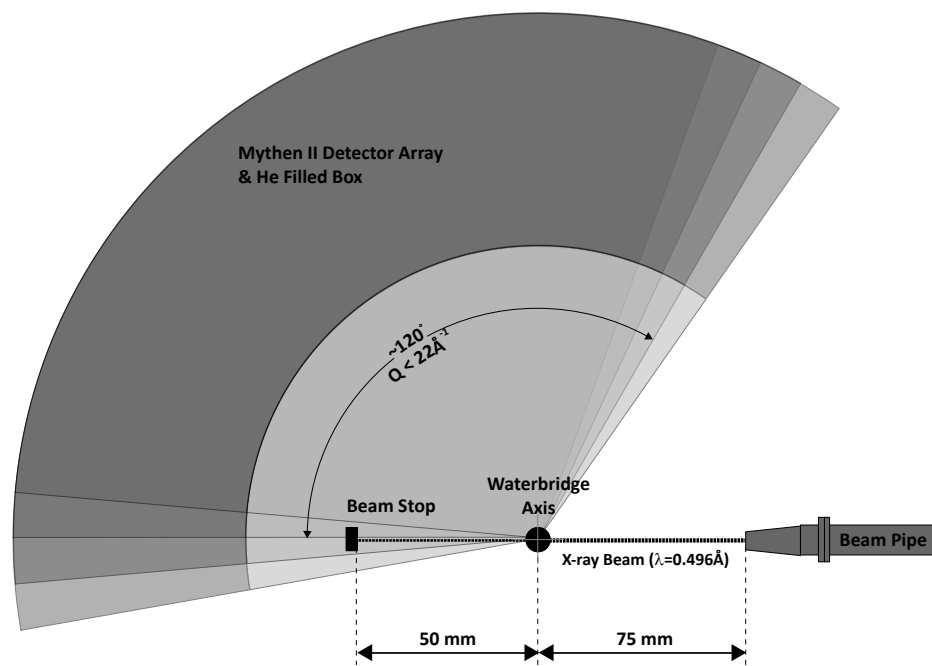


Figure 3.4 Schematic representation of the experimental setup. The beakers and electrodes are not shown for clarity.

The differential scattering cross-section was calculated from merged normalized data sets for the measured total scattering profile using GudrunX [28]. The background scattering correction was derived from the empty beam (air) with the armature in place. The Fourier transform over the measured  $q$  range gave reliable results of the radial distribution function between 0.3 Å and 10 Å.

### 3.5.2 Temperature effect on total X-ray scattering and tetrahedrality

Temperature affects the density of liquid water and thus the effect on the scattering profile is a non-trivial manner [29], [30]. The first two peaks from the corrected X-ray scattering data of the reference jets and the combined water bridge samples were fitted as a function of temperature (Fig. 3.5). Temperature references were prepared to compare the bridge to. However, it is known that the actually temperature in an operating bridge will fluctuate by as much as 10 °C and that local heating may transiently occur. Thus rather than attempting to fit the temperatures directly to the position of the first two  $S(Q)$  peaks,  $S_1$  and  $S_2$ , as has been done previously [31] a different approach which checks that the relationship between the magnitude of the second  $g(r)$  peak,  $g_2$ , as a function of the splitting,  $\Delta q$ , between  $S_1$  and  $S_2$ .

The collected data is in agreement with a previous small angle X-ray scattering study [32] and shows that for the extracted scattering data the principle difference in position and intensity correlates well with temperature effects. This correlation reveals that the effect of temperature on physical quantities such as density are within the expected bounds and helps in providing a good point of comparison with reference scattering intensities and subsequent derived quantities from water samples under zero applied potential.

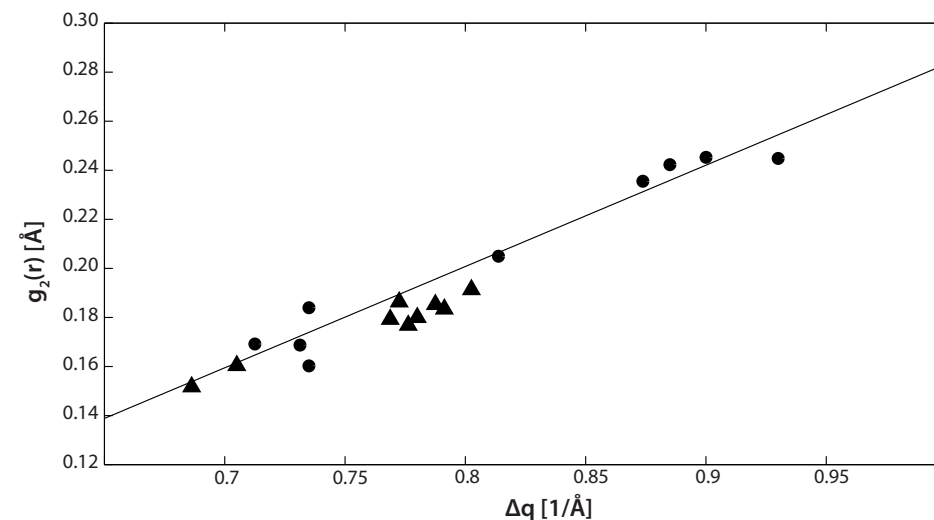


Figure 3.5: A check of whether the temperature dependence on tetrahedral order holds in the presence of moderate intensity electric fields. Water bridge data (triangles) is in good agreement with reference data (circles). The line is a guide to the eye and fit from only the reference data ( $R^2=0.9375$ )

### 3.5.3 Small Angle Neutron Scattering (SANS)

The neutron scattering experiments were carried out at the ISIS pulsed neutron source, Rutherford Appleton Laboratory, United Kingdom, on the neutron diffractometer SANDALS allowing the observation of large scattering vectors with a high resolution. The wavelength of the incident neutrons was between  $\lambda=0.05$  Å and  $\lambda=4.95$  Å, the dimensions of the beam were 7 mm horizontal x 20 mm vertical and the scattered intensity was measured with a ZnS detector which has 660 cells. Due to the time-of-flight principle, momentum transfers from  $q=0.5$  Å<sup>-1</sup> to 50 Å<sup>-1</sup> are accessible. The floating aqueous bridges with 10 mm in length were set up as described in section §3.2.1 with glass beakers using a specially constructed remote-control and monitoring set-up inside the SANDALS sample chamber. This allowed reproducing the beaker position and the bridge length with a precision of < 0.1 mm. A sketch of the measurement geometry is given in figure 3.6.

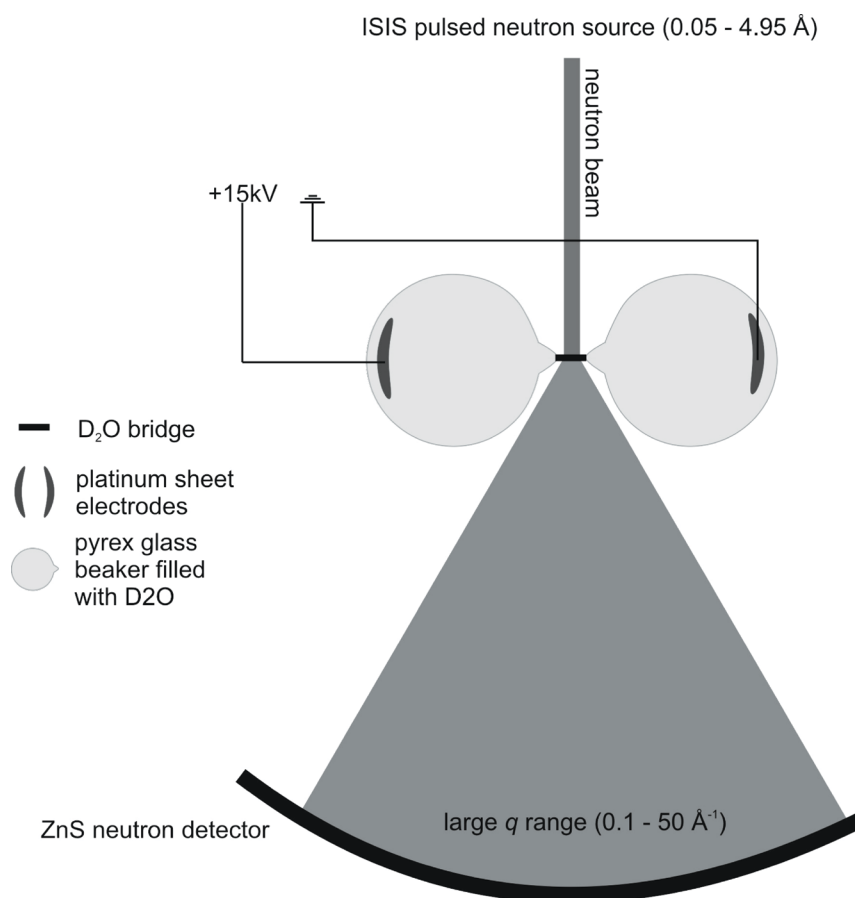


Figure 3.6 the aqueous bridge set-up at the SANDALS instrument

The bridge system during operation is considered as three connected liquid bodies: the anolyte, the catholyte, and the bridge itself. After bridge operation ceases only the former two bodies remain.

The water bridge formed between two beakers placed horizontally on either side of the neutron beam as soon as the voltage was applied. Operating at ~12-15 kV, the bridges that formed looked alike for light water (H<sub>2</sub>O), heavy water (D<sub>2</sub>O) and a “null” mixture (0.6407 H<sub>2</sub>O : 0.3593 D<sub>2</sub>O) of light and heavy waters with diameters oscillating between 1-3 mm. The use of isotope substitution in neutron scattering improves the site-site radial distribution function resolution. In null water, the hydrogen atom has zero scattering length on average, thus in principle the O-O correlation can be measured directly. However, the O-O signal constitutes only 12% of the total signal compared to the incoherent background from the hydrogen, thus a very high signal-to-noise ratio is required for this measurement.

The experiment was run in air, since an evacuation of the chamber was, for obvious reasons, not possible, and previous studies [33] have shown that the bridge is unstable or even unachievable in noble gas atmospheres. Thus, a large volume of air (~400 mm diameter) had to be traversed by the neutron beam, creating a large background scattering which significantly reduced the quality of the data from the water bridge.

A horizontal vanadium rod (6 mm diameter) was used to calibrate data on an absolute scale. The beam size was set to 7 mm horizontal x 30 mm vertical, using adjustable slits in the beam line and a fixed aperture which was inserted just before the sample. In order to verify the calibration procedure a rod of amorphous SiO<sub>2</sub> with 4 mm diameter was placed between the beakers at the exact position of the water bridge. Figure 3.7 shows the structure factor from this rod, after corrections, and compares with data obtained from a 3 mm solid slab of silica measured on SANDALS under the same conditions as the present study, but using the full beam size, 30 x 30 mm. This measurement confirms that accurate data are obtainable using the water bridge geometry, but also shows that the statistics are likely to be poor due to the reduced sample volume in the beam (about 0.1 mL in this case) and the large air scattering from around the bridge. For the water bridges, the diameter was typically smaller than that of the silica, so that the volume of the sample in the beam was even less, around 0.03 mL, which is about 40 times smaller than is normally used on SANDALS.

The corrections for normalizing to the incident beam monitor, background subtraction, calibration against the vanadium sample scattering, and corrections for multiple scattering and attenuation were applied using the GudrunN [28] software package. The data were analyzed detector by detector, and only added together at the very end. About 5% of the detectors showed low counts due to electronic faults or masking by the vacuum tank and were therefore excluded from the analysis.

Due to the dynamic nature of the phenomenon, the diameter of the floating bridges changed from 1-3 mm. Thus, in order to put the diffraction data on an absolute scale, it was necessary to assume the density of the bridge water was the same as bulk water, and use the diameter as an adjustable parameter to give the correct overall scattering level. At this point it should be noted that a previous neutron scattering study showed that the micro-density of a D<sub>2</sub>O bridge is sensibly the same as the bulk D<sub>2</sub>O density [34]. Therefore using bulk density for this calculation is a valid assumption.

The average diameters obtained over several bridges and many (e.g. 8+) hours of up-time were 1.60 mm (H<sub>2</sub>O), 1.80 mm (D<sub>2</sub>O) and 1.56 mm (null water). These diameters gave scattering levels typical to those found in similar experiments on the bulk versions of these samples. Typically, the scattering level for light and null water is a few percent below the theoretical limit due to inelasticity effects at the larger scattering angles.

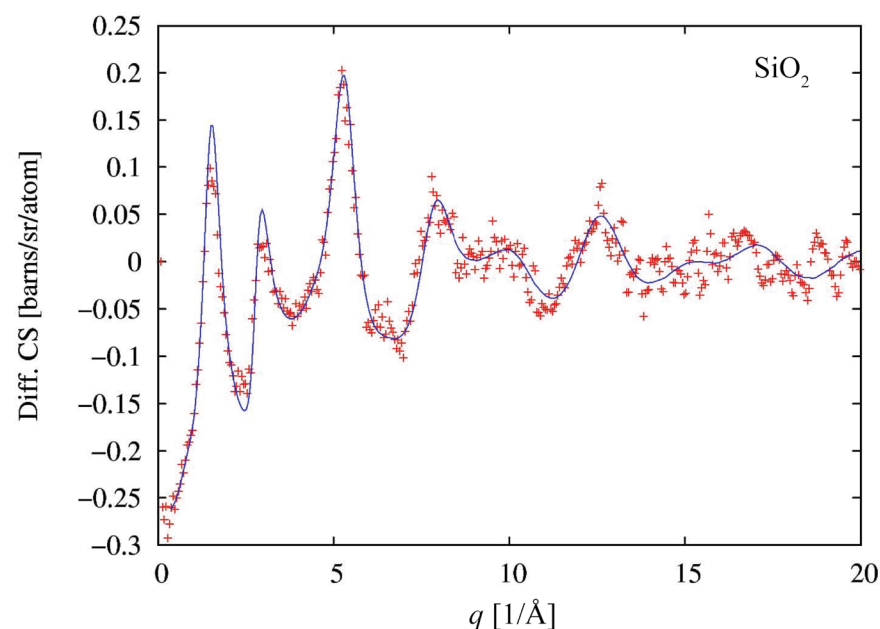


Figure 3.7: Interference differential scattering cross section for a horizontal amorphous silica rod 4mm in diameter placed at the same position as the water bridge (red crosses). The corresponding data from a 3 mm slab of amorphous silica is shown as the solid blue line.

### 3.5.4 Anolyte and Catholyte Neutron Scattering Cross-section

In addition to the measurements on the water bridge itself, samples of water were taken from the beakers after running the bridge and were subject to a standard diffraction measurement on the new NIMROD diffractometer in order to check whether the observed differences (see §4.2.1) in the anolyte and catholyte chemistry before and after bridge operation affected the scattering profile; this comparison is shown in figure 3.8.

The small differences between the anolyte, catholyte, and bulk water are due to differences between SANDALS and NIMROD instrument performance and not due to structural changes in the water. The structure below  $\sim 1 \text{ \AA}^{-1}$  should be ignored as it is due to mismatch between different detector banks. This mismatch is particularly true for the NIMROD data since the instrument was being commissioned at the time the measurements were being made so the low  $q$  region was not fully optimized.

For these measurements the samples were contained in closed 1 mm flat plate cans, so the thickness was known within a few percent. Since the scattering level for  $\text{D}_2\text{O}$  and null water was exactly as expected for these samples, there cannot have been any significant exchange of  $\text{H}_2\text{O}$  for  $\text{D}_2\text{O}$  (e.g. light water contamination) while the bridge was running.

The discrepancies between the different measurements are within the experimental uncertainties. When, e.g., a certain pressure is applied or solutes added [35], [36] to water, the trends in the structure factors are clearly visible which is not the case for the data presented. Therefore, we conclude that the water in the beakers after bridge operation is, with regards to this measurement and within the detection limits, identical to bulk water. It is noteworthy that there was no change in the overall scattering level of the null water from the two beakers, the scattering levels are equal within 1%, indicating there was no discernible electrophoretic separation of  $\text{H}_2\text{O}$  from  $\text{D}_2\text{O}$ .

### 3.5.5 Empirical potential structure refinement

The method and limitations of analyzing combined X-ray and neutron data from disordered materials is covered extensively in the literature [37]–[39]. The methods used herein are consistent with those used for liquid materials and specifically water. In the case of the use of an EHD bridge as sample it bears to briefly remind the reader of potential pitfalls in using the standard approach. The detector geometries are somewhat biased in relation to the imposed electric field parallel to the longitudinal bridge axis. On average the neutron

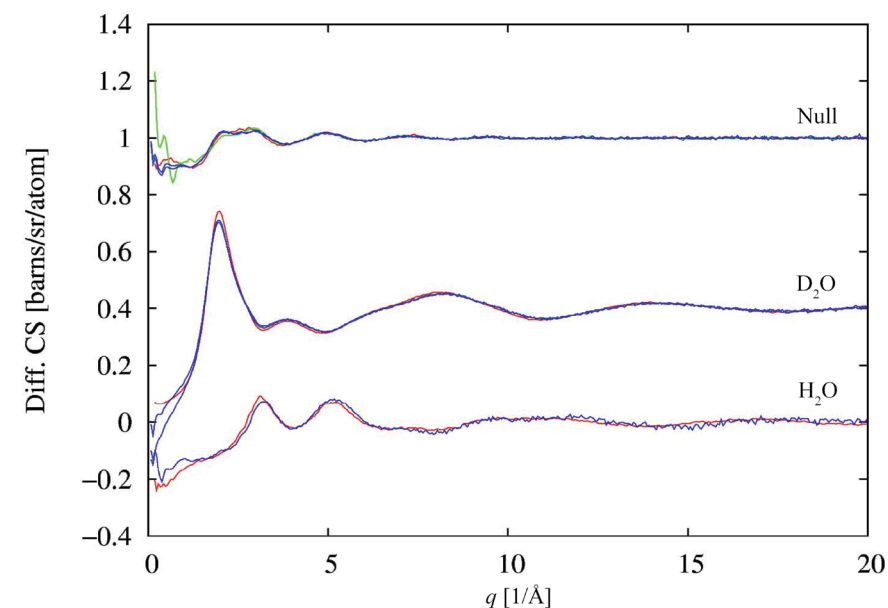


Figure 3.8: Diffraction pattern from the water in the beakers after the bridge operation. The spectra from the grounded beaker and that from the HV beaker are shown as solid blue lines as measured on NIMROD, while earlier results from bulk water on SANDALS ( $\text{H}_2\text{O}$ ,  $\text{D}_2\text{O}$  and null) are shown as the red lines. For  $\text{H}_2\text{O}$  only the catholyte data is shown, for  $\text{D}_2\text{O}$ , both electrolyte solutions are plotted, and for null water, the green line represents a bulk water spectrum run on NIMROD.

scattering vector is along the bridge axis, whereas X-rays scatter in a perpendicular direction. However, the neutron detectors on SANDALS are designed for large square samples and thus span a range of azimuthal angles, depending on the scattering angle, which means that in practice there can be quite a few off-axis scattering vectors included in the average signal. This problem is essentially non-existent in the MYTHEN II detector as this system is optimized for cylindrical samples and covers an azimuthal distance (8 mm) which is close to the incident beam width (4 mm). The atomic form factors, inelastic scattering contributions, and material density are considered unchanged from that of bulk water throughout the data reduction and subsequent analysis. Empirical structure refinement was conducted using the EPSR24 distribution [40] using the TIP4P/2005 force field [41]. This model has been previously shown to quantitatively agree with small angle X-ray scattering data [42], matches well to key physical parameters such as the density maximum of water [41], and has been used for other combined neutron X-ray refinement studies [43], [44] and explorations of intermediate-range order in water [45]. The simulation box contained 1000 molecules with a number density of 0.1002 molecules/Å<sup>3</sup>. The molecules were randomized and brought to equilibrium without the application of the empirical potential for 100 cycles. Identical copies of this box were loaded as the starting point for the simulations where an empirical potential was applied to force the scattering profile of the simulation to approach that of the measured differential scattering cross-section. Both simulations ran simultaneously on the same computer so that the effect of the pseudo random number generator producing artifacts would be minimized. The simulations were also run for a large number of accumulations to reduce the output to a statistically significant and stable configuration. For every five steps in the simulation an output file was recorded and these were compounded into the stable configuration which included 23650 snapshots.

## 3.6 Quasi-Elastic Neutron Scattering (QENS)

*QENS is a special case of inelastic scattering which permits the measurement of diffusion, relaxation, and other slow energy or mass transfer modes in materials using a time-of-flight spectrometer. This data complements NMR methods.*

### 3.6.1 QENS Theory

The scattering relationships of matter-matter interaction are very similar to those for photon-matter experiments. The scattering is said to be quasi-elastic as the change in energy of the scattered (μeV) vs incident particles (meV) is small. QENS is able to probe interaction length scales from 1-100 Å and time scales on the order of ps – ns. The method is well suited for probing incoherent scattering processes like the molecular diffusion of hydrogen with minimal contributions from coherent signal arising from the material structure and collective nuclear dynamics. The method returns the time scale of atomic motion (protons in this case) in the intermediate scattering function derived from the Fourier transform of the

autocorrelation and pair correlation functions and provide the spatial dynamics as well. Thus with this method it is possible to not only derive the diffusion rates but also the jump length of the probed atom.

### 3.6.2 General experimental considerations

In order to investigate the molecular properties in the water bridge with QENS, one is faced with a serious challenge: whereas normally shape and geometry of a sample are rather independent from its molecular properties, previous studies [46] have shown that applying an electric field to bulk water in a single beaker does not turn it into the “water bridge water” tested here. Submerging two electrodes in one beaker will result in too low voltages or too high currents – recalling the concept of the “leaky dielectric”. In order to see minute influence from high electric fields – e.g. different relaxation times – only small currents normally in the range between 0.1 and 1 mA are allowed when high voltages are applied, otherwise ohmic heating will render the experiments impossible. In the experimental setup used the required high voltage (~10kV) can be applied since the hanging water rope acts as an aqueous resistor limiting the current. Therefore, if such an aqueous resistor is needed to record molecular data by QENS, one must measure in this very specific water bridge setup – including its beakers, cables, electrodes, etc. Thus one must deal with the disadvantages of such an approach: Sample surface is much too low (20-30 mm<sup>2</sup> instead of 25 cm<sup>2</sup>), and the additional tools required for the creation of the bridge do block the scattered neutrons in certain directions resulting in substantial data loss. Moreover, the sample thickness (2-3 mm instead of 0.1 mm) causes multiple scattering which is next to impossible to compensate for mathematically. The only viable option to correctly interpret data from a water bridge set-up is a comparison to a bulk water sample with the same suboptimal geometry, and to compare that sample to an optimal sample and the calculated values. This option is the path that was chosen in this work: an aluminum cylinder filled with deionized water positioned between the beakers was measured at the exact position where the water bridge formed. Aluminum has the advantage of practically being invisible for the chosen neutron wave length and angular range. In order to make up for some of the loss due to the beaker shadows, this approach was carried out in two configurations, one for small angles, and one for large angles.

### 3.6.3 QENS Protocol

The QENS experiment was carried out at the Laboratoire Leon Brillouin (LLB) in Saclay, France, using the time-of-flight spectrometer MiBeMol. The incident monochromatic neutron wavelength was 6.0 Å ( $E=2.27$  meV), which resulted in an energy resolution (FWHM) of 92.7 μeV. Water bridges were created using a pair of borosilicate beakers filled with de-ionized water as per the protocol described in section §3.2. The applied operating voltage varied between 10 and 15 kV, at currents on the order of ~0.3 mA. The bridge length was  $10 \pm 1$  mm with a diameter of ~2 mm.



As mentioned in §3.6.2, two different geometries were applied. In the “small angles” geometry (a), the bridge was placed perpendicular to the beam, and only detectors 6-19 were evaluated. In “large angles” geometry (b), the bridge turned counterclockwise by 40°, and only detectors 61-84 were evaluated. Detectors with known issues were identified and omitted in all analyses (2,3,4,5,69,75,84). All parts of the set-up except for the bridge were protected from the incident neutrons by Cadmium shielding. Photographs with explanatory sketches of the actual set-ups are given in Fig. 3.9a (“small angles scattering” geometry) and Fig. 3.9b (“large angles” scattering geometry).

The data were normalized using the scattering intensity from a thin vanadium cylinder (2mm diameter) which was placed at the position of the bridge. For comparison, for the reasons explained above, an Al cylinder with a 2 mm inner diameter was filled with deionized water and also measured at the position of the water bridge.

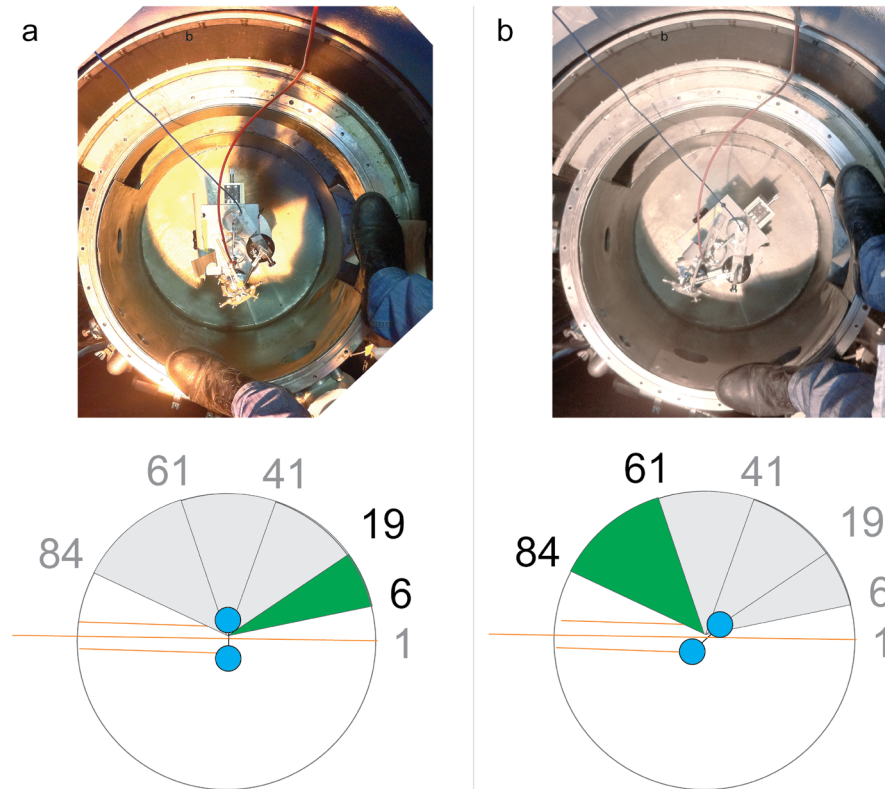


**Figure 3.9** Photographs and sketches of the measurement geometries: a) “small angles” scattering geometry: bridge perpendicular to the beam, detectors 6-19 evaluated. b) “large angles” geometry: bridge turned 40° counterclockwise, detectors 61-84 evaluated.

### 3.6.4 QENS Data Analysis

Under optimal conditions QENS data is evaluated assuming that in the region of small energy transfers the scattered intensity is represented by the dynamical structure factor  $S(Q, \omega)$ :

$$S(Q, \omega) = \exp\left[\frac{-Q^2 \langle u^2 \rangle}{3}\right] T(Q, \omega) \otimes R(Q, \omega) \quad (\text{Eq. 3.9})$$

which includes a Debye–Waller factor (the exponent) accounting for time-independent contributions due to atomic vibrations. Where  $\langle u^2 \rangle$  is the mean square amplitude of the vibration modes of the protons and represent contributions from translations and rotations, respectively [47], [48]. According to the model of Sears [49], rotations can be separated from translations assuming independence of the two. The rotational term can be reduced to the sum of a  $\delta$ -function plus a Lorentzian with HWHM equal to  $1/(3\tau_1)$  [47] where  $\tau_1$  represents the relaxation time associated with rotational diffusion. It has an Arrhenius type of behavior and can be written as

$$\tau_1 = 0.0485 \exp\left[\frac{E_A}{k_B T}\right] \quad (\text{Eq. 3.10})$$

where  $k_B$  is the Boltzmann constant,  $T$  the absolute temperature, and  $D_r$  the rotational diffusion constant.  $E_A = 1.85 \text{ kcal mol}^{-1}$  and can be associated with the hydrogen bond strength [47]. Ultrafast vibrational spectroscopy measurements presented in §4.7 have shown that the hydrogen bonds in a water bridge system are significantly stronger than in bulk water due to the applied high voltage, meaning that  $E_{A(\text{water bridge})} \gg E_{A(\text{bulk water})}$ . In the model of Sears [49], the relative intensities of the two contributions (translation and rotation) are linked by Bessel functions. A higher energy reduces the temperature dependence of  $\tau_1$ . For the small angle data, because of the value of the Bessel function, the contribution of the rotational line is negligible and will be neglected in the present analysis.

In order to link the QENS data to a more fundamental interpretation one must keep in mind that previous experiments have shown that the water in the water bridge is not in a liquid bulk water state. According to the results from §4.7 and Teschke *et al.* [50], the water in the water bridge is in a state between liquid and solid in terms of the vibrational lifetime of the OH-stretch vibration of HDO molecules in HDO:D<sub>2</sub>O; and viscoelastic behaviour of the bridge. The vibrational life time in the bridge was determined to be  $630 \pm 50 \text{ fs}$ , in between that of ice ( $384 \pm 16 \text{ fs}$ ) and the bulk at 0°C ( $740 \pm 40 \text{ fs}$ ) [46]; the viscoelastic behaviour was described in terms of the Young modulus (24 MPa) [50].

Together with these findings and based upon infrared emission spectroscopy §4.4.4, a model for a cooperative proton transfer is proposed: In the bridge hydrogen-bonding between H<sub>2</sub>O molecules is strongly enhanced, and two proton populations can be distinguished: One

consisting of protons strongly bound to the oxygen atoms with very slow diffusion as in a viscous liquid (immobile population), and a second one of more delocalised, quasi-free protons (mobile population).

In QENS the translational diffusion of the first population (strongly bound to the oxygen atom) is drastically slowed down, to the point that the measured correlation time is out of the instrumental window. While in water at room temperature the re-orientation takes places in the sub-ps range, the situation is formally that of orientational crystals where molecules turn at fixed sites of a crystalline lattice, although one has to also assume a weak diffusion outside the experimental window. So these protons are expected to show elastic scattering behavior in the current experiment. The second population – the quasi-free protons – are more mobile from a quantum-mechanical proton channel perspective than protons in bulk water, and are expected to scatter inelastically significantly more than protons in bulk water. A proper formula used for the curve fitting of the data based on the assumptions above is given in equation (3.11). Here, the Debye-Waller factor is suppressed,  $S(Q, \omega)$ , represented by one Lorentzian for the inelastically and a  $\delta(\omega)$  function for the elastically scattered neutrons,

$$S(Q, \omega) = I_{El} \delta(\omega) + A \frac{\Gamma}{\Gamma^2 + \omega^2} \quad (\text{Eq. 3.11})$$

$\omega$  is the elastic peak shift,  $I_{El}$  the elastic peak intensity,  $A$  the Lorentzian intensity, and  $\Gamma$  the Lorentzian's HWHM. Naturally, in a purely liquid sample, the expected contribution of is zero, but should be significant in the water bridge. The Lorentzian is expected to be much broader in the water bridge than in the bulk; in both cases it is supposed to be broader than under optimum conditions due to multiple scattering.

## 3.7 Nuclear Magnetic Resonance (NMR)

*The NMR methods used herein specifically probe the environment of protons in the system under study and provides clues about the strength of both intra- intermolecular coupling in the system.*

### 3.7.1 Magnetic resonance principles

The positively charged nucleus of every atom is positively charged and possesses a quantity associated with angular momentum described by the spin quantum number. The effectively spinning charge of the nucleus generates a small magnetic field, the orientation of which is described the nuclear magnetic dipole vector,  $\mu$ . The external application of a strong magnetic field will partially align the nuclear dipoles, temporarily pinning a certain population of them against thermal agitation. Of those aligned dipoles two populations will emerge a high energy and a low energy population depending on relative polarity of the external magnetic  $B_0$  and nuclear magnetic field vectors. The energy difference ( $\Delta E$ ) between these two levels

is dependent upon the magnetic field intensity and the gyromagnetic constant related to the magnitude of the nuclear dipole moment:

$$\Delta E = \gamma \hbar B_0 \quad (\text{Eq. 3.12})$$

where,  $\hbar$ , is the Dirac constant. The stronger the external field the greater the energy splitting. This has implications because conservation of angular momentum will require  $\mu$  to precess about direction (z-axis) of  $B_0$ . The precession (Larmor) frequency of  $M_0$  is related to  $\Delta E$  by the transition frequency,  $\nu_0$ , between the two energy levels:

$$\nu_0 = \gamma B_0 / 2\pi \quad (\text{Eq. 3.13})$$

and determines the operational frequency of magnetic resonance spectrometers and imaging scanners. These instruments use radio frequency (RF) pulses with a defined bandwidth and centered on the Larmor frequency of the nucleus under study. For the investigations discussed currently, only the spin  $1/2$ , single proton of the hydrogen nucleus ( $^1\text{H}$ ) was probed. By shaping the phase and timing of the applied RF pulses it is possible to interrogate the unit vector contributions to the net magnetization vector,  $M_0$ , of the precessing nuclear dipole population. By convention, the longitudinal vector is labeled  $M_z$ , whereas the transverse components  $M_x$  and  $M_y$  lie in the x-y plane.

There are many types of pulses and pulse sequences employed in modern nuclear magnetic methods [51] however only two will be discussed in this introduction:  $90^\circ$  and  $180^\circ$  pulses. The difference between these two pulses are in how they affect either  $M_0$  or alternatively the population distribution between upper and lower energy states. For example, a  $90^\circ$  pulse will rotate  $M_0$   $\pi/2$  radians so that  $M_0$  is rotated towards the laboratory frame y-axis unit vector. In a similar fashion the  $180^\circ$  pulse will turn invert the direction of  $M_0$ , rotating the vector through  $\pi$  radians. Quantum mechanically speaking the action of a  $90^\circ$  pulse is to promote the excess spin population to the less populated level (usually excited) thus creating an equal spin distribution between the two levels. By doubling the pulse duration to produce a  $180^\circ$  pulse the excess population becomes inverted. The decay of these various magnetic polarization states provides information on the local nuclear environment being probed. Pulses perform both pump and probe operations however, the stimulation and detection schemes differ depending on which type of physical quantity one wishes to probe. The three observables investigated in this research are the proton chemical shift,  $\delta$ , longitudinal relaxation time,  $T_1$ , and transverse relaxation time,  $T_2$ .

Relaxation times are the time required for a particular component of  $M_0$  to return to the thermal equilibrium value prior to excitation.  $T_1$  is derived from the recovery of the full magnitude in the direction  $M_z$  and is also known as the spin-lattice relaxation as the absorbed energy is redistribute to the thermal bath providing a measure of the enthalpy

of the system.  $T_2$ , or spin-spin relaxation, describes the loss of phase coherence between neighboring spins which for a hydrogen bonding liquid includes not only intramolecular modes but also local intermolecular modes. Transverse relaxation is an adiabatic process whereby energy is redistributed locally but without the whole spin system losing energy, this provides a measure of the local entropy of the spin system. The physical causes of relaxation are dependent upon the sample composition but spin  $\frac{1}{2}$  protons in a simple polar liquid like water or glycerol only a few interactions contribute significantly [52]: intermolecular dipole-dipole (near field modulated), scalar coupling (electron field modulated dipole-dipole), spin-rotational coupling (diffusion and translation), and a very small contribution from chemical shift anisotropy (slow tumbling asymmetric molecules). This last difference can be seen in figure 4.32 as the slopes of the relaxation shift are different for different proton populations. For example, the relaxation change of the alkyl protons are less affected by temperature than the alcohol protons. For those protons involved in hydrogen bonding the dipole-dipole interaction will contribute most significantly to  $T_1$ . Strong coupling constants yield shorter relaxation times as the absorbed energy is quickly lost to the bath. Whereas, the bandwidth of the excited nuclear spins will undergo spectral diffusion through scalar and spin-rotational coupling and this will impact  $T_2$ . Transverse relaxation can also occur without  $T_1$  via what is known as spin-spin flip-flop which is a dipole mediated exchange whereby two opposite spins flip polarizations, the change of polarity induces a small transition dipole moment that decays in the transverse plane. The less coherent the interacting system of spins the longer  $T_2$  relaxation will take (with  $T_1$  setting the upper limit).

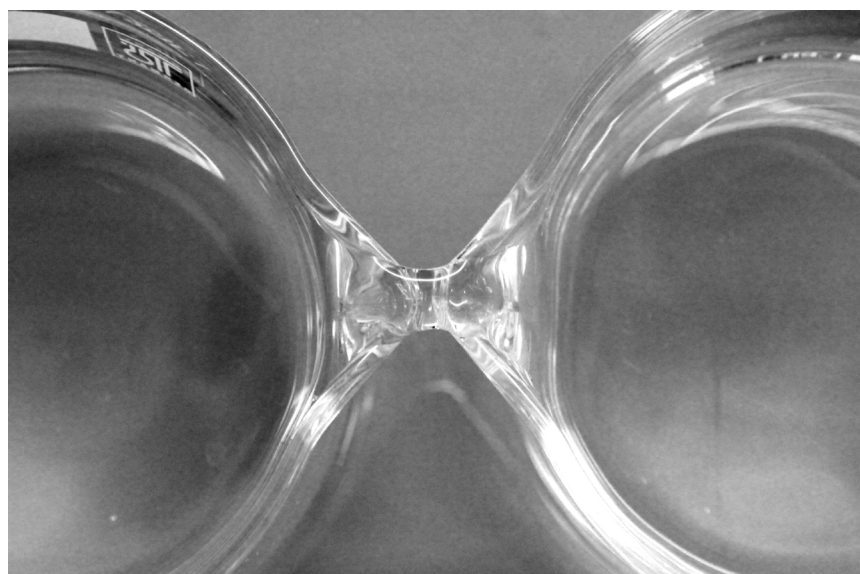


**Figure 3.10 Zero-distance EHD bridge prepared with ultrapure light water. The bridge waist diameter in this image is 6 mm.**

The identification of different proton groups in a sample is done using the chemical shift. This is a small change in the Larmor frequency of the probe nucleus due to the presence of neighboring atoms within the same molecule. These nuclei also produce their own magnetic field (and precess at their own Larmor frequency as  $\gamma$  is different for each nucleus) which adds to and augments  $B_0$  resulting in a change of the local magnetic environment. The applied field also induces an electron current perpendicular to  $B_0$  which further distorts the local magnetic field. Since all molecules of a given chemical species have essentially the same chemical structure these small changes add up and with the use of a spectrometer the distribution of varying Larmor frequencies can be detected. This powerful tool is most commonly used for structure determination and can also provide information about the interaction between two chemical species.

### 3.7.2 EHD Bridges in high magnetic field environment

EHD bridges were prepared in a manner consistent with the method described in §3.2 and modified to be compatible with the magnetic environment in a medical MRI scanner (Magnetom Sonata, Siemens Healthcare GmbH, Erlangen, Germany). Non-magnetic materials were used in the construction of the fixating armature, cable supports, and electrode mounts. The beaker spouts were left in contact throughout the measurements to reduce the chance of bridge rupture, liquid leakage, and electrical arcing – all of which could pose a hazard to the MRI scanner. Though this produced a bridge system without a free-hanging section these “zero-length” bridges (see figure 3.10) behaved in a manner consistent with extended bridges. The seven EHD bridges used in this study, four for isotope mixture measurements and three for flow investigations, were operated in a voltage limiting regime between 15.00-18.00 kV and open currents between 600-1600  $\mu$ A. The higher current than previously reported is due to the larger diameter of the bridge ~6-8 mm on account of the zero-length. The experimental set-up, illustrated in figure 3.11, was placed within a standard circular-polarized knee coil, and aligned so that the long axis of the bridge was parallel to the main magnetic field  $B_0$ . The bridge center was located at the isocenter in the head-feet and right-left directions, and several millimeters above the isocenter in anterior-posterior direction.

The bridges were always arranged with the anode placed towards the foot end of the patient table and cathode towards the head end. A plastic box filled with 500 mL agar and covered with a glass plate formed the electrically insulating support base for the beakers. The agar phantom was used as a signal reference for intensity normalization. All materials were fixed in place using MR compatible tape which does not produce artifacts in the recorded images. Platinum foil (99.999% Pt, MaTeck GmbH, Jülich, Germany) was soldered to both the high voltage (HV) and ground leads. These wires were sufficiently long (~10 m) to reach from the experiment at the MR scanner isocenter to the power supply located just outside the room via an RF suppressing pass-through in the Faraday cage wall. A low voltage resonant RLC tank circuit installed on the HV coaxial shield and ground wires shifted most of the induced radio



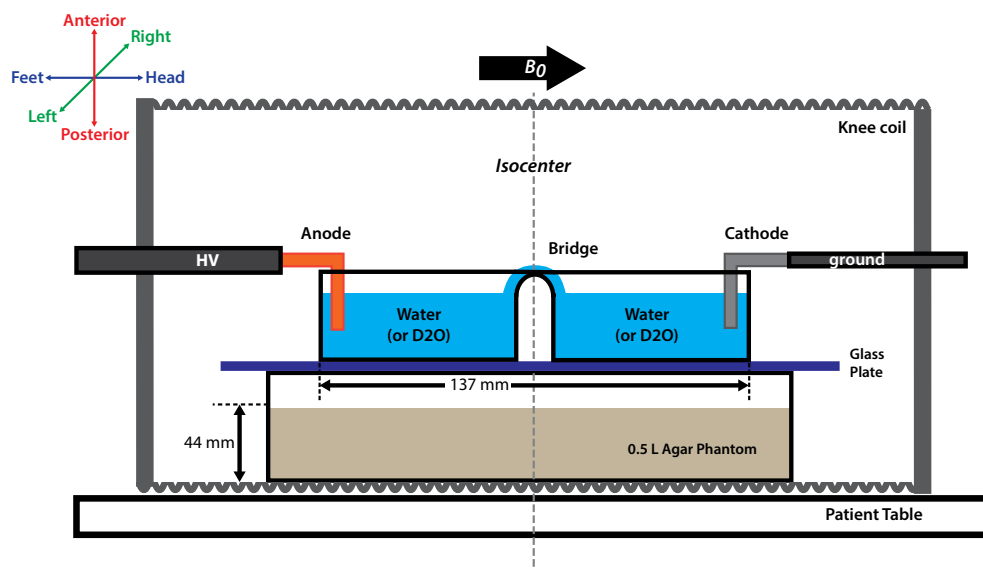


**Figure 3.11** Diagram of the experimental setup used for the presented study. Main orthogonal directions (feet-head, anterior-posterior and left-right) are indicated in the upper left corner.

frequency interference (RFI) bands outside the operational frequency range of the scanner, however one band persisted. Mass flow was tracked by filling the one beaker with heavy water (99.9 % D<sub>2</sub>O, DLM-4-100, Cambridge Isotope Laboratories, Inc., Andover, MA, USA) and the other with an equal volume of freshly prepared ultrapure light water (~99.98 % H<sub>2</sub>O).

The starting mass used in these experiments was 61.3±0.7 g light water, 65.5±2.3 g heavy water corresponding to a starting volume of ~63 mL in each beaker. The variability in mass was due to the criterion that the liquid levels at the spouts be equal. Heavy water produces no signal as the precession frequency of the deuterium (<sup>2</sup>H or D) nucleus at 1.5 T is outside the operating bandwidth of the MRI scanner [53] thus it is possible to track the mass transfer and mixing rates of protium (<sup>1</sup>H or H) nuclei in an operating bridge as a function of both intensity and location [54]. In all experiments the starting conductivity of the water was below 1 μS·cm<sup>-1</sup>. MR flow imaging used equal volumes of light water (67.0±0.5 g) in both beakers.

### 3.7.3 High Field NMR Spectroscopy

#### 3.7.3.1 Sample preparation for nuclear magnetic resonance (NMR) spectroscopy

To obtain samples for NMR measurement neat liquids (H<sub>2</sub>O, glycerol, or defined mixtures of these two compounds) have been used. The liquids were filled into 5 mm high precision NMR sample tubes (Wilma 507 PP 8"). A C<sub>6</sub>D<sub>6</sub> vortex capillary was added to the probes to avoid mixtures between the deuterated substance use for the lock and the investigated liquids. Comparable systems have been described earlier [55], [56].

#### 3.7.3.2 Nuclear magnetic resonance (NMR) spectroscopy

All spectra were recorded on a DRX-400 AVANCE spectrometer (Bruker, Billerica, MA, USA) with a two channel z-gradient inverse probe head using the bundled software (Topspin 1.3, Bruker, Billerica, MA, USA). Irradiation and measurement frequency was 400.13 MHz for protons (<sup>1</sup>H). Temperature was adjusted between in the range between 300 K and 328 K (27 °C - 55°C) with an accuracy of ±0.05 K (°C). The NMR tube was rotated during the measurements. The C<sub>6</sub>D<sub>6</sub>H of residual from the not fully deuterated C<sub>6</sub>D<sub>6</sub> in the vortex capillary was used as external reference (δ = 7.15 ppm) [57].

One dimensional proton (<sup>1</sup>H) spectra were recorded with a <sup>1</sup>H-pulse flip angle of 30°, acquisition of 32k data points and a relaxation delay of 1.0 s. Free induction decays (FID) of eight scan were added for one spectrum. After zero filling to 64k data points the summed FID was directly Fourier transformed to gain spectra with a spectral range of 6,000 Hz.

Longitudinal relaxation time constants (*T*<sub>1</sub>) were determined by the inversion recovery method changing the recovery delays in eight steps from 10.0 ms to 5.0 s. [58] For each scan a 180°<sub>y</sub> pulse, the recovery delay and a 90°<sub>-y</sub> pulse were followed by the acquisition. During acquisition 32k data points were collected and the subsequent relaxation delay took 5.0 s. FIDs resulting from eight scans were added prior to Fourier transformation which led to spectra with a spectral range of 6,000 Hz.

The transversal relaxation time constants (*T*<sub>2</sub>) were measured with the spin-echo sequence (CPMG) using a τ of 10.0 ms and varying the number of spin-echo blocks (2τ-times) from 2 to 50 [59]. For each scan a 90°<sub>y</sub> pulse was followed by the series of spin-echo blocks (τ - 180°<sub>y</sub> pulse - τ) prior to the acquisition. During acquisition 32k data points were collected and the subsequent relaxation delay took 5.0 s. FIDs resulting from eight scans were added prior to Fourier transformation which led to spectra with a spectral range of 6,000 Hz.

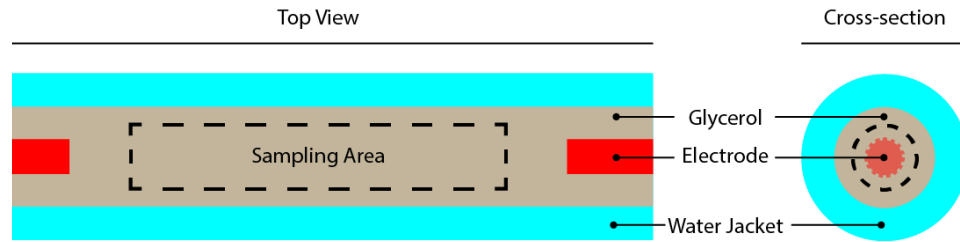


**Figure 3.12** Diagram of the coaxial temperature controlled sample cell for low field NMR spectroscopy with static electric field in glycerol

### 3.7.4 Low Field NMR Spectroscopy

A special temperature controlled sample cell (Fig. 3.12) was prepared for low field spectroscopy that consisted of a coaxial arrangement whereby the liquid under study was contained in the central tube and the outer jacket carried recirculated water in a closed heating/cooling loop to provide constant temperature. The inner sample tube was closed on both ends with glass encased potted electrodes that allowed the generation of electric fields up to  $300 \text{ V cm}^{-1}$ . Dielectric failure of the electrode casing on the anode prevented investigation of higher field strengths. A fiber optic temperature probe embedded in the tip of each electrode provided temperature readings and showed the temperature was constant throughout the measurement series at  $35 \pm 0.01 \text{ }^{\circ}\text{C}$ .

### 3.7.5 MRI sequences and protocols for isotope and flow analysis

The bridges studied under this protocol were composed of water or heavy water as described in section §3.7.2. Isotope mixture and flow experiments were started with the acquisition of an isotropic 3-dimensional (3D) spoiled fast low-angle shot (FLASH) sequence (Bernstein et al. 2004) covering the experimental set-up. Protocol parameters were as follows: Echo time (TE), 3.5 ms; repetition time (TR), 9.3 ms; flip angle,  $5^{\circ}$ ; resolution  $0.7 \times 0.7 \times 0.7 \text{ mm}^3$ ; bandwidth, 130 Hz/pixel; field-of-view (FOV),  $140 \times 140 \text{ mm}^2$ ; number of slices, 88. The sagittal (or almost sagittal, in case of small experimental misalignment) plane containing the exact long axis of the bridge was reconstructed from the 3D data set by multiplanar reformatting (see figure 3.13) and was used as central imaging plane for further measurements. This sampling volume reveals all salient features of an operating EHD bridge system – i.e. anolyte, catholyte, and bridge.

Isotope mixture was visualized by repeated acquisition of a 3D FLASH measurement with protocol parameters: TE, 1.9 ms; TR, 4.5 ms; flip angle,  $5^{\circ}$ ; resolution  $1.3 \times 1.3 \times 5.0 \text{ mm}^3$ ; bandwidth, 300 Hz/pixel; FOV,  $160 \times 160 \text{ mm}^2$ ; number of slices, 16. The acquisition time of 3 s per 3D slab determined the time resolution of the imaged mixture process.

For flow measurements a 2D FLASH-based phase contrast sequence with three-directional velocity encoding by a simple four-point velocity encoding scheme (Bernstein et al. 2004) was employed. Velocity encoding (VENC) was set to 70 cm/s in all directions. Further protocol parameters were as follows: TE, 5.1 ms; TR, 41 ms; flip angle,  $10^{\circ}$ ; resolution  $0.5 \times 0.8 \times 4.0 \text{ mm}^3$ ; bandwidth, 225 Hz/pixel; FOV,  $140 \times 140 \text{ mm}^2$ ; number of averages, 19. The bridge volume was covered with 7-9 parallel overlapping slices (slice distance of 2 mm) in (almost) sagittal image orientation determined by the planning procedure described above.

### 3.7.6 Image analysis

To study isotope mixture, the time evolution of mean signal intensities for anolyte ( $SI_{\text{anolyte}}$ ), catholyte ( $SI_{\text{catholyte}}$ ) and agar phantom ( $SI_{\text{reference}}$ ) were derived in the central sagittal slice employing standard MR software (syngo.MR, Siemens Healthcare GmbH, Erlangen, Germany). The regions of interest (ROI) in the anolyte ( $ROI_{\text{anolyte}}$ ) and catholyte ( $ROI_{\text{catholyte}}$ )

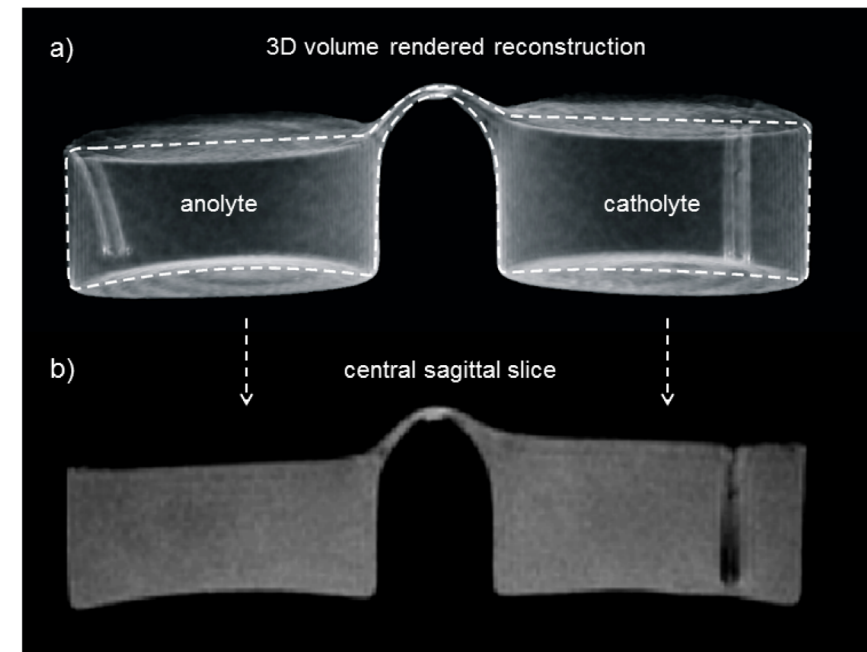


**Figure 3.13** Tomographic volume rendering of a typical water bridge (a) and the multiplanar reformatted central sagittal slice (b) used in this study.

comprised the respective fluid volumes and were manually adapted in each time frame; the ROI in the agar phantom ( $ROI_{reference}$ ) was kept fixed (figure 3.14). Relative volumes of anolyte ( $relVol_{anolyte}$ ) and catholyte ( $relVol_{catholyte}$ ) at a time  $t$  were estimated according to

$$relVol_i(t) = \frac{ROI_i(t)}{ROI_i(t_0)}, \quad (Eq. 3.14)$$

with  $i$  = anolyte or catholyte and  $t_0$  the time of bridge ignition.

Relative total fluid volume ( $relVol_{total}$ ) at a time  $t$  was determined as:

$$relVol_{total}(t) = \frac{ROI_{anolyte}(t) + ROI_{catholyte}(t)}{ROI_{anolyte}(t_0) + ROI_{catholyte}(t_0)}. \quad (Eq. 3.15)$$

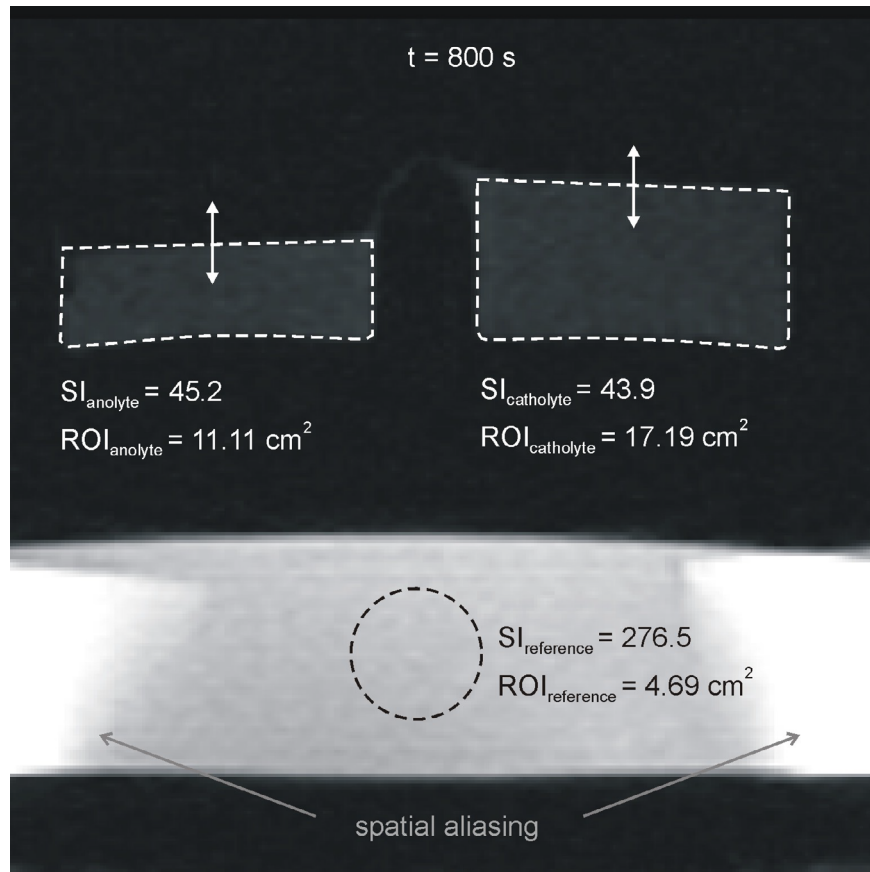


**Figure 3.14** Definition of regions of interest in the isotope mixture experiments. Fluid levels of anolyte and catholyte (here at  $t = 800$  s) were adapted in each time frame (as indicated by arrows). The bridge was excluded from analysis.

As signal intensity in FLASH sequence is proportional to proton density (Bernstein et al. 2004), relative signal intensities ( $relSI$ ) of the anolyte  $relSI_{anolyte} = SI_{anolyte}/(SI_{anolyte} + SI_{catholyte})$  and catholyte  $relSI_{catholyte} = SI_{catholyte}/(SI_{anolyte} + SI_{catholyte})$  were employed as measures of proton densities in respective beakers. By choosing low flip angle and short echo time, the FLASH signal intensity depended only moderately on changes in  $T_1$  and  $T_2^*$  relaxation times, which might be caused by chemical exchange of hydrogen isotopes and/or heating during mixture [51].

The change of relative total signal intensity for anolyte and catholyte with respect to the reference signal  $SI_{reference}$  is defined as:

$$relSI_{total}(t) = \frac{SI_{anolyte}(t) \cdot ROI_{anolyte}(t) + SI_{catholyte}(t) \cdot ROI_{catholyte}(t)}{ROI_{anolyte}(t) + ROI_{catholyte}(t)} / SI_{reference}(t) \quad (Eq. 3.16)$$

and was used to check for possible relaxation time changes during the experiment.

Phase contrast images of light water flow experiments were evaluated by means of prototype software (4D Flow, Siemens Healthcare GmbH, Erlangen, Germany) allowing visualization and analysis of 3D velocity fields [60].

### 3.7.7 MR Relaxation Mapping and Thermometry

#### 3.7.7.1 Glycerol bridges

The bridges studied for this section were prepared from glycerol rather than water. This was done for two reasons: 1) the relaxation times of glycerol ( $\sim 50$ - $500$  ms) are much shorter than that of water ( $\sim 3000$ - $4000$  ms) at 1.5 T which meant that multiple complete measurement sets could be completed in a single measurement period and, 2) the higher viscosity of glycerol (1.412 Pa·s) [61] compared to water ( $8.9 \times 10^{-4}$  Pa·s) [62] reduced the influence of motion artifacts on the resulting relaxation maps. The same experimental set-up as was used for the water studies described above (§3.7.2, Fig. 3.11) was used except anhydrous glycerol (49767-100ML, Lot # BCBK7056V, Sigma Life Science, St. Louis, MO, USA) was used instead. A total of 31 pairs of  $T_1$  and  $T_2$  measurements were made using data collected from nine glycerol bridges operated at 16 kV and 10-20  $\mu$ A. Glycerol temperature was measured before and after bridge operation in both the anode and cathode beaker with an alcohol thermometer. The typical temperature rise in the beakers after the entire measurement lifetime of the bridge was only  $1.5 \pm 0.5$  °C.

#### 3.7.7.2 MR imaging of glycerol bridges

MR imaging of the glycerol bridges was performed at 1.5 T (MAGNETOM Sonata, Siemens, Erlangen, Germany) using a standard circular-polarized knee coil. The glycerol bridge was aligned so that the long axis of the bridge was parallel to the main magnetic field

with the anode placed towards the foot end of the patient table and the cathode towards the head end; the bridge center was located in the isocenter in head-feet direction, in right-left direction, and some millimeters above the isocenter in anterior-posterior direction (Figure 3.11).

Before applying voltage an isotropic three-dimensional spoiled fast low-angle shot (FLASH) sequence covering the experimental set-up was employed to optimize and fix the sagittal imaging plane visualizing beakers and the glycerol bridge. Estimation of relaxation times in these regions before bridge ignition, during the existence of a bridge (voltage applied, typically for more than one hour) and after bridge termination was based on two-dimensional spin echo measurements in this plane.

For  $T_1$  estimation spin echo sequences with two different repetition times (TR) were acquired with the following protocol parameters: TR, 70/300 ms; echo time (TE), 8 ms; bandwidth, 170 Hz/pixel; field-of-view, 150x150 mm<sup>2</sup>; resolution, 0.8x0.8x3.0 mm<sup>3</sup>, number of averages, 1; imaging time, 17 s / 1 min 01 s. For  $T_2$  estimation a multi-echo spin echo sequence with sixteen different echo times (8.3/16.6/24.9/33.2/41.5/49.8/58.1/66.4/74.7/83.0/91.3/99.6/107.9/116.2/124.5/132.8 ms) was used. Further protocol parameters were as follows: TR, 400 ms; bandwidth, 280 Hz/pixel; field-of-view, 150x150 mm<sup>2</sup>; resolution, 0.8x0.8x3.0 mm<sup>3</sup>; number of averages, 3; imaging time, 3 min 54 s. To compensate for decreased signal-to-noise ratio in the images during the existence of the bridge, measurements for  $T_1$  determination were three-fold averaged and measurements for  $T_2$  determination six-fold, such that correspondingly longer imaging times resulted.

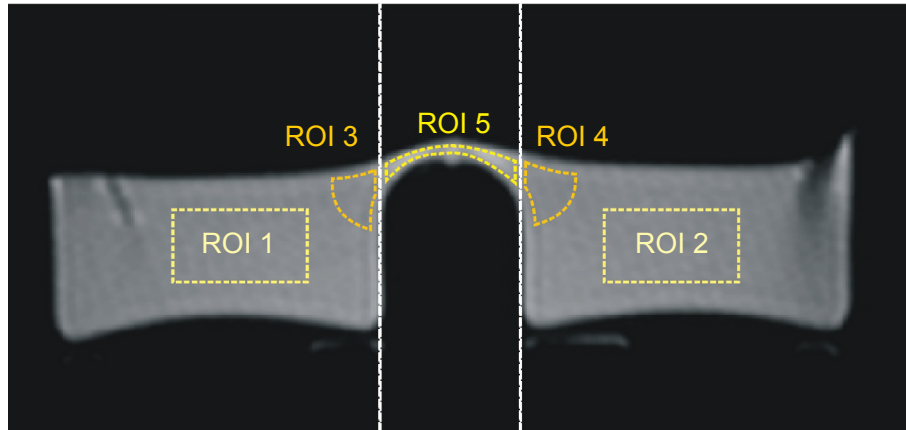


**Figure 3.15 Segmentation of five regions-of-interest (ROIs) in the glycerol bridge for determination of magnetic relaxation times. ROI 1, anode beaker; ROI 2, cathode beaker; ROI 3, tip of anode beaker; ROI 4, tip of cathode beaker; ROI 5, bridge section.**

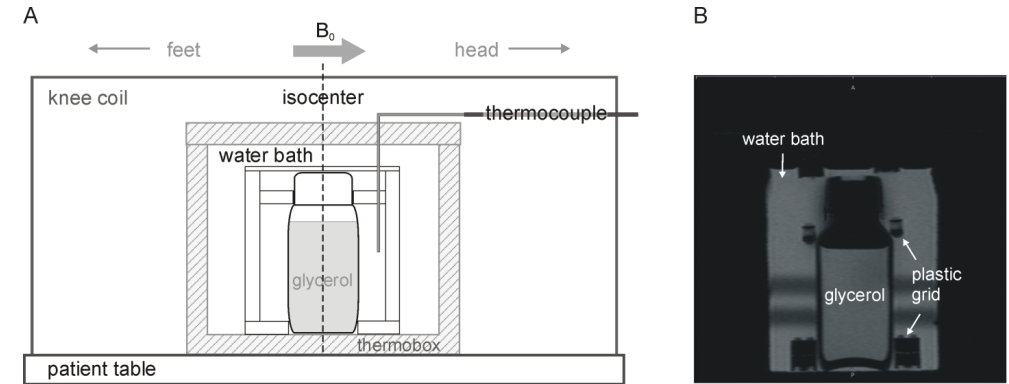


**Figure 3.16 experimental setup for the calibration of temperature behavior of relaxation times of glycerol. Panel A provides a diagrammatic representation of the experimental apparatus, a frame made of plastic grid material was used to secure the bottle in place against the forces of buoyancy. Panel B is a representative MR image of the glycerol bottle in the water bath.**

### 3.7.7.3 MR image analysis

For each pair of spin echo images (with different TR times) and each multi-echo spin echo measurement, average relaxation times were estimated in five regions-of-interest (ROIs); in both beakers, near the spouts or bridge base, and in the bridge itself (Figure 3.15).

In both spin echo images with different TR times mean ROI signal intensities were derived from ROIs drawn as similar as possible, but carefully excluding electronic noise artifacts and partial volume areas in the time-varying bridge. Mean  $T_1$  times at the five localizations were determined from fitting the mean signal intensities of corresponding ROI pairs to the spin echo signal intensity equation [51].

$$\text{signal intensity} = A \left( 1 - 2e^{-(TR - \frac{TE}{2})/T_1} + e^{-TR/T_1} \right) \quad (\text{Eq. 3.17})$$

where A and (mean)  $T_1$  are the fitting constants.

For  $T_2$  estimation the image with the lowest echo time (TE = 8.3 ms) and images with predominant noise contribution (typically TE > 83 ms) were excluded from the series of multi-echo spin echo images. Pixel signal intensities of the remaining multi-echo spin echo images were fitted to the signal intensity equation

$$\text{signal intensity} = A e^{-TE/T_2} \quad (\text{Eq. 3.18})$$

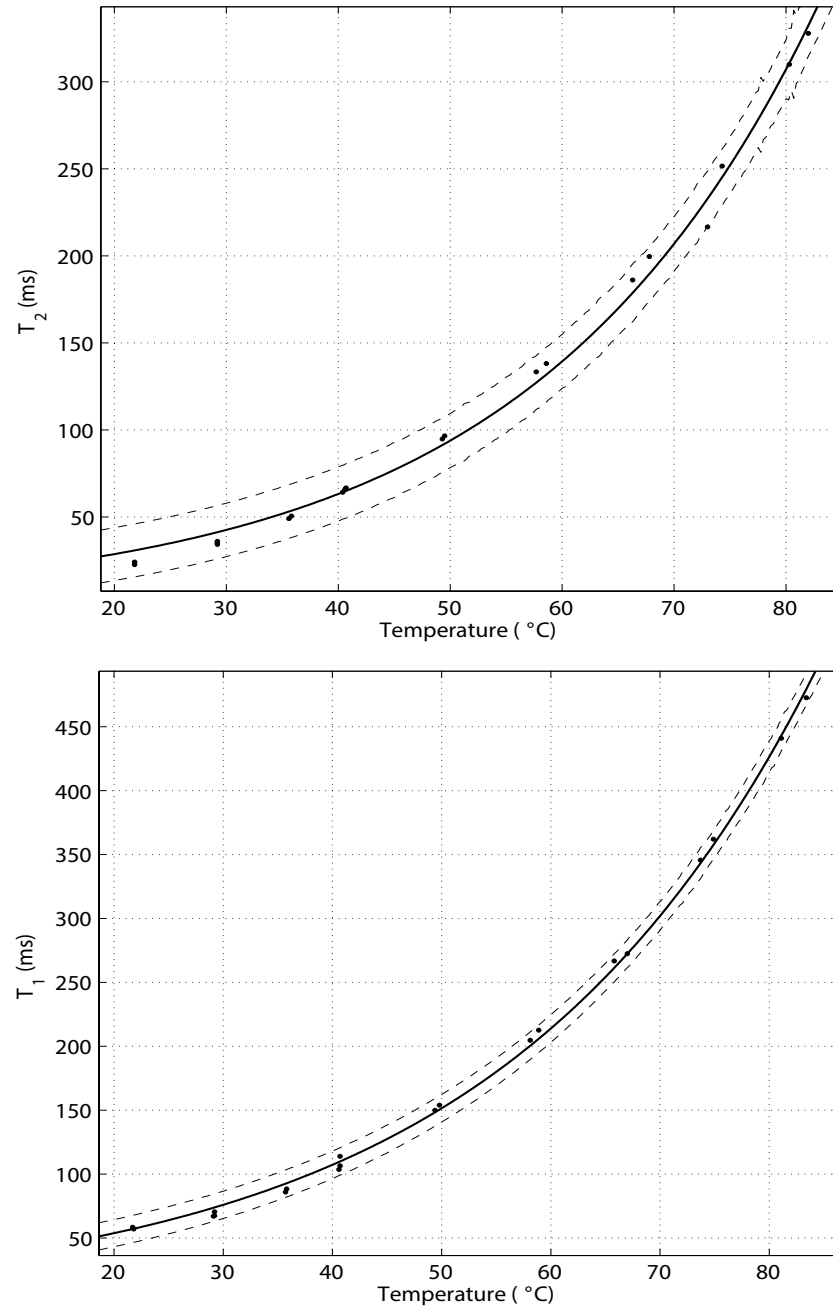


Figure 3.17 Temperature calibration curves for  $T_1$  and  $T_2$ . Fit is according to Eq.3.19 and uses a robust Levenberg-Marquardt non-linear least squares fit, 99% confidence bounds are shown as dashed lines.  $R^2$  values of 0.9982 and 0.9956 for  $T_1$  and  $T_2$  respectively.

to determine  $T_2$  of the pixel (and an additional fitting constant A). This calculation was performed for any pixel by the scanner software to produce a  $T_2$ -map. Mean  $T_2$  values in both beakers, at both beakers' tips and in the bridge were determined from corresponding ROIs drawn on the  $T_2$ -map.

#### 3.7.7.4 Calibration of temperature behavior of relaxation times of glycerol

In order to perform relaxation based thermometry a calibration standard was imaged and processed using the same methods as described for the bridge. The temperature calibration sample was a sealed bottle of anhydrous glycerol immersed in a water bath held in an insulating box. A thermocouple recorded the temperature of the sample which was allowed to equilibrate between temperature steps. A diagram of the set-up is shown in figure 3.16a, while 3.16b shows a representative MR image. The normalized temperature calibration measurement data for  $T_1$  and  $T_2$  were then fitted using an Arrhenius type exponential function as given in equation 3.19, and plotted in figure 3.17a for  $T_1$  and 3.17b for  $T_2$ . The fit coefficients were derived using a bisquare robust, Levenberg-Marquardt non-linear least squares routine in MATLAB. (R2014a, Mathworks, Natick, MA, USA). The plot shows the 99% confidence bounds, with  $R^2$  values of 0.9982 and 0.9956 for  $T_1$  and  $T_2$  respectively.

$$T_{1,2} = ae^{\left(\frac{b}{T}\right)} + c \quad (\text{Eq. 3.19})$$

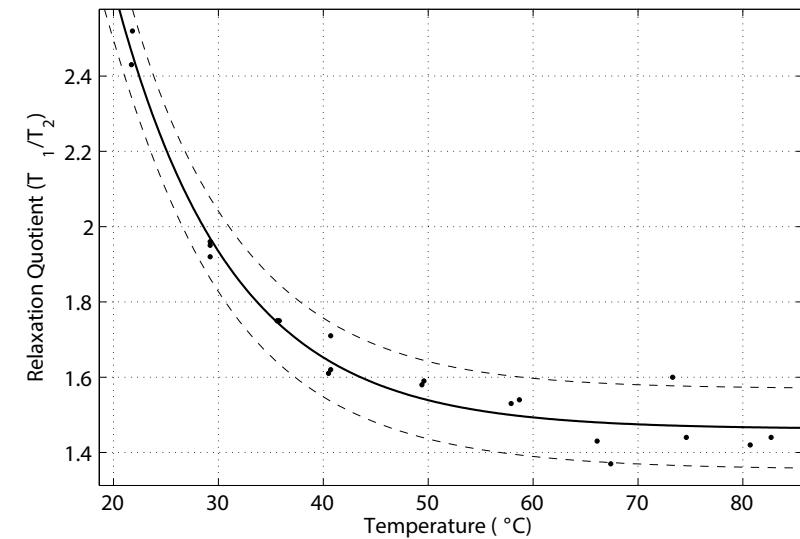


Figure 3.18 Relaxation quotient correction plot, ( $Q = T_1/T_2$ ). Fit is according to Eq.3.19 and uses a robust Levenberg-Marquardt non-linear least squares fit, 95% confidence bounds are shown as dashed lines.  $R^2$  is 0.9874



It was also necessary to correct for non-linear behavior between  $T_1$  and  $T_2$  thermometry. This is due to the connection between the two relaxation constants, namely that transverse relaxation not only loses energy due to dephasing but also to the longitudinal relaxation of the sample. The effect in glycerol becomes more pronounced at lower temperatures. There is an additional systematic error that relates to the selection of  $TR$  for the  $T_2$  measurements at very high temperatures. In this regime the values of  $T_1$  and  $T_2$  converge which means that much of the energy originally present in the transverse magnetization plane is lost and this affects the statistics of the measurement which reduces the fidelity of  $T_2$  at temperatures  $>60$  °C however this is much higher than measured in the bridge system which tended to operate  $<50$  °C. The quotient factor is a convenient tool for correcting these divergences and is derived by comparing the ratio between  $T_1$  and  $T_2$  values at known temperatures. The fitting coefficients are derived in the same manner as for the relaxation times (Eq. 3.19). The results of the fit are shown in figure 3.18, the confidence bounds are 90% and  $R^2$  is 0.9705. The quotient value was used to correct the  $T_2$  times measured from the mapping experiments using the temperature derived from flanking  $T_1$  measurements, the expectation is that the two values will converge if there are no other changes to the relaxation dynamics of the liquid.

### 3.8 Inhomogeneous Electric Field Experiments

*In order to examine the role that the electric field gradient plays in the observed molecular changes found in EHD bridges a simple point-plane electrode system was employed.*

EHD liquid bridges are a complex system which makes characterization of the underlying physics challenging. In order to explore the influence a strong electric field gradient has on the liquid under study a method was devised which could produce strong field gradients ( $10^{10}$  V/m<sup>2</sup>) with very little current injection (nA). This method also provides observation of the liquid response not only close to but many tens of mm distant from the electrode and is well suited to many optical methods such as interferometry and spectroscopic imaging.

The inhomogeneous electric field was produced using a point-plane electrode geometry and is illustrated in figure 3.19, panel a. Type I HPLC grade purified water (18.2 M $\Omega$ , Cat No. ZMQSP0D01, Millipore Corp., MA, USA) was filled into a glass cuvette (52 mm x 52 mm x 14 mm, Cat. No. 704.003, Hellma analytics, Müllheim, Germany), and this was then placed in between the electrodes. The planar electrode is made from copper foil (Cat. No. 1181 3M, MN, USA) which is embedded in an insulating PMMA block (100 mm x 100 mm x 25 mm) and connected to the high voltage output of a DC power supply (HCP 30000-300, FuG Elektronik GmbH, Schechen, Germany). The PMMA block had a 5 mm deep groove machined into the top where the cuvette was placed into direct contact with the upper electrode surface. The planar electrode had nearly the same dimensions (9.5 mm x 50 mm x 2.6 mm) as the bottom of the cuvette. A stainless steel acupuncture needle (SJ.25x40, 40 mm x 0.25 mm, Seirin Corp., Shizuoka, Japan) was used to form the point electrode and connected to the ground terminal of the high voltage source. The electrode was affixed to a rigid insulating armature

constructed from polypropylene. The needle was bent at a right angle  $\sim 5$  mm beyond the handle in a manner so as to prevent the electrode from blocking the incident laser beam. For each experiment the electric potential was set to 20 kV and applied as a step function. During operation a small leakage current  $<10$   $\mu$ A could be measured and was presumably due to corona discharge. The electric field for this configuration was modeled using COMSOL Multiphysics (v. 5.0 Comsol, Inc., Stockholm, Sweden) and is shown in figure 3.19b-c.

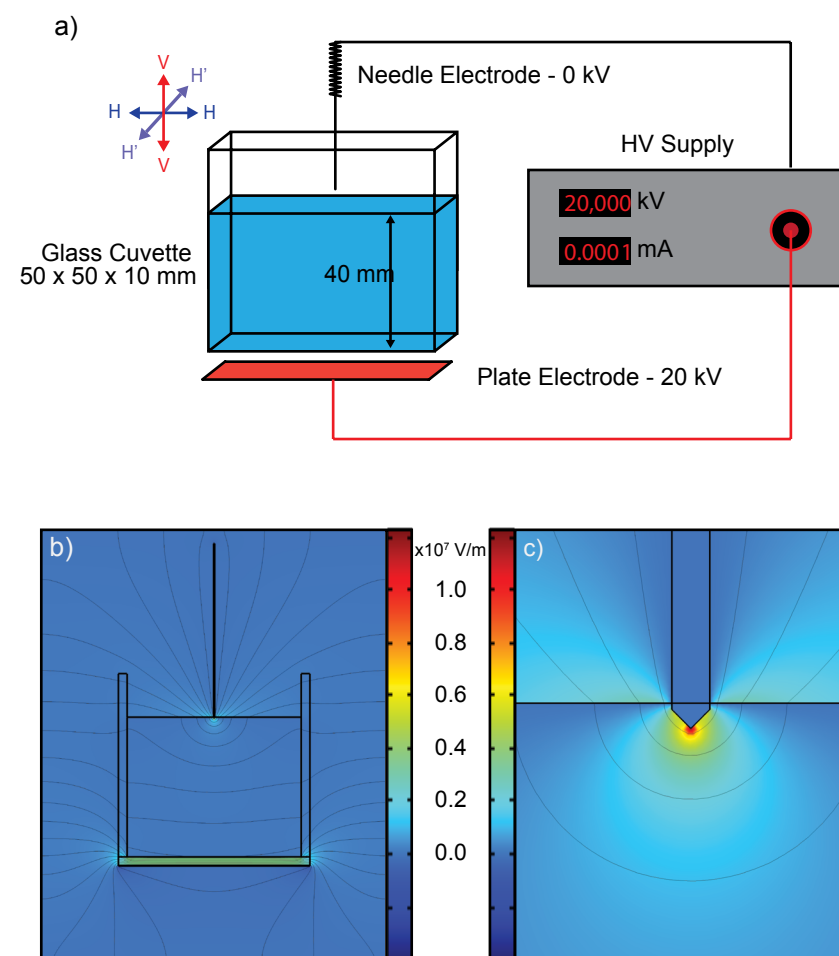


**Figure 3.19** Experimental configuration used in this study. The point plane electrode and liquid cuvette (panel a) is modeled to show (b) the electric field ( $\times 10^7$  V m<sup>-1</sup>) and equipotential lines (1000 V per contour) and (c) the localized electric field ( $\times 10^7$  V m<sup>-1</sup>) strength just beneath the ground (needle) electrode. The electric field polarizations referred to in the Raman data §4.4.3 are shown in the upper left of panel (a).

Twenty milliliters (20 mL) of water were used for each measurement. This brought the liquid surface to a height of 40mm from the bottom of the cuvette and to within 1mm from the tip of the needle. The water for the interferometric investigations was kept in borosilicate glass bottles heated in a water bath to 70°C and transferred to the unheated cuvette just prior to energizing the experiment and the water replaced for every new measurement. The elevated temperature enhanced the polarization response of water and the resulting relative shift in refractive index meant changes were better resolved by the interferometer. Raman measurements were conducted using room temperature water ( $20 \pm 1^\circ\text{C}$ ). Temperature was measured during the experiments using a fiber optic probe (OTG-F, ProSens, OpSens Inc., Quebec, Canada) which could be placed at several locations in the experiment including directly beneath the point electrode. The sensor system spectroscopically monitors the band gap energy of a GaAs crystal to measure temperature and as such is not affected by the applied electric field nor any field induced changes in the sample. This probe has a maximum resolution of  $0.01^\circ\text{C}$  and readout speed up to one kHz repetition rate. During interferometric measurement the most significant response was observed in less than 10 seconds so the overall temperature change in the liquid was negligible relative to the field effect.

### 3.9 Interferometry

*Very small perturbations in the optical properties of a liquid can be detected using interferometry, these ultimately reflect changes in the polarizability of the liquid which can arise from changes in physical properties.*

#### 3.9.1 Interferometry principles

In an interferometer the light path is split at the first beam splitter into a reference and test arm, the latter passes through the test section, in this case the cuvette, before both beams are recombined in the second beam splitter. The light passing through the sample suffers a phase lag which is dependent upon the refractive index of the material. Depending upon the phase lag the light will interfere constructively or destructively and creates bright and dark bands or interference fringes. The measurement is line-of-sight, meaning that it is only sensitive to light whose propagation direction (i.e. pointing vector) is towards the detector, off axis or scattered radiation is not detected, and the phase lag is integrated over the path in the cuvette. This makes interferometry quite sensitive to local perturbations in the complex dielectric permittivity (i.e. refractive index) of the material under study and provides a measure of the polarizability as well as the dipole number density in the material.

#### 3.9.2 Interferometry measurement

A Mach-Zehnder interferometer was constructed with 2 meter base length and is diagrammed in figure 3.20. The source laser was a frequency stabilized continuous wave single-line mode diode laser (DL640-050-S, P=50mW,  $\lambda=635 \pm 2$  nm, 1.1 mm Gaussian beam diameter, 1 mrad

divergence, Crystalsaser, NV, USA) with built in optical isolator and polarization ratio 100:1, a half wave plate was positioned to rotate the polarization direction in the interferometer. The beam was spatially filtered using a 20x microscope objective and  $5\mu\text{m}$  pinhole, subsequently over expanded with a biconcave lens and finally collimated using a large diameter plano-convex lens. The over-expanded beam was blocked with a square aperture placed at the entry port of the first beam splitter cube. This assured that the most central portion of the Gaussian beam filled the full aperture and provided good uniformity of illumination throughout the test subject. The mirrors in the interferometer section were inclined slightly to produce a carrier fringe system that allowed the disambiguation of the phase shift in the recovered interferograms. The cuvette test section was position in the interferometer in direct view of the recording camera (Photron FASTCAM SA1.1) fitted with an 18-270 mm, F/3.5-6.3 zoom lens (Cat. No. B008, Tamron, NY, USA). Images were collected at 50 frames per second full frame resolution (1024x1024 pixels). The recorded images were evaluated using IDEA software (<http://optics.tugraz.at/>) using a fast Fourier transform (FFT) based digital fringe evaluation [63]. For the interferometry studies the time-resolved response of the sample was recorded as the voltage was applied according to a rectangular step function. The voltage profile was to step between 0 and 20 kV with a rising edge <500 ms, a stable plateau between 10 – 60 seconds and a falling edge which fully discharged the experiment back to ground potential in under 2 s.

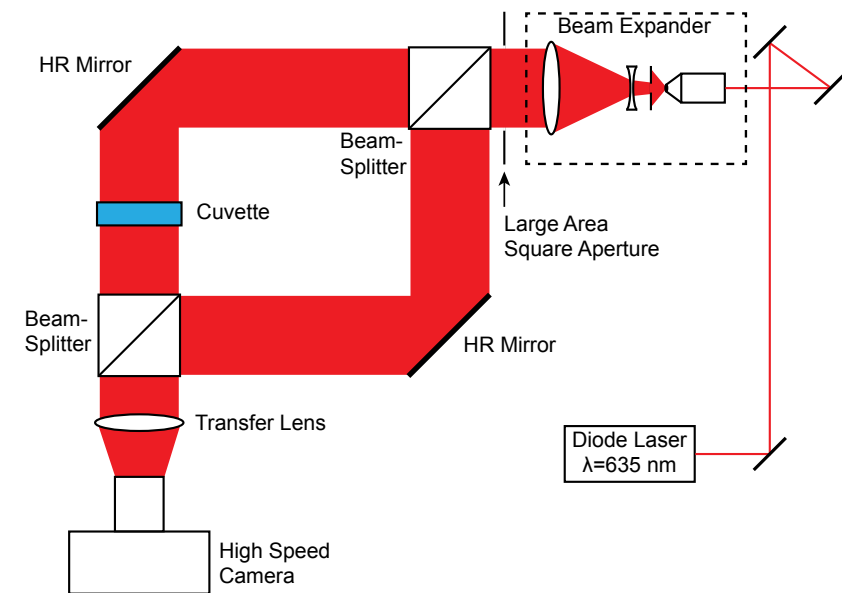


**Figure 3.20** Diagram of the Mach-Zehnder interferometer. 2 m base length, 50 mm<sup>2</sup> clear aperture. The beam expander consisted of a 20x objective, 5  $\mu\text{m}$  pinhole, and several lenses to further diverge and collimate the spatially filtered beam.



## 3.10 Raman Spectral Imaging

Raman scattering is an inelastic method which can probe changes to the polarizability of a liquid that reflect shifts in the local molecular environment and can be used to determine both local and non-local vibrational coupling.

### 3.10.1 Raman Principles

In a similar manner to interferometry Raman spectroscopy also probes the electric polarization of molecules - the difference is in the spatial resolution. Unlike the macroscopic refractive index interrogated by interferometry the Raman bands are a probe of the molecular transition dipole population distribution in the focal region of the laser beam. The connection between the vibrational line shape and molecular environment which make up these bands is an ongoing effort [64], [65] and like most spectral features in condensed matter is obscured by inhomogeneous broadening [66], [67]. The vibrational modes of water are both infrared and Raman active. The shape of these bands are complex as expected for condensed matter and have been extensively discussed elsewhere [68]–[70] and will be summarized here. The Raman scattering spectrum provide ensemble information on the coupling between vibrational oscillators in the liquid. The isotropic spectrum has a somewhat complex shape which has been the subject of much scrutiny. Suffice it to say that those oscillators with lower wavenumber ( $3250\text{ cm}^{-1}$ ) on the red-side of the distribution correspond to vibrational oscillators which are damped by interactions with their local environment. Those oscillators with less degrees of interaction have higher frequencies ( $3490\text{ cm}^{-1}$ ) and the small shoulder on the blue-side of the distribution at  $3650\text{ cm}^{-1}$  has been shown through computer simulation using experimental data as fit to belong to free oscillators which behave as single-particles [71]. The lifetime of such free particles is considered to be quite short lived.

The polarized Raman spectrum is obtained when the analyzer and incident electric field are aligned. Similarly when the analyzer is rotated perpendicular to  $E_0$  the anisotropic depolarized spectrum is recorded. The isotropic spectrum can be recovered from the measured spectra via:

$$I_{iso}(\omega) = I_{VV}(\omega) - \frac{4}{3}I_{VH}(\omega) \quad (\text{Eq. 3.20})$$

Whereas, the anisotropic spectrum is contained entirely in the depolarized spectrum  $I_{VH}(\omega)$ .

The Raman active bands in water can be attributed to a number of physical quantities, fundamental to all is the electric polarizability of the molecule which is probed directly by the electric field of the off-resonant incident linearly polarized pump radiation. The decay of the induced transition dipoles results in a frequency shifted Raman emission which contains contributions from the isotropic and anisotropic polarizabilities.

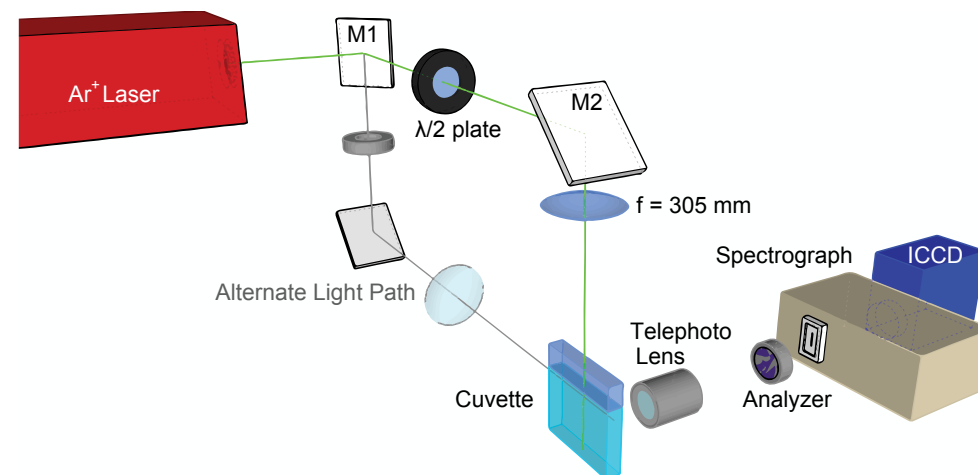


Figure 3.21 Diagram of the Imaging Raman spectrometer used in this study. Both light paths used are shown.

### 3.10.2 Raman measurement details

The mid-infrared (mid-IR) vibrational modes of water are Raman active and can be accessed using visible lasers of high power which have better penetration depth than direct mid-IR spectroscopy. This is ideal for probing the spatial variation in the vibrational modes of water under electrical stress. The cuvette point-plane electrode system previously described was arranged as shown in figure 3.21. A collimated and polarization controlled beam from an argon ion laser (Innova 6W Ar+, P=400mW, 514.5 nm, 1.5 mm beam diameter, 0.5 mrad divergence, Coherent, USA) was guided into the cuvette either perpendicular or parallel to the liquid surface. The beam delivery optics provide a very uniform and tight focus over several centimeters, given the beam characteristics stated above, the focal spot size is  $150\text{ }\mu\text{m}$  and the confocal parameter is 58.89 mm which is broader than the entire sample cuvette. Thus it is assured that within the interrogated spectral imaging region the illumination power and beam shape are uniform. For water at ambient conditions the extinction coefficient for water at 515nm is  $3.96 \times 10^{-4}\text{ cm}^{-1}$ , note unit is in terms of propagation distance and not wavenumbers.

The incident electric field polarization ( $E_0$ ) of the laser beam was controlled by a zero-order half wave plate. When the beam was parallel to the liquid surface  $E_0$  was also parallel to the central axis of the applied static electric field gradient ( $E_a$ ) imposed by the needle electrode. When  $E_0$  was perpendicular to the liquid surface it was also perpendicular to  $E_a$ . In order to maintain the imaging condition the entrance slit and laser beam direction were kept parallel. This effectively meant turning the spectrograph on its side when the beam was parallel to the liquid surface. This also reduced systematic error due to polarization dependent

differences in the dispersion efficiency of the spectrograph gratings as the relative orientation of the grating rulings and  $E_0$  was maintained throughout the experiments. There are a number of electric field vectors to keep track of in the experiments considered here. For simplicity we will only use the vertical (V) and horizontal (H) directions in discussing each. The first field is that of the voltage applied to the point plane electrodes, while the real field is a gradient with complex shape (see figures 3.19b and 3.19c) the needle geometry defines the principal axis of the field ( $E_a$ ) as V polarized. The electric field of the laser beam ( $E_0$ ) must be orthogonal to the beam propagation Poynting vector and was rotated by the  $\lambda/2$  plate to be parallel to the long axis of the cuvette. Thus when the beam was parallel to the liquid surface  $E_0$  was V polarized, and when the beam was perpendicular  $E_0$  was H polarized. The electric field of the scattered light ( $E_s$ ) was analyzed in both the H and V polarizations. For each experimental configuration four sets of spectra were recorded, two VV (or HH) orientations and two VH (or HV) orientations depending on the beam Poynting vector.

The Stokes shifted Raman scattered light was collected using a photographic lens (Mamiya Secor SX135 mm F 2.8, Mamiya, Japan) positioned to image the fluid region nearest the tip of the needle onto the entrance slit of a spectrograph (Acton SpectraPro 2300i, 600 lines/mm grating, 30  $\mu\text{m}$  entrance slit, resolution 3.9  $\text{cm}^{-1}$ , Acton, NJ, USA). Prior to the vertical entrance slit the light passed through a linear polarizing filter that could be rotated so the transmitted electric field vector was either parallel or perpendicular to the normal of the electric field gradient. The monochromator produced spectrally dispersed light which was imaged using a cooled, intensified CCD camera (NanoStar, LaVision, Göttingen, Germany). The integration time for each collected frame was 100 milliseconds with an intensifier gain of 50. For each experimental configuration 50 frames were collected and summed together. Each frame contained 512 spectra with 640 spectral points each. The sum of the background intensity images recorded with the entrance slit blocked was subsequently subtracted from the experimental images. This effectively removed signal contributions due to thermal, electronic readout, and shot noise and improved the resulting image contrast. All image recording and post-processing was carried out using Lavision DaVis 7.2.1.64 software (Lavision, Göttingen, Germany). The applied electric field intensity was either zero or 20 kV. Voltage was applied as a step function however, now the system was allowed to equilibrate for at least one minute prior to recording spectra.

## Bibliography

- [1] Y. G. Ma, C. K. Ong, T. Tyc, and U. Leonhardt, "An omnidirectional retroreflector based on the transmutation of dielectric singularities," *Nat. Mater.*, vol. 8, no. 8, pp. 639–42, Aug. 2009.
- [2] R. H. Dicke, "Coherence in Spontaneous Radiation Processes," *Phys. Rev.*, vol. 93, no. 1, pp. 99–110, Jan. 1954.
- [3] S. M. Dutra, *Cavity Quantum Electrodynamics: The Strange Theory of Light in a Box*. John Wiley & Sons, 2005.
- [4] W. H. Physiker and Deutschland, *Die physikalischen Prinzipien der Quantentheorie*. Hirzel, 1942.
- [5] F. A. Popp, K. H. Li, Q. Gu, *Recent Advances in Biophoton Research and Its Applications*. World Scientific, 1992.
- [6] R. H. Dicke, "Quantum Electronics," in *Quantum Electronics*, N. Bloembergen and P. Grivet, Eds. Paris: Dunod et Cie, 1964.
- [7] E. Del Giudice and G. Vitiello, "Role of the electromagnetic field in the formation of domains in the process of symmetry-breaking phase transitions," *Phys. Rev. A*, vol. 74, no. 2, p. 022105, Aug. 2006.
- [8] J. R. Melcher and G. I. Taylor, "Electrohydrodynamics: A Review of the Role of Interfacial Shear Stresses," *Annu. Rev. Fluid Mech.*, vol. 1, no. 1, pp. 111–146, Jan. 1969.
- [9] C. L. Burcham and D. a. Saville, "Electrohydrodynamic stability: Taylor–Melcher theory for a liquid bridge suspended in a dielectric gas," *J. Fluid Mech.*, vol. 452, pp. 163–187, Feb. 2002.
- [10] L. Onsager, "Deviations from Ohm's Law in Weak Electrolytes," *J. Chem. Phys.*, vol. 2, no. 9, p. 599, 1934.
- [11] S. Jeong, J. Seyed-yagoobi, S. Member, and P. Atten, "Theoretical / Numerical Study of Electrohydrodynamic Pumping Through Conduction Phenomenon," vol. 39, no. 2, pp. 355–361, 2003.
- [12] S. I. Jeong and J. Seyed-Yagoobi, "Fluid circulation in an enclosure generated by electrohydrodynamic conduction phenomenon," *IEEE Trans. Dielectr. Electr. Insul.*, vol. 11, no. 5, pp. 899–910, Oct. 2004.
- [13] A. Castellanos, *Electrohydrodynamics*. Springer-Verlag, 1998.
- [14] H. Jansson, R. Bergman, and J. Swenson, "Slow dielectric response of Debye-type in water and other hydrogen bonded liquids," *J. Mol. Struct.*, vol. 972, no. 1–3, pp. 92–98, May 2010.
- [15] H. Jansson, R. Bergman, and J. Swenson, "Hidden Slow Dynamics in Water," *Phys. Rev. Lett.*, vol. 104, no. 1, p. 017802, Jan. 2010.
- [16] U. Kaatz and Y. Feldman, "Broadband dielectric spectrometry of liquids and biosystems," *Meas. Sci. Technol.*, vol. 17, no. 2, pp. R17–R35, Feb. 2006.
- [17] R. Buchner, J. Barthel, and J. Stauber, "The dielectric relaxation of water between 0 °C and 35 °C," vol. 2, no. June, 1999.

- [18] A. D. Wexler, M. López Sáenz, O. Schreer, J. Woissetschläger, and E. C. Fuchs, "The preparation of electrohydrodynamic bridges from polar dielectric liquids," *J. Vis. Exp.*, no. 91, p. e51819, Jan. 2014.
- [19] J. Kendall, "THE SPECIFIC CONDUCTIVITY OF PURE WATER IN EQUILIBRIUM WITH ATMOSPHERIC CARBON DIOXIDE," *J. Am. Chem. Soc.*, vol. 38, no. 8, pp. 1480–1497, Aug. 1916.
- [20] J. Woissetschläger, K. Gatterer, and E. C. Fuchs, "Experiments in a floating water bridge," *Exp. Fluids*, vol. 48, no. 1, pp. 121–131, Jul. 2010.
- [21] CIE, *CIE Technical Report CIE 13.3-1995*. 1995.
- [22] R. W. G. Hunt and M. R. Pointer, *Measuring Colour*. 2011.
- [23] A. S. Bondarenko and G. A. Ragoisha, "EIS Spectrum Analyser," in *Progress in Chemometrics Research*, A. L. Pomerantsev, Ed. New York: Nova Science Publishers, 2005, pp. 89–102.
- [24] M. J. D. Powell, "An efficient method for finding the minimum of a function of several variables without calculating derivatives," *Comput. J.*, vol. 7, no. 2, pp. 155–162, Feb. 1964.
- [25] P. R. Willmott, D. Meister, S. J. Leake, M. Lange, A. Bergamaschi, M. Böge, M. Calvi, C. Cancellieri, N. Casati, A. Cervellino, Q. Chen, C. David, U. Flechsig, F. Gozzo, B. Henrich, S. Jäggi-Spielmann, B. Jakob, I. Kalichava, P. Karvinen, J. Krempasky, A. Lüdeke, R. Lüscher, S. Maag, C. Quitmann, M. L. Reinle-Schmitt, T. Schmidt, B. Schmitt, A. Streun, I. Vartiainen, M. Vitins, X. Wang, and R. Wulschleger, "The Materials Science beamline upgrade at the Swiss Light Source," *J. Synchrotron Radiat.*, vol. 20, no. Pt 5, pp. 667–82, 2013.
- [26] A. Bergamaschi, A. Cervellino, R. Dinapoli, F. Gozzo, B. Henrich, I. Johnson, P. Kraft, A. Mozzanica, B. Schmitt, and X. Shi, "The MYTHEN detector for X-ray powder diffraction experiments at the Swiss Light Source," *J. Synchrotron Radiat.*, vol. 17, no. 5, pp. 653–68, Sep. 2010.
- [27] J. Woissetschläger, A. D. Wexler, G. Holler, M. Eisenhut, K. Gatterer, and E. C. Fuchs, "Horizontal bridges in polar dielectric liquids," *Exp. Fluids*, vol. 52, no. 1, pp. 193–205, Oct. 2012.
- [28] A. K. Soper, "GudrunN and GudrunX Table of Contents," 2012.
- [29] G. Hura, D. Russo, R. M. Glaeser, T. Head-Gordon, M. Krack, and M. Parrinello, "Water structure as a function of temperature from X-ray scattering experiments and ab initio molecular dynamics," *Phys. Chem. Chem. Phys.*, vol. 5, no. 10, p. 1981, May 2003.
- [30] J. A. Sellberg, "Temperature-dependent X-ray Scattering of Liquid Water," Stockholm University, 2012.
- [31] J. A. Sellberg, C. Huang, T. a McQueen, N. D. Loh, H. Laksmono, D. Schlesinger, R. G. Sierra, D. Nordlund, C. Y. Hampton, D. Starodub, D. P. DePonte, M. Beye, C. Chen, a V Martin, a Barty, K. T. Wikfeldt, T. M. Weiss, C. Caronna, J. Feldkamp, L. B. Skinner, M. M. Seibert, M. Messerschmidt, G. J. Williams, S. Boutet, L. G. M. Pettersson, M. J. Bogan, and a Nilsson, "Ultrafast X-ray probing of water structure below the homogeneous ice nucleation temperature," *Nature*, vol. 509, no. 7505, pp. 381–4, 2014.
- [32] L. B. Skinner, C. J. Benmore, B. Shyam, J. K. R. Weber, and J. B. Parise, "Structure of the floating water bridge and water in an electric field," *Proc. Natl. Acad. Sci. U. S. A.*, vol. 109, no. 41, pp. 16463–8, Oct. 2012.
- [33] E. C. Fuchs, K. Gatterer, G. Holler, and J. Woissetschläger, "Dynamics of the floating water bridge," *J. Phys. D: Appl. Phys.*, vol. 41, no. 18, p. 185502, Sep. 2008.
- [34] E. C. Fuchs, B. Bitschnau, J. Woissetschläger, E. Maier, B. Beuneu, and J. Teixeira, "Neutron scattering of a floating heavy water bridge," *J. Phys. D: Appl. Phys.*, vol. 42, no. 6, p. 065502, Mar. 2009.
- [35] A. K. Soper, "The radial distribution functions of water and ice from 220 to 673 K and at pressures up to 400 MPa," *Chem. Phys.*, vol. 258, no. 2–3, pp. 121–137, Aug. 2000.
- [36] R. Mancinelli, a Botti, F. Bruni, M. a Ricci, F. E. Amaldi, R. Tre, and V. Navale, "Hydration of Sodium, Potassium, and Chloride Ions in Solution and the Concept of Structure Maker / Breaker," *Simulation*, pp. 13570–13577, 2007.
- [37] G. Hura, J. M. Sorenson, R. M. Glaeser, and T. Head-Gordon, "A high-quality x-ray scattering experiment on liquid water at ambient conditions," *J. Chem. Phys.*, vol. 113, no. 20, p. 9140, 2000.
- [38] X. F. Pang, "The conductivity properties of protons in ice and mechanism of magnetization of liquid water," *Eur. Phys. J. B*, vol. 49, no. 1, pp. 5–23, 2006.
- [39] A. Giuliani, M. A. Ricci, and F. Bruni, "Water Proton Environment: A New Water Anomaly at Atomic Scale?," in *Liquid Polymorphism, Vol. 152*, H. E. Stanley, Ed. Hoboken, NJ, USA: John Wiley & Sons, Inc., 2013, pp. 175–187.
- [40] H. Thompson, F. Bruni, M. A. Ricci, S. McClain, S. Klotz, T. Straessle, S. Imberti, and R. Hargreaves, "Empirical Potential Structure Refinement - EPSRshell A User's Guide," no. Version 24, 2015.
- [41] J. L. Abascal and C. Vega, "A general purpose model for the condensed phases of water: TIP4P/2005," *J. Chem. Phys.*, vol. 123, no. 23, p. 234505, 2005.
- [42] F. Sedlmeier, D. Horinek, and R. R. Netz, "Spatial correlations of density and structural fluctuations in liquid water: A comparative simulation study," *J. Am. Chem. Soc.*, vol. 133, no. 5, pp. 1391–1398, 2011.
- [43] T. Head-Gordon and M. E. Johnson, "Tetrahedral structure or chains for liquid water," *Proc. Natl. Acad. Sci. U. S. A.*, vol. 103, no. 21, pp. 7973–7977, 2006.
- [44] A. K. Soper, "Joint structure refinement of x-ray and neutron diffraction data on disordered materials: application to liquid water," *J. Phys. Condens. Matter*, vol. 19, p. 335206, 2007.
- [45] C. Huang, K. T. Wikfeldt, D. Nordlund, U. Bergmann, T. McQueen, J. Sellberg, L. G. M. Pettersson, and a Nilsson, "Wide-angle X-ray diffraction and molecular dynamics study of medium-range order in ambient and hot water," *Phys. Chem. Chem. Phys.*, vol. 13, no. 44, pp. 19997–20007, Nov. 2011.
- [46] L. Piatkowski, A. D. Wexler, E. C. Fuchs, H. Schoenmaker, and H. J. Bakker, "Ultrafast vibrational energy relaxation of the water bridge," *Phys. Chem. Chem. Phys.*, vol. 14, no. 18, pp. 6160–4, May 2012.
- [47] J. Teixeira, M.-C. Bellissent-Funel, S. H. Chen, and A. J. Dianoux, "Experimental determination of the nature of diffusive motions of water molecules at low temperatures," *Phys. Rev. A*, vol. 31, no. 3, pp. 1913–1917, 1985.

- [48] I.A. Beta, J.-C. Li, and M.-C. Bellissent-Funel, "A quasi-elastic neutron scattering study of the dynamics of supercritical water," *Chem. Phys.*, vol. 292, no. 2–3, pp. 229–234, Aug. 2003.
- [49] V. F. Sears, "THEORY OF COLD NEUTRON SCATTERING BY HOMONUCLEAR DIATOMIC LIQUIDS: I. FREE ROTATION," *Can. J. Phys.*, vol. 44, no. 6, pp. 1279–1297, Jun. 1966.
- [50] O. Teschke, D. Mendez Soares, and J. F. Valente Filho, "Floating liquid bridge tensile behavior: Electric-field-induced Young's modulus measurements," *Appl. Phys. Lett.*, vol. 103, no. 25, p. 251608, 2013.
- [51] M. A. Bernstein, K. F. King, and X. J. Zhou, *Handbook of MRI Pulse Sequences*. 2004.
- [52] J. McConnell, *The Theory of Nuclear Magnetic Relaxation in Liquids*. Cambridge University Press, 2009.
- [53] J. Graessner, "Bandwidth in MRI ?," pp. 3–8, 2013.
- [54] F. N. Wang, S. L. Peng, C. T. Lu, H. H. Peng, and T. C. Yeh, "Water signal attenuation by D2O infusion as a novel contrast mechanism for 1H perfusion MRI," *NMR Biomed.*, vol. 26, no. 6, pp. 692–698, 2013.
- [55] L. Brecker, M. Pogorelec, H. Griengl, W. Steiner, T. Kappe, and D. W. Ribbons, "Synthesis of 2,4-diketoacids and their aqueous solution structures," *New J. Chem.*, vol. 23, no. 4, pp. 437–446, Jan. 1999.
- [56] S. Berger and S. Braun, *200 and More NMR Experiments*. 2004.
- [57] H. E. Gottlieb, V. Kotlyar, and A. Nudelman, "NMR Chemical Shifts of Common Laboratory Solvents as Trace Impurities," *J. Org. Chem.*, vol. 62, no. 21, pp. 7512–7515, Oct. 1997.
- [58] R. L. Vold, "Measurement of Spin Relaxation in Complex Systems," *J. Chem. Phys.*, vol. 48, no. 8, p. 3831, Sep. 1968.
- [59] S. Meiboom and D. Gill, "Modified Spin-Echo Method for Measuring Nuclear Relaxation Times," *Rev. Sci. Instrum.*, vol. 29, no. 8, p. 688, Dec. 1958.
- [60] U. Reiter, G. Reiter, G. Kovacs, A. F. Stalder, M. A. Gulsun, A. Greiser, H. Olschewski, and M. Fuchsjaeger, "Evaluation of elevated mean pulmonary arterial pressure based on magnetic resonance 4D velocity mapping: comparison of visualization techniques," *PLoS One*, vol. 8, no. 12, p. e82212, Jan. 2013.
- [61] J. B. Segur and H. E. Oberstar, "Viscosity of Glycerol and Its Aqueous Solutions," *Ind. Eng. Chem.*, vol. 43, no. 9, pp. 2117–2120, Sep. 1951.
- [62] IAWPS, "The International Association for the Properties of Water and Steam Revised Release on the IAPWS Industrial Formulation 1997 for the Thermodynamic Properties of Water and Steam," 2008.
- [63] M. Hipp, J. Woisetschlager, P. Reiterer, and T. Neger, "Digital evaluation of interferograms," *Measurement*, vol. 36, no. 1, pp. 53–66, Jul. 2004.
- [64] L. Shi, Y. Ni, S. E. P. Drews, and J. L. Skinner, "Dielectric constant and low-frequency infrared spectra for liquid water and ice Ih within the E3B model," *J. Chem. Phys.*, vol. 141, no. 8, p. 084508, 2014.

- [65] C. J. Tainter, L. Shi, and J. L. Skinner, "Reparametrized E3B (Explicit Three-Body) Water Model Using the TIP4P/2005 Model as a Reference," *J. Chem. Theory Comput.*, vol. 11, no. 5, pp. 2268–2277, 2015.
- [66] M. Yang and J. L. Skinner, "Signatures of coherent vibrational energy transfer in IR and Raman line shapes for liquid water," *Phys. Chem. Chem. Phys.*, vol. 12, pp. 982–991, 2010.
- [67] L. Shi, S. M. Gruenbaum, and J. L. Skinner, "Interpretation of IR and Raman line shapes for H2O and D2O ice Ih," *J. Phys. Chem. B*, vol. 116, no. 47, pp. 13821–30, 2012.
- [68] H. J. Bakker and J. L. Skinner, "Vibrational spectroscopy as a probe of structure and dynamics in liquid water," *Chem. Rev.*, vol. 110, no. 3, pp. 1498–517, Mar. 2010.
- [69] G. E. Walrafen, "Dispersion of the Raman depolarization ratio of HDO in water and heavy water from 295 to 368 K, and from concentrated NaClO4D2OH2O," *J. Chem. Phys.*, vol. 122, no. 17, p. 174502, May 2005.
- [70] B. M. Auer and J. L. Skinner, "Water: Hydrogen bonding and vibrational spectroscopy, in the bulk liquid and at the liquid/vapor interface," *Chem. Phys. Lett.*, vol. 470, no. 1–3, pp. 13–20, Feb. 2009.
- [71] J. Skinner, B. Auer, and Y. Lin, "Vibrational line shapes, spectral diffusion, and hydrogen bonding in liquid water," *Adv. Chem. Phys.*, vol. 142, 2010.

Photo credit chapter 3 overleaf: *Carved Table, Mont St. Michel Abbey*, ©A.D. Wexler, 2015

## Appendix B Electromagnetic Radiation and Matter

*The isotropic interaction of matter and EM radiation are derived from first principles.*

### B.1 Electromagnetic Interactions with Matter

Common atomic matter is comprised of two electrically responsive sub-particles namely electrons and protons which for all intents and purposes of this thesis shall be considered sufficient to explain the phenomena discussed forthwith. Particles of matter are thus able to obtain charge and can interact with the electric and magnetic fields arising from electromagnetic waves. The interaction is governed by Maxwell's equations (1865) in matter which are given here in their derivative form:

Gauss' Law for electric flux

$$\nabla \cdot \mathbf{D} = \rho_f \quad (\text{Eq.B.1})$$

Gauss' Law for magnetism

$$\nabla \cdot \mathbf{B} = 0 \quad (\text{Eq.B.2})$$

Faraday's Law

$$\nabla \times \mathbf{E} = -\frac{\partial \mathbf{B}}{\partial t} \quad (\text{Eq.B.3})$$

Ampere's Law

$$\nabla \times \mathbf{H} = \mathbf{J}_f + \frac{\partial \mathbf{D}}{\partial t} \quad (\text{Eq.B.4})$$

where  $\mathbf{D}$  is the electric displacement field vector,  $\mathbf{B}$  is magnetic field vector in free space,  $\mathbf{H}$  is the magnetic field vector in matter,  $\mathbf{E}$  is the electric field vector in free space,  $\rho$  is the polarization density, and  $\mathbf{J}$  is the current density. This form of Maxwell's equations is used to treat the propagation of electromagnetic waves in matter rather than in the vacuum and so requires the introduction of new terms. The electric displacement field  $\mathbf{D}$  accounts for free charges in matter and is synonymous with the flux density in free space:

$$\mathbf{D} \equiv \epsilon_0 \mathbf{E} + \mathbf{P} \quad (\text{Eq.B.5})$$

where  $\epsilon_0$  is the vacuum permittivity and  $\mathbf{P}$  is the polarization density (polarizability) which

is the density of permanent or induced dipole moments in the material and reflects the rearrangement of bound charges in the material. The polarizability is strongly dependent on the electric permittivity ( $\epsilon$ ) and its related quantity – electric susceptibility ( $\chi$ ). Permittivity is a measure of the resistance a specific material has to the formation of electric fields within a given volume of that material. Susceptibility likewise is a measure of how strongly the inducing field polarizes the same material. They are related to one another by the following relationship:

$$\epsilon = \epsilon_r \epsilon_0 = (1 - \chi) \epsilon_0 \quad (\text{Eq.B.6})$$

where  $\chi$  is the electric susceptibility;  $\epsilon_r$  is the relative *static* permittivity measured as the ratio between the material in a test capacitor and the same capacitor with vacuum between the plates. Absolute permittivity has the units F/m while relative permittivity and susceptibility are dimensionless quantities and thus provide a useful means of comparing the electrical properties of diverse materials. The total charge density of the material is given by:

$$\rho = \rho_b + \rho_f \quad (\text{Eq.B.7})$$

where  $\rho_b$  is the bound charge density due to distortion of the electron distribution within the material and  $\rho_f$  is the free charge density related to the electric flux. Both quantities play important roles in how a given material responds to an externally applied electric field. The non-reflection symmetric boundary conditions at the material surface result in a surface charge density ( $\sigma_s$ ) given by the scalar product of the polarization density and the vector normal to the surface:

$$\sigma_s = \mathbf{P} \cdot \hat{\mathbf{n}} \quad (\text{Eq.B.8})$$

It is important to note that if the polarization density is uniform within the material then the only bound charge appears at the surface and is critical in the evolution of deformation forces in dielectric materials as shall be discussed in the section on the Maxwell stress tensor.

Because we will consider the propagation of electromagnetic waves in matter it is also important to note that in Ampere's law the magnetic  $\mathbf{B}$ -field is replaced with the magnetic  $\mathbf{H}$ -field, which is simply the magnetic field arising from within a material. The  $\mathbf{H}$ -field can be conceptually distinguished by the observation that the field lines must begin and end at describable points in space (e.g. at the ends of a magnet) whereas  $\mathbf{B}$ -field lines can stretch to infinity. The source of current in matter in an electric field is related to changes in the polarization density  $\mathbf{P}$  and gives rise to a frequency dependent polarization current density:

$$\mathbf{J}_p = \frac{\partial \mathbf{P}}{\partial t} \quad (\text{Eq.B.9})$$

The liquids used thus far in liquid bridges possess weak magnetic moments the magnetization current total current density is negligible and thus the total current density  $J$  becomes:

$$J = J_p + J_f \quad (\text{Eq.B.10})$$

This is another factor that becomes important in the formation of liquid bridges in that this relationship sets a maximum solution conductivity above which DC biased bridges will not form. This upper bound is frequency dependent as we shall see in the section on impedance and indicates that AC fields may be able to produce bridges with higher conductivity liquids, provided the polarizability is uniform enough throughout the fluid.

## B.2 Electromagnetic Wave Propagation

The propagation of electromagnetic (EM) waves in matter is important to the work presented here not only for the production of the liquid bridging phenomenon but also for the implementation and interpretation of the measurement techniques used. The triumph of Maxwell's work was in predicting the propagation of light as electromagnetic waves which Hertz later confirmed and characterized. Despite more recent work on the particle-wave duality of light and Feynman's declaration that "light is most certainly a particle"; the wave approximation is a good starting point for following the experiments performed in this work and where necessary quantum mechanical concepts will be introduced and discussed elsewhere.

The propagation of electromagnetic waves in real matter results in various non-linear responses such as scattering, absorption and dispersion which result in a significant deviation in the behavior of light, especially that of mixed wavelengths, from that of free space. It is nonetheless useful to consider the propagation form of light in the vacuum and the resulting vector quantities before proceeding further.

From Maxwell's equations it is apparent that the electric and magnetic fields are interrelated via the symmetric equations and the fields lie orthogonal to each other. A vectorial solution, in generic matter, to the two fields can be found by applying the Laplacian:

$$\nabla^2 E = \mu\epsilon \frac{\partial^2 E}{\partial t^2} \quad (\text{Eq.B.11})$$

$$\nabla^2 B = \mu\epsilon \frac{\partial^2 B}{\partial t^2} \quad (\text{Eq.B.12})$$

these field specific solutions can be further reduced to a single expression in terms of the wave propagation speed ( $c$ ) and frequency ( $\omega$ ) using the Helmholtz equation:

$$\nabla^2 \omega = \frac{1}{c} \frac{\partial^2 \omega}{\partial t^2} \quad (\text{Eq.B.13})$$

this equation can be further solved in the limiting case of a harmonically propagating planar wavefront for the flow of energy in the direction of the propagation vector for isotropic media yielding the Poynting vector by taking the cross product of the  $E$  and  $B$  vectors from Eq. B.11 and Eq. B.12. Further, because the harmonic period of the EM radiation is very rapid in most cases the time averaged form of the Poynting vector is used and more commonly referred to as the Irradiance (intensity):

$$I \equiv S_T = \frac{c\epsilon_0}{2} E_0^2 \quad (\text{Eq.B.14})$$

which in an isotropic, homogenous, linear dielectric becomes:

$$I = \epsilon v \langle E^2 \rangle_T \quad (\text{Eq.B.15})$$

where  $v$  is the propagation speed in the medium. Thus, the irradiance is proportional to the time-averaged amplitude of the electric field which again raises the importance of polarization dynamics in understanding light-matter interaction.

As stated previously, Maxwell's treatment fails to satisfactorily treat matter treating it as continuous and representing the material response using constant values for  $\epsilon$  and  $\mu$ . Static values for the permittivity and permeability erroneously gives rise to a frequency independent index of refraction. The dispersion phenomenon by which prisms split white light into its constituent colors for example demonstrates that such a simplification is invalid. The incident electric field polarizes permanent dipoles to align with the field, the electronic distribution of bound electrons in a dielectric are likewise perturbed resulting in induced dipoles. Condensed matter can be thought of as a collection of classical forced oscillators *in vacuo* driven by the time varying electric field. The process of induction and relaxation are dependent on the material properties and are fundamental to the dispersion characteristic of the material as represented in the dispersion equation:

$$n(\omega) = 1 + \frac{Nq_e^2}{\epsilon_0 m_e} \left( \frac{1}{\omega_0^2 - \omega^2} \right) \quad (\text{Eq.B.16})$$

where  $n(\omega)$  is the frequency dependent index of refraction,  $q_e$  the charge on a single dipole,  $N$  the number of dipoles per unit volume, and  $m_e$  the dipole mass,  $\omega_0$  is the resonance frequency of the dipole in the absence of a driving force,  $\omega$  is the incident radiation frequency. In the most basic system, the dipole is simply an electron, but the relationship holds even at



the molecular level, especially where permanent dipoles are concerned as in polar liquids like water. According to the superposition principle, the frequency difference determines the resulting phase ( $\varphi$ ) relationship between the incident radiation and the oscillating dipole which now acts as an emitter of the incident wave. The implication is that the index of refraction changes with wavelength accordingly:

| Resonance Condition           | Resulting Phase          | Index of Refraction |
|-------------------------------|--------------------------|---------------------|
| $(\omega_0^2 - \omega^2) < 0$ | $\varphi \sim 180^\circ$ | $n(\omega) > 1$     |
| $(\omega_0^2 - \omega^2) > 0$ | $\varphi \sim 0^\circ$   | $n(\omega) < 1$     |

If the index of refraction for a given material is examined over a wide range of wavelengths it will be observed that the index of refraction undergoes several transition between  $n > 1$  and  $n < 1$ . Thus it can be considered that there are many fundamental resonance modes in a real system of  $N$  molecules per unit volume with  $f_j$  oscillators having base frequencies  $\omega_{0j}$  with  $j = 1, 2, 3, \dots$ . Additionally, the energy lost on radiation by the oscillator results in a damping term ( $i\gamma_j\omega$ ) which also includes frictional losses with neighboring dipoles. Finally, the collective modes of neighboring oscillating dipoles results in a local electric field ( $P(t)/3\epsilon_0$ ) which further damps the system. These conditions prevalent in the materials under study here results in the more complete dispersion relation for condensed matter:

$$\frac{n^2 - 1}{n^2 + 2} = \frac{Nq_e^2}{3\epsilon_0 m_e} \sum_j \frac{f_j}{\omega_{0j}^2 - \omega^2 + i\gamma_j\omega} \quad (\text{Eq. B.17})$$

In the case where  $dn/d\omega$  is positive and the material is transparent to the incident EM wave, as  $\omega$  approaches  $\omega_{0j}$   $dn/d\omega$  becomes negative and the oscillators begin to resonate strongly resulting in absorption of the incident light wave. The inclusion of absorption necessitates that the dielectric permittivity become a complex quantity given by the relation:

$$\hat{\epsilon}(\omega) = \epsilon'(\omega) + i\epsilon''(\omega) = \frac{D_0}{E_0}(\cos\delta + i\sin\delta) \quad (\text{Eq. B.18})$$

the real component relates to the polarization of the medium and the imaginary part accounts for the phase loss associated with absorption of the incident radiation field. The periodic formulation of the complex permittivity shows this relationship more clearly as the ratio between the displacement and electric fields in the complex plane as a function of the phase difference between the two fields.

The above dispersion relationships hold for dielectric materials; however, in the case of metals or other materials which possess free charges (e.g. plasmas) the dispersion relationship changes yet again. This is because free electrons typically lack a fundamental frequency and

those oscillating  $180^\circ$  out-of-phase with the incident wave will reradiate cancelling wavelets thus attenuating the incoming radiation. This, for example, leads to the reflectivity of metal surfaces in the optical frequency range. It is important to note that in plasmas the free electrons do have a natural frequency  $\omega_{op}$  known as the plasma frequency which is given by:

$$\omega_{op} = \sqrt{\frac{Nq_e^2}{\epsilon_0 m_e}} \quad (\text{Eq. B.19})$$

The importance of the plasma frequency is that it is a critical limit below which the index of refraction becomes complex and the incident wave is exponentially attenuated; in a similar manner dielectrics will behave like conductors when an incident radiation field sufficiently ionizes the material generating a plasma.

The dispersion relationship also reveals the processes underlying scattering at the continuum level. When a very large ensemble of molecules is probed the isotropic limit once again restores these quantized states to a smooth distribution as the total number of contributions from many processes present in the real material field are superimposed. As previously stated if the incident EM wave is resonant with the intervening matter absorption will occur, however, if the electronic structure is non-resonant then the incident field is scattered. The mechanics of the scattering is dependent on the material properties. If the scatterers are far apart or weakly interacting (at that frequency) the incident light is reradiated without a change in photon energy, but with a phase shift dependent on the size of the scatterer. If the particles are small compared to the wavelength the incident wave induces a dipole oscillation resulting in a radial scattering angle that is strongly wavelength dependent with zero emission in the direction of, a process known as Rayleigh scattering. Conversely, particles much larger than the incident wavelength will develop multi-pole oscillations which when taken together reinforce in the forward direction, this process is known as Mie scattering. Scattering will result in an angle dependent polarization of the incident light due to the shift in the phase velocity such that in the forward direction no polarization occurs, with increasing polarization at higher angles. In the case of a polarized incident wave the phase velocity will not change however there will be no radiation in the direction of the induced dipole oscillation.

In dense matter these scattering relationships also result in diffraction of the wavefront which is again wavelength dependent. In the case where the atoms or molecules in the absorbing material are strongly coupled the absorbed energy can be partly transferred between oscillators and the emitted photon will have a different energy level than the incident wave, this inelastic scattering is known generally as Raman scattering and can yield useful information about the kinds of coupling present between oscillators in a sample. This process is related to but distinct from vibrational relaxation spectroscopy techniques.

### B.3 Electromagnetic Emission

Surrounding an oscillating dipole it is possible to discern three distinct regions as a function of distance ( $r$ ): the reactive near-field, the radiative near-field and the radiation zone or far-field. In the near-field close to the dipole ( $r < \lambda$ ) the  $E$ -field is static as the field lines have not closed upon themselves. The reactive near-field region ( $r < \lambda/2\pi$ ) is special in that the antenna and the environment are mutually reactive to each other. The electric and magnetic flux lines are unpredictable in this region and issues like self-capacitance become important. This is precisely the reason why the density of scattering bodies determines the resulting radiation propagation features as already discussed and can lend useful information about the local environment of atomic level emitters. In the far-field ( $r > \lambda$ ) the electric field is far simpler to characterize and fulfills the following condition:

$$E = \frac{p_0 k^2 \sin\theta \cos(\vec{k} \cdot \vec{r} - \omega t)}{4\pi\epsilon_0 r} \quad (\text{Eq. B.20})$$

$p_0$  is the time-dependent dipole moment,  $\theta$  the phase angle, the propagation vector, the positional vector, and  $k$  the dispersion coefficient. In practical systems the irradiance ( $I$ ) of the oscillating electric field at a given point falls off with the square of the distance  $r$ :

$$I(\theta) = \frac{p_0^2 \omega^4 \sin^2\theta}{32\pi^2 \epsilon_0^2 r^2} \quad (\text{Eq. B.21})$$

The geometry of the emitting body can influence the way in which the radiation pattern propagates and is a concern in practical radiation sources.





# 4

## Water Speaks

### *Experimental Results*

*The experimental observations are presented and combined to overcome limitations and uncertainty inherent to each technique. Key findings are highlighted throughout and reveal a non-equilibrium proton population, charge sequestration, and the emergence of dynamic heterogeneity in the electrically excited liquid.*

## 4.1 Unveiling hidden flow structures with proton imaging – The water bridge in a medical MR-scanner

*MRI is used to observe the flow field present in the bridge without the use of tracer particles but rather using the water protons themselves to generate the signal, with heavy water serving as contrast agent. An opportunity to observe the flow pattern without the complication of additional dielectric interfaces can better reveal the precise shape of the electric field in the bridge. From these measurements we find that the bridge has a layered structure, with distinct flow regimes lying one on top of the other.*

### 4.1.1 Flow in the bridge

The flow direction in an EHD liquid bridge is a dynamic phenomenon and best understood as the balance of EHD and hydrostatic forces [1]–[3]. The steady state flow direction is material dependent on account of the stability and transport kinetics of ions in the liquid [4]. For water this results in preferential flow from anolyte to catholyte. However, periodic flow reversal is an established trait of EHD bridges and is thought to result from the hydrostatic pressure temporarily overcoming EHD transport. Likewise, reverse flow can occur immediately following bridge ignition and is likely due to brief force imbalances associated with bridge ignition [5]. These types of reverse flow are transient and last no more than a few to tens of seconds in bridges made using identical solutions in both beakers.

The reverse flow observed in the isotope mixing experiments (see appendix C.1.2) is thus an unusual situation. It can be explained as an additional displacement generated by the isotope density difference. That the reverse flow persists for many tens of minutes indicates separate flows of different density ( $H_2O$ ,  $HDO$ ,  $D_2O$ ) within the system. This will retard local mixing and prolong the time require for the system to equilibrate as is seen to be the case. Density gradients are thus a deterministic factor in the dynamic mass balance of a water bridge.

In order to better visualize the flow dynamics and mixing forces in the bridge section 3D velocity maps were recorded for three light water bridges (figure 4.1a). Despite the limitation of averaging non-stationary flow for several minutes of data acquisition the results for the three bridges were consistent and provide a first look at the complex flow dynamics inside the bridge. Previously flow has only been observed optically in EHD liquid bridges using a number of techniques [6], [7] that suffer from limitations due to the variable cylindrical geometry.

**Two counter current flows are present in the bridge (figure 4.1b), one flowing over the other as they cross from one beaker to the other.** The mean peak velocities ( $v_f$  forward direction or  $v_r$  reverse) of these flows were sampled at two positions in the bridge – halfway

between the bridge base and center. Forward flow shall always refer to flow from anode to cathode, and reverse flow the opposite. Mean peak velocities found in the slice half-way between anode base and bridge center (figure 4.1c) were  $v_f = 18 \pm 5$  cm/s and  $v_r = 27 \pm 6$  cm/s, respectively. At half-way between catholyte base and bridge center (figure 4.1d)  $v_f = 22 \pm 2$  cm/s and  $v_r = 26 \pm 4$  cm/s. The deviation values are the standard error of the mean (SEM). These peak velocities in the forward and reverse direction are on the same order of magnitude as those measured for the longitudinal flow using LDA. However, due to the limited spatial resolution of MR phase contrast images it is as yet difficult to determine whether or not the spiral flow observed previously in the outer bridge is a genuine feature present only in a very thin surface shear layer [3]. It can be extrapolated from these measurements that in the normal steady state condition where the forward flow velocity is less than the reverse velocity the cross-sectional area of the forward flow must be greater than that of the reverse flow in order to maintain the equilibrium. Indeed the shape of water bridges is known to be amphora like [8], and furthermore swings in the equilibrium height difference between anolyte and catholyte is associated with bridge diameter fluctuations. Such a relationship is consistent with the Bernoulli flow model discussed in [1]–[3].

It is also interesting to consider the action of the magnetic field on the liquid volume. The configuration of the bridge system was chosen in part to minimize the Lorentz force that would act on the bridge during operation. As a quick check of the maximum forces expected on the system we can quickly calculate the Lorentz force acting on a current carrying wire:

$$F = Il \times B_0 = ||Il|| ||B_0|| \sin\theta \quad (\text{Eq. 4.1})$$

Where  $I$  is the current over the bridge (1.6 mA),  $l$  is the length (<1 cm), and  $B_0$  the magnetic field strength (1.5 T). As the cross-product is sensitive to the relative orientation of the current path and the magnetic field lines in a purely coaxial situation, which is approximately the case here, the net force will be zero as  $\sin(0) = 0$ ; as a worst case scenario one could imagine current conduction perpendicular to  $B_0$ ,  $\sin(90) = 1$ , and thus becomes for the values reported in this study

$$F = ||(1.6 \cdot 10^{-3} \text{ A})(10^{-2} \text{ m})|| ||1.5 \text{ T}|| \sin 90 = 2.4 \cdot 10^{-5} \text{ N} = 2.4 \cdot 10^{-4} \frac{\text{g}}{\text{cm} \cdot \text{s}} \quad (\text{Eq. 4.2})$$

This value is rather small when compared to the EHD forces responsible for the bridge which are capable of lifting and transporting several grams of water per second over barrier heights in excess of 1 cm. Thus, by several orders of magnitude we can see that the observed behavior is likely not the result of magnetic field interactions with charges in the liquid volume and is rather a genuine feature of interacting isotope labelled EHD flows. For a more complete discussion on the role that electromagnetic forces play on polarizable fluid elements see the work of Engel and Friedrichs [9].



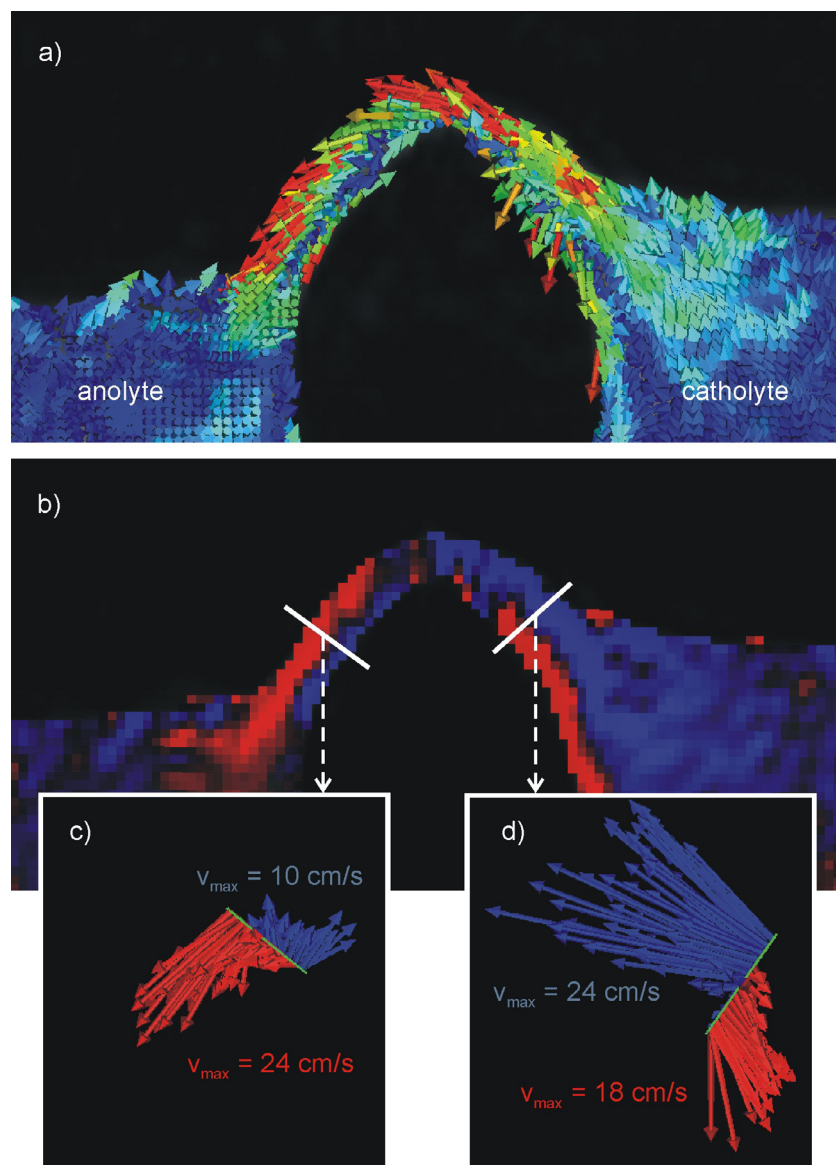


**Figure 4.1** Velocity field in a light water bridge determined by tri-directional MR phase contrast imaging. Upper panel (a) displays velocities in the central sagittal slices as color encoded 3D vectors. For better visualization of layer structure of upward and backward flow, the central panel (b) displays only vertical velocity component (red is downward, blue is upward). Multiplanar reformatted cut planes for peak velocity evaluation are indicated as white lines and respective velocity distributions are shown in 3D vector representation in panels (c) and (d)

## 4.2 The discovery of charged water – Proton Production & Charge Separation

In this section the electrochemistry in the water bridge is investigated. The conductivity of the system is examined and it is found that proton conduction is necessary to fully account for the measured charge transport. The bridge acts as a protonic resistor and impedance spectroscopy corroborates the finding that a proton gradient forms across the entire system.

### 4.2.1 Electrochemistry

The electrolytic production of hydrogen and the characterization of charge carriers is appended in §C.2.

#### 4.2.1.1 Conductivity

In a floating water bridge system, about 87% of the charge carriers responsible for conduction, as calculated using their molar conductivities [10] are protons (see Tables C.3 and C.4). Generally the calculated conductivities  $\Sigma \lambda_i$  are in good agreement with the measured ones  $\lambda_{exp}$  when taking into account their respective errors. Small deviations can be explained by the dynamics of the air/water interface. If, for example, the calculations are carried out with only 80% of the dissolved carbon as starting value, the conductivity of the reference water matches the calculated value exactly. As a matter of fact, if 80%, 90% and 74% of saturation are assumed for experiments 1, 2 and 3, all values match with the calculated ones (within their standard deviation, so  $\Sigma \sigma(\lambda_i) < \Delta \lambda$ ).

Another general behavior catches the eye when looking at Table C.4: The conductivities in the anolyte are higher, the conductivities in the catholyte are lower than that of the reference. This is due to the electric field enriching cations in the catholyte and anions (hydrogen carbonate) in the anolyte. Thus, the proton concentration is also higher in the anolyte, with hydrogen carbonate and protons being mostly responsible for the conductivity, their concentration in the anolyte outweighs the concentrations of the cations in the catholyte by far, resulting in higher conductivities in the anolyte than in the catholyte.

The only cation that showed a higher concentration in the anolyte than in the catholyte is platinum. Platinum was found in all three anolyte solutions (0.07, 0.08 and 0.02  $\mu\text{g L}^{-1}$ ), but only in one catholyte sample, experiment 2 (0.03  $\mu\text{g L}^{-1}$ ). In contrast to the other cations in the solution, platinum is a noble metal, and its ions are easily reduced. Therefore it is straightforward to conclude that platinum ions are rapidly reduced to metallic platinum once they arrive at the cathode, whereas the alkali and earth-alkali metals just accumulate in the catholyte.

In summary, **the most important contribution (87%) to conductivity comes from solvated protons and their concentration is higher in the anolyte.**

4.2.1.2 pH Change

The measurement of pH is typically made in solutions that contain relatively large amounts of acid or base or dissolved salts, conditions under which conventional pH electrodes can make measurements quickly and precisely. Measurements in pure water with low ionic strength are more difficult. Although electrodes respond quickly in buffers, in pure water the electrode response is often unsatisfactory (slow, drifting, noisy, inaccurate, etc.). Naturally, pH electrodes will not work properly under the application of high voltage, since the electronics of such instruments are not designed to operate under these conditions. Using a pH dye has the disadvantage of being much less precise, so small changes of pH will be difficult to measure. Moreover, adding a pH dye can, under these circumstances, influence the pH, because of its intrinsic acidity. If these effects are taken into account, however, it offers the advantage to easily visualize a distribution of pH (a matrix) in real time. This is why the pH change was investigated using three independent methods: 1) the addition of a pH dye (during and after operation), 2) pH dependent fluorescence using an optical fiber (during and after operation), and 3) electrochemically (after operation).

Without proton transport through the bridge, pH shifts according to electrolysis can be easily calculated. Taking the same example as in the previous section and calculating the amount of  $H^+$  and  $OH^-$  being produced starting from an initial pH of the pure water of about 5.5, after 30 minutes of bridge operation, the pH should be  $\sim 2$  in the anolyte and  $\sim 10$  in the catholyte. In this work we show that the actual pH difference is much lower, between 0.1 and 0.3 units, according to all three methods employed. Fig. 4.2 shows the result of the first method, the addition of a pH dye. In order to quantify the colors of the solutions in the subfigures, a colorimetric analysis was performed, the results of which are given in Table 4.1.

**Table 4.1.** Colorimetric evaluation of Fig. 4.2a, c and f. The relative pH shift towards acid (increase of redness) is calculated from the redshift ( $\Delta a^*$ ) of the solutions in linear relation to the redshift of the pH dye reference.

|            | a* Anolyte     | a* Catholyte    | Redshift ( $\Delta a^*$ ) | pH shift         |
|------------|----------------|-----------------|---------------------------|------------------|
| Fig. 4.2a: | $-8.3 \pm 0.2$ | $-7.4 \pm 0.3$  | $-0.9 \pm 0.5$            | $0.04 \pm 0.03$  |
| Fig. 4.2c: | $-5.1 \pm 0.4$ | $-11.6 \pm 0.1$ | $6.5 \pm 0.5$             | $-0.28 \pm 0.03$ |
| Fig. 4.2f: | $-6.1 \pm 0.2$ | $-13.5 \pm 0.5$ | $7.4 \pm 0.7$             | $-0.31 \pm 0.04$ |
| Reference: | pH 5           | pH 6            |                           |                  |
|            | $7.7 \pm 0.1$  | $-15.2 \pm 0.4$ | $22.9 \pm 0.5$            | -1.0             |

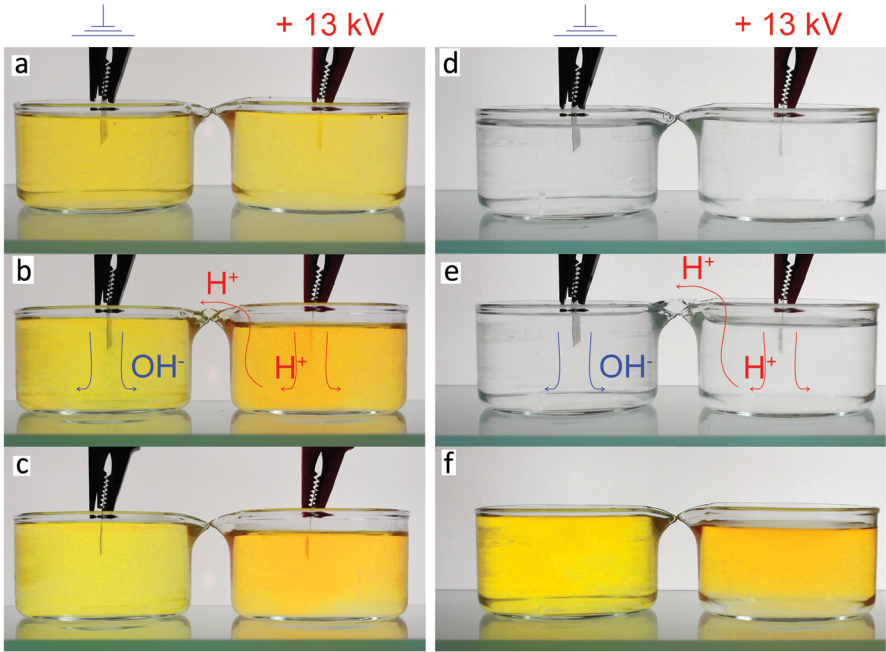


**Figure 4.2 a-c:** A floating water bridge (13 kV, 2.8 mA) run with pH dye; **a:** before bridge formation; **b:** during bridge operation,  $H^+$  and  $OH^-$  production and paths highlighted; **c:** after shut down of bridge operation; **d-f:** A floating water bridge (13 kV, 0.5 mA) run without pH dye; **d:** before bridge formation; **e:** during bridge operation,  $H^+$  and  $OH^-$  production and paths highlighted; **f:** pH dye added after bridge operation.

As second method, in another water bridge experiment, the pH was measured online during bridge operation in both anolyte and catholyte, respectively, using a fiber optic pH sensor. Figure 4.3 shows a consecutive measurement of the pH of anolyte and catholyte for a steady state water bridge.

As a third, independent investigation, 40 water bridge experiments were performed for up to 5 hours each, and the pH of the anolyte and catholyte was measured afterwards with an ion-selective electrode. Averaged over all experiments there is a statistically significant difference between anolyte and catholyte of  $0.27 \pm 0.05\text{pH}$  (t-test,  $P < 0.001$ ). Table 4.2 summarizes the pH measurements and calculations. As mentioned before, the pH dye is slightly acidic, thereby lowering the overall pH of the system compared to the other two methods. All three methods show that there is a pH difference between anolyte and catholyte, **but much lower than the theoretical one based upon electrolysis without considering proton transport and neutralization; the deviation is nearly 7.5 orders of magnitude!**



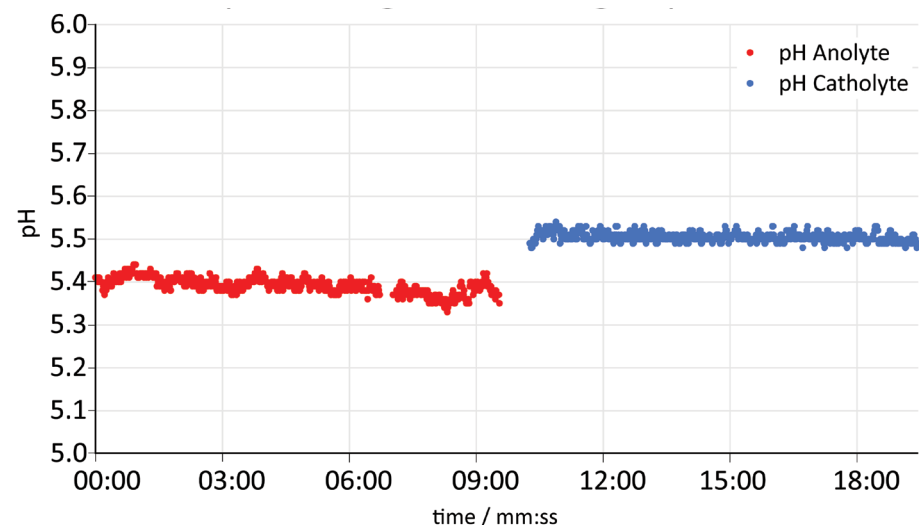


**Figure 4.3** pH measurement during bridge operation using a fiber optic pH sensor. After 9:33 min in the anolyte the sensor was moved from the anolyte to the catholyte.

**Table 4.2:** pH of anolyte and catholyte according to three measurement methods: pH dye, fiber optic sensor and ROSS Ultra electrode compared to theoretical values based upon electrolysis without considering proton transport and neutralization

|              | calculation | pH dye      | Fiber optic sensor | ROSS electrode |
|--------------|-------------|-------------|--------------------|----------------|
| pH anolyte   | 2           | 5.20 ± 0.07 | 5.39 ± 0.02        | 5.45 ± 0.02    |
| pH catholyte | 10          | 5.54 ± 0.03 | 5.50 ± 0.01        | 5.72 ± 0.03    |

#### 4.2.1.3 The proton resistor

The reason why the theoretical pH values (2 and 10) are never reached although the respective protons and hydroxyl ions are produced is the connection between the beakers, the floating water bridge, which provides a gateway for protons. Possible mechanisms for this transport will be discussed later on in regards to the infrared emission of the water bridge (see §4.4.4).

The ionic mobility for an aqueous electrolyte is experimentally determined by the use of an accelerating voltage applied to the solution under study. Accepted values for  $H^+$   $3.623 \cdot 10^{-7} \text{ m}^2 \text{ s}^{-1} \text{ V}^{-1}$  and  $OH^-$   $2.064 \cdot 10^{-7} \text{ m}^2 \text{ s}^{-1} \text{ V}^{-1}$  [11] under a field strength of  $2.0 \cdot 10^5 \text{ V/m}$  in water bridge experiments yield non-negligible ionic drift speeds of  $7.0 \cdot 10^{-2} \text{ m s}^{-1}$  and  $4.0 \cdot 10^{-2} \text{ m s}^{-1}$ .

This field strength was approximated by  $14 \text{ kV} / 7 \text{ cm}$ , but is stronger along the bridge and weaker in the beakers [3]. This taken along with the fast EHD flow present throughout the system it is reasonable to consider that protons travel quickly from the anode to the catholyte where they rapidly recombine with the slower hydroxide ions. This mechanism is visualized in Fig. 4.2b. In order to demonstrate that the pH dye is actually displaying pH changes and is not electrochemically altered or destroyed by the applied current, another experiment was run. After shutdown, the polarity of the voltage was reversed, and the bridge was reignited. This experiment showed the exact same situation as in Fig. 4.2b, only mirrored. Finally, the content of the two beakers was mixed, returning the solution to its original color. Therefore, it is safe to say that the above shown changes in color really correspond to local changes in the pH.

Electrochemical electron transfer reactions take place close to the surface of the electrodes in the interfacial double layer. The characteristic thickness of this layer is called the “Debye length” ( $\kappa^{-1}$ ) [12], a distance indicating the length over which separated charge, and hence electric fields, are screened in an electrolytic solution. It is reciprocally proportional to the square root of the ionic strength. In aqueous solutions it is typically on the scale of a few nanometers, its thickness decreases with increasing concentration of the electrolyte.

In order to enable a Faradaic current and thus electrochemical reactions, the potential established at the electrode surfaces must drop sufficiently rapidly over the Debye length. The Debye length is defined as

$$\kappa^{-1} = \sqrt{\frac{\epsilon_r \epsilon_0 k_B T}{2 N_A e^2 I}} \quad (\text{Eq. 4.3})$$

with  $\epsilon_r$  being the dielectric constant of the medium,  $\epsilon_0$  the permittivity of vacuum,  $k_B$  the Boltzmann constant,  $T$  the absolute temperature,  $N_A$  Avogadro’s number,  $e$  the elementary charge and  $I$  the ionic strength.

In an exemplary low voltage electrolytic cell, the calculation of the field strength across the Debye length is straightforward: With an ion concentration of  $0.1 \text{ M}$  at  $300 \text{ K}$  and an estimated potential drop in the order of  $1 \text{ V}$  and a Debye length of  $\sim 0.96 \text{ nm}$  according to (Eq. 4.3), one obtains a field strength of  $10^7 \text{ V/cm}$ . When pure water ( $\sim 3 \mu\text{mol L}^{-1}$ , calculated from Table C.3) is used instead, the Debye length becomes much larger, about  $175 \text{ nm}$ , meaning that the electric field can penetrate into the solution much further since there are fewer ions to shield it. In order to create a similar situation as in the low voltage example, the potential must be  $\sim 182$  times higher, about  $182 \text{ V}$ . Furthermore, the potential difference between hydrogen evolution reaction and oxygen evolution reaction is thermodynamically  $1.23 \text{ V}$  at any given pH [11]. In practice, the applied potential required for water electrolysis differs from the thermodynamically potential, due to potential losses caused by, e.g., electrolyte resistance (concentration losses) and electrode resistances (activation losses). This potential difference

is called the overpotential. In the water bridge, the electrolyte resistance is expected to be the biggest contribution to the overpotential, since platinum electrodes are used and the pH and temperature are close to standard conditions. Therefore, the overpotential can be estimated using Ohm's law,

$$\eta(V) = i \cdot R \cdot l = i \frac{1}{\lambda} l \quad (\text{Eq. 4.4})$$

with  $I = 1300 \mu\text{A}$  (current applied during  $\text{H}_2$  production experiment),  $\lambda = 0.93 \mu\text{S cm}^{-1}$  (see Table C.3) and  $l = 7 \text{ cm}$ , the overpotential required is  $\sim 9800 \text{ V}$ .

Because the potentials applied to create a water bridge are typically 13 kV and higher, this potential is easily available, and field strengths achieved close to the electrodes are sufficient to drive the Faradaic process. From the considerations above it is obvious that electrolysis of deionized water would not take place using usual, approximately a 1000 times lower electrolytic voltages. Moreover, it is impossible to achieve the electric characteristics of the system by placing two electrodes in one beaker. Water acts as an Ohmic resistor ("leaky dielectric" [13]). If placed in one beaker, the high voltage and currents will lead to quickly heating the system to the boiling point, at which break-down events are likely to occur and destroy the set-up [14]. Only when a "proton resistor" – like the water bridge – limits the current can the safe and stable operation of a high voltage electrolysis system be maintained.

## 4.2.2 Impedance Spectroscopy

Fig. 4.4 shows the measured spectrum of a fresh Milli-Q water sample used in this work (dots) and the calculated spectrum (line) fitted according to the model shown in the insert. The values of  $R_{\text{aq}}$  and  $C$  are  $1.12 \cdot 10^6 \Omega$  and  $8.64 \cdot 10^{-12} \text{ F}$ , respectively. The  $R^2$  value of the fit (amplitude) is 0.00036.

Fresh milli-Q water quickly absorbs  $\text{CO}_2$  from the atmosphere causing the impedance to decrease as discussed in §C.2.3. This effect is visible in Fig. 4.5 which shows an example for a measured spectrum of anolyte (rectangles) and catholyte (dots) taken during bridge operation in a Teflon beaker and manually fitted spectra (lines) according to the models shown in the insert. For the anolyte the values of  $R_{1A}$  and  $R_{2A}$  are  $6.67 \cdot 10^5 \Omega$  and  $3500 \Omega$  the values for  $C_{1A}$  and  $C_{2A}$  are  $8.17 \cdot 10^{-12} \text{ F}$  and  $1.26 \cdot 10^{-7} \text{ F}$ , respectively. For the catholyte the values of  $R_{1C}$  and  $R_{2C}$  are  $1.03 \cdot 10^6 \Omega$  and  $6000 \Omega$  the values for  $C_{1C}$  and  $L$  are  $8.72 \cdot 10^{-12} \text{ F}$  and  $8.0 \text{ H}$ , respectively. The spectra were fitted by manual adjustment of the parameters, since none of the automated fitting algorithms successfully reproduced the pseudo-inductance and the pseudo-capacitance features represented by the resistor/inductance and resistor/capacitor elements satisfactorily. This feature is visible as a small, (anti-)clockwise pointing tails on the real axis, lower frequency right-hand side of the spectra.

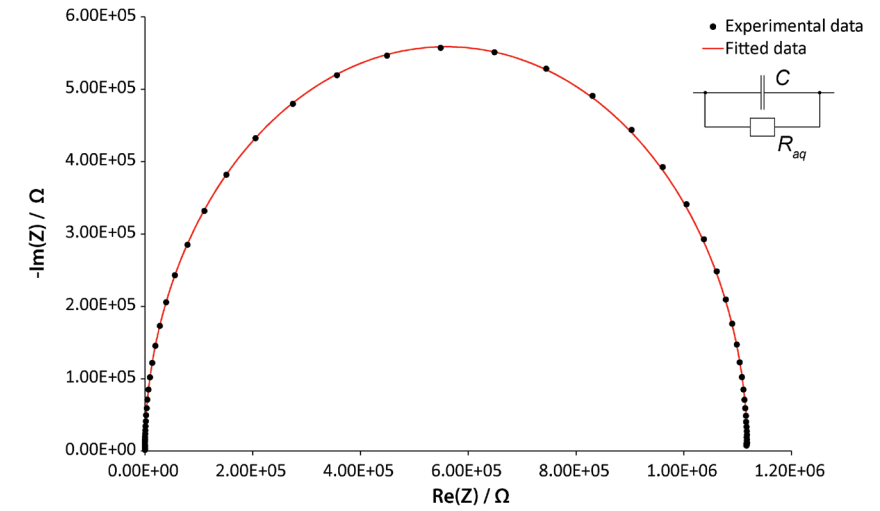


Figure 4.4 Impedance analysis of fresh milli-Q water (black dots) and a simulation using the circuit shown in the right insert (red line). The values of  $R_{\text{aq}}$  and  $C$  are  $1.12 \cdot 10^6 \Omega$  and  $8.64 \cdot 10^{-12} \text{ F}$ , respectively.

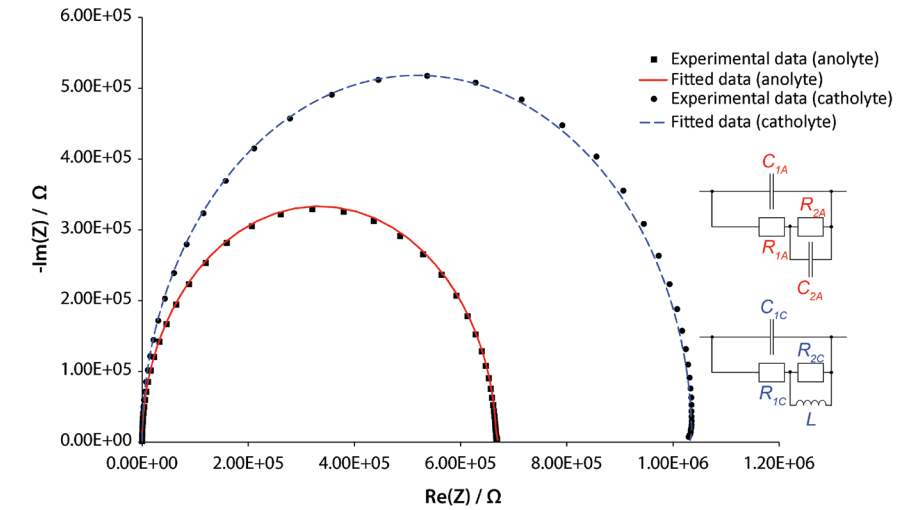


Figure 4.5 Impedance analysis of an anolyte (black squares) and catholyte (black circles) taken during bridge operation in Teflon beakers and a simulation using the circuits shown in the right insert. The values of  $R_{1A}$  and  $R_{2A}$  are  $6.67 \cdot 10^5 \Omega$  and  $3500 \Omega$ ; the values for  $C_{1A}$  and  $C_{2A}$  are  $8.17 \cdot 10^{-12} \text{ F}$  and  $1.26 \cdot 10^{-7} \text{ F}$ ; the values of  $R_{1C}$  and  $R_{2C}$  are  $1.03 \cdot 10^6 \Omega$  and  $6000 \Omega$ ; and the values for  $C_{1C}$  and  $L$  are  $8.72 \cdot 10^{-12} \text{ F}$  and  $8.0 \text{ H}$ , respectively. The resistor/inductance and resistor/capacitor elements are visible as a small, (anti-)clockwise pointing tails on the real axis, lower frequency right-hand side.

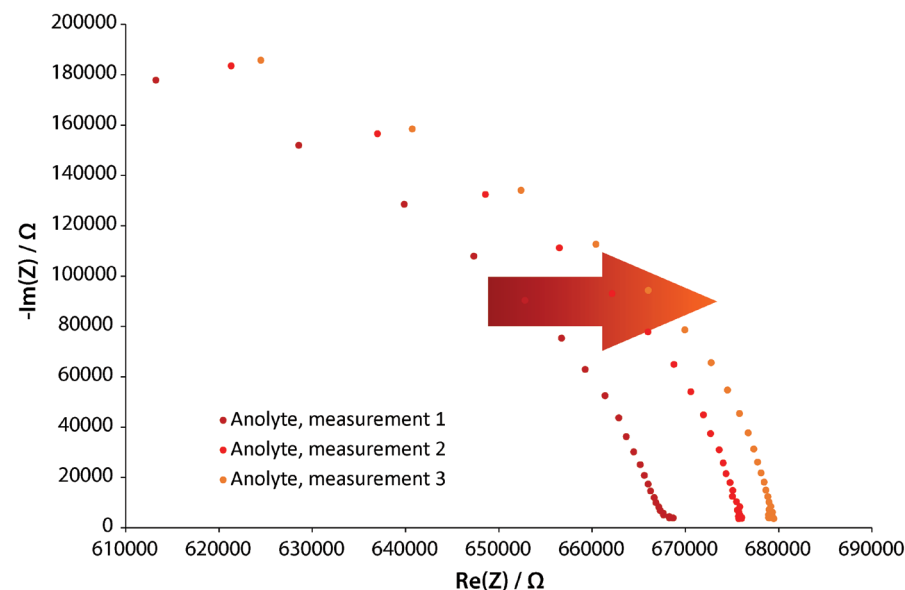


Figure 4.6 Three consecutive impedance measurements of the anolyte taken from an operating floating water bridge set-up using Teflon beakers.

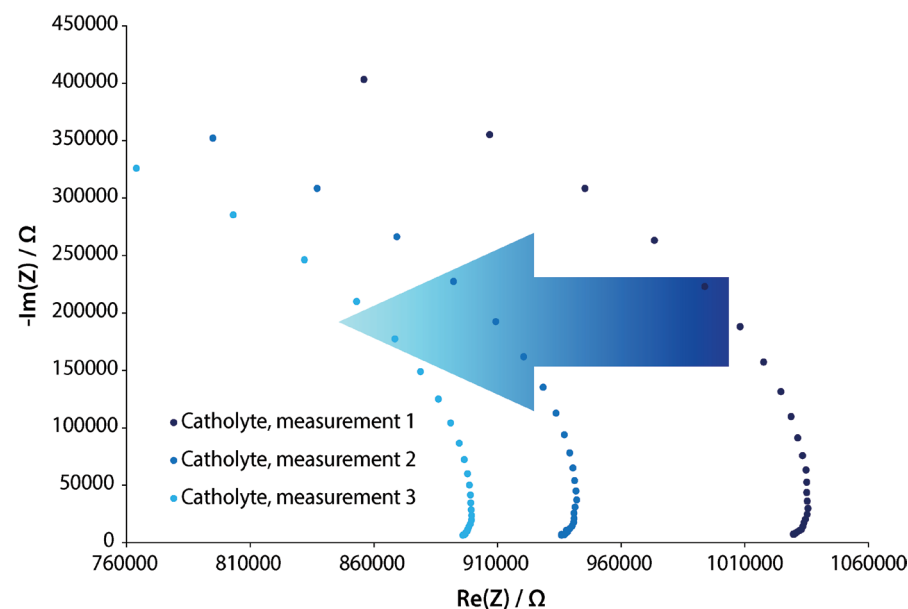


Figure 4.7 Three consecutive impedance measurements of the catholyte taken from an operating floating water bridge set-up using Teflon beakers.

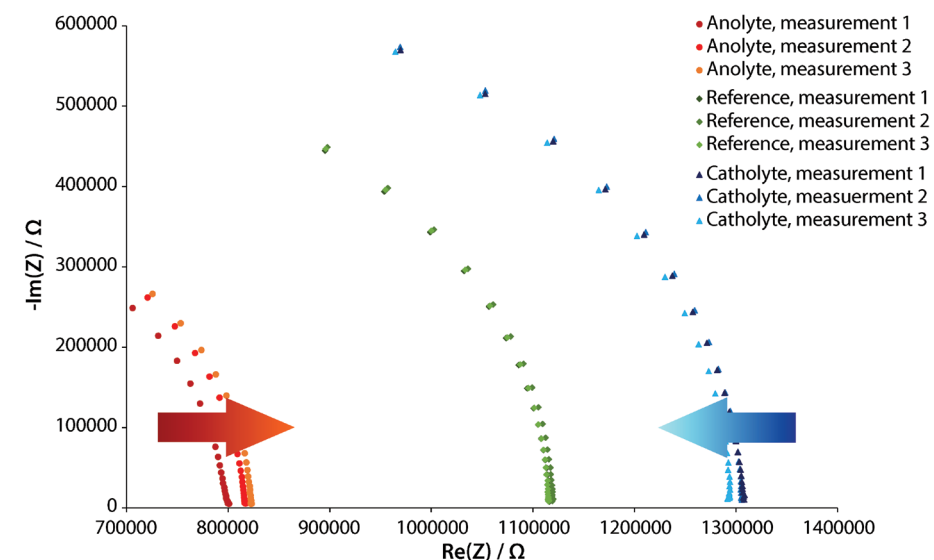


Figure 4.8 Three consecutive impedance measurements of anolyte, reference water and catholyte taken from the beakers after 20min of floating water bridge operation using glass beakers.

Three consecutive measurements of an anolyte extracted from an operating bridge using Teflon beakers are shown in Fig. 4.6. The observed impedance shift between first and third measurement on the real axis is about  $13 \text{ k}\Omega$ , corresponding to a conductivity decrease by  $0.03 \mu\text{S cm}^{-1}$ . **This impedance shift is due to the fact that the read-out process in the spectrometer destroys excess protonic and aterprotonic charge (ancient Greek ἀτερ, “without”) as discussed in §5.2.1.** The anti-clockwise tail on the real axis lower frequency signifying an electrochemical reduction is clearly visible in the first measurement. This conductivity shift amounts to 33% of the theoretical, maximum possible conductivity shift calculated in Appendix §C.2.

Fig. 4.7 shows three consecutive measurements of a catholyte extracted from an operating bridge using Teflon beakers. The observed impedance shift between first and third measurement is about  $135 \text{ k}\Omega$ , corresponding to a conductivity increase by  $0.14 \mu\text{S cm}^{-1}$ . This conductivity shift amounts to 61% of the theoretical, maximum possible conductivity shift calculated in Appendix §C.2.

Fig. 4.8 shows three consecutive measurements of an anolyte, a catholyte and the original (reference) water measured about 2 hours after a bridge operation for about 20 minutes in glass beakers. In contrast to Figs. 4.5-4.7 all solutions are now saturated with  $\text{CO}_2$ . The observed impedance shift on the real axis for all three measurements (anolyte, catholyte, reference) in

Fig. 4.8 compared to Figs 4.6 and 4.7 is due to the low frequency components associated with ion drift. Similar effects as for the measurements in Fig. 4.6 and 4.7 where samples were taken during bridge operation are visible. The resistor/inductance and resistor/capacitor elements for catholyte and anolyte are again visible as a small, (anti-) clockwise pointing tails on the real axis. The difference between the three reference water measurements is small and shows the reproducibility of the measurement.

In order to investigate the life time of the charged solutions, we ran another experiment where we stored the water after bridge operation from Teflon beakers in Greiner tubes (Sigma-Aldrich T1943, polypropylene) and measured the impedance after two and seven days (data not shown). Whereas the results after two days were comparable to the ones shown in Fig. 4.8, after seven days the effects associated with excess charge could not be reproduced, indicating a limited life time of the excess charge in the order of hours to days.

## 4.3 Coupling Local Structures in an Electrically Stressed Polar Liquid

*In this section the interaction between the local coulombic and the externally applied field is examined. While the static structure is found to be unchanged within the given accuracy of the employed measurements, the systematic analysis of the data using computer simulation reveals changes in the dynamic environment that are reliable above the limited instrument precision. The imposed electric field of an EHD bridge is shown to distort the probability distribution of the local coulombic interaction between molecules in the bridge.*

### 4.3.1 Total scattering of water under moderate electric field

A comparison of the corrected differential scattering intensity from both neutron and X-ray experiments for bridge and bulk water is shown in figure 4.9. Differences are evident in the scattering signal in the range  $1\text{--}5\text{ \AA}^{-1}$ . Small changes in intensity for the X-ray data are evident for larger  $q$  range whereas at low  $q$  the departure between the two data sets becomes more pronounced. The first peak in the heavy water neutron scattering shifts to higher  $q$  in contradiction to previous work [15]. Oscillations at high  $q$  are also more pronounced in the case of the electrically stressed bridge water. The electric field steepens the transition between the first and second peaks in the neutron scattering data from light water. Null water in the bridge is particularly interesting since it shows very little of the characteristic oscillatory structure up to  $10\text{ \AA}^{-1}$  which is present in the bulk liquid (reference water, no electric field). This is usually indicative of the pronounced O-O distance of  $\sim 2.8\text{ \AA}$  which is seemingly less pronounced in the electrically stressed bridge water. Another feature is that for both  $\text{H}_2\text{O}$  and  $\text{D}_2\text{O}$  the high  $q$  oscillations do not decay quite as rapidly with increasing  $q$  in the bridge compared to bulk. The Fourier transform of the scattering intensity provides the molecular radial distribution function (RDF) (figure 4.10). The previous features are again visible,

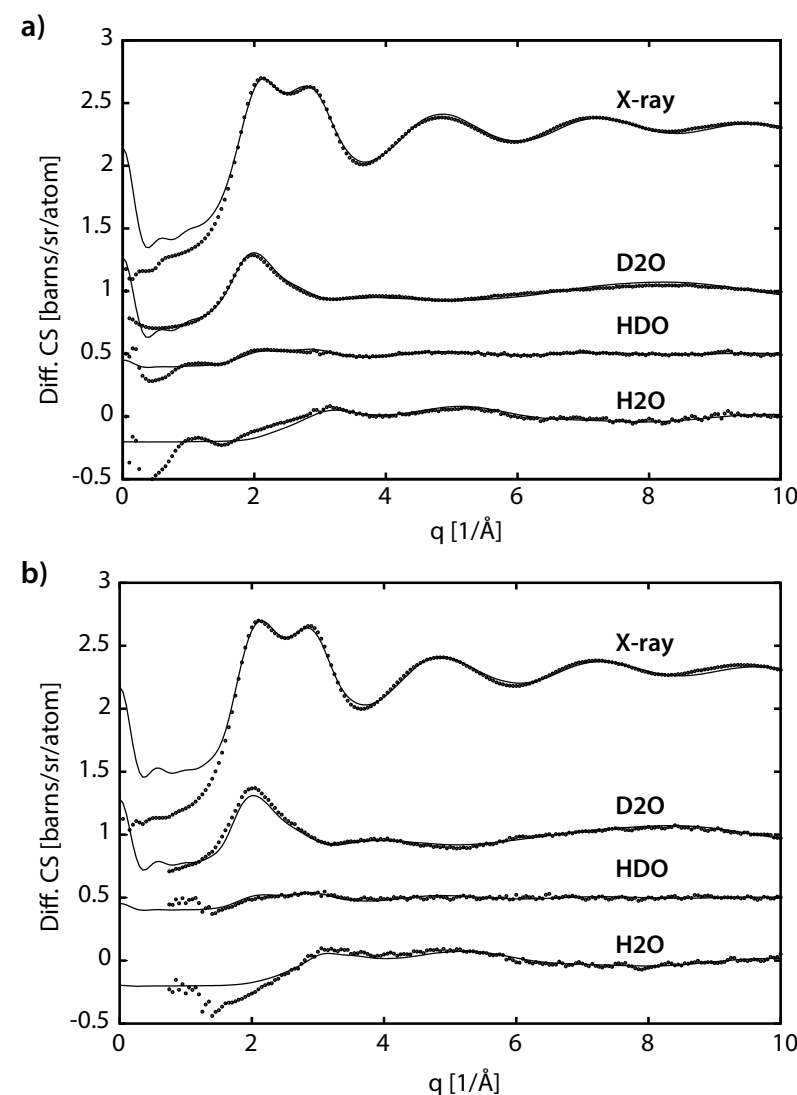


**Figure 4.9:** Comparison of the corrected scattering data (open-circles) and the EPSR generated fits (lines) for a) ground potential liquid water at  $40^\circ\text{C}$  and b) electrically stressed bridge water at  $40^\circ\text{C}$ . The neutron scattering data from (a) was collected on the NIMROD instrument using a can geometry, while that of (b) on SANDALS with the cylindrical bridge geometry. For both cases the X-ray instrument was identical (MS04) as was the sample geometry (e.g. cylindrical bridge or jet). Close inspection of these curves reveals some misfits, but these fits appear to be the best that can be achieved with the present programs and data analysis.

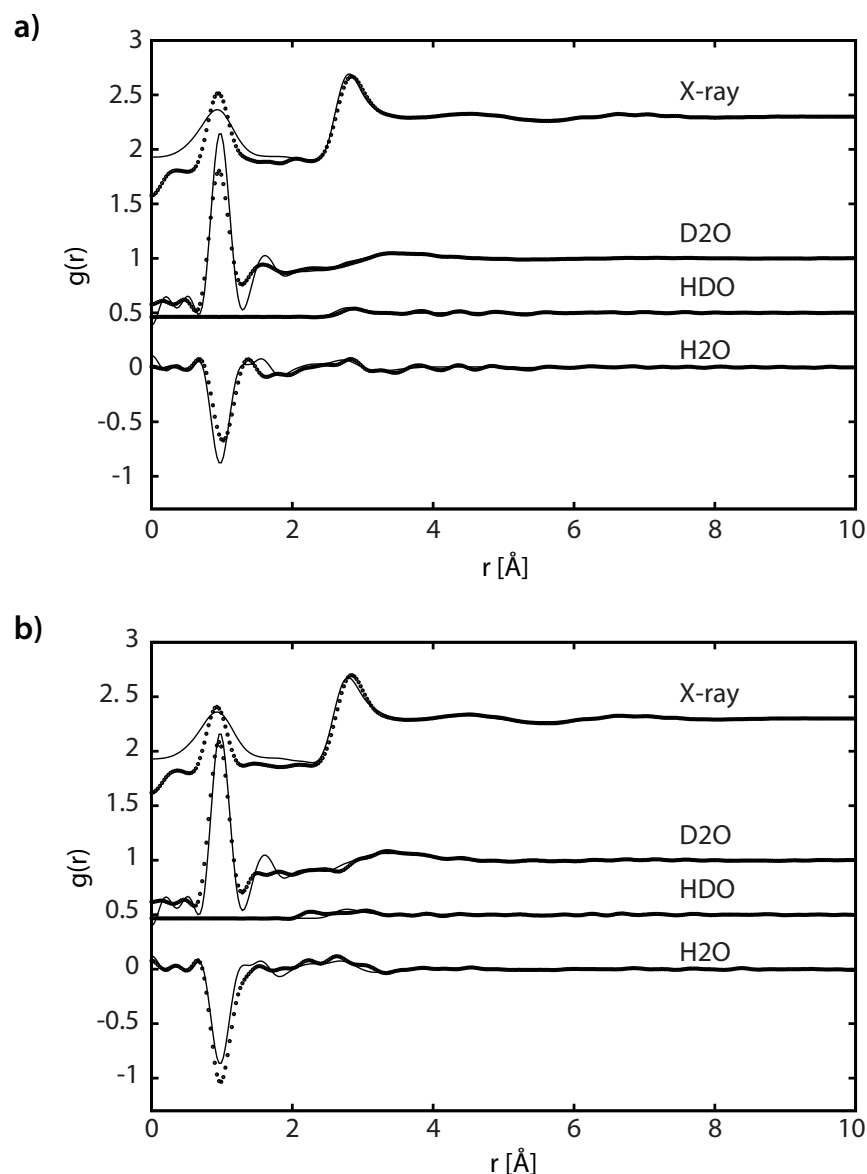


**Figure 4.10:** Molecular radial distribution functions derived from the Fourier transforms of either the EPSR generated fits (lines) or scattering data (open-circles) from a) ground potential water (can or jet) at 40°C for X-ray and neutron (NIMROD) or b) from electrically stressed bridge water at 40°C for X-ray and neutron (SANDALS). The small misfits carry over from the scattering data and again appear to be the best that can be achieved with the present programs and data analysis. The RMS noise in  $g(r)$  is  $1.3E-04$  for reference water (a) and  $1.2E-03$  for bridge water (b).

namely a slightly weaker intensity in the first X-ray peak along with reduced oscillations between  $1-3 \text{ \AA}^{-1}$ . The first peaks for both heavy and light water are both stronger in the bridge, and again the oscillations up to  $3 \text{ \AA}^{-1}$  are more strongly pronounced. These effects are known but not satisfactorily understood within the field and are often attributed to problems in the inelastic correction. A novel feature is visible in the null water transform near  $2.2 \text{ \AA}^{-1}$ , a feature which is also more enhanced in the light water scatter from the bridge.

### 4.3.2 Structure refinement to extract site-site radial distribution functions

The combined X-ray and neutron data sets discussed previously form a complete basis for the determination of the order parameters within liquid systems [16] and thus it is possible to extract the site-site radial distribution functions (RDF), namely H-H, O-H, and O-O for water. Comparison of the simulated and measured scattering data shows a reasonable level of agreement for both the water bridge (Fig. 4.9b, 4.10b) and bulk water samples (no electric field, Fig. 4.9b, 4.10b). Again, the small discrepancies are likely due to poor inelasticity correction. Furthermore, the agreement for the respective site-site RDFs is acceptable. The differences between fit and data for the first peaks can, in part, be attributed to the structural differences expected between heavy and light water as in the simulation they are assumed to be structurally identical. The variance in oscillatory behavior is likewise partially attributed to the degree of disordering between isotope variants; where light water is expected to be the slightly more disordered species [17, p. 53]. The enhanced oscillations at high  $q$  may also indicate the onset of long-range dynamic reorganization in advance of electrically induced phase transitions [18], [19] indicative of increasing local structure which generates medium range order even in the face of elevated temperature [20].

The relative differences between scattering with and without electric field can be discerned in the site-site RDFs shown in figure 4.11. One reason for examining the site-site RDF is that these distributions, unlike the molecular RDF and differential scattering intensity, are largely unaffected by changes in temperature [21], [22]. The O-O RDF for the electrically stressed bridge water is shifted to shorter distances, a trend observed for all three site-site RDFs. The second peak in the O-H RDF also has increased intensity and a narrower distribution a feature shared by both of the first two peaks in the H-H RDF. Some of these shifts are reminiscent of liquid water at elevated temperatures and pressures well above the liquid critical point where the site-site RDFs are compressed in reflection of the partial collapse of the molecular coordination [23] but the bridge data does not show the peak broadening also associated with pressure effects.

The measured site-site RDFs also show similarities to those reported for concentrated hydrogen chloride solutions [24], but it is uncertain whether the proton concentration in the bridge is high enough [25] to change the local structure. Solvated protons carry an intense

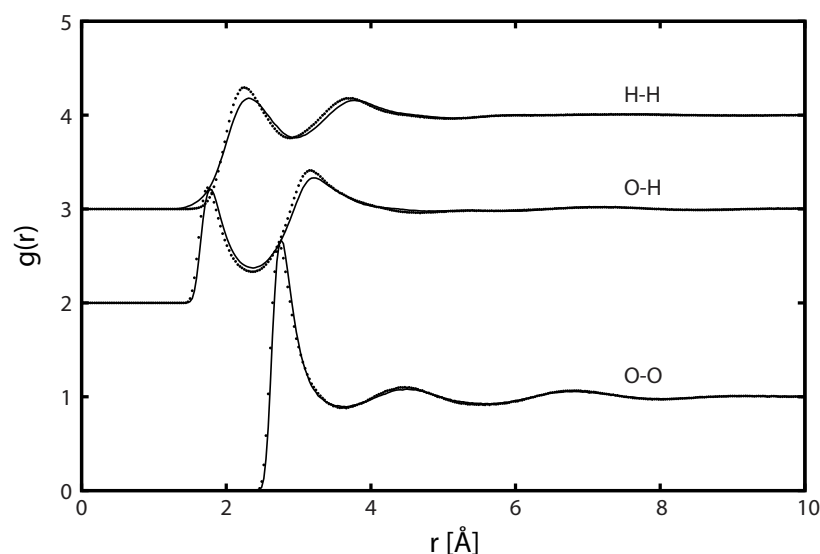


**Figure 4.11** Comparison of the site-site RDFs recovered from the EPSR simulations for electrically stressed bridge water data (symbols), bulk reference without electric field (line). Plots are offset for clarity. While differences are readily observable the shifts are within the recognized uncertainty of the applied methods.

electric field around them which distorts the local intrinsic electric field. It has been suggested that solvated protons act as an inverse-polaron [26], [27] whereby the proton defect perturbs the local order and it is possible that the applied electric field is behaving in a similar way – reducing the interaction distance between molecules by strengthening the effective dipole via the action of induced dipole moments in the neighboring molecules as described by Lorentz-Lorenz theory and discussed for water ice  $I_h$  [28]. The resulting local anisotropic distribution of the electric field polarizability will distort the local dipoles establishing strongly coupled local structures. Changes in the local environment will in turn distort the intramolecular potentials which cannot be captured by a rigid water model but are nonetheless captured in the raw scattering data as small changes in high  $q$  oscillations (see figures 4.9a and 4.9b). The implications of changes in molecular geometry by a moderate electric field are indeed surprising and illustrates that the assumptions under Born-Oppenheimer provide an incomplete basis for systems like water. **The imposed electric field, though weak compared to the local interaction potential, will polarize a subpopulation of dipoles leading to further distortion of the local electron density. This will have a non-negligible effect on the light hydrogen nucleus and thus the two fields can no longer be considered as decoupled.**

The recovered H-H pair potentials hint at this though not significantly, however it must be kept in mind that the RDFs are modeled parameters and differences in experimental data must be considered alongside the simulation results.

The RDFs are the convolution of two quantities: the imposed reference potential ( $RP$ ) and the empirical potential ( $EP$ ). Examination of these contribution gives the opportunity to check how the simulation applies interaction forces in order to converge simulation and scattering data. Since a rigid non-polarizable model is used the extracted  $RP$ s are identical for both simulations and the Morse and Leonard-Jones potential are thus identical. The site-site empirical potentials ( $EP_{\alpha\beta}$ ) shown in figure 4.12, however, are quite different even though the requested magnitude of the  $EP$  is identical for both systems. In EPSR there are no rules governing the shape of the  $EP$  and it is allowed to freely evolve to arrive at the best fit of simulation and experiment possible. Thus an examination of the empirical potential provides clues about how the energetic environment in the two simulations differ. The observed changes show three patterns:  $EP_{HH}$  amplifies the second peak from the bulk (figure 4.12),  $EP_{OH}$  is roughly anti-phase to that of the bulk,  $EP_{OO}$  merges the two bulk peaks into a broad distribution. Thus, the forces acting upon the atom pairs are non-equivalent between the two simulation sets and this must be considered as deriving from the experimental data as all other

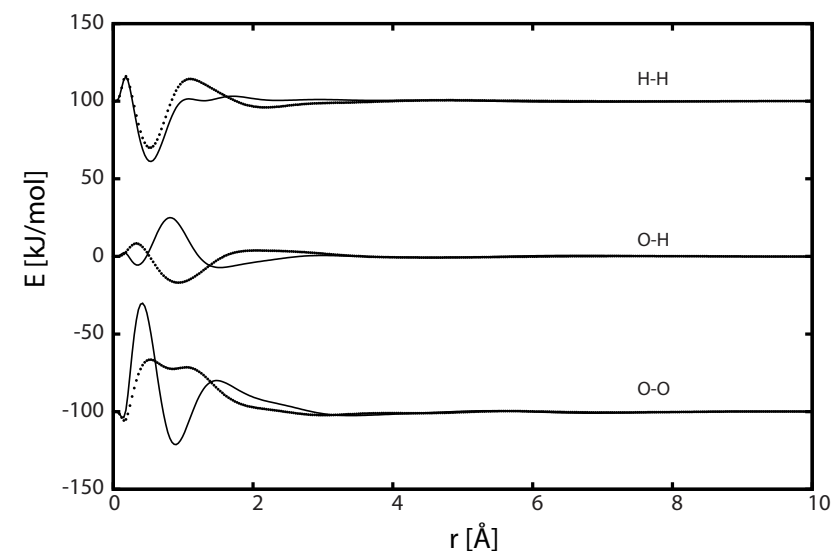


**Figure 4.12:** Comparison of the empirical potentials from the EPSR simulations from reference water without electric field (lines) and electrically stressed bridge water (symbols). It is clear that the applied empirical potential distributions vary significantly between the two simulations. Such a mismatch is not currently reported in the literature and illustrates the underlying differences behind the smaller shifts in the site-site RDFs.



parameters are equivalent. Disordered materials such as liquid water cannot be satisfactorily described using only two body correlation functions such as the RDF and work is ongoing to develop three-body correlated models for computer simulation [29].

### 4.3.3 Analysis of the EPSR simulation

The differences in the results of the structure refinement are close to the uncertainty level, however, the simulations also provide additional information – e.g. intermolecular energy ( $U_i$ ), pressure ( $P_i$ ), and the chi-squared ( $\chi^2$ ) value of the fit to scatter data – that can show non-structural differences between the two experimental cases. These are typically monitored to check that the values obtained are realistic and the system has settled into equilibrium (i.e. not exploding nor imploding). Since the requested empirical potential is a user selected variable, the choice of which must be carefully considered, for the comparisons thus far in the work a value of  $EP_{req} = 20$  kJ/mol was selected for both systems as there is precedent in the literature for liquid water and ice under varying conditions [22]. **It was noticed that the two systems (bulk vs. bridge) do not settle into the same thermodynamic regime which indicated that the generated static structure changes were also reflected in the iterative dynamics of the simulation.** It is important to clarify that the ‘dynamics’ discussed here are not molecular dynamics since EPSR, like the reverse Monte Carlo simulation method it is based on, lacks a meaningful time metric [30]. Rather the dynamics refer to how simulation parameters vary in response to pseudo-random perturbations. It is thus a measure of the stability of the simulation which is expected to converge if the two systems are identical. Two approaches were taken to better understand the response of the simulations to variation in  $EP_{req}$ : A symmetric approach where  $EP_{req}$  was varied equally for both simulations between 0 kJ/mol – i.e. reference potential only – and 100 kJ/mol; and an asymmetric analysis of the response where the established value of  $EP_{req} = 20$  kJ/mol was held constant for the bulk water simulation and  $EP_{req}$  varied between 16-37 kJ/mol for the bridge system. This range was selected as it was within a basin of stability which provided the best fit and physically reasonable parameters. The starting point for the simulations used to check the  $EP_{req}$  response was an identical configuration take from the equilibrated simulation where  $EP_{req} = 20$  kJ/mol one for each of the two data sets. The symmetric approach was run for a minimum of 5000 iterations, whereas, the asymmetric analysis run only for 500 iterations. In both cases however, the behavior of the systems were stable within a narrow band of random oscillations as evidenced by small values of the standard error of the mean on the order of  $5 \cdot 10^{-2}$  and  $4 \cdot 10^{-2}$  for  $U_i$  and  $P_i$  respectively. An increase in  $EP_{req}$  reduces  $U_i$  in both systems, however, the electric field of the bridge damps this response and the two values diverge quickly and can be compared in Table 4.3. In a similar manner increasing values of  $EP_{req}$  drives  $P_i$  ever lower indicating that the system heads toward implosion. Again however, in the presence of the moderate electric field of the bridge the simulated system uniquely resists this trend and  $P_i$  stabilizes even at the highest requested potentials. While enticing to consider the implications

Table 4.3: Comparison of how changing the requested empirical potential affects the environmental parameters in the simulation environment used to refine the data from reference (0 V/m) and bridge (1E6 V/m) water.

| Requested Empirical Potential ( $EP_{req}$ ) [kJ/mol] | Applied Electric Field Strength [V/m] | Intermolecular Energy ( $U_i$ ) [kJ/mol] | Standard Deviation Energy $\sigma_U$ | Intermolecular Pressure ( $P_i$ ) [kbar] | Standard Deviation Pressure $\sigma_P$ | Quality of Fit $\chi^2$ | Standard Deviation squared $\sigma_\chi$ |
|---|---------------------------------------|--|--------------------------------------|--|--|-------------------------|--|
| 0   | 0E0                                   | -4.27E+01                                | 4.30E-03                             | 5.44E+00                                 | 8.35E-03                               | 4.14E-03                | 7.91E-06                                 |
| 0   | 1E6                                   | -4.27E+01                                | 4.23E-03                             | 5.45E+00                                 | 8.01E-03                               | 5.48E-03                | 9.38E-06                                 |
| 10  | 0E0                                   | -5.28E+01                                | 1.65E-02                             | 2.85E+00                                 | 1.14E-02                               | 2.91E-03                | 6.87E-06                                 |
| 10  | 1E6                                   | -4.97E+01                                | 1.15E-02                             | 4.15E+00                                 | 1.09E-02                               | 4.10E-03                | 7.81E-06                                 |
| 20  | 0E0                                   | -6.15E+01                                | 1.98E-02                             | -6.30E-01                                | 1.34E-02                               | 2.90E-03                | 7.00E-06                                 |
| 20  | 1E6                                   | -5.62E+01                                | 1.60E-02                             | 1.98E+00                                 | 1.40E-02                               | 4.45E-03                | 9.83E-06                                 |
| 30  | 0E0                                   | -6.93E+01                                | 2.56E-02                             | -3.94E+00                                | 1.63E-02                               | 2.84E-03                | 7.28E-06                                 |
| 30  | 1E6                                   | -6.24E+01                                | 1.90E-02                             | -5.80E-02                                | 1.53E-02                               | 4.58E-03                | 9.15E-06                                 |
| 50  | 0E0                                   | -8.51E+01                                | 2.68E-02                             | -1.05E+01                                | 1.75E-02                               | 2.91E-03                | 8.20E-06                                 |
| 50  | 1E6                                   | -7.07E+01                                | 1.79E-02                             | 7.69E-01                                 | 1.70E-02                               | 3.78E-02                | 1.47E-04                                 |
| 70  | 0E0                                   | -1.01E+02                                | 3.30E-02                             | -1.71E+01                                | 1.95E-02                               | 3.07E-03                | 7.72E-06                                 |
| 70  | 1E6                                   | -8.15E+01                                | 3.14E-02                             | -7.21E-01                                | 2.06E-02                               | 7.12E-02                | 4.21E-04                                 |
| 100   | 0E0                                   | -1.16E+02                                | 9.07E-02                             | -2.04E+01                                | 6.67E-02                               | 1.62E-02                | 1.30E-04                                 |
| 100   | 1E6                                   | -9.99E+01                                | 2.55E-02                             | -2.92E+00                                | 2.15E-02                               | 1.73E-01                | 4.02E-04                                 |

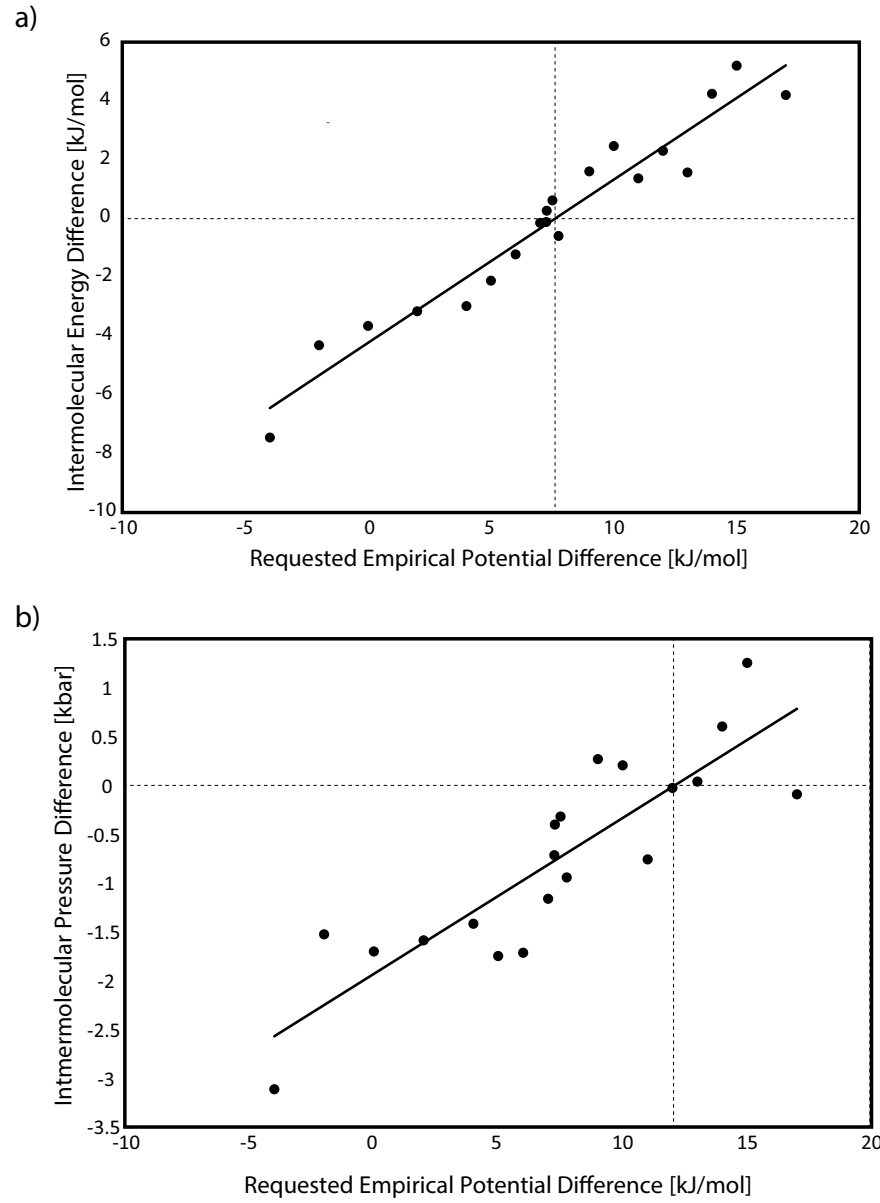


**Figure 4.13:** A comparison of the a) differential intermolecular energy ( $U_i$ ) or b) intermolecular pressure ( $P_i$ ) reported in 500 configurations for difference in requested empirical potential ( $d_{EP} = EP_{bridge} - EP_{bulk}$ ). An equivalency in  $U_i$  is found at an excess energy of 7.5 kJ/mol requested for the bridge simulation. The pressure term requires more energy ~12 kJ/mol requested in order for the bridge simulation to approach that of the reference water. Fit values of  $R^2(a) = 0.9378$  and  $R^2(b) = 0.7498$  also show that the terms are not equivalent in sensitivity to noise

of such trends in terms of the experimental system a check of  $\chi^2$  also shows a quickly decaying quality of fit in the electrically stressed bridge system at  $EP_{req}$  values above 30 kJ/mol. Thus, it is best to restrict our search for energetically equivalent simulations to  $EP_{req}$  below this value. Here we define a new quantity – the excess empirical potential  $EP_{ex}$  – which is simply the additional energy in terms of  $EP_{req}$  necessary to force the two simulations to energetically converge and is defined as

$$EP_{ex} = EP_{bridge} - EP_{bulk} \quad (\text{Eq. 4.5})$$

where  $EP_{bridge}$  and  $EP_{bulk}$  are the requested empirical potentials for the simulation. The response of  $U_i$  and  $P_i$  are different and it is thus expected that the equivalent values for these parameters may lie at different values of  $EP_{req}$ . Figure 4.13a shows the plot of  $dU_i/dEP_{ex}$  yielding an equivalence point between simulations of 7-8 kJ/mol  $EP_{ex}$ . Figure 4.13b likewise shows the response of  $P_i$  to  $EP_{ex}$  and as expected the resulting equivalence point is around 12-13 kJ/mol  $EP_{ex}$ , however, the regression  $R^2$  is not as good for the pressure as for the energy ~0.75 vs. ~0.94, respectively. One possible reason for the observed discrepancy may lie in the method by which these two quantities are calculated [31], [32] and the assumed interactions in the TIP4P/2005 force field [33]. It may also reflect the development of dynamically heterogeneous distributions which is expected when quantum mechanical forces are turned on in the simulation [34].

## 4.4 Excitation of Water by an Electric Field Gradient – change in molecular polarisation

*The electric field in the bridge system is not uniform. Strong field gradients are present at a number of locations and this establishes a spatial non-equilibrium which assures that the liquid will be continually excited and de-excited as the molecules, protons, and proton-holes flow through the gradient regions. This stimulates a change in the molecular polarizability, evolves physical gradients, and restricts the allowed rovibrational relaxation transitions.*

### 4.4.1 Interferometry

In an interferometer the light path is split at the first beam splitter into a reference and test arm, the latter passes through the test section, in this case the cuvette, before both beams are recombined in the second beam splitter. The light passing through the test section suffers a phase lag which is dependent upon the refractive index of the material. Depending upon the phase lag the light will interfere constructively or destructively and creates bright and dark bands or interference fringes. The measurement is line-of-sight, meaning that it is only sensitive to light whose propagation direction (i.e. pointing vector) is towards the detector, off axis or scattered radiation is not detected, and the phase lag is integrated over the path in the cuvette.

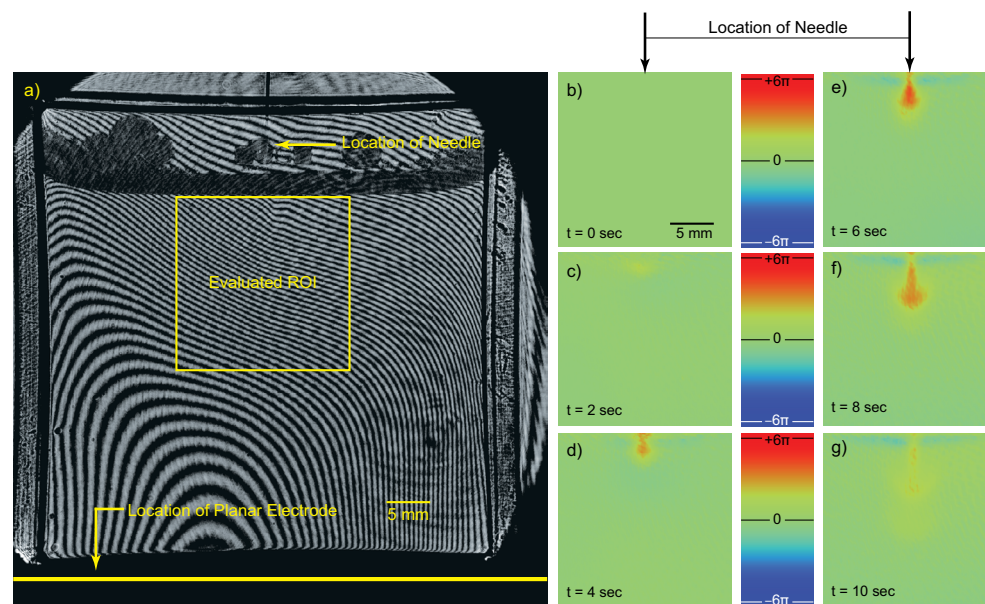


**Figure 4.14: Interferogram of the water filled cuvette and point plane system showing the locations of electrodes and evaluated region of interest (a). Time evolution (panels b–g) for the response of the liquid to from the evaluated interferograms shows the formation of a dense downward jet of liquid (a Woisetschläger jet) constrained between regions of less dense water just below the surface.**

This makes interferometry quite sensitive to local perturbations in the complex dielectric permittivity (i.e. refractive index) of the material under study and provides a measure of the polarizability as well as the dipole number density in the material.

The recorded interferograms clearly show that application of a dense inhomogeneous electric field of the magnitude used in these experiments ( $\nabla^2 E_a \approx 10^{10} \text{ V/m}^2$ ) will generate polarization forces which disturb not only the liquid nearest the point electrode but generate perturbations along the entire air-liquid surface and deep into the bulk. The processed results from the interferometric investigations are shown in figure 4.14. A representative image from a raw interferogram showing the placement of the two electrodes as well as the evaluated region of interest (ROI) is displayed in panel (4.14a). The evaluated data panels (4.14b) to (4.14g) with correction for phase ambiguity (i.e. positive phase shift for increase in density) show that there are several responses of the liquid and that the time evolution of each feature is different. Two major responses will be discussed: surface polarization and downward jets<sup>1</sup>.

1 These jets are hereby named Woisetschläger jets both for their discoverer – Jakob Woisetschläger of the TU Graz – and for the etymology of the name as it represents a clearing cut into the deep woods (*schlag*, from the middle high German word *slac*) by a warrior (*voj*, from old Slavic which evolved into *woiset*). More information on the name and the man is available at <http://ttm.tugraz.at/jw/?seite=wois>

The application of the electric field results in a strong bending of the fringes in the top few millimeters of liquid and likewise the removal of the field causes the fringes to return to their original position. The magnitude of response is dependent upon the surface forces as well as the dielectric properties of the liquid, thus in water even at room temperature the force of the reaction field is much less pronounced and thus harder to evaluate with this method. Surface polarization spreads along the entire surface of the liquid, and it is interesting that in the case of water a region of liquid accumulates in a band that has an apparently lower refractive index (density). This band is visible in the phase images as a blue colored feature that lies in a stable position a few millimeters beneath the surface. The region above it (that is just below the air-water interface) subsequently appears to have a normal number density. This low density band feature is slow to develop and only becomes pronounced several seconds after the field is activated.

The low density band is interrupted in the immediate vicinity of the needle electrode. Here we see that within a very short time ( $<1$  sec) after the field is switched on, a higher refractive index (density) region develops, quite diffuse at first and steadily becoming more pronounced and localized close to the point electrode. The density continues to increase and the region affected shrinks in size until this more dense fluid begins to sink and forms a downward moving jet of liquid. It is a natural assumption to think that this liquid must be denser because it is colder, and indeed this is the case. When the fiber optic temperature probe was placed into the liquid beneath the needle a temperature difference of  $\sim 1^{\circ}\text{C}$  was measured. It is interesting to note that moving the probe further away from the needle did not recover any areas where the water was warmer as one might think to be the case for the band of apparently less dense water just below the surface. So it appears that while temperature does play a role in the phenomenon it is not the only parameter being affected by the field.

It should be noted that the change in the electric field plays a role in the observations. **Switching the electric field on or off yields the most dramatic response and with regards to the jets the change in electric field state (i.e. on or off) elicits the same response.** In the steady state, the dynamics are far more irregular with jets coming and going, and is likely due to instabilities in the system caused by temperature driven dynamics or ionic wind along the surface. There is a clear difference, however, between the jets which form during a change in the field and those that are present during steady state conditions. The later tend to move slowly back and forth along the surface at a rate of  $\sim 0.2 - 0.5$  mm/s whereas the jets produced by the voltage step form directly below the needle and do not drift along the surface but rather propagate downward  $\sim 0.8$  mm/s and dissipate within 10 seconds. Additionally, the jets present during steady state conditions have a weaker effect on the optical phase rarely exceeding  $+3\pi$  radians compared the  $+6\pi$  radians shift when the field change is applied.



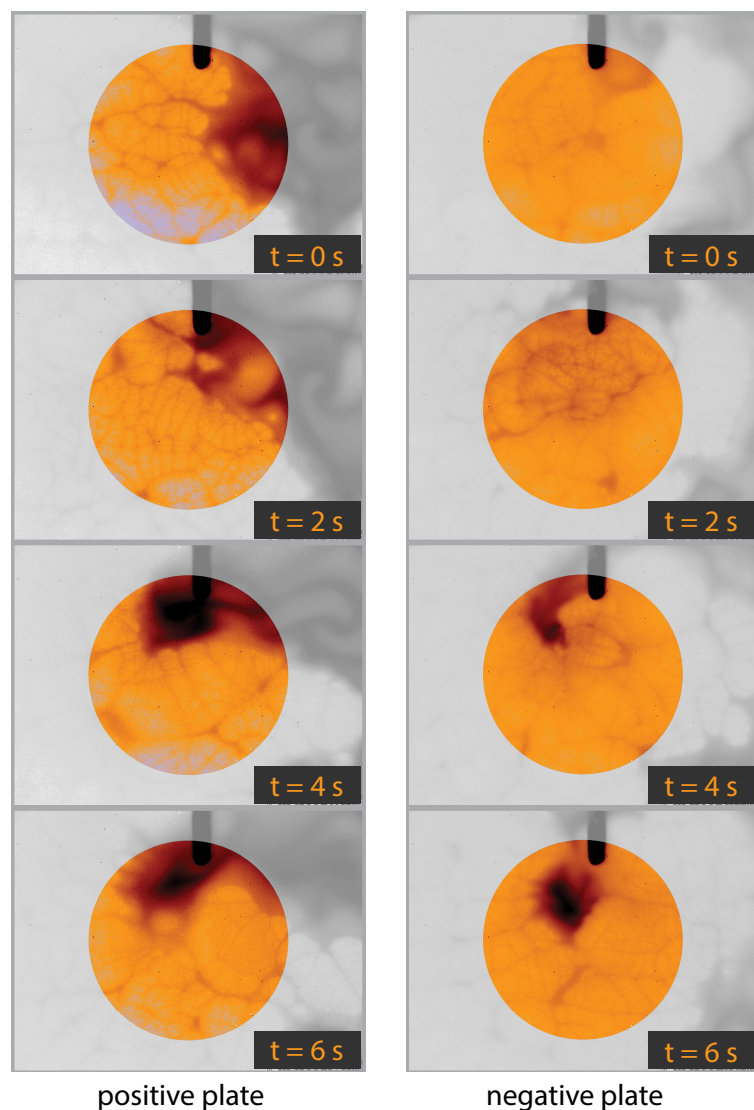


**Figure 4.15** Thermographic images of the surface of water (70 °C) in the point plane electrode set-up. The scale ranges from black (cold) to white (hot) with an orange overlay to enhance visibility. Both electrical polarities were investigated, plate electrode positive polarity (left), and negative (right). The time in seconds is shown in the lower right corner of each frame.

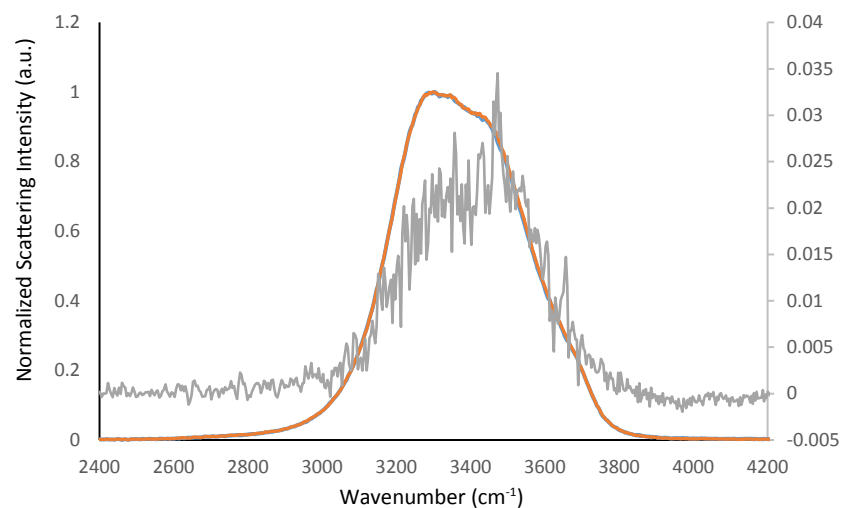
#### 4.4.2 Thermographic Imaging of the Polarized Surface

Thermal imaging of the water surface (Fig. 4.15) corroborates the interferometric information. The needle is in air a few mm above the liquid surface. Upon a change in the field gradient (either switching on or off) there is first a brief release of heat from the surface followed by the development of a stable cool spot. Both electrical polarities produce this response. The motion of the liquid can be seen as distortions in the boundaries between more or less emissive regions. There is a stable downward flow from the surface down into the jet. However, the liquid surface loses emissive energy quickly upon entering the area focused under the needle. The flow of the liquid into the region of the highest field gradient is caused by the dielectrophoretic forces which act asymmetrically along the direction of flow further accelerating the interacting dipoles towards the region of the greatest field intensity. Through viscous coupling a volume of liquid cannot remain in a fixed position and the system establishes a stationary flow regime. The thermal gradient in turn also develops an electric field gradient which can in the system studied here achieve an order of magnitude of nearly the same order of magnitude as that induced by the electrodes [35]. The resulting thermoelectric effect generates a semi-open feedback loop and fluid elements flowing in will exchange their thermal state for electrical polarization which will in turn transform the polarization to velocity. This relationship will be further discussed in §5.6.

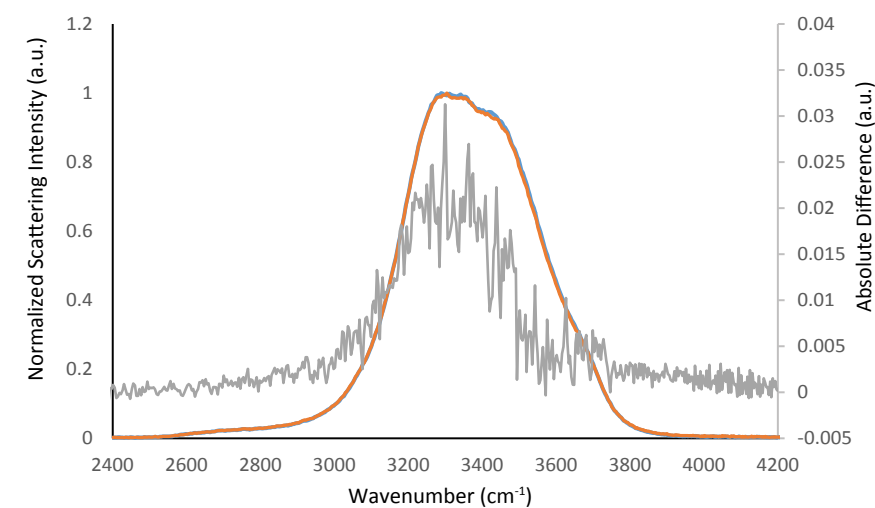
#### 4.4.3 Mid-Infrared Raman Imaging Spectroscopy – polarizability and extinction ratio

In a similar manner to interferometry Raman spectroscopy also probes the electric polarization of molecules – the difference is in the spatial resolution. Unlike the macroscopic refractive index interrogated by interferometry the Raman bands are a probe of the molecular transition dipole population distribution in the focal region of the laser beam. The connection between the vibrational line shape and molecular environment which make up these bands is an ongoing effort [29], [36] and like most spectral features in condensed matter is obscured by inhomogeneous broadening [37], [38]. The vibrational modes of water are both infrared and Raman active. The shape of these bands are complex as expected for condensed matter and have been extensively discussed elsewhere [39]–[41] and will be summarized here. The Raman scattering spectrum provide ensemble information on the coupling between vibrational oscillators in the liquid. The isotropic spectrum has a somewhat complex shape which has been the subject of much scrutiny. Suffice it to say that those oscillators with lower wavenumber (3250  $\text{cm}^{-1}$ ) on the red-side of the distribution correspond to vibrational oscillators which are damped by interactions with their local environment. Those oscillators with less degrees of interaction have higher frequencies (3490  $\text{cm}^{-1}$ ) and the small shoulder on the blue-side of the distribution at 3650  $\text{cm}^{-1}$  has been shown through computer simulation

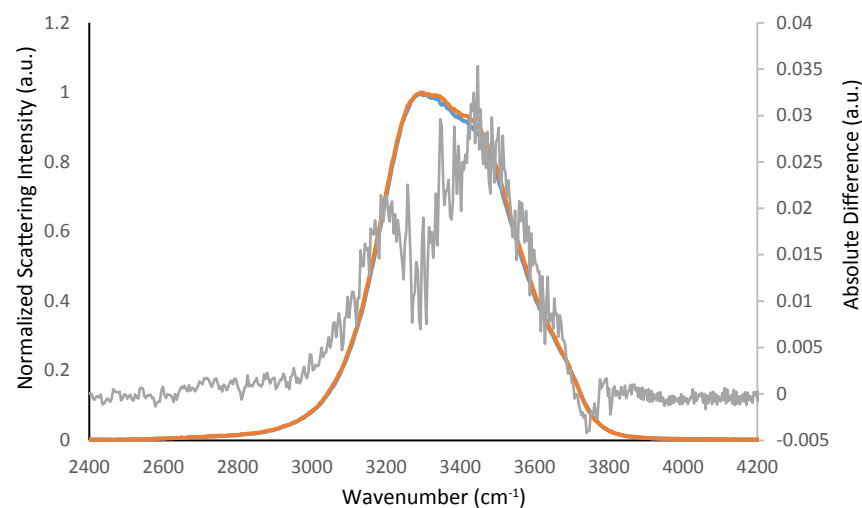
a) Laser Beam Parallel, Needle in Air



c) Laser Beam Parallel, Needle Submerged Below Laser Beam



b) Laser Beam Parallel, Needle Submerged Above Laser Beam



d) Laser Beam Perpendicular, Needle Submerged

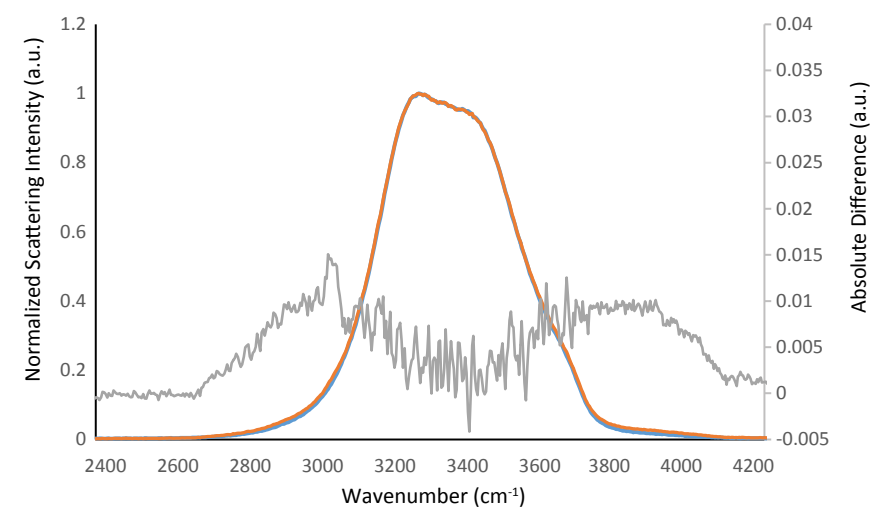


**Figure 4.16** Normalized isotropic Raman spectra for the different measurement cases. The laser beam was oriented either parallel to the liquid surface (a-c) or perpendicular (d). In the parallel case, the laser beam was 5 mm below the surface. The needle depth was also varied so as to be (a) 2mm above the water surface, (b,d) 4 mm or (c) 6 mm below the water surface.

The spectrum collected when 20kV is applied (orange line) and when no voltage is applied (blue line) are subtracted to yield the absolute difference spectrum (grey line). The normalized scattering intensity and the absolute difference is given by the left and right ordinate scales respectively.

using experimental data as fit to belong to free oscillators which behave as single-particles [42]. The lifetime of free particles is considered to be quite short lived.

The polarized Raman spectrum is obtained when the analyzer and incident electric field are aligned. Similarly when the analyzer is rotated perpendicular to  $E_0$  the anisotropic depolarized spectrum is recorded. The isotropic spectrum can be recovered from the measured spectra via:

$$I_{iso}(\omega) = I_{VV}(\omega) - \frac{4}{3}I_{VH}(\omega) \quad (\text{Eq. 4.6})$$

Whereas, the anisotropic spectrum is contained entirely in the depolarized spectrum.

The Raman active bands in water can be attributed to a number of physical quantities, fundamental to all is the electric polarizability of the molecule which is probed directly by the electric field of the off-resonant incident linearly polarized pump radiation. The decay of the induced transition dipoles results in a frequency shifted Raman emission which contains contributions from the isotropic and anisotropic polarizabilities.

Three experimental variables in addition to the scattering polarization were examined:

1. needle position relative to the water surface
2. laser beam orientation relative to the liquids surface, and
3. the applied DC electric field either on or off.

The isotropic Raman spectra for each of the experimental configurations are shown in figure 5 and reveal small changes in intensity when voltage is applied. Each of the 25,600 single spectra are background subtracted, summed and then intensity normalized; providing the cumulative polarizability response of water to steady state electric field. When (4.16a) the needle is in air ~2 mm above the liquid surface and the laser beam parallel the least amount of change in the spectrum is observed. When the needle is subsequently submerged 4 mm below the liquid surface (4.16b) so that the laser beam is now probing the area 1 mm deeper than the needle the intensity increases most. Submerging the needle further (4.16c) to a depth of 6 mm – 1 mm deeper than the laser beam – reduces the scattering intensity of the central frequencies. This contrasts the response when the laser beam is perpendicular to the liquid surface (4.16d) and the needle is submerged 4 mm now there is no observable change in the central frequencies but rather enhancement in both wings of the isotropic spectrum as a result of the applied voltage.

In order to recover changes in the frequency distributions of the probed chromophores in response to the applied field, the absolute difference spectrum (grey solid line) was calculated and plotted on the second y-axis in figure 4.16a-4.16d. In both panels (4.16a) and (4.16c) the shape is similar and is what would be expected given a small shift in temperature [43]. The peak frequency of the difference spectrum shifts more towards the blue side (4.16a) when the

needle is in the air indicative of heating, whereas the red shift when the needle is submerged (4.16c) fits in the case of cooling. The spectral shape of (4.16b) and (4.16d) have a bimodal distribution although (4.16b) is much narrower than (4.16d). These spectra are obtained from areas where the grad  $E_a$  is the strongest. In the case of  $E_0$  parallel to  $E_a$  ( $E_0 \parallel E_a$  4.16b) the residual difference resembles a superposition of those from (4.16a) and (4.16c). Whereas when  $E_0$  perpendicular to  $E_a$  ( $E_0 \perp E_a$  4.16d) there is a clear enhancement in both the red and blue wings of the spectrum. This situation is perplexing as it would appear to indicate that competing energy modes – cooperative and single particle vibrational relaxation – are enhanced rather than the expected behavior where the population density shifts from one mode to the other. This indicates a departure of the system from the ground equilibrium state.

In order to better ascertain the positional dependency of these observed changes the spectral imaging maps are examined in figures 4.17 where  $E_0 \parallel E_a$  and figure 4.18 where  $E_0 \perp E_a$ . The maps are the average of 50 images filtered using an asymmetric, 2D, third order, Savitzky-Golay filter to reduce spurious noise and intensity fluctuations between adjacent spectra. The resulting maps without applied voltage are then subtracted from those with voltage for both the isotropic and anisotropic polarizability tensor and are displayed in the panels right and left, respectively, of center. The resulting maps provide an image of the difference in the molecular polarizability density of states caused by  $E_a$ . The displayed orientation of the maps matches that of the laser beam (and entrance slit) so that in figure 4.17 distance is plotted along the abscissa whereas in figure 4.18 it is plotted along the ordinate. This is done to reduce confusion regarding relative orientations between configurations. The experimental configuration used is illustrated in the central panel for each row. The needle electrode is the solid black line whose top location is highlighted within a circle and the height indicated by the dashed line. The red solid line indicates the laser beam location, and the grey square the area imaged, however, only the illuminated volume of the beam is sampled and additional spatial filtering is provided by the spectrograph entrance slit. The spectra are mapped over the same frequency range ( $2400 \text{ cm}^{-1} - 4200 \text{ cm}^{-1}$ ) as is done throughout the paper. When the beam is parallel to the surface we have the opportunity to examine the lateral dissipation of any induced polarization. The location of the needle is shown with a black dashed line. Adjacent to each spectral map is an additional panel where three spectra are displayed that represent the summed difference intensities from one of three regions on the map. The color of the line corresponds with the highlight color on the distance axis and follows the progression red, green, blue moving successively further from the needle electrode. The red curve corresponds to the region closest to the needle in all measurements.

Let us first examine the results when  $E_0 \parallel E_a$  shown in Figure 4.17. The central frequencies of the anisotropic polarizability are suppressed when the needle is in air (position I) and the voltage is applied. The response is most strongest closer to the needle as can be seen in the red spectrum. Once the needle is submerged (positions II and III) this response is inverted, the central frequencies are now enhanced. When the beam is nearest the needle (position II) the



response is the weakest, the extracted signal is close to the noise floor, and there appears to be no spatial variance. With the needle deeper (position III) the response becomes stronger, the voltage enhances the anisotropic polarizability. Thus, central frequencies of the anisotropic response appear to be tuneable by varying location of a dense inhomogeneous electric field with respect to the liquid surface.

The isotropic polarizability is much stronger than the anisotropic and it is thus better suited for observing changes due to polarization. When the needle is in air (position I) the blue side of the spectrum shows strong enhancement similar to what is found in figure 4.16a and this is again strongest nearest the needle where the field density is highest. The blue curve shows a bimodal distribution enhancement furthest from the intense field.

Submerging the needle has an exceptionally strong effect on the isotropic spectrum when the beam is just below the needle (position II). This is the area where the magnitude of  $E_a$  is the greatest and the effects of local refractive index change may play a non-trivial role in the resulting spectral maps. Indeed the intensity is found to fall off quite quickly once the beam passes the needle's position. Potentially trivial causes of the observed spatial changes in the recovered intensity can be ascribed to either the deflection of the beam due to local refractive index changes associated with the cold jets or geometric misalignment. However, it is expected that such changes in scattering due to the propagation of the pump radiation would also be observed in the anisotropic spectrum (Fig. 4.17 left panels) which it is not. Additionally, the absorption cross section and expected scattering losses over the mm length scale are considered too small to play any significant role. The overall enhancement of intensity is strongest before reaching the needle and is more than 4x stronger than in the case of position I. The relative change of the mode density is more symmetric than in position I. With the needle fully submerged (position III) the isotropic modes are now suppressed furthest from the needle and weakly enhanced closes to the needle. The spatial image is also quite intriguing as nearest the needle the intensity difference becomes weakly positive. This may be due to the reflection of scattered radiation back towards the detector by the needle which was placed behind the laser beam. The red curve shows what would be expected for a decrease in temperature – namely the enhancement of the low frequency collective mode and loss of high frequency single-particle modes.

Rotating the laser beam perpendicular to the surface also changes the orientation of the probing electric field,, the results are shown in figure 4.18. The laser beam was focused next to the needle electrode and the region of interest positioned so that the needle was less than 1mm below the top of the frame thus minimal optical interaction is expected with the needle and the scattered radiation. In both the anisotropic and isotropic spectral maps there is a clear effect of the electric field on the scattering intensity. **The greatest influence is found where the electric field gradient is the strongest. While the central frequencies of the isotropic spectra are clearly depleted by the field, those oscillators with frequencies at the**

**extremes of the bandwidth are enhanced** in agreement with figure 4.16d. This observation brings back the question of a bimodal distribution in the vibrational band structure of water under the influence of an inhomogeneous field. An estimate of population size, taken from the integrated intensity values, that is affected by the field shows this number to be quite small ~1% of the probe volume which corresponds to approximately  $7 \times 10^{16}$  oscillators.

The influence of temperature on the Raman spectra of water in the presence of inhomogeneous electric field gradients bears further investigation, however, direct measurement of the region directly beneath the needle using the fiber optic temperature probe found the temperature decreased ~0.3°C when the inhomogeneous field was applied to 20°C water.

In summary, the applied inhomogeneous electric field redistributes the vibrational population of ambient water. The effect is dependent upon the magnitude of the field gradient. The polarization response tends toward a bimodal distribution where the gradient is strongest. Where the field is weaker temperature effects become apparent in the spectra. This is consistent with the anatomy of the flow dynamics observed from interferometry. A locally focused region of cooler liquid confined below the needle electrode moves downward and dissipates several tens of mm below the surface.

#### 4.4.4 Mid-Infrared Emission Imaging

Fig. 4.19 shows the mid-IR emission spectrum of bulk water at 37°C and 47°C compared to black body emission of these temperatures. The emission has a broad maximum centered at ~2150cm<sup>-1</sup> (peak **a**). Peak **b** is the unresolved envelop of the C-O stretching vibration mode of molecular CO<sub>2</sub> at 2350cm<sup>-1</sup> combining with rotational modes [26]. Peak **c** shows the resolved combination bands of the H-O-H bending mode with rotational modes of molecular H<sub>2</sub>O [27-29].

Fig. 4.20 displays a comparison between the water bridge emission and bulk water at 37°C and 47°C, respectively. The thermographic and the optical images of the water bridge in comparison with bulk water are given in Fig. 4.21. All emission curves were scaled and offset-corrected. The bridge water emission curve was scaled so that it overlapped with the 37°C bulk water curve in the 8-12µm region, resulting in a gross overlap with the emission curve of water at 47°C in the 3-5µm region. This effect is also visible in the thermographic imagery in Fig. 4.21. Whereas bulk water shows the same temperature in both regions (50°C), the bridge appears brighter (equivalent to 47°C) in the 3-5µm region and darker (equivalent to 37°C) in the 8-12µm region.

In order to rule out chemical reactions with the atmosphere as source of the additional IR peak, an additional experiment was performed: The IR emission was recorded thermographically in the 3-5µm region both in a normal air atmosphere and in pure nitrogen (data not shown). No significant differences were found.

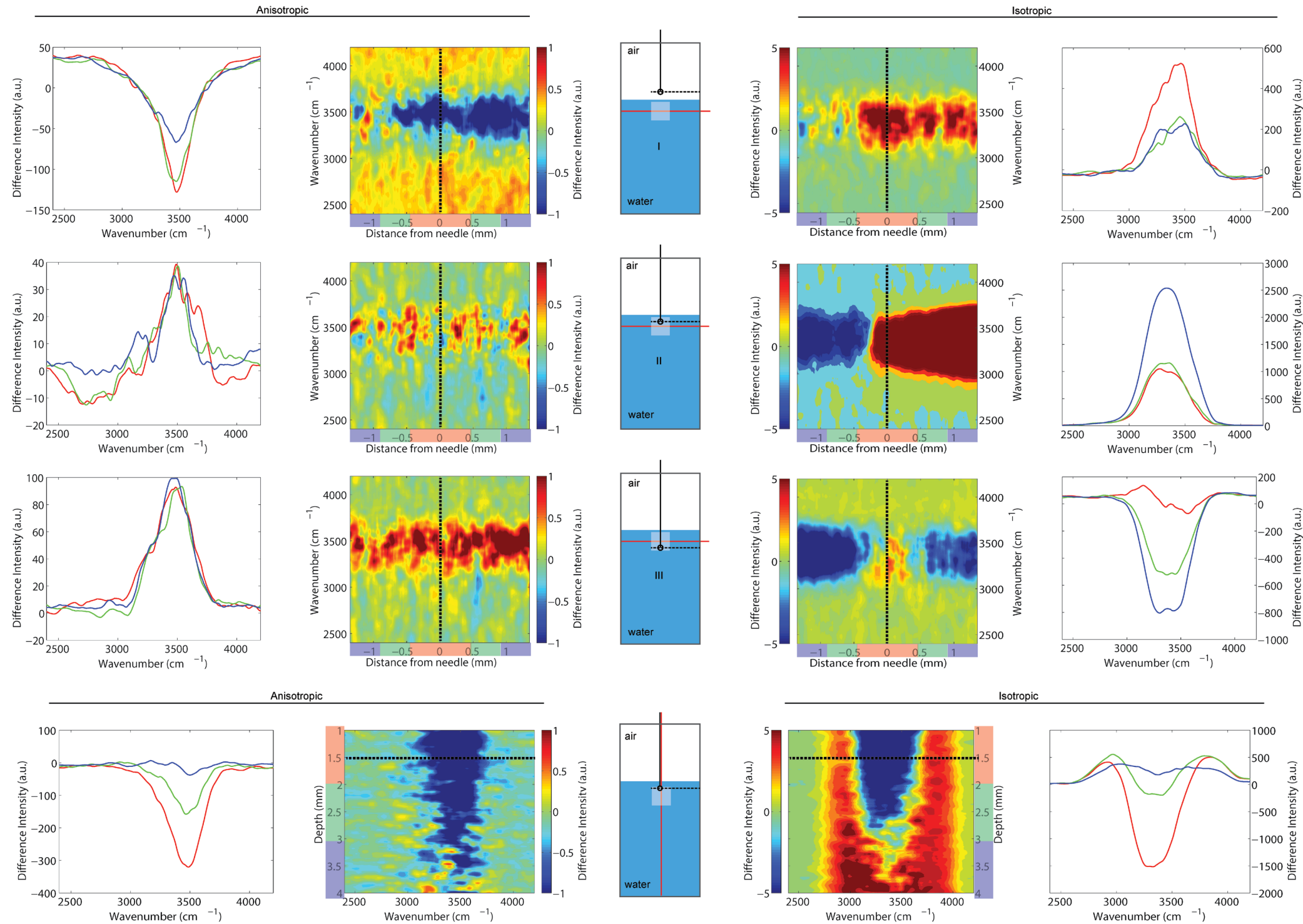
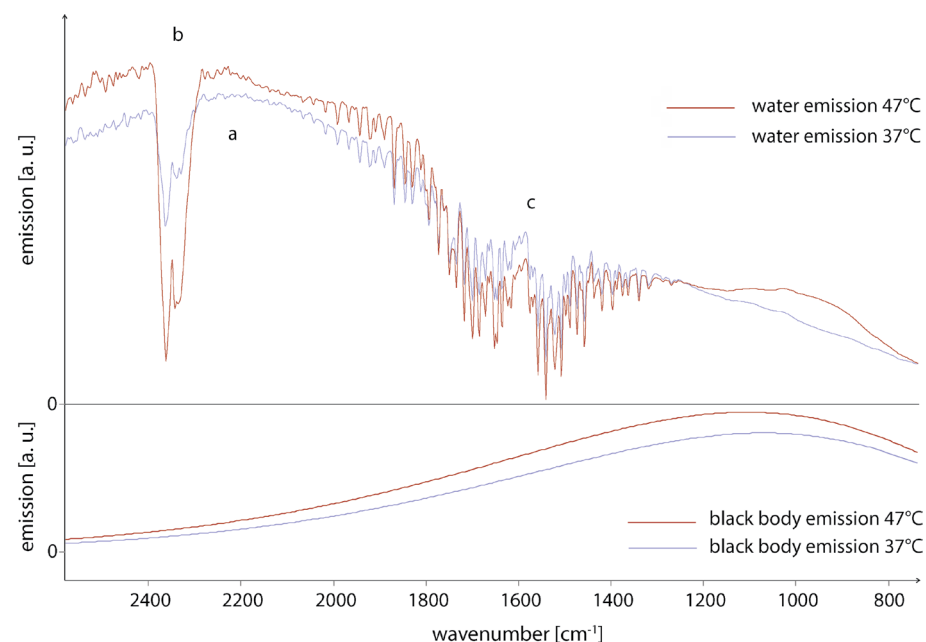


Figure 4.17 (opposite, top three rows) Raman spectral imaging with the laser beam parallel to the liquid surface. The center diagram shows the orientation of the needle (black line), the laser beam (red line), and the imaged region of interest (grey square). Three different needle depths are examined and move progressively deeper with each row. Difference spectral maps obtained by subtracting the spectra with (20 kV) and without (0 kV) electric field with the beam parallel to the liquid surface. The anisotropic map (left) and isotropic map (right) have different intensity scales. Three equal area segments from the maps are binned together to produce the line plots and are show as a shaded overlay on the abscissa of the 2D plots. The region closest to the needle corresponding to the red spectrum, the region flanking this to the left and right in green, and finally the region furthest from the needle in blue.

Figure 4.18 (opposite, bottom row) Raman spectral imaging with the laser beam perpendicular to the liquid surface. The center diagram shows the orientation of the needle (black line), the laser beam (red line), and the imaged region of interest (grey square). Difference spectral maps obtained by subtracting the spectra with (20 kV) and without (0 kV) electric field with the beam parallel to the needle. The anisotropic map (left) and isotropic map (right) have different intensity scales. Three equal area segments from the maps are binned together, according to the color overlay on the ordinate, and give the extracted spectra shown in the line plots. Red curves are the shallowest and closest to the needle, blue the deepest and furthest from the electrode.



**Figure 4.19** Infrared emission spectra of liquid, bulk water at 37 and 47°C compared to black body emission curves of the same temperatures. The letters signify the different peaks: a- broad emission peak centred around  $2150\text{cm}^{-1}$ , b-  $\text{CO}_2$  absorption peak, c- water vapour absorption lines arising from  $\text{H}_2\text{O}$  molecules in the air above the water surface.

#### 4.4.4.1 Bulk water emission

Bulk water closely resembles a black body when keeping in mind that the Planck formula is used to calculate the radiation intensity of a spectral region and that the peak position is somewhat arbitrary, depending on the physical quantity used during integration [30]. In Fig. 4.19, the Planck formula was integrated using wavelengths (in  $\mu\text{m}$ ) and afterwards converted to wavenumbers (in  $\text{cm}^{-1}$ ). The intensity increase from 37°C to 47°C for a black body is  $\sim 22\%$  (whole spectral range); when looking at a region without an absorption peak water shows a similar behavior. On the low-energy end (e.g.  $700 - 1180\text{cm}^{-1}$ ) the intensity increases by 22% as well, and at the high-energy end of the spectrum ( $2400 - 2640\text{cm}^{-1}$ ) the increase amounts to 19%.

The emission of water exhibits a broad maximum at  $\sim 2200\text{cm}^{-1}$ , always keeping in mind, however, that the spectra as shown are obtained from a ratio of sample and background spectra, both represented by Planck radiation curves. Whilst resembling black body concerning the continuous emission intensity, water molecules vibrate at quantized levels, giving rise to narrow emission and/or absorption bands [31,32]. When looking at water

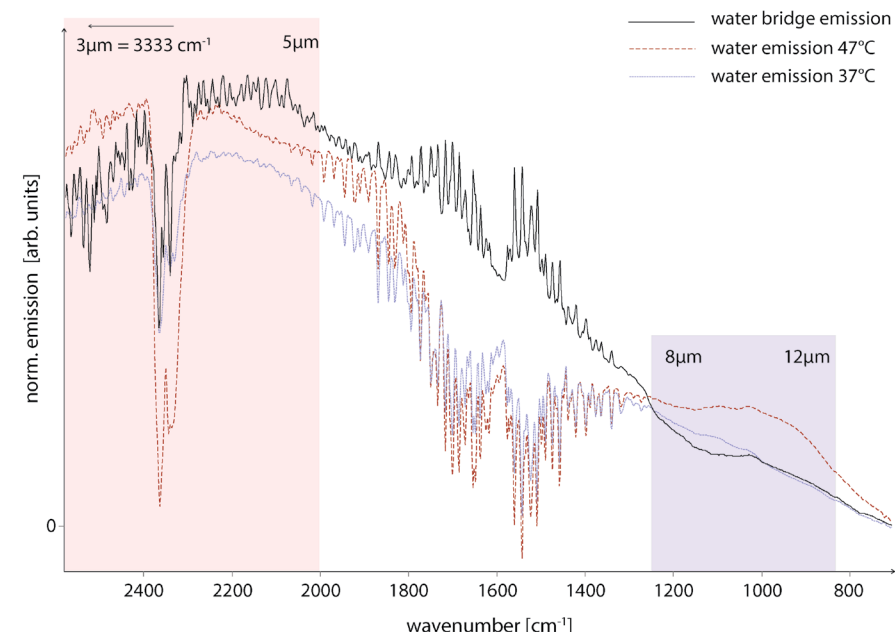


**Figure 4.20** Comparison of the water bridge emission with water emission of 37°C and 47°C, respectively. The shaded areas mark the sensitivity ranges of the thermographic camera (3-5  $\mu\text{m}$  and 8-12  $\mu\text{m}$ ).

absorption spectra, the band closest to the  $2200\text{cm}^{-1}$  emission band is at  $\sim 2150\text{cm}^{-1}$ . It can be assigned either to a combination of the bending and libration modes 33,34 or to the third overtone of the libration band [31]. It is weak in absorption but appears to dominate the emission spectrum as evidence by Fig. 4.19. Due to the broadness of this emission band, it is certainly composed of all other possible modes and their overtones, dominated by librational modes of the ensemble of water molecules in the liquid state. The libration or “hindered rotation” originates from the fact that the water molecules are restricted in their motion by their neighbors. Whereas bending or stretching are vibrations of a single molecule, the librational modes require intermolecular forces – otherwise the molecule would freely rotate. Within the hydrogen-bonded network any (vibrational) motion of a single water molecule will inevitably cause the surrounding water molecules to respond, thus any vibration of one molecule will cause librations in the surrounding molecules, which will again cause librations. It has been suggested that vibrations of the water molecules are coupled to some extent [21], but it is expected that such domains would be microscopic and the water molecules around them would again respond via librational movements. Therefore, in the emission spectrum, the vibrational energy within water will assert itself mostly as the form of librational modes.

4.4.4.2 Water bridge emission

The bridge water emission spectrum differs from the emission of bulk water in two aspects: (i) the emission intensity is higher in the 3-5 $\mu$ m range when compared to that of bulk water at 37°C, and (ii) the width and/or position of the emission peak at  $\sim$ 2200 $\text{cm}^{-1}$  is shifted compared to that of 47°C water. Its broad maximum lies at 2150 $\text{cm}^{-1}$ , exactly at the same position as the corresponding absorption peak. Two Gaussians are fitted into the emission curves (fitting region 1800-2613  $\text{cm}^{-1}$ ). The CO<sub>2</sub> absorption double peak is approximated by a single Gaussian. The fitted Gaussians are given in Table 4.4.

Whereas the actual boundaries of the broad peaks cannot be seen, the data at hand indicates that the water emission is somewhat ( $347 \pm 45\text{cm}^{-1}$ ) broader than the water bridge emission (see Fig. 4.22). **This suggests that the probability density function is red-shifted and narrower in the water bridge, indicating that the number of spectral diffusion modes is reduced.** The described effect would cause a slightly preferential orientational motion of the water molecules compared to the motions in bulk water.

Table 4.4: Data for the peak fitting shown in Fig. 4.22.

| Peak                                    | Position [ $\text{cm}^{-1}$ ] | Width [ $\text{cm}^{-1}$ ] | Correlation ( $R^2$ ) |
|---|-------------------------------|----------------------------|-----------------------|
| water 47°C CO <sub>2</sub> absorption   | $2346.53 \pm 0.55$            | $57.04 \pm 1.40$           |                       |
| water 47°C emission                     | $2314.34 \pm 8.02$            | $1518.84 \pm 44.76$        | 0.92                  |
| water bridge CO <sub>2</sub> absorption | $2356.84 \pm 1.27$            | $40.31 \pm 3.11$           |                       |
| water bridge emission                   | $2166.16 \pm 4.44$            | $1171.85 \pm 22.43$        | 0.84                  |

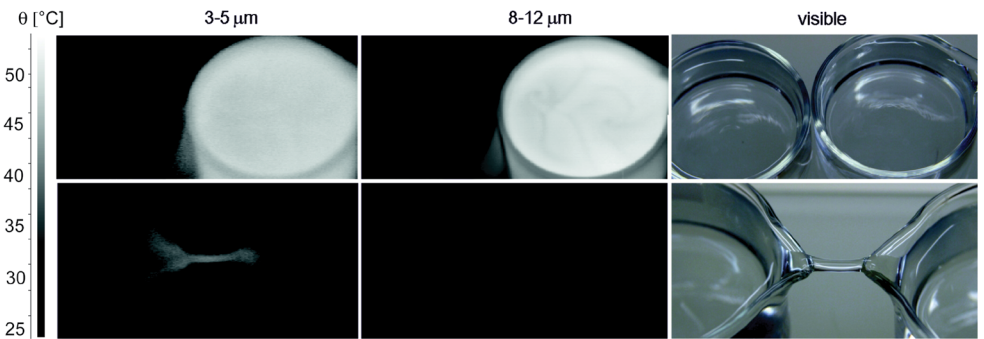


Figure 4.21 Upper row: Thermographic images at two IR wavelength ranges and photographic image in the visible range of two beakers with bulk water at 27°C (left beaker) and 50°C (right beaker); Lower row: same images of the water bridge. The radiative temperature of the bridge appears as 47°C when recorded at 3-5 $\mu$ m and as 37°C when recorded at 8-12 $\mu$ m.

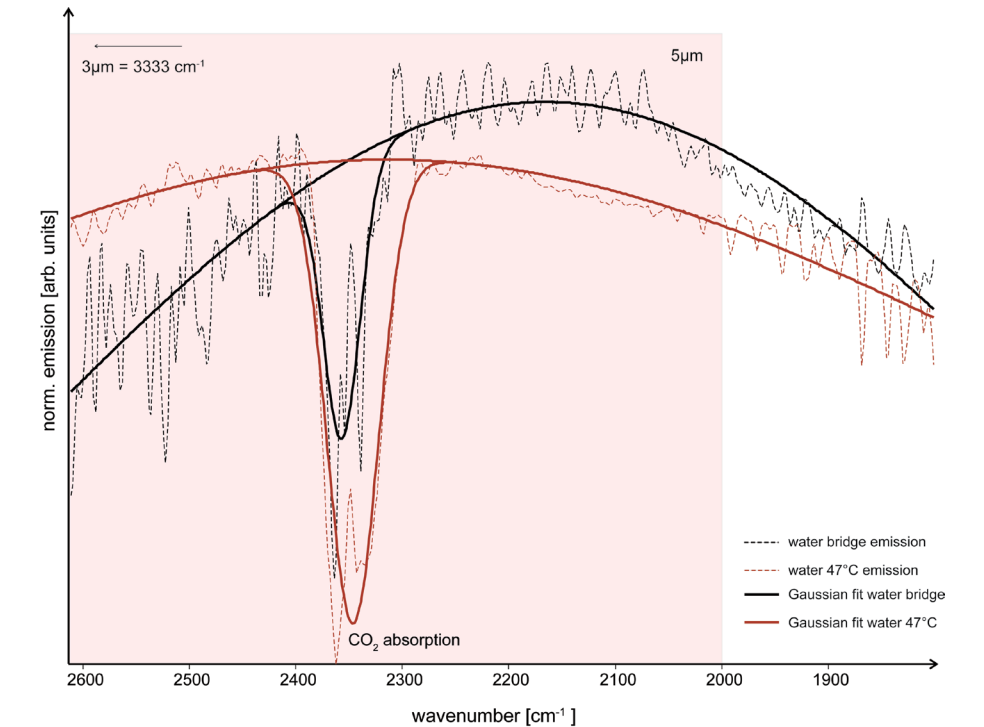


Figure 4.22 Water bridge and water emission (47°C) spectra fitted with two Gaussians using GRAMS AI software. The spectra are fitted with two Gaussians each, one for the CO<sub>2</sub> absorption and one for the emission. The reddish area shows one sensitivity range of the thermographic camera (3-5  $\mu$ m); the data on the fitted peaks is given in Table 4.4



## 4.5 Proton transport in water bridges – Quantification by QENS

The proton mobility in the water bridge is quantified and compared to the reported literature values. The derived mobility corroborates the findings thus far presented and shows that electrically stressed liquid water can support a highly mobile proton population.

Figures 4.23 and 4.24 show the raw data of the water bridge and water in an Al cylinder for both configurations in terms of  $S(\omega)$ , thus an addition of all Q data of the evaluated angles as shown in the insets in both figures, respectively. The additional peak on the right end of Fig. 4.24 is due to an adventitious reflection from a metal surface of the set-up.

When the data was fitted using Eq. 3.32, the elastic part measured from the water in the aluminum cylinder was negligible (peak fitting resulted in 0 intensity for the delta function for the small angle geometry), whereas for the water bridge data, this was not the case. Here, the data could be fitted better with a contribution of the delta function with values between 5% and 30% of the total intensity, representing the immobile proton population. Since the present data quality does not justify a more detailed analysis or interpretation of these values, future work is needed to address this issue with an improved experiment at a different instrument.

Figure 4.25 shows an exemplary fit of an  $S(Q, \omega)$  data set for one specific angle for the water bridge data with a Lorentzian and the remaining elastic contribution.

In order to learn about the second population the HWHM of the Lorentzian was further analyzed. **The Lorentzian describes the contribution of the quasi-free, quantum-mechanically mobile protons (“excess protons” on a proton channel).** Their movement through the oxygen lattice is approximated by the random jump diffusion model, where the protons movements are considered as transitioning between vacant lattice sites, with the “jump”-time assumed to be very short, near-zero, and the proton diffusion described in terms of a residence time  $\tau_0$  and a translational diffusion coefficient  $D$ :

$$\Gamma(Q) = \frac{DQ^2}{1 + DQ^2 \tau_0} \quad (\text{Eq. 4.7})$$

Normally this model is used to describe the movement of water molecules in the bulk and can thus be also applied to the data gathered from the water in the Al cylinder, keeping in mind that in this case there is only one proton population with a strong intramolecular bonding, and a weak intermolecular interaction. In other words, in bulk water, the vast majority of the protons are staying with a water molecule, and their diffusion constant is commonly associated with that of the water molecules (at ideal conditions only  $10^{-7} \text{ mol / L} = 10^{-7} \text{ mol / 55.5 mol} = 18 \text{ ppb}$  of the  $\text{H}_2\text{O}$  molecules are dissociated).

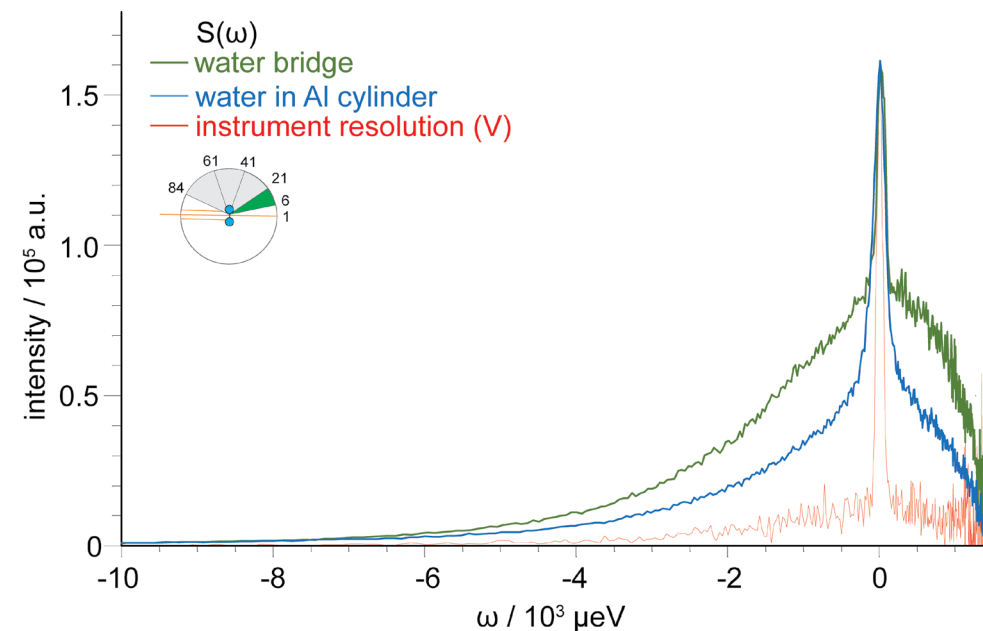


Figure 4.23  $S(\omega)$  of the water bridge and water in an Al cylinder, “smaller angles” geometry, and a vanadium (V) rod showing the instrument resolution.

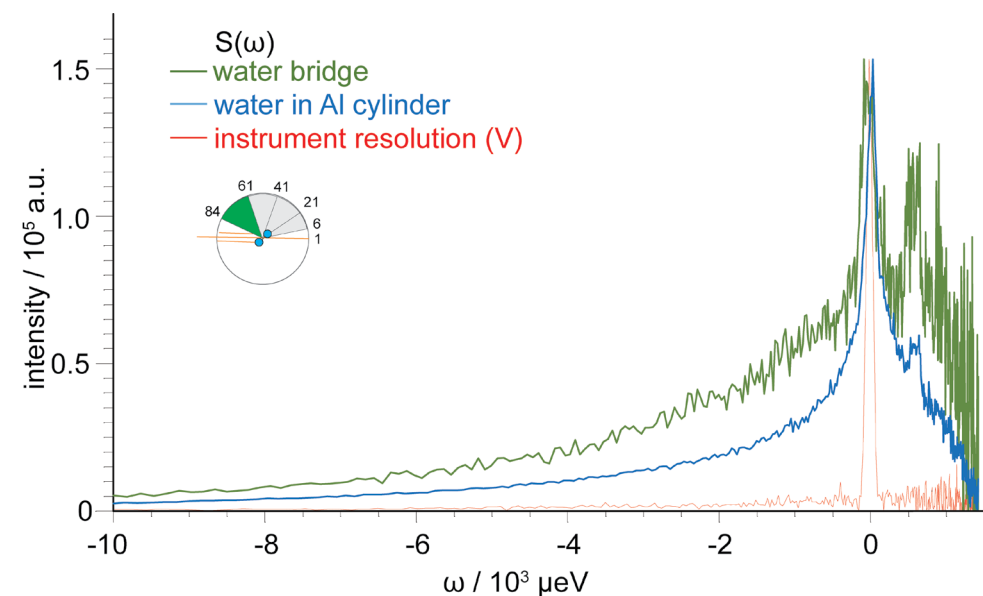


Figure 4.24  $S(\omega)$  of the water bridge, water in an Al cylinder, “larger angles” geometry, and a vanadium (V) rod showing the instrument resolution.. The additional peaks on the right end are due to reflections from a metal surface of the set-up.



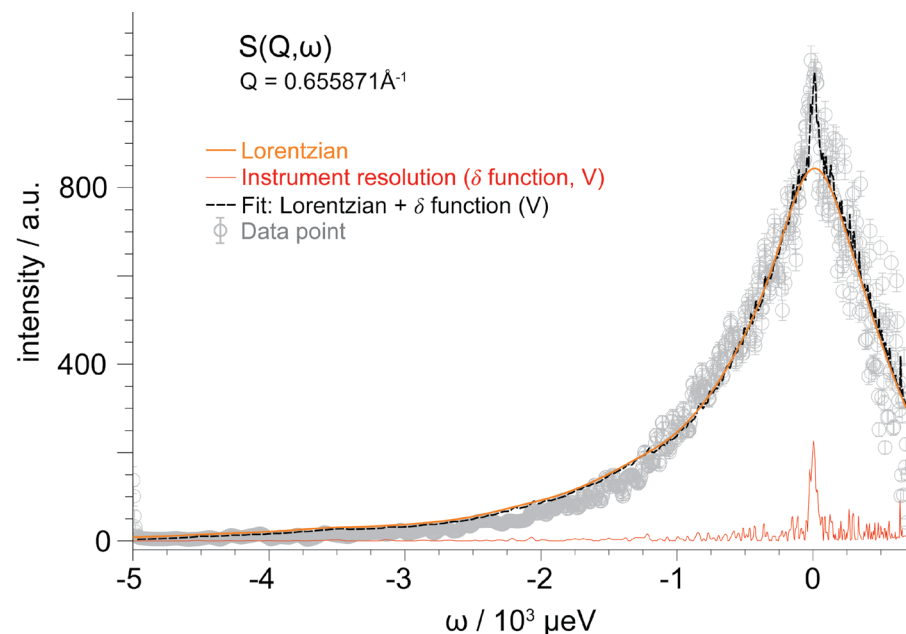


Figure 4.25  $S(Q, \omega)$  of the water bridge for  $Q=0.655871 \text{ \AA}^{-1}$ . The grey dots are the original data points. Black (Lorentzian) and red curve (elastic line) are the two components of the fit (orange curve).

Moreover, the mechanism normally accepted to take into account pH is not based on molecular dissociation. Instead, it is based on “hopping”, the possibility for a hydrogen engaged in a bond to jump from one to another of the two minima, forming for a short time the two ionized species  $\text{OH}^-$  and  $\text{H}_3\text{O}^+$ . This Grotthuss mechanism [20] describes the motion of this “defect” without any motion of the molecules, even not of the hydrogen atom at the origin of the process, because it may be that it is another proton that jumps next.

Figure 4.26 shows water at room temperature in the Al cylinder to test the influence of the water bridge geometry on the experimental results. The recorded data are compared to the predictions of the random jump model for water at room temperature ( $20^\circ\text{C}$ ) using the optimum test cell geometry with  $D_{20^\circ\text{C}}=2.22 \times 10^{-5} \text{ cm}^2\text{s}^{-1}$  and  $\tau_{0,20^\circ\text{C}}=1.25 \text{ ps}$ , respectively [17]. Under optimum conditions, the data calculated using this model (blue line in Fig.4.26) matches with the experimental data almost exactly [12]. The deviations observed when probing the water in the Al cylinder (bridge geometry) are what is to be expected under the experimental circumstances as explained above, and they tell the observer which deviations are to be expected from the water bridge geometry: increased values due to multiple neutron scattering, and an increasing spread of with increasing  $Q$ . The translational diffusion coefficient and the residence time derived from these values are, naturally, higher.

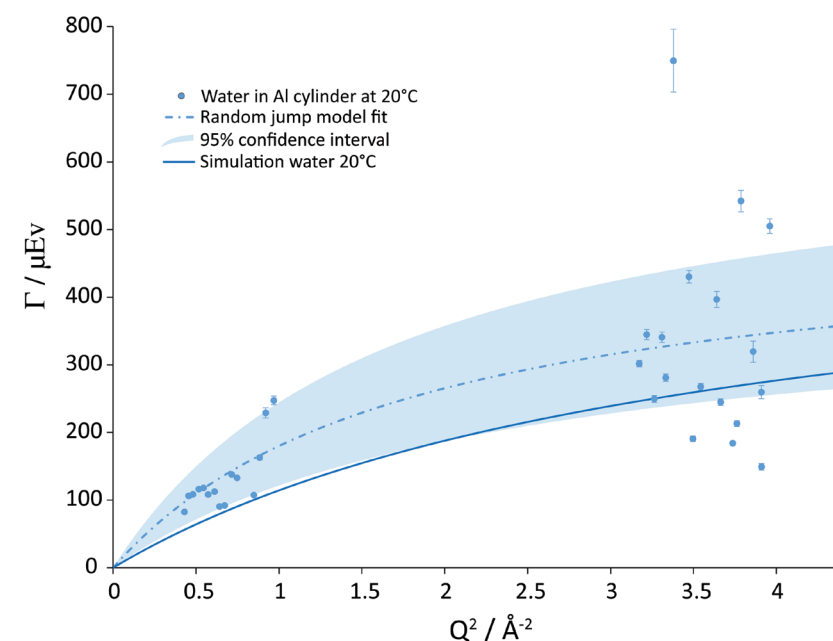


Figure 4.26 Quasi-elastic scattering data of water in an Al cylinder placed at the exact position of the floating water bridge compared to fitted and published [17] random jump curves of water measured at optimum conditions using  $D_{20^\circ\text{C}}=2.22 \times 10^{-5} \text{ cm}^2\text{s}^{-1}$ ; and  $\tau_{0,20^\circ\text{C}}=1.25 \text{ ps}$ , respectively. The gap between 1 and  $3 \text{ \AA}^{-2}$  is due to the shadows of the beakers.

As a first approximation in the interpretation of the water bridge results, one can assume that relative increases of  $D$  and  $\tau_0$  due to multiple scattering are the same for both samples – for the water bridge sample and the geometrically identical Al-cylinder sample (Fig. 4.26). The difference between fitted (experimental, index ‘exp’) variables and the published ones from a geometrically optimum Al cell (index ‘pub’) can then be used to estimate the real values of the water bridge data with correction terms derived from the Al cylinder experiment, the Fuchs-Teixeira<sup>2</sup> relation:

$$D_{pub} \approx 0.52x D_{exp} \quad (\text{Eq. 4.8})$$

$$\tau_{0,pub} \approx 0.94x \tau_{0,exp} \quad (\text{Eq. 4.9})$$

A water bridge, created with the given parameters ( $I \sim 0.3 \text{ mA}$ ,  $10\text{--}15 \text{ kV}$ ) typically warms up until reaching an equilibrium temperature of  $45\text{--}50^\circ\text{C}$  [16]. Using the empirically derived

2 Named in recognition of the extensive contribution to this work by Elmar C. Fuchs of Wetsus and José Teixeira of Laboratoire Léon Brillouin.

Fuchs-Teixeira (FT) relation the position of the theoretical curve for a water cylinder at 50°C with multiple scattering can be calculated assuming temperature effects on the correction values to be small.

On the other hand, from the parameters fitted through the water bridge data, values of  $D$  and  $\tau_0$  can be estimated by compensating for the systematic error from multiple scattering using the . A comparison of these values is depicted in Fig. 4.27 which compares all data considered and where the derived values are given in Table 4.5. Blue dots present the QENS results from the Al cylinder with water bridge geometry, with the blue dashed-dotted line plotting the data fit. The blue solid line represents the theoretical data at 20°C and the red dashed line shows the calculated QENS data for water at 50°C under water bridge geometry again corrected for multiple scatter by the FT relation.

The green triangles present the QENS data from the floating water bridge under the given conditions with the green dashed-dotted line representing the data fit (nonlinear least square method, Levenberg-Marquardt algorithm [21,22]). The solid green line is the water bridge data using the FT correction for multiple scattering.

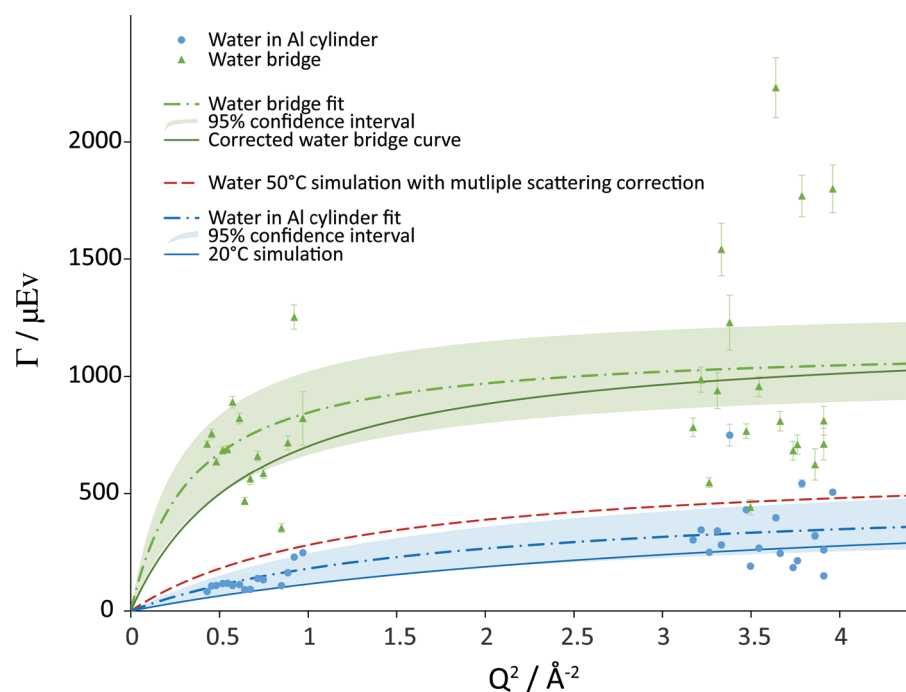


**Figure 4.27** Line widths from the Lorentzian fits of water in a water bridge and water in an Al cylinder placed at the exact position of the floating water bridge compared to simulated curves of water at 50°C corrected for multiple scattering. The values for  $D$  and  $\tau_0$  are given in Table 4.5. Errors of the fits are shown as 95% confidence interval.

**Table 4.5:** Diffusion coefficients ( $D$ ) and residence times ( $\tau_0$ ) of water at different temperatures (representing water molecules) and the water bridge (representing protons only) with and without corrections for multiple scattering.

| Sample  | $D / 10^{-5} \text{ cm}^2 \text{ s}^{-1}$ | $\tau_0 / \text{ps}$ |
|---|---|----------------------|
| Water, 20°C, simulation   | 2.218                                     | 1.25                 |
| Water, 20°C, in Al cylinder (fitted data)   | $4.249 \pm 1.612$                         | $1.30 \pm 0.32$      |
| Water, 50°C (not shown)   | 4.0                                       | 1.00                 |
| Water, 50°C, simulation corrected to include multiple scattering using Fuchs-Teixeira   | 7.7                                       | 1.04                 |
| Water bridge, ~50°C, fitted data  | $50 \pm 20$                               | $0.58 \pm 0.08$      |
| Water bridge, ~50°C, fitted data corrected for multiple scattering using Fuchs-Teixeira | $26 \pm 10$                               | $0.55 \pm 0.08$      |

## 4.6 Ultrafast relaxation revisited

The results from ultrafast work are presented here in a more detailed manner despite not being included as a method in this thesis for the reason that careful consideration of this data in conjunction with the rest of the data presented in this thesis is necessary to come to a consistent and general understanding of the molecular response of water to the electric field gradients present in the bridge.

Ultrafast mid-IR vibrational spectroscopy can measure the vibrational lifetime of the OH stretch vibration of HDO molecules. Measurement on HDO:D<sub>2</sub>O water bridges found that the relaxation time was shorter in the bridge ( $630 \pm 30$  fs) than for HDO molecules in bulk HDO:D<sub>2</sub>O ( $740 \pm 40$  fs). The vibrational relaxation time constants were calculated using a single exponential fit to the anisotropy decay vs delay shown in figure 4.28. The pump beam polarization was aligned either parallel (p-polarized) or perpendicular (s-polarized) to the long axis of the water bridge. For both configurations we observed a vibrational lifetime of  $600 \pm 30$  fs. **Hence, the vibrational relaxation does not depend on the orientation of the excited OH vibrations in the water bridge.**

One may think that the shorter vibrational lifetime of the water bridge could be the result of a local heating effect, as the current running through the water bridge leads to a local rise in temperature [44]. For most substances, an increase in temperature leads to an acceleration of vibrational energy transfer processes. However, one of the anomalous properties of water is that its vibrational lifetime increases with rising temperature [45]. This anomalous behavior can be explained by the blue-shift of the OH stretch vibrational spectrum with temperature. Due to this blue-shift, the coupling to lower-frequency accepting modes decreases, and thus

the  $T_a$  lifetime increases. In a Raman study of the water bridge a small blue-shift of the OH stretch vibration spectrum was observed [46], which is thus also consistent with a heating effect in the water bridge. Hence, based on the temperature effect, a small increase of the vibrational lifetime of the water bridge would have been expected, which makes the observed shortening of this lifetime all the more surprising. For a bulk liquid HDO:D2O sample the observed lifetime of  $\sim 600 \pm 30$  fs would correspond to a temperature below  $0^\circ\text{C}$  [45]. The water bridge is not supercooled but had a temperature of  $25 \pm 2^\circ\text{C}$  (measured with a thermographic camera calibrated to the emissivity of water [5]), slightly warmer than the water in the beakers.

Figure 4.29 shows the result of a global fit to the data at all probe frequencies. The left panel depicts the population dynamics following the relaxation of the OH stretch mode for the water bridge (in blue) and the bulk sample (in black). The fitting results are represented by solid lines. The fit to the three-level model yields a similar time constant for the excited state relaxation of the OH stretch vibration as was obtained from the analysis of the data in the frequency regions where the heating effect on the signal is negligible. We found  $T_{aWB} = 630 \pm 50$  fs and  $T_{aBulk} = 740 \pm 40$  fs.

Interestingly, it is found that the rise of the thermally equilibrated end level is much slower for the water bridge ( $T_{eqWB} = 1.5 \pm 0.4$  ps) than for the bulk sample ( $T_{eqBulk} = 250 \pm 90$  fs). The right panel in figure 4.29 presents the extracted relaxation time constants. The error bars reflect the spread of the lifetimes over all the analyzed data sets (15 for the water bridge – including data at higher and lower potential and s excitation polarization, and 15 for the reference sample).

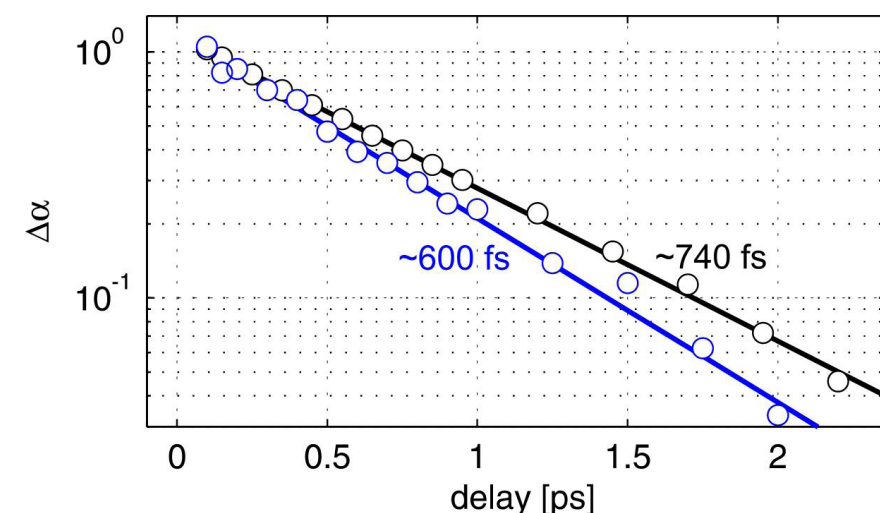


Figure 4.28 Normalized delay traces for the water bridge (blue circles) and for the reference bulk sample (black circles). The traces are measured at a probe frequency of  $3500\text{ cm}^{-1}$ , where the heating effect is negligible. The lines are guide to the eyes resulting from mono-exponential fit.

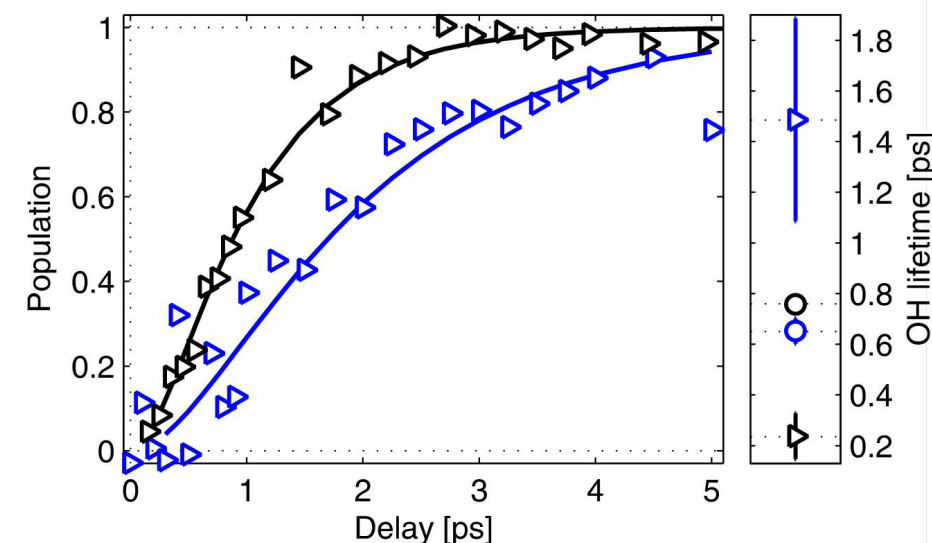


Figure 4.29 Thermalization dynamics of the water bridge (in blue) and the bulk sample (black) following the relaxation of the OH stretch mode. Right panel shows the extracted lifetimes for the excited (circles) and intermediate states (triangles).

## 4.7 Probing the Nuclear Environment for Coherent Spin Coupling

The nuclear spin environment is another sensitive probe of proton mobility and molecular coupling in liquids. Here glycerol is used instead of water to provide a check of the generality of the findings presented for water, and for the practical reason that the shorter relaxation times allow for the thorough collection of data. The basic spectroscopy and environmental influences are presented in appendix C.5. Evidence of the partial collapse of the hydrogen bond network is again found.

### 4.5.1 MR Relaxation Mapping and Thermometry

The results from the combined relaxation mapping on nine glycerol bridges are shown in figure 4.30. The data are given as temperatures derived from the calibrated relaxation times for glycerol in the absence of an electric field. If there is no effect from the electric field in the bridge on the relaxation processes then it is expected that the two derived temperatures will agree and should line up with the grey dashed line. However, this is clearly not the case.  **$T_2$  clearly shows a tendency to overestimate the temperature.** By examining the spatial variance of the data it is also clear that the effect is dependent upon where in the system the measurement is made. The beakers tend to show the smallest error, however, a discrepancy between anode and cathode side is clear. The magnitude of the electric field and the field gradient density is expected to be higher at the high potential electrode than near the ground electrode on account of additional losses from the experimental set-up (e.g. leaking of charge to the atmosphere, and support plate). The data from both bridge bases corroborates this observation as here the field gradient is very strong. The highest values of  $T(T_2)$  are reported in the bridge section however data becomes much more disperse. Several measurement artifacts are likely the cause of the increased variability. Fluid flow will transport signal out of the measurement volume and large temperature fluctuations during measurement times will introduce non-linearities in the relaxation dynamics. Flow may also play a role in the dispersion of the cathode data as this area also exhibits rapid fluid motion. Ignoring the outliers for the moment there is a clear trend away from the expectation values for transverse relaxation in the bridge system.

### 4.5.2 Water – Glycerol Interaction

From the literature there are some things known about the way water and glycerol mixtures will interact and in particular how the two liquids change the dielectric properties. The dielectric constant will decrease as glycerol content increase. As temperature increases the permittivity will also rise. These two trends would indicate that as a glycerol bridge which at first contained anhydrous glycerol it is expected that there will be a slow and steady increase in  $\epsilon$ , where the temperatures are higher (e.g. bridge) this effect will be magnified.

The expectation is that the total water content will never exceed a few percent in practice on account of the dry atmosphere in the measurement environment, however no quantitative measurement of the relative change in water content was made. A critical water content that could affect the hydrogen bonding dynamics is expected at 77.3 wt.% glycerol as previous studies have reported a transition in the free volume of the liquid undergoing vitrification and which was attributed to an inhomogeneous to homogeneous distribution of the water hydrogen bond network [47]. Infrared vibrational spectroscopy and MD simulation on water:glycerol mixture found that high glycerol content mimics the hydrogen bonding dynamics of ice without the structural transition [48], [49]. Glycerol slows water dynamics even at room temperature and concentrations between 43-60 wt.% [50].

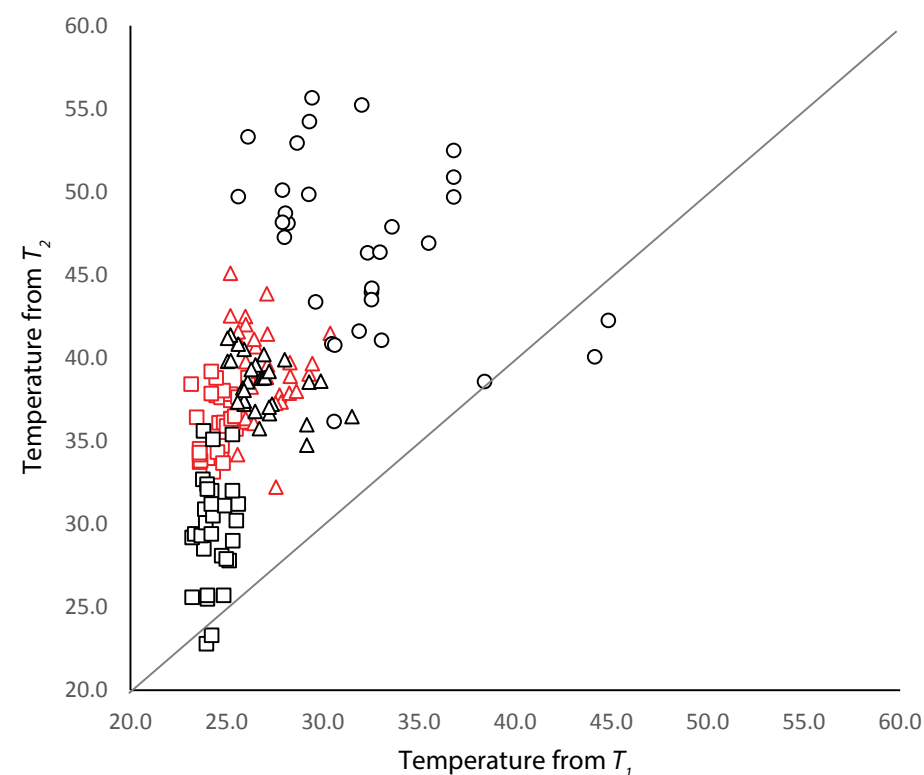
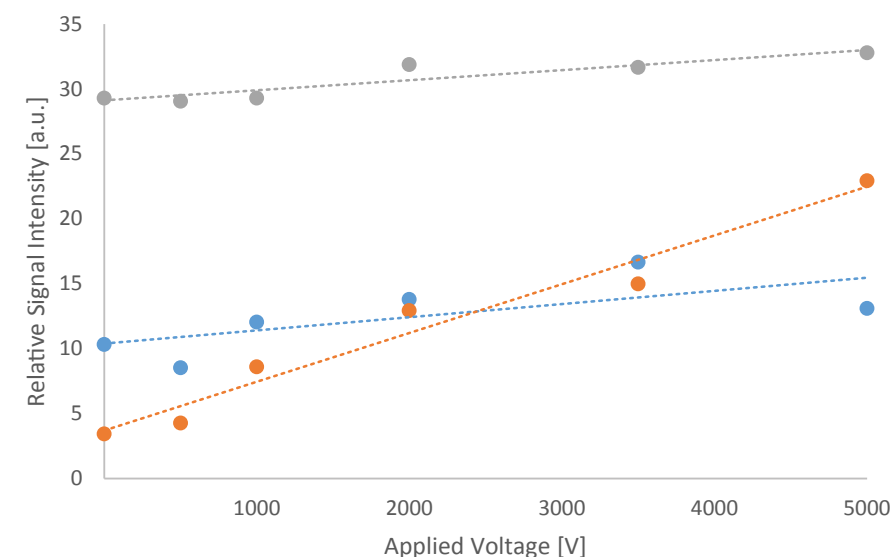


Figure 4.30 Comparison of relaxation derived temperatures taken from nine glycerol bridges.  $T_2$  is shown to overestimate the temperature indicating a slow dephasing of couple nuclear spins. The fitted temperatures derived from  $T_1$  and  $T_2$  are plotted against each other, the dashed line is a guide for the eye representing agreement in derived temperature. Relaxation times were extracted from five regions of interest (see figure 3.15): bulk anolyte (ROI1 red squares), bulk catholyte (ROI2 black squares), anode bridge base (ROI3 red triangles), cathode bridge base (ROI4 black triangles), and the bridge itself (ROI5 black circles). Red indicates those data from the high voltage beaker.

### 4.5.3 Low-field eNMR – The echo of free protons

The  $^1\text{H}$  spectrum of anhydrous glycerol under voltage using the set-up described in §3.7.4. The spectra at 1.5 T are not as well resolved as at 9.4 T and a strong water signal from the cooling jacket dominate. Regardless of these limitations two peaks could be identified corresponding to the different proton populations of glycerol though it is difficult to precisely assign them to specific chemical groups since the MRI magnet is not well suited for detailed spectroscopic studies. This is primarily due to the large bore and field inhomogeneity that reduce spectrometer resolution. Coupling effects are also dependent upon the magnetic field strength and so it is also not reliable to compare signal patterns with higher field spectra to infer peak assignment. The intensity of glycerol peaks are plotted at six applied voltages in figure 4.31. It is clear however that two peaks, at 4.5 ppm (blue circles) and 5.0 ppm (grey circles), are largely unaffected as the applied electric field intensity increases. These are always present and can be assumed to be part of the normal 'bound' proton population. **A third peak at about 5.7 ppm (orange circles) is shown to steadily grow in intensity along with the increasing electric field.** This peak may represent the emergence of a mobile proton population in response to the applied electric field gradient. Linear fits are provided as a guide to the data and are meant to clarify the rapid growth in the peak at 5.7 ppm. The statistical significance of the fit to the normal proton populations indicates that these spectra are not entirely reliable, especially for the lower intensity peak at 4.5 ppm (blue dashed line,  $R^2=0.4779$ ) which hints that there is relatively poor signal to noise in the imaging spectrometer. For the more intense peak at 5.0 ppm (grey dashed line,  $R^2=0.8977$ ) the signal intensity is sufficient to be less strongly affected. Thus, it is quite striking that the relatively weak peak at 5.7 ppm has such a good fit  $R^2=0.9641$ . This provides confidence in considering the underlying mechanism further, and will be discussed in §5.6 along with the results of the nuclear magnetic relaxation mapping. It must be clearly stated, however, that these findings are still preliminary and that a more systematic approach must be adopted in order to first confirm the findings and second to test the proposed underlying mechanism of a quasi-free proton population. It is also necessary to examine whether the generally of these findings hold in another liquid such as methanol or water.



**Figure 4.31** Peak intensity from 1.5T (63MHz)  $^1\text{H}$  spectra of glycerol under increasing electric field intensity. The peaks assignments are not specific however the peaks at 4.5 ppm (blue circles) and 5.0 ppm (grey circles) likely belong to the ground state protons of glycerol. The signal at 5.7 ppm is barely detectable at 0 volts and grows quickly in response to increasing voltage. This may be a signal related to a quasi-free proton population.  $R^2$  values for the linear fits are as follows: blue 0.4779, grey 0.8977, and orange 0.9641.



## Bibliography

- [1] A. Widom, J. Swain, J. Silverberg, S. Sivasubramanian, and Y. Srivastava, "Theory of the Maxwell pressure tensor and the tension in a water bridge," *Phys. Rev. E*, vol. 80, no. 1, p. 016301, Jul. 2009.
- [2] A. G. Marín and D. Lohse, "Building water bridges in air: Electrohydrodynamics of the floating water bridge," *Phys. Fluids*, vol. 22, no. 12, p. 122104, 2010.
- [3] J. Woisetschlager, A. D. Wexler, G. Holler, M. Eisenhut, K. Gatterer, and E. C. Fuchs, "Horizontal bridges in polar dielectric liquids," *Exp. Fluids*, vol. 52, no. 1, pp. 193–205, Oct. 2012.
- [4] J. Woisetschlager, A. D. Wexler, G. Holler, M. Eisenhut, K. Gatterer, and E. C. Fuchs, "Horizontal bridges in polar dielectric liquids," *Exp. Fluids*, vol. 52, no. 1, pp. 193–205, 2012.
- [5] J. Woisetschlager, K. Gatterer, and E. C. Fuchs, "Experiments in a floating water bridge," *Exp. Fluids*, vol. 48, no. 1, pp. 121–131, Jul. 2010.
- [6] E. C. Fuchs, J. Woisetschlager, K. Gatterer, E. Maier, R. Pecnik, G. Holler, and H. Eisenkölbl, "The floating water bridge," *J. Phys. D: Appl. Phys.*, vol. 40, no. 19, pp. 6112–6114, Oct. 2007.
- [7] E. C. Fuchs, K. Gatterer, G. Holler, and J. Woisetschlager, "Dynamics of the floating water bridge," *J. Phys. D: Appl. Phys.*, vol. 41, p. 185502, 2008.
- [8] K. Morawetz, "Theory of water and charged liquid bridges," *Phys. Rev. E - Stat. Nonlinear, Soft Matter Phys.*, vol. 86, no. 2, pp. 1–9, 2012.
- [9] A. Engel and R. Friedrichs, "On the electromagnetic force on a polarizable body," *Am. J. Phys.*, vol. 70, no. 4, p. 428, Apr. 2002.
- [10] D. R. Lide, W. M. M. Haynes, G. Baysinger, L. I. Berger, D. L. Roth, D. Zwillinger, M. Frenkel, and R. N. Goldberg, "CRC Handbook of Chemistry and Physics," 2010.
- [11] P. Atkins and J. De Paula, "Atkins Physical Chemistry (8th Edition)," pp. 682–683, 2006.
- [12] W. B. Russel, D. A. Saville, and W. R. Schowalter, *Colloidal Dispersions*. Cambridge University Press, 1992.
- [13] C. L. Burcham and D. A. Saville, "Electrohydrodynamic stability: Taylor–Melcher theory for a liquid bridge suspended in a dielectric gas," *J. Fluid Mech.*, vol. 452, pp. 163–187, Feb. 2002.
- [14] M. Zahn and T. Takada, "High voltage electric field and space-charge distributions in highly purified water," *J. Appl. Phys.*, vol. 54, no. 9, pp. 4762–4775, 1983.
- [15] E. C. Fuchs, B. Bitschnau, J. Woisetschlager, E. Maier, B. Beuneu, and J. Teixeira, "Neutron scattering of a floating heavy water bridge," *J. Phys. D: Appl. Phys.*, vol. 42, no. 6, p. 065502, Mar. 2009.
- [16] A. K. Soper, "Joint structure refinement of x-ray and neutron diffraction data on disordered materials: application to liquid water," *J. Phys. Condens. Matter*, vol. 19, p. 335206, 2007.
- [17] T. L. Beck, M. E. Paulaitis, and L. R. Pratt, *The Potential Distribution Theorem and Models of Molecular Solutions*. Cambridge University Press, 2006.
- [18] D. Rai, A. D. Kulkarni, S. P. Gejji, and R. K. Pathak, "Water clusters (H<sub>2</sub>O)<sub>n</sub>, n=6-8, in external electric fields," *J. Chem. Phys.*, vol. 128, no. 3, p. 034310, Jan. 2008.
- [19] D. Rai, "Ab Initio Investigations on Some Dipole-Bonded Molecular Clusters, Their Interaction with Water Molecules, and Externally Applied Electric Field," University of Pune, Pune, India, 2008.
- [20] C. Huang, K. T. Wikfeldt, D. Nordlund, U. Bergmann, T. McQueen, J. Sellberg, L. G. M. Pettersson, and A. Nilsson, "Wide-angle X-ray diffraction and molecular dynamics study of medium-range order in ambient and hot water," *Phys. Chem. Chem. Phys.*, vol. 13, no. 44, pp. 19997–20007, Nov. 2011.
- [21] A. K. Soper, "The radial distribution functions of water and ice from 220 to 673 K and at pressures up to 400 MPa," *Chem. Phys.*, vol. 258, no. 2–3, pp. 121–137, Aug. 2000.
- [22] A. K. Soper, "Water and ice structure in the range 220 - 365K from radiation total scattering experiments," *ArXiv*, 2014.
- [23] T. Strässle, A. M. Saitta, Y. L. Godec, G. Hamel, S. Klotz, J. S. Loveday, and R. J. Nelmes, "Structure of dense liquid water by neutron scattering to 6.5 GPa and 670 K," *Phys. Rev. Lett.*, vol. 96, no. 6, pp. 1–4, 2006.
- [24] A. Botti, F. Bruni, S. Imberti, M. a. Ricci, and A. K. Soper, "Ions in water: The microscopic structure of a concentrated HCl solution," *J. Chem. Phys.*, vol. 121, no. 16, pp. 7840–7848, 2004.
- [25] M. Sammer, A. Wexler, P. Kuntke, H. Wilsche, N. Stanulewicz, E. Lankmayr, J. Woisetschlager, and E. Fuchs, "Proton production, neutralisation and reduction in a floating water bridge," *J. Phys. D: Appl. Phys.*, 2015.
- [26] K.-J. Tielrooij, "Molecular Motions of Water," University of Amsterdam, 2010.
- [27] K. J. Tielrooij, R. L. a. Timmer, H. J. Bakker, and M. Bonn, "Structure Dynamics of the Proton in Liquid Water Probed with Terahertz Time-Domain Spectroscopy," *Phys. Rev. Lett.*, vol. 102, no. 19, p. 198303, May 2009.
- [28] P. Minton and A. P. Minton, "Relations between Crystal Structure," vol. 606, no. 2, pp. 886–889, 1971.
- [29] C. J. Tainter, L. Shi, and J. L. Skinner, "Reparametrized E3B (Explicit Three-Body) Water Model Using the TIP4P/2005 Model as a Reference," *J. Chem. Theory Comput.*, vol. 11, no. 5, pp. 2268–2277, 2015.
- [30] N. J. English and C. J. Waldron, "Perspectives on external electric fields in molecular simulation: progress, prospects and challenges," *Phys. Chem. Chem. Phys.*, vol. 17, no. 19, pp. 12407–40, May 2015.
- [31] H. Thompson, F. Bruni, M. A. Ricci, S. Mclain, S. Klotz, T. Straessle, S. Imberti, and R. Hargreaves, "Empirical Potential Structure Refinement - EPSRshell A User's Guide," no. July, 2013.
- [32] A. K. Soper, "Tests of the empirical potential structure refinement method and a new method of application to neutron diffraction data on water," *Mol. Phys.*, vol. 99, no. 17, pp. 1503–1516, 2001.
- [33] M. A. González and J. L. F. Abascal, "A flexible model for water based on TIP4P/2005," *J. Chem. Phys.*, vol. 135, no. 22, 2011.

- [34] S. Habershon, T. E. Markland, and D. E. Manolopoulos, "Competing quantum effects in the dynamics of a flexible water model," *J. Chem. Phys.*, vol. 131, no. 2009, 2009.
- [35] F. Bresme, A. Lervik, D. Bedeaux, and S. Kjelstrup, "Water polarization under thermal gradients," *Phys. Rev. Lett.*, vol. 101, no. July, pp. 2–5, 2008.
- [36] L. Shi, Y. Ni, S. E. P. Drews, and J. L. Skinner, "Dielectric constant and low-frequency infrared spectra for liquid water and ice Ih within the E3B model," *J. Chem. Phys.*, vol. 141, no. 8, p. 084508, 2014.
- [37] M. Yang and J. L. Skinner, "Signatures of coherent vibrational energy transfer in IR and Raman line shapes for liquid water," *Phys. Chem. Chem. Phys.*, vol. 12, pp. 982–991, 2010.
- [38] L. Shi, S. M. Gruenbaum, and J. L. Skinner, "Interpretation of IR and Raman line shapes for H<sub>2</sub>O and D<sub>2</sub>O ice Ih," *J. Phys. Chem. B*, vol. 116, no. 47, pp. 13821–30, 2012.
- [39] H. J. Bakker and J. L. Skinner, "Vibrational spectroscopy as a probe of structure and dynamics in liquid water," *Chem. Rev.*, vol. 110, no. 3, pp. 1498–517, Mar. 2010.
- [40] G. E. Walrafen, "Dispersion of the Raman depolarization ratio of HDO in water and heavy water from 295 to 368 K, and from concentrated NaClO<sub>4</sub>D<sub>2</sub>OH<sub>2</sub>O," *J. Chem. Phys.*, vol. 122, no. 17, p. 174502, May 2005.
- [41] B. M. Auer and J. L. Skinner, "Water: Hydrogen bonding and vibrational spectroscopy, in the bulk liquid and at the liquid/vapor interface," *Chem. Phys. Lett.*, vol. 470, no. 1–3, pp. 13–20, Feb. 2009.
- [42] J. Skinner, B. Auer, and Y. Lin, "Vibrational line shapes, spectral diffusion, and hydrogen bonding in liquid water," *Adv. Chem. Phys.*, vol. 142, 2010.
- [43] H. Torii, "Time-domain calculations of the polarized Raman spectra, the transient infrared absorption anisotropy, and the extent of delocalization of the OH stretching mode of liquid water," *J. Phys. Chem. A*, vol. 110, no. 30, pp. 9469–9477, 2006.
- [44] E. Del Giudice, E. C. Fuchs, and G. Vitiello, "Collective Molecular Dynamics of a Floating Water Bridge," *Water*, no. July, p. 11, 2010.
- [45] S. Woutersen, U. Emmerichs, H.-K. Nienhuys, and H. Bakker, "Anomalous Temperature Dependence of Vibrational Lifetimes in Water and Ice," *Phys. Rev. Lett.*, vol. 81, pp. 1106–1109, 1998.
- [46] R. C. Ponterio, M. Pochylski, F. Aliotta, C. Vasi, M. E. Fontanella, and F. Saija, "Raman scattering measurements on a floating water bridge," *J. Phys. D: Appl. Phys.*, vol. 43, no. 17, p. 175405, May 2010.
- [47] D. Banerjee and S. V. Bhat, "Vitrification, relaxation and free volume in glycerol–water binary liquid mixture: Spin probe ESR studies," *J. Non. Cryst. Solids*, vol. 355, no. 50–51, pp. 2433–2438, Dec. 2009.
- [48] J. L. Dashnau, N. V. Nucci, K. A. Sharp, J. M. Vanderkooi, V. Pennsylv, and V. Pennsylv, "Hydrogen Bonding and the Cryoprotective Properties of Glycerol / Water Mixtures," vol. 11, pp. 13670–13677, 2006.
- [49] J. L. Dashnau and J. M. Vanderkooi, "Computational Approaches to Investigate How Biological Macromolecules Can Be," *J. Food Sci.*, vol. 72, no. 1, 2007.
- [50] A. V. Egorov, A. P. Lyubartsev, and A. Laaksonen, "Molecular dynamics simulation study of glycerol–water liquid mixtures," *J. Phys. Chem. B*, vol. 115, no. 49, pp. 14572–81, Dec. 2011.
- [51] D. Weishaupt, V. D. Köchli, and B. Marincek, *How does MRI work?: An Introduction to the Physics and Function of Magnetic Resonance Imaging*. Springer Science & Business Media, 2008.
- [52] J. N. Smith, R. C. Flagan, and J. L. Beauchamp, "Droplet evaporation and discharge dynamics in electrospray ionization," *J. Phys. Chem. A*, vol. 106, no. 42, pp. 9957–9967, 2002.
- [53] F. N. Wang, S. L. Peng, C. T. Lu, H. H. Peng, and T. C. Yeh, "Water signal attenuation by D<sub>2</sub>O infusion as a novel contrast mechanism for 1H perfusion MRI," *NMR Biomed.*, vol. 26, no. 6, pp. 692–698, 2013.
- [54] A. Narten, "Thermodynamic Effects of Mixing Light and Heavy Water," *J. Chem. Phys.*, vol. 41, no. 5, p. 1318, Jul. 1964.
- [55] B. Quesson, J. A. de Zwart, and C. T. Moonen, "Magnetic resonance temperature imaging for guidance of thermotherapy," *J. Magn. Reson. Imaging*, vol. 12, no. 4, pp. 525–33, Oct. 2000.
- [56] E. C. Fuchs, A. D. Wexler, A. H. Paulitsch-Fuchs, L. L. F. Agostinho, D. Yntema, and J. Woisetschläger, "The Armstrong experiment revisited," *Eur. Phys. J. Spec. Top.*, vol. 223, no. 5, pp. 959–977, Aug. 2014.
- [57] J. F. de la Mora, G. J. van Berkel, C. G. Enke, R. B. Cole, M. Martinez-Sanchez, and J. B. Fenn, "Electrochemical processes in electrospray ionization mass spectrometry," *J. Mass Spectrom.*, vol. 35, pp. 939–952, 2000.
- [58] J. Kendall, "THE SPECIFIC CONDUCTIVITY OF PURE WATER IN EQUILIBRIUM WITH ATMOSPHERIC CARBON DIOXIDE," *J. Am. Chem. Soc.*, vol. 38, no. 8, pp. 1480–1497, Aug. 1916.
- [59] E. C. Fuchs, L. L. F. Agostinho, M. Eisenhut, and J. Woisetschläger, "Mass and charge transfer within a floating water bridge," *Proc. SPIE*, vol. 7376, p. 73761E–73761E–15, Jun. 2010.
- [60] M. Eisenhut, X. Guo, A. H. Paulitsch-Fuchs, and E. C. Fuchs, "Aqueous phenol and ethylene glycol solutions in electrohydrodynamic liquid bridging," *Cent. Eur. J. Chem.*, vol. 9, no. 3, pp. 391–403, Mar. 2011.
- [61] V. B. Oshurko, A. A. Ropyanov, A. N. Fedorov, M. V. Fedosov, and N. A. Shelaeva, "Spectrum of OH-stretching vibrations of water in a 'floating' water bridge," *Tech. Phys.*, vol. 57, no. 11, pp. 1589–1592, Nov. 2012.
- [62] GATS Inc., "Spectralcalc." 11864 Canon Blvd., Suite 101, Newport News, VA 23606 USA., 2011.
- [63] L. L. Gordley, B. T. Marshall, and D. Allen Chu, "Linepak: Algorithms for modeling spectral transmittance and radiance," *J. Quant. Spectrosc. Radiat. Transf.*, vol. 52, no. 5, pp. 563–580, 1994.
- [64] S. A. Clough, F. X. Kneizys, and R. W. Davies, "Line shape and the water vapor continuum," *Atmos. Res.*, vol. 23, no. 3–4, pp. 229–241, 1989.
- [65] J. Darabi, M. M. Ohadi, and S. V. Desiatoun, "Falling Film and Spray Evaporation Enhancement Using an Applied Electric Field," *J. Heat Transf.*, vol. 122, pp. 741–748, 2000.

- [66] R. P.A. Hartman, D. J. Brunner, D. M. a. Camelot, J. C. M. Marijnissen, and B. Scarlett, "Jet Break-Up in Electrohydrodynamic Atomization in the Cone-Jet Mode," *J. Aerosol Sci.*, vol. 31, no. 1, pp. 65–95, Jan. 2000.
- [67] W. C. Hinds, *Aerosol Technology*, 2nd ed., Wiley Interscience, 1998.
- [68] R. Hartman, "Detailed simulations of liquid and liquid-solid mixing—turbulent agitated flow and mass transfer," TU Delft, 1998.
- [69] N. Bloembergen, "Spin Relaxation Processes in a Two-Proton System," *Phys. Rev.*, vol. 104, no. 6, pp. 1542–1547, 1956.
- [70] D. Kruk, R. Meier, and E. a. Rössler, "Translational and rotational diffusion of glycerol by means of field cycling 1H NMR relaxometry," *J. Phys. Chem. B*, vol. 115, no. 5, pp. 951–957, 2011.
- [71] P. K. Ghattyenkatakrishna and E. C. Uberbacher, "Hydrogen-Bond Dynamics of Water."
- [72] N. Bloembergen, E. M. Purcell, and R. V. Pound, "Relaxation Effects in Nuclear in Nuclear Magnetic Resonance Absorption," *Physical Review*, vol. 73, no. 7. p. 679, 1948.
- [73] G. Adam and J. H. Gibbs, "On the Temperature Dependence of Cooperative Relaxation Properties in Glass-Forming Liquids\*," *J. Chem. Phys.*, vol. 43, no. 1, pp. 139–146, 1965.

Photo credit chapter 4 overleaf: *Morning Surf, Maspalomas*, ©A.D. Wexler, 2015

## Appendix C: Supplemental Results

### C.1 Supplemental MRI Results

#### C.1.1 Electrical polarization, bridge ignition and noise

Prior to the existence of a bridge the experiment can be understood as a simple dielectric capacitor. As the applied voltage is ramped electrical energy is stored within the liquid and other dielectric materials present. These materials become polarized and will leak charge into the surrounding environment. The DC power is converted to material fluctuations in the Hz to kHz range which generates an audible sound commonly encountered in capacitor charging circuits. Additionally, the system will leak and spray charge in the form of ion or corona wind by which air is charged at sharp edges or points in the setup, this plasma will generate broadband radio frequency interference (RFI) the intensity of which is maximum in the seconds preceding and during bridge ignition. Image acquisition in the isotope mixture experiments was begun prior to the application of electrical energy ( $t=0$  s) thus it is possible to observe the charging of the system in the radio frequency domain as shown in figure C.1. The voltage ramping rate was between 800-1000 V/s with bridge ignition occurring between 10-15 kV ( $t=12-15$  s). The impulsive stochastic noise which covers the entire image frame becomes spatially constrained ( $t=21-24$  s) after the bridge is established. This indicates that the interfering signal is now confined to a narrower frequency band introducing zipper-like artifacts parallel to phase encoding direction [51]. Between subsequent frames the artifact showed a slow drift movement indicating that the extraneous frequency is time varying. In case of flow experiments, image slices with zipper-like artifacts close to the bridge were repeatedly measured.

#### C.1.2 Mass transport and isotope mixing

Two experimental cases were prepared to track mass transport:

- Case 1 heavy water anolyte and light water catholyte;
- Case 2 light water anolyte and heavy water catholyte.

Both cases were investigated twice, however, in only one instance of each case did the system completely mix as evidenced visually and by converged relative signal intensity (relSI, Eq. 3.16) values. The reason for this is not readily apparent and did not correlate with the variations in starting mass.

A summary sequence of representative images at regular time intervals from the two experimental cases is shown in figure C.2. A movie compiled from the MR images stack of a single instance for case 1 is provided in the supplemental materials. In both cases the bright signal from  $^1\text{H}$  labeled molecules are transported across the bridge. The light water floats on top of the heavier deuterated water as expected given the density difference between isotopes.

As the experiment progresses the light water spreads throughout both beakers. The proton signal moves slowly downward into the originally deuterated volume. At the same time the signal intensity in both beakers falls. Most of the mixing is observed to occur in the upper fluid volume and along the bridge itself but is not especially strong in the vicinity of the electrodes. Schlieren flow visualization figure C.6 has shown that a downward flow is present at both electrodes, however, in the case of the heavy water volume this flow is insufficient to overcome the density gradient resulting in an upward buoyancy force that repels lower density flows of H<sub>2</sub>O and HDO. Heating in the bridge section will further enhance any buoyancy forces in the system. Thus, an unmixed volume of heavy water remains at the bottom of the respective beaker. In case 1 (heavy water anolyte, figure C.2a) this unmixed layer persists for nearly the entire experiment (~1700 s), whereas in case 2 (heavy water catholyte, figure C.2b) mixing is nearly complete within 900 seconds. The duration of the experiments is listed in Table C.1 and it can be seen that in general case 1 required much longer to mix than case 2.

In addition dynamics in the relative volume are visible as changes in the respective liquid levels of each beaker. In case 1 (figure C.2a) the initial net mass flow is towards the anode after some time this flow reverses and the catholyte volume increases significantly. Volume only flows from anode to cathode in case 2 (figure C.2b). For simplicity we will use the convention throughout this section that forward flow is from the anode to the cathode, and reverse flow from the cathode towards the anode. Forward flow the typical behavior for water bridges prepared with a uniform isotope composition.

At the conclusion of the MR measurements the final weight of the liquid in each reservoir along with the temperature was recorded and is compared in Table C.1. The deviation values

**Table C.1** Comparison of relative changes in mass and temperature for the two cases considered. The starting mass was 61.3±0.7 g light water and 65.5±2.3 g heavy water. All bridges lost some mass during operation. The starting temperature for all liquids was 23°C.

| Case              | Duration [s] | Rel. mass change anolyte [g] | Rel. mass change catholyte [g] | Rel. mass change total [g] | Rel. temp. change anolyte [°C] | Rel. temp. change catholyte [°C] |
|-------------------|--------------|------------------------------|--------------------------------|----------------------------|--------------------------------|----------------------------------|
| 1 (D2O Anolyte)   | 1794 ±5      | -22.0±2.0                    | 10.5±1.1                       | -11.5±1.1                  | 31.3±0.5                       | 34.8±0.2                         |
| 2 (D2O Catholyte) | 1029±109     | -17.0±0.1                    | 7.5±1.8                        | -7.5±1.8                   | 24.3±2.4                       | 27.1±1.6                         |

are the standard error of the mean (SEM). In all bridges measured some mass was lost, this is presumed due to evaporation during the measurement time caused by Ohmic heating and electrospray [52]. The average final solution temperature was 52.3±1.6 °C. This indicates operation temperatures higher than typically encountered in normal water bridges and may be due in part to energy liberated by isotope mixing. The temperatures in the catholyte were consistently higher than the anolyte for both cases.

The time courses of relSI (upper panels) and relVol (lower panels) for both anolyte and catholyte were measured using the ROIs illustrated in figure C.3. Data show that in one instance of each case the relSI converge to the same value and these systems are called ‘fully mixed’ (figure C.3a, C.3b) as compared to ‘partially mixed’ (figure C.3c, C.3d) where the values have not yet converge. It is assumed that given enough time all systems will become fully mixed. Calculations based on the final relVol<sub>total</sub> values confirms that material is lost in the experiments as shown in Table C.1 and Figure C.3 (lower panels). The discrepancy between volume and mass loss measurements is likely related to a reduced density at the elevated temperatures found in these bridges. The agreement is nonetheless within a few percent and is given in Table C.2. The duration of the reverse flow from case 1 is taken to be the elapsed time before the anolyte and catholyte volumes again become equivalent. Similar times were recorded for the fully mixed case 873 s (Figure C.3b) and the partially mixed case 900 s (figure C.3d), although in the latter the cross-over is less well pronounced. The bridge system regardless of case eventually reaches a steady state where the relative volumes are ~0.75-0.8 and ~1.2-1.25 for the anolyte and catholyte, respectively. The change of relative signal intensity in all four experiments (Table C.2) initially proceeds at approximately the same rate, and requires on average 378±8 s to reach a level where change in relSI has reached half of the fully mixed equilibrium value.

**Table C.2** Comparison of ROI based measurements for the two cases in both the fully and partially mixed states. The relative loss of volume, and signal intensity are compared to the time to half mixed.

| Initial D2O Volume | State of Mixing | relative volume loss | Time to halfway mixed state [s] | relSI <sub>total</sub> loss |
|--------------------|-----------------|----------------------|---------------------------------|-----------------------------|
| Anolyte            | full            | 2.2%                 | 382                             | 62%                         |
|                    | partial         | 5.1%                 | 399                             | 62%                         |
| Catholyte          | full            | 5.0%                 | 355                             | 55%                         |
|                    | partial         | 3.4%                 | 376                             | 58%                         |

Measurement of the local proton density is central to following the mixing dynamics. Figure C.4 shows the time courses of the relative total signal intensities of anolyte and catholyte in the case of heavy water anolyte and light water catholyte and in the case of light water anolyte and heavy water catholyte, respectively. The decrease of  $\text{relSI}_{\text{total}}$  is monotonic and reaches similar final values in all cases. This indicates changes of signal intensities due to changes in  $T_1$  and/or  $T_2^*$ , which in turn should be caused by both, chemical exchange of hydrogen isotopes [53] and/or substantial heating during mixture [54], [55] as indicated in Table C.1. This substantially decreases proportionality between signal intensity and proton density.

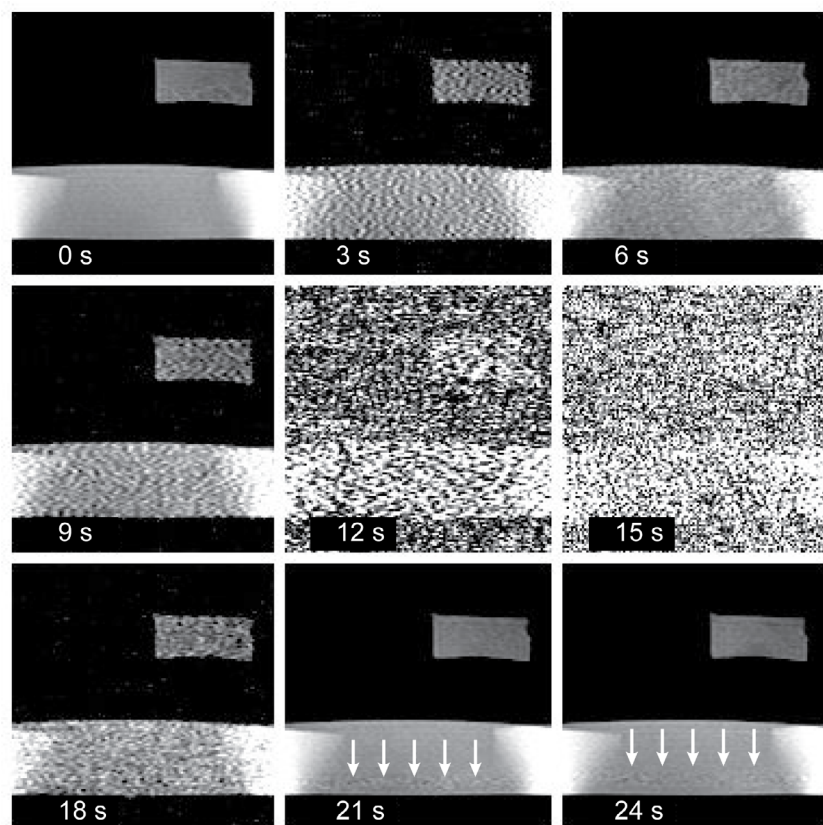


**Figure C.1** Noise from radio frequency interference imaged during bridge charging, ignition, and operation. Impulse noise is visible beginning shortly after the application of high voltage ( $t = 3$  s). As the voltage increases the noise intensity builds and reduces image contrast. Bridge ignition ( $t = 12$ - $15$  s) is accompanied by a brief electromagnetic pulse that obscures the field of view. Starting at  $t = 21$  s a zipper-like artifact is visible parallel to the phase encoding direction.

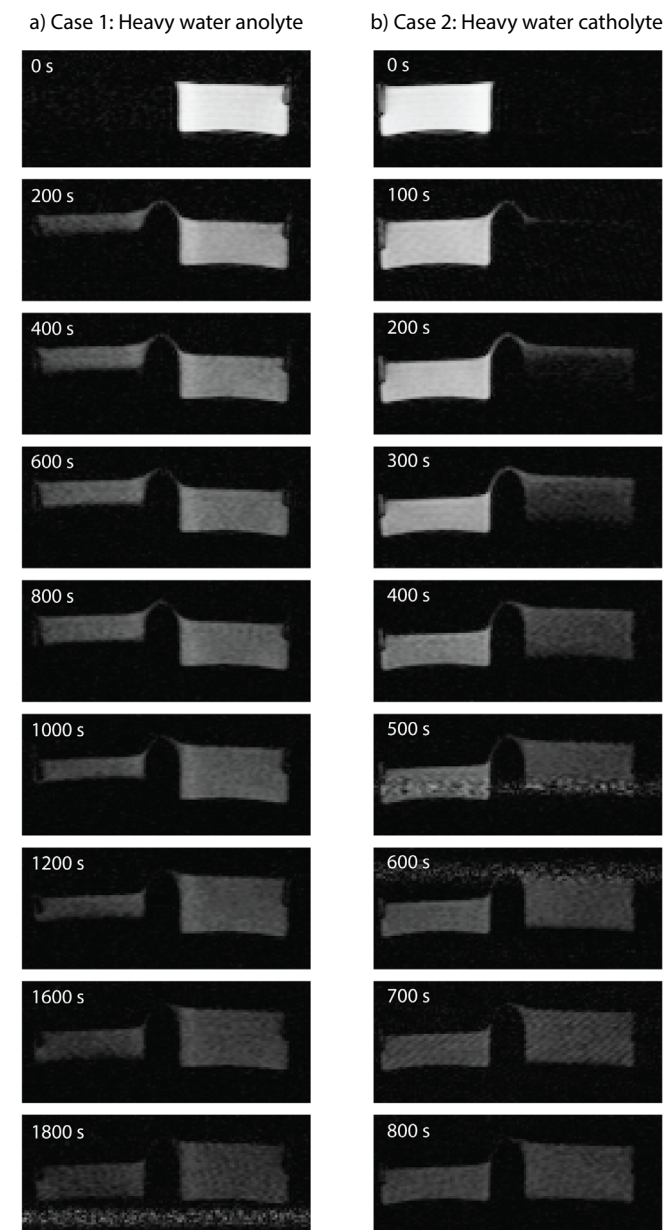


**Figure C.2** Representative image sequence showing the transport of  $^1\text{H}$  nuclei (brighter signal) in the bridge beginning with light water in the cathode (panel a) or anode (panel b) beakers. The transport and mixing of light water with heavy water is much faster in the case where the anolyte is the  $^1\text{H}$  source, requiring half as much time and producing fully mixed volumes. Zipper-like artifact can be seen moving through the measurement frames. The agar signal phantom is not shown for clarity.



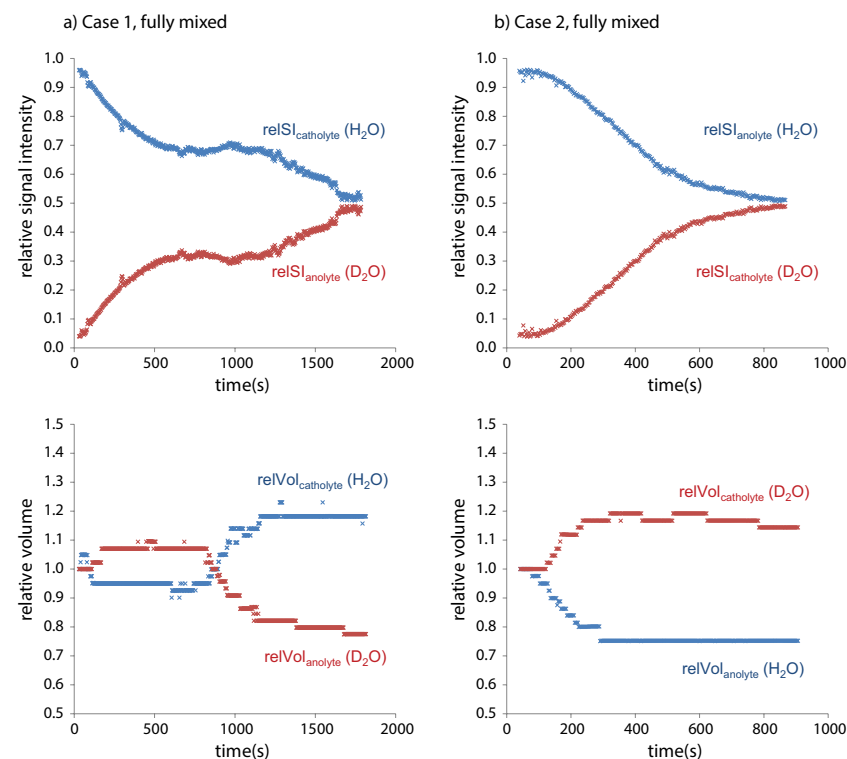
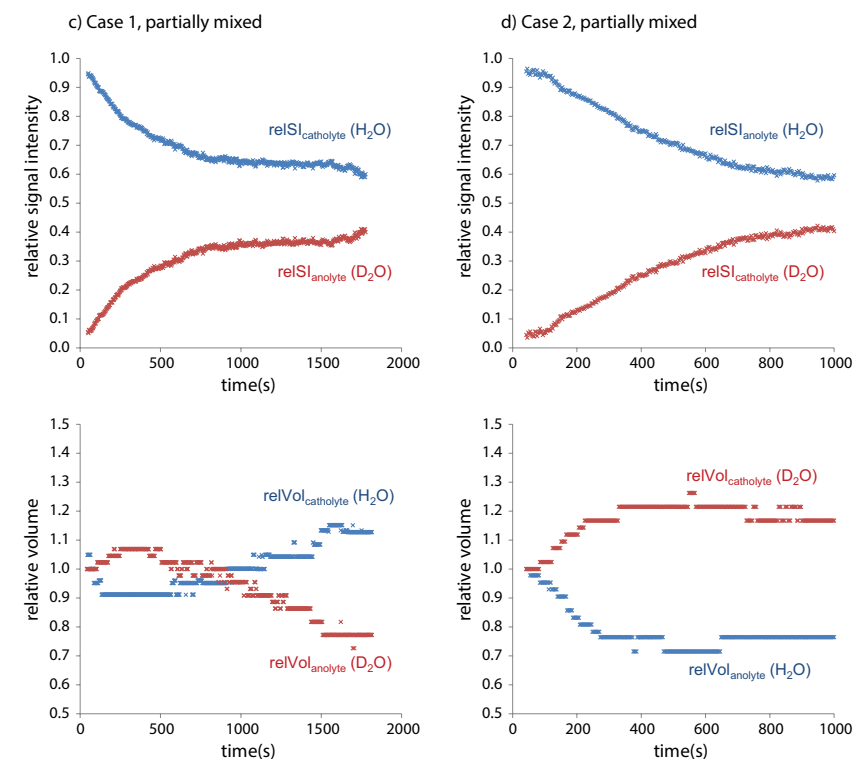


Figure C.3 (both pages upper panels) Time courses of relative signal intensities of the anolyte and catholyte (upper panels) as well as their relative volumes (lower panels). Results from both the fully mixed (7a, 7b) and partially mixed (7c, 7d) systems are shown.  $\text{D}_2\text{O}$  beaker data are displayed in red,



$\text{H}_2\text{O}$  beaker data in blue. The cross-over from reverse to forward flow in both instances of case 1 is clearly visible in the lower panels.

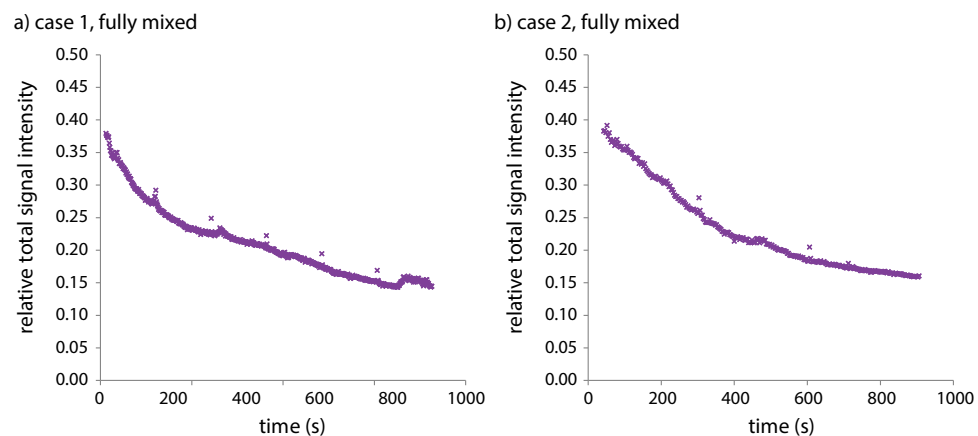
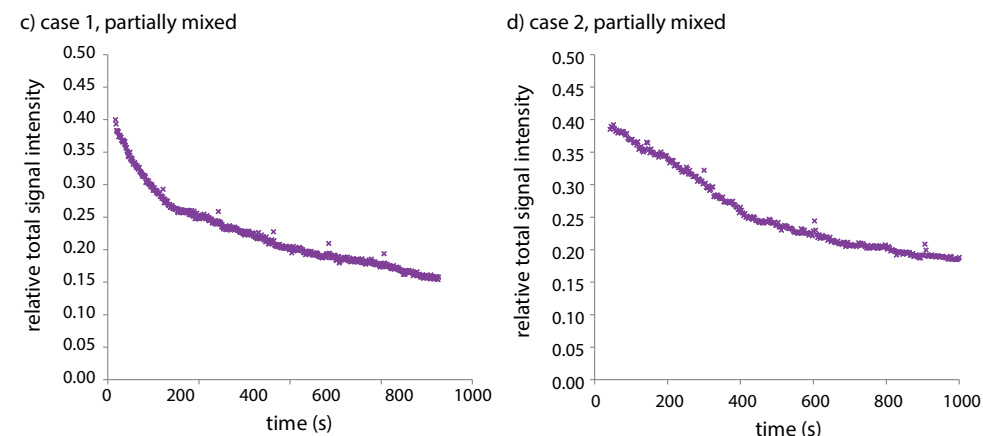


Figure C.4 (both pages lower panels) Time courses of the relative total signal intensities of anolyte and catholyte showing either full mixing or partial mixing of the initial volumes of isotopes. Isotope



starting compositions varied between case 1 using heavy water anolyte and light water catholyte (panels a,c) and in case 2 using light water anolyte and heavy water catholyte (panels b,d).

## C.2 Electrochemistry

### C.2.1 Trace elements from the electrodes

Platinum electrodes were used almost exclusively for water bridge experiments [56]. Although it is safe to assume that due to its nobility this metal is not oxidized and dissolved, an actual analysis of the Pt content after bridge operation has not been done during previous research. The oxidation of metals at high voltages is possible and has been described for electrospray ionization [57]. The Pt concentration of blank, anolyte and catholyte was carried out using ICP-MS with the Pt concentration measured three times per sample. In the reference water no Pt was found above the LOQ (limit of quantification, here  $0.02 \mu\text{g L}^{-1}$ ); the concentrations in the anolyte were 0.07, 0.08 and  $0.02 \mu\text{g L}^{-1}$ , respectively. Only experiment 2 showed a quantifiable Pt concentration in the catholyte ( $0.03 \mu\text{g L}^{-1}$ ).

### C.2.2 Other trace elements

In most water bridge experiments conducted so far, glass beakers or cuvettes were used, and water was sometimes stored in glass bottles [56]. Although glass is often considered to be an inert and insoluble material, this assumption is not entirely true. Whenever extremely pure water is in contact with glass surfaces, ions from the glass can dissolve into the water. Moreover, although the system was handled extremely carefully, wetting of the alligator clamps through dielectric forces is a possibility, thereby bringing ignoble metals in contact with the solution. Therefore, the solutions were investigated for all elements detectable with ICP analyses including ignoble metals such as Fe, Cu and Ni, but only a few elements were found: Na, K and Ca (see Table C.3). These elements are obviously originating from the beakers. Also here, the concentrations in reference, anolyte and catholyte were measured three times per sample.

### C.2.3 Carbon

Carbon originates from the carbon dioxide in the air / water equilibrium [58]. Applying Henry's law for an equilibrated solution under standard atmospheric conditions results in a carbon dioxide concentration of  $1.2 \cdot 10^{-5} \text{ mol L}^{-1}$  and a pH of 5.64. This value corresponds to the reference water's pH which was estimated to be in between 5 and 6 using a pH dye. With this information and the well-known equilibrium,

$$K = \frac{[H^+][HCO_3^-]}{[CO_2(aq)]} = 4.45 \times 10^{-7} \quad (\text{Eq.C.1})$$

the total dissolved carbon concentration  $[(CO_2(aq))]$  can easily be calculated, since the second dissociation of the carbonic acid can be neglected at this pH, and proton and hydrocarbonate concentrations are the same ( $2311 \text{ nmol L}^{-1}$ ). This concentration provides a calibration factor for the ICP measurements, allowing the calculation of the total carbon, hydrogen carbonate and proton concentration (pH) in anolyte and catholyte. The hydroxyl

ion concentration can be calculated via the auto-dissociation constant of water ( $10^{-14}$ ). From the sum of all dissolved ions the theoretical conductivity can be calculated using their molar conductivities. The results of these calculations are shown in Table C.3 and compared to the measured conductivities in Table C.4. All values displayed are above the limit of detection (LOD). It should be pointed out that the sum of the metal ions only cause between 1% and 3% of the total conductivity; 11% are due to  $HCO_3^-$  and 86-88% are due to protons.

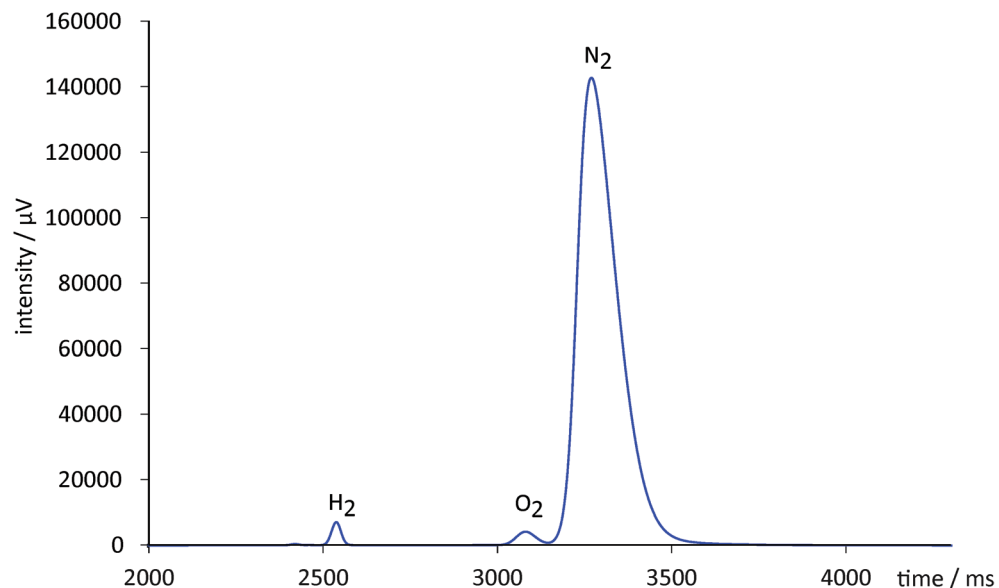
Standard errors of the measurements were used to calculate the sum of the standard deviations of the conductivities  $\Sigma\sigma(\lambda f)$  given in Table C.4. For reasons of clarity and readability these values are not shown in Table C.3.

Table C.3. Measured concentrations and ion conductivities of the ions in reference water I, anolyte (A) and catholyte (C) of experiments 1, 2 and 3.  $\Lambda_i$  values are molar conductivities,  $\lambda_0$  is the limiting molar conductivity of the respective ion [10] (\*... estimated value).

|   | Na <sup>+</sup> | K <sup>+</sup> | Ca <sup>2+</sup> | Pt <sup>2+</sup> | H <sup>+</sup> | OH <sup>-</sup> | HCO <sub>3</sub> <sup>-</sup> |
|---|-----------------|----------------|------------------|------------------|----------------|-----------------|-------------------------------|
| R1 / nmol L <sup>-1</sup>                   | 273.9           | < LOQ          | < LOQ            | < LOQ            | 2311           | 4.3             | 2311                          |
| R2 / nmol L <sup>-1</sup>                   | 427.5           | 72.4           | 47.7             | < LOQ            | 2311           | 4.3             | 2311                          |
| R3 / nmol L <sup>-1</sup>                   | 287.1           | 53.7           | 38.6             | < LOQ            | 2311           | 4.3             | 2311                          |
| A1 / nmol L <sup>-1</sup>                   | 253.1           | < LOQ          | < LOQ            | 0.37             | 2905           | 3.4             | 2905                          |
| A2 / nmol L <sup>-1</sup>                   | 275.3           | < LOQ          | < LOQ            | 0.43             | 2887           | 3.5             | 2887                          |
| A3 / nmol L <sup>-1</sup>                   | 247.0           | < LOQ          | < LOQ            | 0.11             | 3075           | 3.3             | 3075                          |
| C1 / nmol L <sup>-1</sup>                   | 278.2           | < LOQ          | < LOQ            | < LOQ            | 2508           | 4.0             | 2508                          |
| C2 / nmol L <sup>-1</sup>                   | 384.4           | < LOQ          | 40.6             | 0.13             | 2392           | 4.2             | 2392                          |
| C3 / nmol L <sup>-1</sup>                   | 385.7           | 87.5           | 36.9             | < LOQ            | 2380           | 4.2             | 2380                          |
| $\lambda^0 / \text{mS m}^2 \text{mol}^{-1}$ | 50.1            | 73.5           | 119.0            | 110.0*           | 349.8          | 198.6           | 44.5                          |
| $\lambda_{R1} / \text{nS cm}^{-1}$          | 13.7            | -              | -                | -                | 808            | 0.9             | 103                           |
| $\lambda_{R2} / \text{nS cm}^{-1}$          | 21.4            | 5.3            | 5.7              | -                | 808            | 0.9             | 103                           |
| $\lambda_{R3} / \text{nS cm}^{-1}$          | 14.4            | 3.9            | 4.6              | -                | 808            | 0.9             | 103                           |
| $\lambda_{A1} / \text{nS cm}^{-1}$          | 12.7            | -              | -                | 0.04             | 1016           | 0.7             | 129                           |
| $\lambda_{A2} / \text{nS cm}^{-1}$          | 13.8            | -              | -                | 0.05             | 1010           | 0.7             | 129                           |
| $\lambda_{A3} / \text{nS cm}^{-1}$          | 12.4            | -              | -                | 0.01             | 1076           | 0.6             | 137                           |
| $\lambda_{C1} / \text{nS cm}^{-1}$          | 13.9            | -              | -                | -                | 876            | 0.8             | 112                           |
| $\lambda_{C3} / \text{nS cm}^{-1}$          | 19.3            | -              | 4.8              | 0.01             | 837            | 0.8             | 106                           |
| $\lambda_{C3} / \text{nS cm}^{-1}$          | 19.3            | 6.4            | 4.4              | -                | 832            | 0.8             | 106                           |

**Table C.4.** Comparison of calculated and measured conductivities.  $\Sigma\lambda_f$  is the calculated conductivity,  $\sigma(\lambda_f)$  is the standard deviation of the calculated conductivities,  $\lambda_{exp}$  is the measured conductivities,  $\sigma(\lambda_{exp})$  are the standard deviations of the measured conductivities  $\Sigma\sigma(\lambda_f)$  is the sum of the standard deviations of calculated and measured conductivities, and  $\Delta\lambda$  is the differences between experimental and calculated conductivities. R... reference, A...anolyte, C...catholyte; 1,2,3: number of experiment

|     | $\Sigma\lambda_f$<br>$\mu S\ cm^{-1}$ | $\sigma(\lambda_f)$<br>$\mu S\ cm^{-1}$ | $\lambda_{exp}$<br>$\mu S\ cm^{-1}$ | $\sigma(\lambda_{exp})$<br>$\mu S\ cm^{-1}$ | $\Sigma\sigma(\lambda_f)$<br>$\mu S\ cm^{-1}$ | $\Delta\lambda$<br>$\mu S\ cm^{-1}$ |
|-----|---------------------------------------|---|-------------------------------------|---|---|-------------------------------------|
| R 1 | 0.93                                  | 0.01                                    | 0.85                                | 0.07  | 0.08  | 0.08                                |
| R 2 | 0.94                                  | 0.01                                    | 1.04                                | 0.08  | 0.10  | -0.09                               |
| R 3 | 0.93                                  | 0.02                                    | 0.89                                | 0.02  | 0.04  | 0.05                                |
| A 1 | 1.16                                  | 0.01                                    | 1.08                                | 0.01  | 0.03  | 0.08                                |
| A 2 | 1.15                                  | 0.01                                    | 1.07                                | 0.03  | 0.04  | 0.08                                |
| A 3 | 1.23                                  | 0.02                                    | 1.08                                | 0.03  | 0.05  | 0.14                                |
| C 1 | 1.00                                  | 0.03                                    | 0.87                                | 0.01  | 0.04  | 0.13                                |
| C 2 | 0.97                                  | 0.05                                    | 0.92                                | 0.01  | 0.06  | 0.05                                |
| C 3 | 0.97                                  | 0.02                                    | 0.82                                | 0.01  | 0.03  | 0.15                                |



**Figure C.5** Exemplary chromatogram of the atmosphere inside the dome above the water bridge after 100 minutes up-time showing significant quantities of  $H_2$  and  $O_2$ . Samples measured before bridge operation contained the  $N_2$  peak only (data not shown).

### C.2.4 Hydrogen production and measurement

An important feature of electrolysis is the production of oxygen and hydrogen. In order to investigate whether such a reaction was taking place, experiments were run under nitrogen atmosphere under a glass dome using Pt wires as electrodes coming in from below (Fig. 3.2). Gas samples were taken from the atmosphere inside of a glass dome, before and after 100 minutes of bridge operation with about 1.3 mA at initially 14 kV. In order to keep the current approximately constant, the voltage was gradually increased during the bridge operation to 16.4 kV. An exemplary resultant chromatogram is given in Fig. C.5.

The GC analysis of the atmosphere inside the gas detection water bridge set-up showed in pure nitrogen prior to the experiment and 0.1 mol% hydrogen for the measurement after 100min of bridge operation. Assuming an ideal gas, this value equals also 0.1vol%. The dome has an inner volume of approximately ( $\pm 10\%$ ) 880 mL, 0.1% of which equal ( $0.88 \pm 0.09$ ) mL. According to the Faraday equation,

$$n = \frac{I \cdot t}{z \cdot F} \quad (\text{Eq. C.2})$$

electrolysis for 100 minutes ( $t=6000$  seconds) at  $I=0.0013A$  equals  $4.04 \cdot 10^{-5}$  mol or 0.99mL  $H_2$  (with  $z=2$  electrons per mole gas and  $F = 96485\ C\ mol^{-1}$ ). Taking into account that hydrogen will concentrate on the top of the dome where the sample was taken, this calculation is in good agreement with the experiment, giving a quantitative proof for electrolysis taking place. So although the conductivity of the water used was low ( $\sim 0.9\ \mu S\ cm^{-1}$ , see Table C.4) it was sufficient to allow a current flow and thereby oxidation and reduction of water at the electrodes. At the anode, water is oxidized to oxygen (Eq. C.3), at the cathode, water is reduced to hydrogen (Eq. C.4a). Additional electrochemical considerations are given at the end of this work.



This solvent oxidation (Eq. C.3) and comparable reduction reactions which are common knowledge for low voltage electrolysis, have been suggested for high voltage applications before, e.g. electrospray ionization [57]. In an acidic system such as the presented one ( $pH < 7$ ), protons can also be reduced to hydrogen directly,



### C.2.5 EHD flow and microbubbles

The liquid flow in a floating water bridge system was visualized using a schlieren / shadowgraph technique as shown in Fig. C.6. The schlieren are visualizations of refractive index changes due to Ohmic heating of the water (in the bridge) and related density reduction when this warmer water is flowing into the colder anolyte and catholyte. They show movement towards the electrodes close to the water surface, jets downwards from the electrodes and movement back towards the bridge section and to the opposite electrode. This observation can be summarized as a lemniscate ( $\infty$ ) shaped overall flow pattern (see also [3], [59]).

The Faraday equation (C.2) describes how much gas is produced over time in an electrochemical system when a current is applied. With typical water bridge values like  $I = 400 \mu\text{A}$ ,  $t = 30 \text{ min}$ , it is straightforward that the amounts of hydrogen and oxygen produced are  $\sim 7.5 \mu\text{mol}$  and  $\sim 3.7 \mu\text{mol}$ , respectively.

At  $25^\circ\text{C}$  one mole of an ideal gas occupies 24.465 L. If  $\text{O}_2$  and  $\text{H}_2$  are considered ideal gasses, their volumes amount to 91 and 183  $\mu\text{L}$ , respectively. If those gasses would form bubbles at the electrode, there should be 174  $\text{O}_2$  bubbles and 349  $\text{H}_2$  bubbles formed over 30 minutes assuming 1 mm as bubble diameter; or one bubble every 10 and 5 seconds, respectively. This is not much, but should be observable. The fact that most of the time no bubble formation is observed, is due to the EHD shear flow which occurs close to the electrodes [59]. This flow detaches the bubbles during their growth while they are still microscopic. After that, the gas bubble starts to dissolve through the interface into the surrounding liquid. For any Euclidian body, the ratio of surface against volume decreases with increasing volume, meaning that in a smaller bubble a higher percentage of the gas molecules is in contact with the liquid than in a larger bubble. So if a bubble is detached from the electrode before it would do so naturally due to its buoyancy, it will dissolve faster than if it had a chance to grow to a larger volume. Besides, the EHD flow at the electrodes points downwards first the electrode and

then upwards again towards the bridge (see Fig. C.6a), therefore the path of the bubble in the water is longer compared to a direct path from the electrode to the surface. Therefore the EHD flow promotes enhanced gas solvation.

Bubbles in the bridge have been observed before. Microbubbles have been suggested to be source of light scattering in the outer layer of the bridge [5], [7]. Larger bubbles were observed directly using high speed visualization, as described in reference [5] on page 126: "... Occasionally, single tiny gas bubbles crossed the bridge..." The origin of these bubbles was hitherto not explained satisfactorily.

In an EHD bridge system where hydroquinone solution was decomposed, sometimes the formation of a large bubble inside of the bridge was observed (Fig. 2g and h in reference [60]). This bubble consisted of  $\text{CO}_2$  whose solubility also decreases with temperature. Therefore, although the chemistry is different, the physics of the two systems are comparable, validating the mechanism depicted in Fig. C.6b.

### C.2.6 Direct gas solvation

Oshurko *et al.* [61] suggested that the gasses may also dissolve in the liquid immediately and never form bubbles at all due to the enormously high overpotential. If this is correct, keeping in mind that the solubility of both oxygen and hydrogen decreases with temperature, the water bridge itself becomes the probable location for degassing of the solution: In a water bridge set-up there is a temperature gradient present where the bridge is hottest, with temperature differences between bridge and beaker water up to  $20^\circ\text{C}$  and more [3]. Therefore, water with dissolved oxygen and hydrogen partly degasses when passing through the warmer bridge, saturation of hydrogen and oxygen are never be reached, and no visible gas bubbles are formed at the electrodes.

### C.3 Vapour emission between 1300 and 2000 $\text{cm}^{-1}$

Region c in Fig. 4.19 shows a fine structure which appears as absorption in case of bulk water and as emission in case of the water bridge (see Fig. 4.20). For Fig. C.7 this region was baseline corrected and is compared to water vapour transmission bands calculated with the GATS simulator software using the HITRAN data base [62]–[64] with a line width of  $5 \text{ cm}^{-1}$ .

Fig. C.7 clearly shows that the fine structure of the bridge emission includes the molecular rotation spectrum of water molecules in the vapor phase. The fact that these lines appear as emission lines in the case of the bridge can be related to and explained by the effect of the strong electric field on water. The temperature of the bridge ( $37^\circ\text{C}$ ) is slightly elevated compared to that of the water in the beakers ( $22^\circ\text{C}$ ). Another important point is the presence of surface charge on the liquid interface. According to [65], [66] the electrostatic stress created by the presence of these charges counteracts the surface tension stress on the liquid surface. The net effect is a reduction of the liquid surface tension which allows higher diffusion of molecules through the interface, hence evaporation.

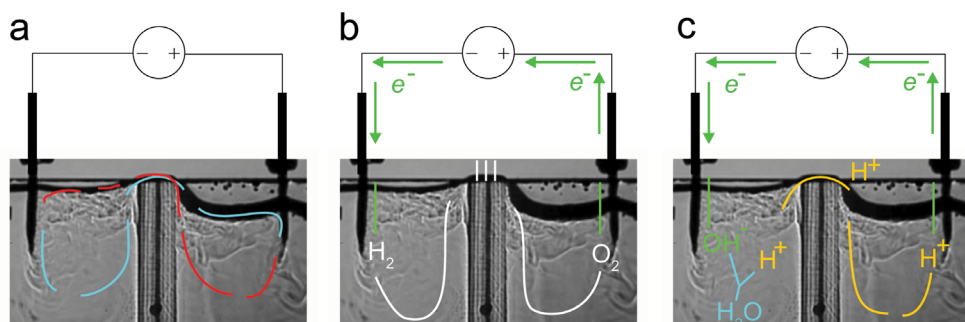
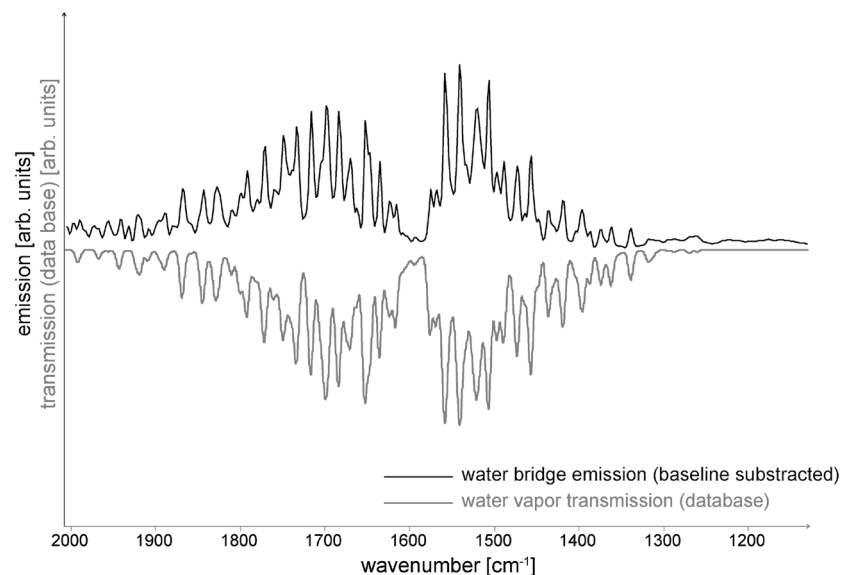


Figure C.6 Schlieren image of a water bridge between two cuvettes at  $\sim 9 \text{ kV DC}$ . a) EHD flow (blue and red arrows), b) gas flow (white arrows) and electrons (green arrows), c) proton flow (yellow), equilibration (blue) and electron flow (green).





**Figure C.7** Water bridge emission (baseline corrected) compared to the calculated molecular transmission spectrum of water vapor (GATS simulator, HITRAN data base,  $5\text{cm}^{-1}$  line width).

Finally, some micro-droplets could be visualized with laser sheet measurements in the region of the bridge (see Fig. C.8). The origin of these micro-droplets can be by both electrospray processes taking place at regions where the electric field is strongest and by the break-up of micro jets due to capillary waves on the liquid surface. Once airborne they will be exposed to an electrostatic stress caused by the electric field. Many authors have studied the stability of charged droplets in strong electric fields. It is well known that, depending on the liquid properties and droplet size, these droplets can gradually evaporate increasing their surface charge density until they reach the so-called Rayleigh limit after which they “explode” into smaller droplets. These smaller droplets evaporate again, and the process restarts. In the presence of a strong electric field electro-convection can further reduce the disruption threshold to 80% of the Rayleigh Limit. Normally, depending on the environment temperature and mean free path of the surrounding gas, this disruption can continue until the droplet starts to produce mono charged ions and molecules, like commonly seen in electrospray ionization. In addition, the presence of smaller droplets increases the liquid-air interface thereby increasing vaporization.

The airspace above the set-up was probed using laser-sheet visualization. For that purpose three  $\text{Ar}^+$  ion laser sheets,  $\sim 3\text{ mm}$  wide, separated in the vertical direction by  $\sim 3\text{ mm}$ , were directed parallel to the bridge axis thus illuminating micro-droplets above the set-up in three levels. In order to ease the visibility of these droplets, the negative of the actual image is shown in Fig. C.8.



**Figure C.8**  $\text{Ar}^+$  laser sheet visualization of microdroplets above the water bridge with an unfocused beam.  $\sim 3\text{ mm}$  wide sheets, separated in the vertical direction by  $\sim 3\text{ mm}$ , were directed parallel to the bridge axis, viewed at a right angle to the axis of the water bridge. For better visibility the negative of the actual image is presented.

The most probable reason why gas phase water molecules would emit rather than absorb IR radiation is their collision with ions accelerated by the electric field. It is well known that free electrons are rare in air [67], but they can be produced by collisions between electrons and molecules, between ions and molecules, by photo-ionization of gas molecules, by photo-electric emission from a cathode and by ionization of a metastable gas [68]. In the specific case of the water bridge next to the ions naturally occurring in the atmosphere, ions are also produced by electrospray as described above. After colliding with other gas molecules more ions will be produced and an avalanche is formed. The presence of these charged molecules in the air above the bridge between the electrodes creates a relative potential which affects the local electric field intensity creating an oscillation in the field. These field oscillations interact with the water air contact line and are responsible for the formation of waves on the bridge surface due to the sheer stresses induced [4]. These waves have been visualized with Schlieren and contouring techniques [5]. It is straight forward to estimate that positive ions deflected only by the electric field at a distance which is equivalent to the mean free path of air under normal conditions have enough energy to excite the water molecules present in the surroundings of the bridge: The mean free path of the air under normal condition [67] is  $6.6 \cdot 10^{-8}\text{m}$ , but will in this case possibly be an order of magnitude smaller due to the presence of the ionized air and the water molecules themselves. With the electrical mobility of a positive air ion [67] being  $1.4 \cdot 10^{-4}\text{ m}^2/(\text{V}\cdot\text{s})$  such a particle, being accelerated in the electric field, would have an energy of  $\sim 2 \cdot 10^{-4}\text{ eV}$ , which is about 4 orders of magnitude higher than the energy emitted ( $4.9 \cdot 10^{-8}\text{ eV}$  or  $\sim 2500\text{ cm}^{-1}$ ). Thus, a cloud of space charge travelling between the two electrodes will constantly produces new ions, which, after colliding with the water molecules, can excite them to emit the observed vapor emission lines. Since these lines are in between the spectral regions covered by the two thermographic cameras (see Fig.4.20), they are not observable on the thermographic images.



C.4 Diagnostic Values from EPSR simulation used for PSF recovery

Table C.5: Analysis of the simulation outputs used for the structure refinement presented in this study. Note that these values are not identical to those presented in table 4.3. This is due to the differences in the way the simulations were run. The data in this table is from ~20x more configurations. The trends in  $U_r$ ,  $P_r$ ,  $X^2$  qualitatively hold.

| EP <sub>req</sub> = 20 kJ/mol                      | Water bridge | Pure Water 40°C |
|--|--------------|-----------------|
| Number of Configurations                           | 23651        | 23654           |
| Number density [N <sub>H2O</sub> /Å <sup>3</sup> ] | 0.10020      | 0.10020         |
| Chi-squared  | 0.00548      | 0.00280         |
| Noise in Average g(r)                              | 0.00119      | 0.00013         |
| R-factor H <sub>2</sub> O neutron fit              | 0.00136      | 0.00213         |
| R-factor D <sub>2</sub> O neutron fit              | 0.00021      | 0.00081         |
| R-factor HDO neutron fit                           | 0.00031      | 0.00036         |
| R-factor X-ray fit                                 | 0.02004      | 0.00790         |
| Intermolecular pressure (P <sub>i</sub> ) [kbar]   | -2.60345     | -0.00235        |
| Intermolecular energy (U <sub>i</sub> ) [kJ/mol]   | -90.58690    | -61.34600       |
| Repulsive pair energies [kJ/mol]                   | -56.33250    | -61.34670       |
| Harmonic pair energies [kJ/mol]                    | 6.81611      | 7.22784         |

C.5 NMR spectroscopy of, and environmental effects on, dry glycerol

The proton 1H NMR spectrum for (nearly) anhydrous glycerol at 300 K (27 °C) is shown in figure C.9.

Three peak groups are readily apparent namely a multiplet from the alkyl protons (3.4-3.75 ppm), a doublet from the alcohol protons (5.05-5.35 ppm), and weak contribution by hydration water (4.63 ppm) a small amount of which enters even very pure samples due to preparation in open air. The contribution to the total signal from the hydration water is negligible even at relatively high water content (~37 wt% water) where the chemical shift peak at 4.63 ppm generates <5% of the total signal. The remaining water signal will merge with alcohol peak at 5.15 ppm. The response of the chemical shift to variations in water content and temperature are shown in figure C.10. As is expected the chemical shift effect will weaken slightly as temperature increases due to a redistribution of instantaneous intramolecular configurations and reduced intermolecular coupling as the hydrogen bonds weaken. Indeed loss of hydration water is seen in the reduction of intensity and broadening of the hydration water peak with increasing temperature. The other proton populations also show a response to increases in temperature. For alcohols the doublet merges into a single broad distribution whereas the fine splitting of the alkyl protons becomes more pronounced (data not shown). Both of these trend again fit with the view that as temperature increases the interaction

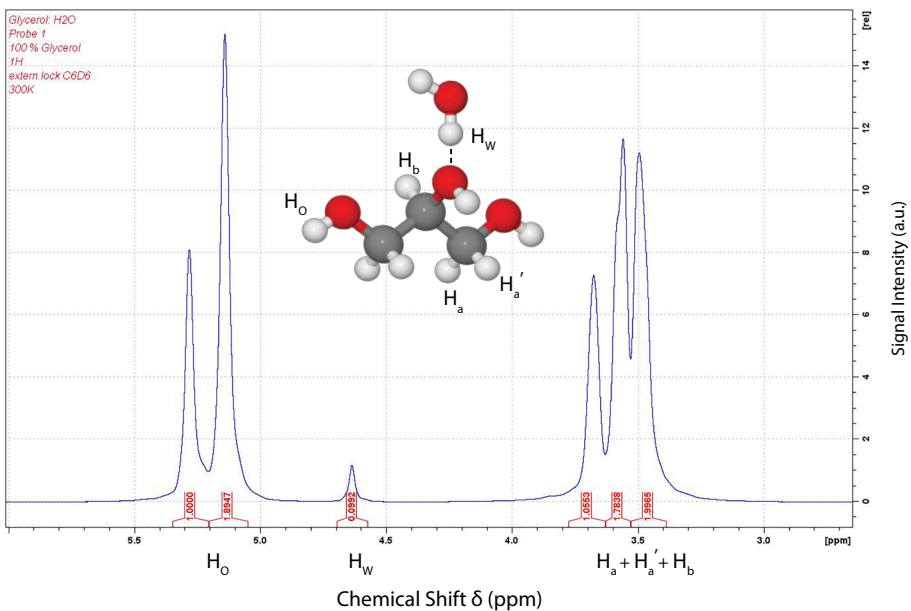


Figure C.9 Glycerol 1H Spectrum at 300K (27 °C) with peak assignments as per the molecular model shown.

between neighboring molecules weakens. For the hydrophobic alkyl groups the decreased dipole interference enhances the splitting due to J-coupling. The merging of the broad doublet into a narrower singlet peak for alcohol protons is due to the redistribution spin phase energy into a single Boltzmann like distribution indicating reduced dipole-dipole coupling. The spectral line width of a chemical shift signal has a connection to the  $T_2$  relaxation time for that group of protons as it describes the distribution of angular momentum frequencies in the spin ensemble.

Values of  $T_1$  and  $T_2$  relaxation in glycerol and glycerol: water mixtures at varying temperatures for each of the three peak groups previously discussed are plotted in figure C.11.  $T_1$  increases with temperature for all three groups of protons and shows only a small sensitivity to water content. The rather large deviation value in  $T_1$  for the hydration water peak in dry glycerol is likely an artifact due to poor signal intensity at elevated temperatures. Thus it can be assumed that  $T_1$  is largely insensitive to the chemical environment but rather sensitive to the thermal bath coordinates. This is in agreement with the thermodynamic interpretation linking spin-lattice relaxation and enthalpy. Furthermore, it reveals that  $T_1$  will tend to provide a reasonably accurate measure of temperature based solely on the arrangement of molecules

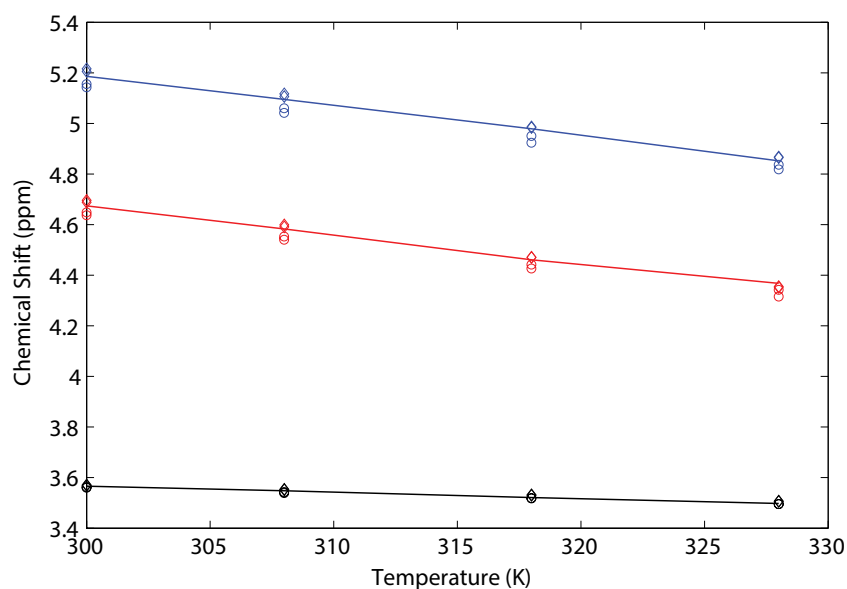


Figure C.11 (facing page) Effect of temperature and water content on relaxation times of the three peak groups measured for glycerol. Proton relaxation times from alkyl (red), alcohol (green), and hydration water (blue) follow similar trends but deviate in magnitude of response. Data from the water peak is missing in some cases, particularly at high temperature (and mostly for  $T_2$ ) as the signal intensity became too weak to reliably measure.

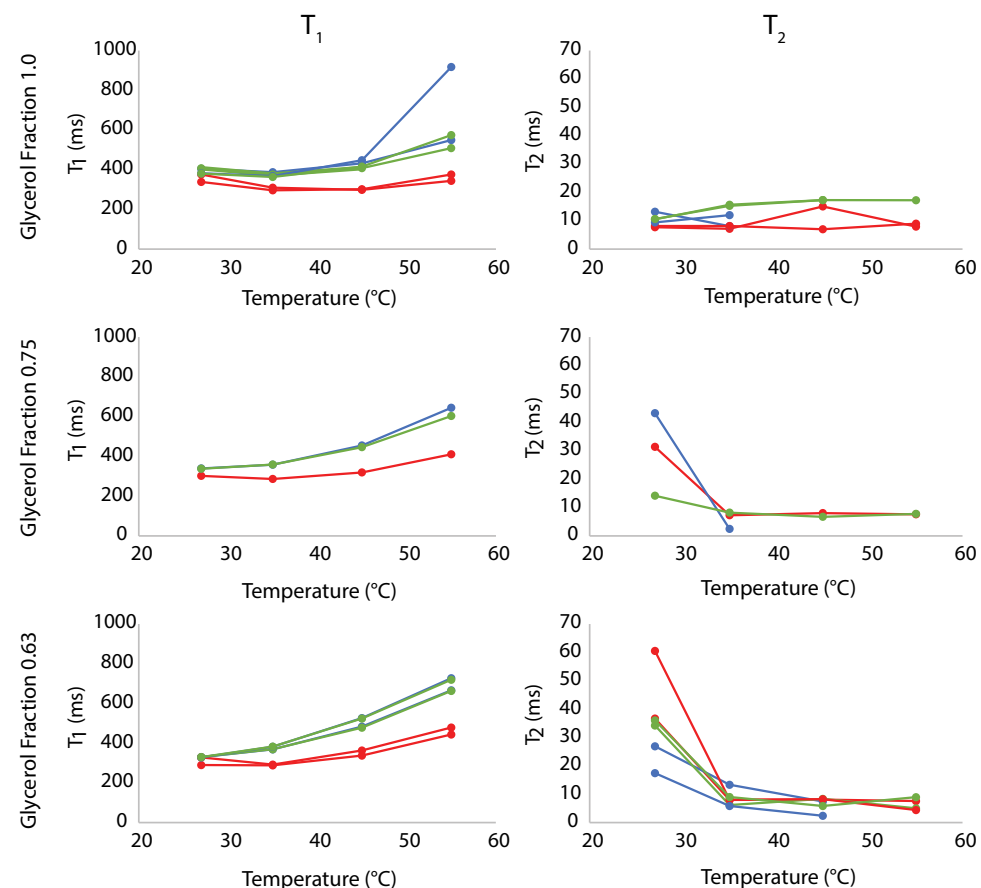
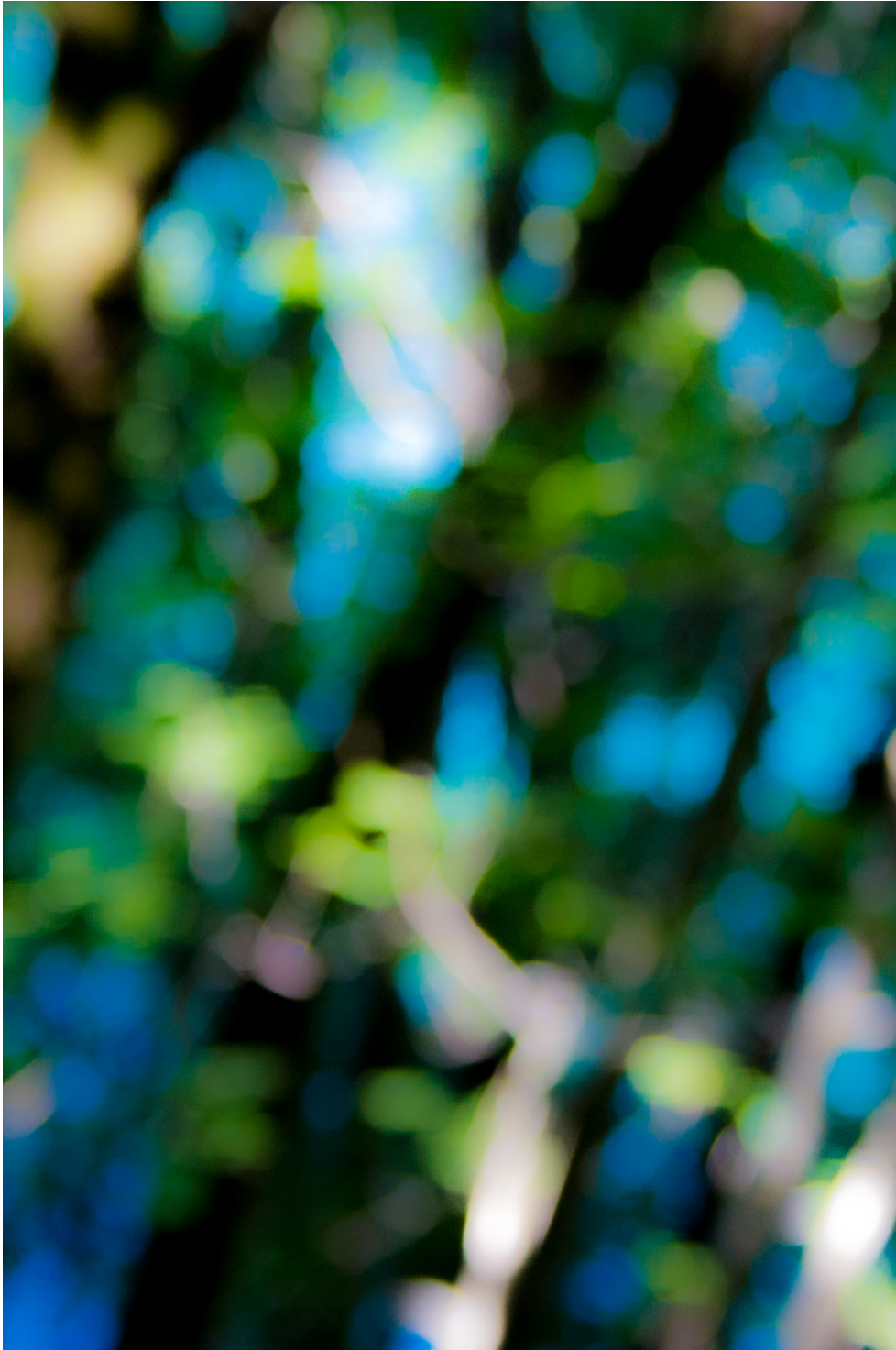


Figure C.10 Effect of temperature and water content on the chemical shift in the three peak groups of glycerol. Chemical shift value is taken from the center of mass for the alcohol doublet (blue), hydration water singlet (red), and the multiplet from alkyl protons (black). Three volume fractions of glycerol were measured: 1.0 (diamonds), 0.75 (solid line), 0.63 (circles).

in the liquid and thus forms a useful base of comparison to  $T_2$  derived temperatures. The transverse relaxation time is much more susceptible to variations of the local magnetic field. The strongest spin-spin coupling is between neighboring spins on the same molecule.  $T_2$  probes the stability of phase coherence across the molecular population [69]. This quantity has been extrapolated to intermolecular physical processes such as hydrogen bonding strength and molecular tumbling rates [70], [71]. These interpretations scale well with bulk physical properties such as viscosity [72]. However, in order to make an interpretation of  $T_2$  over the mesoscale it is useful to consider the configurational entropy of the liquid. A system with low configurational entropy will have relatively few local field inhomogeneity and  $T_2$  will be short as the bandwidth for energy redistribution will be narrow. This can easily be seen in plots of  $T_2$  shown on the right column of figure C.11. When the water content is very low  $T_2$  is stable against temperature. With the addition of a small fraction of water the increase in configurational entropy causes a rapid increase in the relaxation time. The distortion of the local field by the presence of hydrogen bonding water retards the dissipation of the transverse magnetic relaxation due to enhanced phase decoherence. It is interesting to note that this behavior disappears with increasing temperature and  $T_2$  becomes insensitive to temperature. This is due to the disruption of the glycerol-water hydrogen bond which drives a second order transition whereby the configurational entropy vanishes [73]. The transverse relaxation of glycerol, with a few wt.% water, will be insensitive to temperature at the expected bridge temperature  $\sim 40^\circ\text{C}$ . Any changes recorded in  $T_2$  that do not provide a good agreement with temperature most clearly point to a change in magnetic field distributions within the liquid. Furthermore, it is typically assumed when interpreting the relaxation response functions that all interactions have the same correlation time [72].





# 5

## Excited Liquid Water

*The electrically pumped non-equilibrium excited state at the mesoscale*

*We now derive a coherent picture of how the electric field gradients, proton mobilities, and other salient features of the floating water bridge reveal the molecular basis operating within EHD phenomena. Dynamic heterogeneity can be excited in liquid water which is stabilized at the mesoscale by the emergence of delocalized protons.*

## 5.1 Introduction

The challenge in this work is that we are dealing with processes that occur both on the classical and on the quantum level. The mixing of these two well defined worlds is the basic concept defining the mesoscale which is not as a physical 'size' but rather the onset of mixed quantum and classical behavior, which is marked by dynamic chaotic behavior. The difficulty is that as of yet no definitive single test for this mesoscale behavior exists. Rather, the behavior can be inferred by examining the experimental evidence in toto. EHD bridges thus serve as a model system for building cross-correlated data sets for mechanism elucidation.

## 5.2 The discovery of charge imbalance in EHD bridges

### 5.2.1 Impedance spectroscopy of pure water

Impedance spectroscopy allows the depiction and simulation of a complex system like an aqueous solution as a simple electric circuit. As shown in Fig. 4.4 an aqueous solution behaves like a resistor and a capacitor in parallel. In other words, the passage of charge carriers has a scattering component proportional to the accelerating voltage; many of which become locally trapped in the material resulting in a heterogeneous distribution of charges whose spatial density is dependent upon the current density and relaxation dynamics of the polarized medium.

### 5.2.2 Conductivity shift of anolyte and catholyte

The reason for the difference in conductivity between anolyte and catholyte is due to concentration increase of carbonic acid in the anolyte and decrease in catholyte during bridge operation [1]. In the present work we show that there is an additional small contribution which cannot be measured with a conductivity meter, but is clearly visible in an impedance spectrum. This contribution is discussed in detail for both anolyte and catholyte in the following sections.

### 5.2.3 Anolyte

In an EHD bridge in water, electrolysis takes place, and protons are transported from the anolyte to the catholyte as discussed in §4.2. The number of protons produced per second can be calculated according to the Faraday equation,

$$\frac{n}{t} = \frac{I}{zF} \quad (\text{Eq.5.1})$$

with  $n$  being the moles  $\text{H}^+$  being produced,  $t$  the time,  $I$  the current,  $z$  the number of electrons per mole substance, and  $F$  the Faraday constant. A typical value for the current is 0.5 mA, meaning that protons are produced at a rate of  $=5.18 \cdot 10^{-9} \text{ mol/s}$ .

The mobility of these protons,  $\mu_B$ , was determined in §4.5 and found to be  $9.34 \cdot 10^{-7} \text{ m}^2/\text{Vs}$ . The electric field strength  $E$  varies over the bridge set-up between 1 kV/cm in the beakers and 5 kV/cm in the bridge. The velocity  $v$  of the protons in the beakers can thus be calculated from

$$v = \mu_B E \quad (\text{Eq.5.2})$$

and yields a value of 9.34 cm/s. In a bridge set-up with beakers of 6 cm diameter and the electrodes placed in the middle, the protons have to travel 3 cm before they enter into the bridge. At the given speed it thus takes the protons 0.32 s to travel from the anode where they are created to the bridge. There they accelerate to 5 times of their original speed due to the stronger electric field. Therefore, with the production rate determined above, at all times during bridge operation, a surplus of  $n \cdot t = 1.66 \cdot 10^{-9} \text{ mol}$  of travelling protons is present in the anolyte. This surplus of protons will also remain in the anolyte if the current is suddenly switched off, since their path to neutralization, the bridge, is no longer available. They are trapped in the anolyte unable to react with the beaker walls, the gas phase, or the platinum electrode.

Being additional charge carriers, these protons increase the conductivity of the anolyte. The measurements reported in §4.2 have shown that even when using glass vessels (even more so when using Teflon beakers), the contribution of ions to the overall conductivity is marginal, 87% of the conductivity of the water in a EHD bridge set-up is due to protons. Therefore, the excess protons trapped in the anolyte increase the number of total protons in the system, and also the conductivity of the liquid. This increase,  $\Delta$ , can be calculated using  $\Delta$ , the limiting molar conductivity of  $\text{H}^+$  in water, considering that the above mentioned number of protons is present in 66 mL,

$$\Delta = c^{0, \text{H}^+} \quad (\text{Eq.5.3})$$

with  $c$  being the concentration of excess protons in  $\text{mol m}^{-3}$  and  $= 349.8 \text{ mS m}^2 \text{ mol}^{-1}$ . The conductivity increase amounts to  $0.088 \mu\text{S cm}^{-1}$ . This increase is rather small and difficult to measure with a normal conductivity meter; however, it is easily recognized if measured with an impedance analyzer. Moreover, if measured consecutively, the conductivity of the same sample will decrease, since these additional free charge carriers are destroyed by the read-out process in the spectrometer (reduced to hydrogen),





The measured difference in conductivity before and after the impedance measurement will certainly be smaller than (or equal to) the calculated shift, since three important factors have not been taken into account:

1. the stability of the free protons in the solution,
2. the unequal distribution of the protons in the beaker during the sample extraction (if extracted during bridge operation), and
3. the fact that the measurement destroys (reduces) the protons during the measurement.

Therefore, an exact quantitative reproducibility of spectra is difficult to achieve. But, two or more consecutive impedance measurements of the anolyte should thus always show two features: increasing impedance with each measurement; and the proton reduction as an additional pseudo-capacity manifesting itself as an anti-clockwise pointing tail in the Nyquist plot [2]. These features are shown in Figs. 4.11 and 4.12, respectively. It is not the platinum which is reduced, but the excess protons. The concentration of Platinum dissolved by this process is more than 3 orders of magnitude lower ( $<1 \text{ nmol L}^{-1}$ , contribution to conductivity  $\leq 0.00005 \mu\text{S cm}^{-1}$ ) than that of the protons, and thus cannot be held responsible the behavior observed (anti-clockwise feature and increase of impedance). In consecutive measurements, the two features diminish due to the reduction of the protons. Finally, it is straightforward to calculate that the above discussed amount of excess protons would yield a total (maximum) charge of the water of  $0.16 \text{ mC}$  per beaker or  $2.4 \text{ mC L}^{-1}$ , and the stoichiometrically correct formula of the anolyte would be  $\text{H}_{2.00000000045} \text{O}^{\delta+}$ .

## 5.2.4 Catholyte

A different situation is encountered in the catholyte. Here, hydroxyl ions are formed. Assuming that the mobility ratio at EHD conditions is comparable to the low voltage situation,  $\mu_{\text{B}}(\text{H}^+)/\mu_{\text{B}}(\text{OH}^-) \approx 0.57$  [3], hydroxyl ions can travel only about half as far as protons in the same time, and should therefore never reach the anolyte. It has indeed been shown experimentally §4.2 that neutralization happens in the catholyte beaker somewhere between the cathode and the bridge.

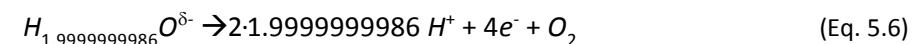
When a sample is extracted close to the cathode, the opposite situation compared to the anolyte is thus expected, specifically a surplus of hydroxide ions. However, the situation clearly differs from the anolyte, and a number of additional points must be considered: First, the catholyte beaker contains *both* free protons and hydroxyl ions depending on where a sample is extracted. It is thus no longer possible to calculate the concentration of  $\text{OH}^-$  by simply assuming the whole beaker volume. For the sake of simplicity and as an estimate from observation, an “effective” volume of  $22 \text{ mL}$  (one third of the beaker volume) will be assumed. Secondly, the pH of the original water in the beakers is about 5.5; thus there are considerably more  $\text{H}^+$  ( $2.3 \mu\text{mol/L}$ ) than  $\text{OH}^-$  ( $0.004 \mu\text{mol/L}$ ). Therefore, the addition of “free”

$\text{OH}^-$  will merely reduce the number of  $\text{H}^+$  due to recombination to  $\text{H}_2\text{O}$ , leading to an overall *decrease* of conductivity and *increase* of impedance. Due to the reduced effective volume in the catholyte, the maximum difference can be up to three times larger, about  $0.24 \mu\text{S cm}^{-1}$ .

Nevertheless, in analogous manner as shown for the anolyte, an excess negative charge remains present in the liquid, in this case up to  $7.3 \text{ mC L}^{-1}$ , and the stoichiometrically correct formula of the catholyte would be  $\text{H}_{1.99999999986} \text{O}^{\delta-}$ . This charge can best be seen as *ater*protons thus it is not electronic, and can therefore, like the proton charge in the anolyte, not discharge at the electrodes. It will, however, be neutralized once an electronic current is applied, namely by the oxidation of  $\text{OH}^-$  to  $\text{O}_2$ .



Naturally, the hydroxyl ions described in eq. (5.5) are not free at a pH of 5.5, but are representative for the excess negative charge. The oxidation could therefore also be written as



This process will “free” the previously occupied protons, and the conductivity will therefore *increase* with each subsequent impedance measurements. Moreover, in a Nyquist plot, a feature signifying an oxidation in terms of a pseudo inductance [2] is visible – a clockwise pointing tail – and diminish if the measurement is repeated. These features are depicted in Figs. 4.6 and 4.8, respectively. Again, in contrast to [2], it has been shown that in this case the concentration of Platinum is too low ( $<0.1 \text{ nmol L}^{-1}$ ; contribution to conductivity  $\leq 0.00005 \mu\text{S cm}^{-1}$ ) to be responsible for the behavior observed.

## 5.3 The emergence of proton channels

### 5.3.1 The infrared signature of Grotthuss librations

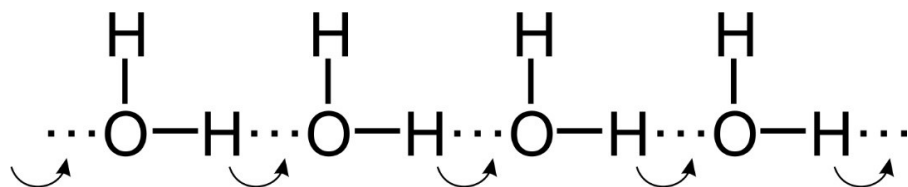
As observed in the IR water bridge emission measurements (§4.4.4.3, [4]), the probability density function is red-shifted and narrower in the water bridge, indicating that the number of spectral diffusion modes is reduced. The described effect would cause a slightly preferential orientational motion of the water molecules compared to the motions in bulk water.

Let us exploit three theoretical approaches to explain this feature:

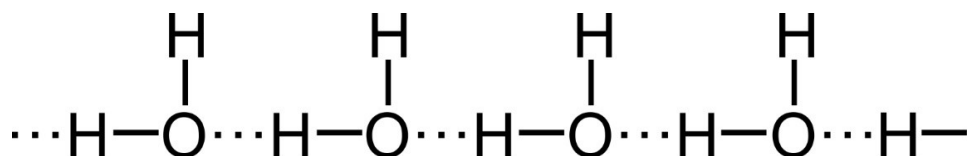
(i) Focusing on the electric field and disregarding the current, one might think that both spectral differences may arise from a librational mode enhancement due to the alignment of the dipolar  $\text{H}_2\text{O}$  molecules in the applied electric field. However, previous neutron and X-ray scattering have suggested that the structure of water in the bridge is similar to that of bulk

water [5]–[7]. This is reasonable because the intermolecular forces are much stronger than any forces exerted by the externally applied field [8] since the electric fields present in the bridge are far too weak to significantly affect the water structure. For example a bridge 1 cm in length under an applied potential of 15 kV, taking the dielectric permittivity of water to be 78.5, the field in the bridge can be calculated as  $15,000 / (78.5 \cdot 0.01) = 1.92 \cdot 10^4 \text{ J} \cdot \text{C}^{-1} \text{ m}^{-1}$ . To put this into perspective consider a dipole of water frozen in the direction of the external field, its energy would be the product of the applied field and the water dipole moment which is  $6.17 \cdot 10^{-30} \text{ C m}$ . Thus, the energy of a “frozen” water dipole would be  $1.18 \cdot 10^{-25} \text{ J}$ . The thermal energy  $k_B T$  at 310 K is  $4.3 \cdot 10^{-21} \text{ J}$ , i.e., more than four orders of magnitude greater. This is why using the homogeneous electric field approximation fails to recover the librational modes.

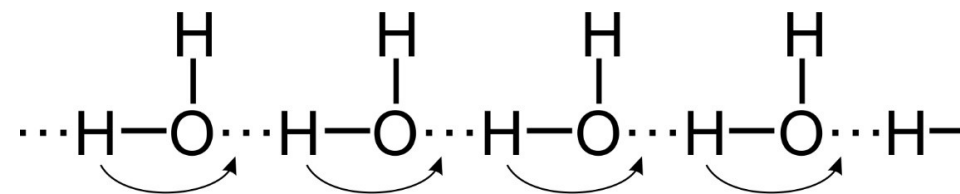
(ii) The second ansatz for the charge transport may be found by considering proton and defect-proton conductivity, more precisely, a mechanism of conduction by cooperative proton transfers [9]. In this mechanism through a chain of linked hydrogen bonds,



cooperative proton transfer can occur yielding, as indicated by the arrows, a hydrogen-bond chain in reversed orientation,



with the net effect of a proton transfer from one end of the chain to the other; or a proton hole in the opposite direction. This process can happen very rapidly if the protons, as a result of their mutual interactions are able to tunnel across the hydrogen bond chain in a concerted fashion. Evidence for such a cooperative transfer would be an exceptional mobility of the proton in the conduction process. Instead of considering separate molecules, the proposed proton transfer with tunneling may be discussed equivalently by considering the protons to exist in a proton conduction band (or better “proton channel”, since conduction band is defined for solids only), so that the material is, according to Onsager [10], a “proton semiconductor”. This proton transfer process is still an incomplete description of conduction though, because it leaves the hydrogen bond chain in a reverse orientation from that in which it originally was, thereby being unable to permit any further proton transfer in this condition. Therefore, a reorientation process of the chain, consisting of librational motions of each molecule, occurs,



This process can be considered as the sequential motion of an orientational (or Bjerrum) defect along the chain [11]. Since the proton conduction is directional, so are the motions, explaining the slightly smaller FWHM of the water bridge emission compared to bulk water. Thus the increase in librations causing the emission band at  $\sim 2200 \text{ cm}^{-1}$  as described in §4.4.4 arises naturally from the proton conduction process.

Let us assume that the high voltage, which allows the water bridge to operate, pumps protons in the somewhat ice-like (from a bond strength point of view, not structurally) water in the bridge from their vibrational O–H stretching ground state  $n=0$  to a level two quantum numbers above the ground state and that this  $n=2$  level acts as a proton channel,  $\text{H}^+$ -PC (proton channel). Protons promoted to the  $\text{H}^+$ -PC will carry an  $\text{H}^+$  current from the cathode to the anode. Let us further assume that there is also a defect proton conduction band,  $\text{H}^-$ -PC, which lies only one quantum number above the ground state, at  $n=1$ . The deprotonated sites on this  $\text{H}^-$ -PC will carry an  $\text{H}^+$  current in the opposite direction, from anode to cathode. The net  $\text{H}^+$  current would be the difference between these two partial  $\text{H}^+$  currents.

Next we ask whether there is spectroscopic evidence consistent with this dual  $\text{H}^+$  current mechanism. The fundamental O–H stretching mode  $\nu_{\text{OH}}$  in  $\text{H}_2\text{O}$  corresponds to the transition from the  $n=0$  level to the  $n=1$  level requiring approximately  $3300 \text{ cm}^{-1}$  [12]. The energy to make the transition from the  $n=1$  to the  $n=2$  state is somewhat less,  $2500\text{--}3000 \text{ cm}^{-1}$  [13]. If the high voltage causes  $\text{H}^+$  pumping to populate the  $n=2$  level of the O–H stretching mode  $\nu_{\text{OH}}$  in excess of the thermal equilibrium value, the  $\text{H}^+$  on  $n=2$  will tend to transition downward to the  $n=0$  level. A direct optical transition spanning two quantum numbers is dipole-forbidden. However, if a fraction of the downward transition energy is used to simultaneously excite a librational mode of the  $\text{H}_2\text{O}$  molecules, the transition becomes allowed. If this process indeed occurs, as the pumped-up  $\text{H}_2\text{O}$  molecules on the  $n=2$  level fall back to the  $n=0$  level, they will emit IR photons corresponding to the energy difference of the  $\nu_{\text{OH}}$  transition from  $n=2$  to  $n=0$  minus the energy that goes into the excitation of the librational mode.

It is tempting to speculate that the broad  $2150 \text{ cm}^{-1}$  emission feature that seems to be characteristic of the water bridge might be the result of such a process where pumped-up  $\text{H}^+$  de-excite across two quantum numbers while transferring some of their energy to the librational modes of the  $\text{H}_2\text{O}$  molecules, emitting the difference in the form of  $2150 \text{ cm}^{-1}$  photons. If this reasoning is correct, there should also be an excess IR emission band at the sum of the frequencies,  $3000 + 2150 = 5150 \text{ cm}^{-1}$ . This hypothesis remains to be tested.

### 5.3.2 Two distinct proton populations

We have measured the quasi-elastic neutron scattering (QENS) of an electrohydrodynamic liquid bridge formed in pure water, a special experiment allowing the investigation of water under high-voltage without high currents. From the two proton populations distinguished one consists of protons strongly bound to oxygen atoms (**immobile population, elastic component**) and a second one of quasi-free protons (**mobile population, inelastic component**). A quantum-mechanical extension of the Grotthuss mechanism is proposed in terms of small scale proton channels (PC) forming in electrically stressed liquid water.

#### 5.3.2.1 Comparison of results to confined water in an electric field

In a recent study QENS measurements have been used to study the effects of electric field on the dynamics of water molecules in the pores of folded silica sheet material FSM-12 at temperatures between 250 and 300K [14]; Diallo *et al.* report that in the absence of a field, molecular diffusion is significantly slowed down with decreasing temperature. The application of an electric field of 25 kV/cm, a field strength about 4 times higher than present in the water bridge, was shown to significantly enhance the translational diffusion of water molecules. The authors interpreted this finding by identifying two distinct translational processes, a local diffusion arising from water molecules restricted within a transient cage made of surrounding water molecules and a slower, unrestricted diffusion due to molecules escaping from the transient cages. Naturally, effects of polarization are more pronounced at very short distances under confinement in a dielectric medium. It is noteworthy though that although setting, temperature and boundary conditions clearly differ from the present study, the results are comparable: In both cases the application of the electric field creates two populations of scatterers with different mobilities, one of which being significantly higher than without an electric field applied. We agree with Diallo *et al.* [14] that it appears that moderate electric fields have significant impact on the hydrogen bond dynamics, and that existing theories applicable at large fields may have to be corrected at moderate fields.

#### 5.3.2.2 Comparisons of results to electrohydrodynamic experiments

Several other authors [15]–[17] used a different but more experimental approach in electrohydrodynamics (EHD) and defined a temperature dependent “proton mobility” for pure water by

$$\mu_q = \mu_{q,0} (1 + a\vartheta) \quad (\text{Eq. 5.7})$$

where  $\vartheta$  is the temperature in °C, the proton mobility at 0°C ( $2.49 \times 10^{-7} \text{ m}^2 \text{V}^{-1} \text{s}^{-1}$ ) and an ion specific constant, in this case  $= 1.83 \times 10^{-3} \text{ }^\circ\text{C}^{-1}$  [15]. When high voltages are applied to liquids, it is known that EHD forces can produce an anomalously high “charge mobility” [18]. Related experimentally observed phenomena are described simply by replacing the “true” mobility with an “apparent” EHD mobility, an expression derived by Ostroumov [19], Stuetzer [20], and

Félici [21], These authors equated the kinetic energy change of the electrohydrodynamically stressed liquid to the electrostatic energy change, resulting in

$$\mu_H = \left( \frac{C_i \varepsilon}{\rho} \right)^{\frac{1}{2}} \quad (\text{Eq. 5.8})$$

Here,  $\varepsilon$  and  $\rho$  are the permittivity and the mass density of the liquid, and  $C_i$  is an electrode dependent factor (“injection strength”) which is sometimes omitted [15], thus its value is presumably  $\sim 1$ . According to Félici [21], the charge mobility defined for EHD purposes can alternatively be calculated from the liquid velocity and the electric field,

$$\mu_H = \frac{v}{E} \quad (\text{Eq. 5.9})$$

where  $v$  is the filament velocity, and  $E$  is the average electric field.

In order to compare the results from EHD research with our findings of the water bridge, Table 5.1 summarizes the values of “proton mobility” obtained from the EHD formulae described above. Using the Stokes-Einstein equation we can relate the diffusion constant  $D$  (QENS) to the individual mobility of a proton  $\mu_q$  (comparable to the EHD defined charge mobility  $\mu_H$ ) with

$$D = \frac{\mu_q k_B T}{q} \quad (\text{Eq. 5.10})$$

with  $k_B$  being the Boltzmann constant,  $q$  the elementary charge (charge of a proton) and  $T$  the absolute temperature.

The proton mobility of the second population, calculated from equation (5.10) using the corrected value for  $D$  from Table 4.5, now matches the “apparent” EHD mobilities from equations (5.8) and (5.9). These values are compared in Table 5.1. The EHD permittivity-dependent mobility (Eq. 5.8) was calculated using density and permittivity values for water at 50°C extrapolated from [22] and [23] assuming  $C_i=1$ ; and the electric field dependent mobility was derived using an average field strength within the bridge of  $3.5 \times 10^5 \text{ V/m}$  [24] and a velocity determined by laser-velocimetry in a previous work by 0.33 m/s [25] (Eq. 5.9).

Table 5.1: Proton mobilities ( $\mu_H$ ) derived from the present experiment, molecular and electrohydrodynamic considerations (last column for reasons of comparison to Table 4.5).

| Method   | Equation nr. | $\mu_H$<br>$10^{-7} \text{ m}^2 \text{ V}^{-1} \text{ s}^{-1}$ | $\mu_H$<br>$10^{-5} \text{ cm}^2 \text{ V}^{-1} \text{ s}^{-1}$ |
|--|--------------|--|---|
| Stokes – Einstein ( $D$ from these measurements) | (5.10)       | 9.34   | 934   |
| Temperature dependent (no E-field, 50°C)         | (5.7)        | 4.77   | 477   |
| Ostroumov, Stuetzer and Félici                   | (5.8)        | 8.42   | 842   |
| Félici   | (5.9)        | 9.43   | 943   |

### 5.3.2.3 Pre-amble for a possible molecular interpretation of the experimental QENS data.

When calculating the mobility of quasi-free protons in the second population based on the diffusion constant obtained by the inelastic scattering, it matches the “electrohydrodynamic mobility” reported in the literature (see table 5.1). This EHD mobility is derived from a field theory approach for “space charges” which are injected into pure water. Its value is found to be generally much higher than diffusion based mobility. The inelastic scattering, which probes protonic diffusion, allows the derivation of that quasi-free protonic mobility, providing data to suggest that the EHD mobility essentially matches the mobility of quasi-free protons in a proton channel. Thus this data offers a molecular confirmation of the EHD mobility being a genuine property of water under strong electric fields often found in literature [18]–[21]. In the following paragraphs, a molecular interpretation will be attempted.

### 5.3.2.4 Proton jumps

The mean jump length  $l$  of a proton, according to the random jump diffusion model, is a function of the diffusion constant  $D$  and the residence time  $t_0$ ,

$$\langle l^2 \rangle_{av} = 6D\tau_0 \quad (\text{Eq. 5.11})$$

Depending on the temperature this jump length varies in regular liquid water between  $\sim 1.4 \text{ \AA}$  (0°C) and  $\sim 1.7 \text{ \AA}$  (96°C) [26]. At 50°C,  $l_{av} = 1.6 \text{ \AA}$ , which indicates a predominant nearest neighbor interaction, consistent with a diffusion probably assisted by rotational jumps as suggested by the Grotthuss mechanism. In the bridge water  $l_{av} \sim 3.0 \text{ \AA}$ , which is about twice the amount of regular bulk water. This greater jump length indicates an increased proton delocalization and a shift from nearest to “next-to-nearest” neighbor interaction. Since this is true for every quasi-free proton they thus no longer belong to single water molecules but constitute a band-like energy structure over small length scales. This idea can also be applied

to regular bulk water, albeit to a lesser extent: Hassanali *et al.* [27] have recently shown that despite, its long successful history, the Grotthuss mechanism oversimplifies and neglects the complexity of the supramolecular structure of water. According to Hassanali *et al.* [27] the motion of protons through the water network is a complex process involving the collective behavior of both structural and dynamical properties of the network. Proton conduction can be imagined as the proton moving through a free-energy landscape along a generalized transfer coordinate.

In this picture, liquid bulk water is no longer considered an ensemble of  $\text{H}_2\text{O}$  molecules, but rather a network of hydrogen and oxygen connected by fluctuating covalent and hydrogen bonds. One could argue that the hydrogen bonds are relatively weak compared to the covalent bond, which is probably the reason why the traditional concept of bulk water has been upheld and successfully applied in simulations. However, if that difference is mitigated by a significant contribution of hydrogen bonds enforced by the high-voltage electric field as it is the case with the water bridge, the idea becomes feasible. The energy surface could be called “proton conduction band” or proton channel, but it differs from its electronic counterpart in semiconductors and proton conduction bands in solids [28], [29] in so far that it is not smooth but rough on short time scales, characterized by minima of varying depths and activation barriers which are constantly fluctuating. Within such an energetic landscape, changing constantly as a function of time, a fraction of the protons can delocalize along the hydrogen bonds [27], [30], making up the proton channel (PC), whereas the rest is more immobile, more strongly bound [31].

### 5.3.2.5 Proton Channels

The present situation can be treated as a two-potential-well case where proton transfer can either take place on the quantum level  $v=0$  or  $v=1$  (relative to the O-H stretching mode, ground levels), coupled to phonons, or on the quantum level  $v=2$  [30] which is assumed to be the onset of the proton channel (PC), allowing protons, which have reached this level, to translate in a single jump over more than one  $\text{H}_2\text{O}$ – $\text{H}_2\text{O}$  distance, irrespective of the relative orientation of the  $\text{H}_2\text{O}$  molecules, which can change only at the phonon frequencies.

In order to approach the idea of proton channels it is useful to consider the effect of a crystallographic defect in ice on the local proton balance as described by Bjerrum [11]. Here the loss or gain of a proton relative to an oxygen lattice site establishes a local charge imbalance that forces the rotational translocation of water molecules. This can be further generalized for the liquid state by considering the classical translation of an excess solvated proton via the Grotthuss mechanism [32], and previously illustrated above, whereby the transition state reaction



can be seen as a special case of the ground level to proton channel (PC) mechanism except that, in the classical case, defect and excess protons are spatially constrained to be on neighboring  $\text{H}_2\text{O}$  sites. The proton transfer between them requires phonons that will align the  $\text{H}_2\text{O}$  in the right way [33]. Once this constraint of proton transfer taking place only between next neighbors is relaxed, it is easy to imagine that the protons would enter a PC and jump over an intermolecular distance of  $n\text{H}_2\text{O}$ , unaffected by the precise alignment of the molecules, with  $n > 1$ . Each proton that has reached the PC and delocalizes leaves behind a deprotonated site, e.g. a defect proton in the ground level, equivalent to an  $\text{OH}^-$ , which can then propagate by a “classical” translocation mechanism similar to Bjerrum and/or Grotthuss or is immediately involved in the next transfer mechanism.

In this context it is important to not fall victim to the misconception that protons in condensed matter can be “free”. They are always associated with an energy level. In a powerful electric field, which can pump protons to a higher quantum level such as  $v=2$ , the  $v=2$  level becomes populated, allowing the proton to enter an energy state, where it can quantum mechanically delocalize over a string of other  $\text{H}_2\text{O}$  unaffected by their orientation relative to each other and relative to the optimal hydrogen bond formation (which probably happens on  $v=1$ ). It is this energy state, presumably at  $v=2$ , which we call the proton channel (PC). It is expected that the mobile proton population would have a spectroscopic signature given the requirements of energy conservation. Indeed the non-thermal emission feature previously discussed in §5.3.1 coincides with the energy transitions between the  $v=1 \rightarrow 0$  and  $v=2 \rightarrow 1$ . These pump energies would provide access to the stable energy minimum for proton delocalization along the PC.

As discussed in the results section the quasi-free proton movement through the oxygen lattice is approximated as hopping between vacant lattice sites, with a jump-time that is assumed to be very short and a quasi-free proton mobility described in terms of a residence time  $t_0$  and a translational diffusion coefficient  $D$ . This residence times derived from the QENS measurements presented here fit well to this PC theory. A residence time (as defined within the jump model) can normally not be expressed in terms of a frequency. However, a time period of 1 ps corresponds to a frequency of  $10^{12}$  Hz. This falls well into the frequency range of phonons at temperatures around 300-320 K, consistent with the classical Grotthuss mechanism.

## 5.4 Approach to radiation scattering in electrically stressed liquid water

Determining how the structure of a polar liquid such as water will be influenced by a moderate electric field in order to promote proton channels is not a straightforward task. The employed scattering methods suffer from inherent variability which is compounded by critical assumptions in data treatment and limitations of simulation based structure refinement [34]. In the experiments conducted here we must also consider the dielectric relaxation process which is typically considered to be a purely macroscopic phenomenon that should have no effect on local structure. However, in branching hydrogen bonded liquids such as water, DMSO, and methanol (all of which can bridge electrohydrodynamically [35]) anomalous behavior which indicates a microscopic relaxation process has been reported by studying the spectral response of small molecular fluorophores [36]. The fluctuating electric field of the relaxing fluorophore induces an extended polarization ensemble that arises from reinforced oscillations in the hydrogen bonded solvent network which differs from the bulk expectation values. The role of the hydrophobic interaction of this system is as yet unclear however dielectric relaxation in water under nanoscale confinement has recently been shown to be strongly anisotropic with respect to the dipole moment [37]. This supports work which showed that the departure from the Debye relaxation model arises from microscopic anisotropy in rotational diffusion [38] which is a known property of neat liquid water [39].

From the experiments performed the local structure of water appears to be unchanged and does not exhibit anisotropy within reasonable uncertainties. However, analysis of the simulation parameters and the modeled potential energy surface reveals a clear departure between the water with and without an external electric field. The intermolecular interaction potentials (Fig.4.13) are not equivalent for a given empirical potential and furthermore the shape of the potentials are significantly different. This is not unexpected given the problems of recovering dielectric properties from simulation using rigid non-polarizable models and without the recently discussed need to correct the parameters used to define the dipole moment and polarization surfaces. Regardless of this limitation, the observed differences in the simulation behavior indicate that the applied field, although weak relative to the intramolecular coulombic field, does significantly affect the local electrical environment.

Liquid water naturally possesses a broad population distribution of molecules which are non-equivalent due to variations in the local potential energy surface. The application of a moderate electric field on the order of mV/nm is insufficient to drive the liquid system into a phase change like anisotropic reorientation of the total population, however, it is sufficient to enforce local changes in the spatially heterogeneous dynamics by distorting the local spatial distribution of molecules with respect to the molecular dipole moment [40]. Unfortunately, the EPSR method using TIP4P/2005 is unable to account for polarization effects and thus the



measured dipole moments do not differ between the simulations presented here. Examining the role electric fields play in local molecular distortions and the emergence of long-range order is important for resolving mesoscale dynamics in liquids.

We would like to point out, though, that the differences determined here, considering the known variability in the method as reported in the literature [34], and the observed shifts in the HH and OH RDFs, are nonetheless more pronounced in the water bridge than those reported for difference between the pure isotopes alone [41].

On the other hand it is known that TIP4P/2005 provides an incorrect description of heavy water, and while quite good at predicting the physical properties of water when compared to other models it falls short. The approach modeled here also fails to accurately reproduce the dielectric constant of water, the reason for which was recently discussed extensively by Vega [42] and which boils down to the incorrect assumption that the parameters used to define the potential energy surface, which determines the allowed steps in the EPSR simulation, can also be used to define the dipole moment surface. This mistake is pervasive throughout computational chemistry and new work is now emerging which takes the more correct approach [43], [44].

## 5.5 The effect of exciting a delocalized vibrational state

Auer and Skinner [45] examined the source of the collective modes which give rise to the band at 3250 cm<sup>-1</sup> and found this oscillator frequency is due to the delocalization of excitation energy over as many as 12 chromophores (i.e. individual vibrational oscillators). Later research also with Skinner's group [46] extended this finding to be the result of the "delicate quantum interference effects" driven by local excited states which spatially extend the eigenstates and thus redistribute vibrational energy within the total population. In other words a small number of local excitations can reshape the frequency distribution of the oscillators. These excitations are not stationary and evolve in the motional limit of the liquid. An extended or coherent oscillator population is observed as an intensity increase relative to the normal total population size. Such an increase is observed in the fluid volume where the inhomogeneous field gradient is strongest – that is, closest to the needle. It is reasonable to consider that this population is the direct result of dielectric polarization. The polarization of the water establishes a dielectric permittivity gradient which further focuses the electric field by the action of dielectric saturation [47] whereby the effective electric field strength is increased due to space charge effects induced by the dielectric medium.[48], [49] The observed changes in the Raman cross section (Fig. 4.17 & 4.18) are reflective of the development of this space charge and can be thought to be similar to the onset of charge density wave effects

observed in solid state materials[50], [51]. The strong degenerate nature of the OH stretch transition frequencies in water means that the vibrational coupling in water is exceptionally strong.[52] This strongly mixed nature of inter- and intra-molecular vibrations in liquid water limits the use of traditional relaxation models when attempting to derive a molecular level interpretation of the resulting shifts in the Raman spectra[53].

Regardless of such limitations, the observed Raman spectra show enhanced intensities under certain conditions, i.e. relative position of the laser beam with respect to the point electrode and beam polarization, which indicates an increased Raman cross section of the observed modes, i.e. an enhanced polarizability change associated with the underlying vibration. Different effects are observed in different parts of the OH-stretch vibrational band in the observed Stoke shift frequency window. The vibrational frequency of intramolecular OH stretch vibrations of water molecules is tightly linked to the connectivity within the local hydrogen bond network[52], [54], [55], which also affects other properties such as the collective or localized character of the vibrational modes, i.e. the distribution of vibrational motion over adjacent molecules[56], [57]. The Polarization of water due to preferential orientation, as well electronic polarization within the molecules within the applied fields employed in this work, are likely responsible for the local changes in the observed vibrational spectra. Modified hydrogen bonding motifs in water with preferentially aligned water molecules are expected to alter vibrational frequencies, while electronic polarization effects will modulate the observed intensities. The stability of local hydrogen bonding motifs has been found to be susceptible to a polarized electric field[8], [58] however, the applied field strengths are three orders of magnitude greater than those employed in this work. In addition the expected preferential molecular orientations appear to be quite weak as evident from 2D neutron diffraction studies of EHD liquid bridges.[6] Thus, we consider that the field gradient rather than the total field magnitude is responsible for the observed changes in the Raman cross-section. The gradient produces a local distortion in the molecular polarizability strong enough that previously forbidden[59] or higher energy transitions become accessible[60]. The emergence of a proton channel and the stable generation of a delocalized proton state in the water molecule previously observed in EHD liquid bridges[4], [61], again become viable mechanisms whereby a physical body couples to and anchors the collective vibrational mode[62].

A small excited state population is stabilized against thermal perturbation because the field gradient introduces an asymmetric polarization of molecular dipoles which establishes a unidirectional heat flow. By the mechanisms discussed above it is expected that once this population reaches a threshold density the delocalized collective oscillations overlap and this will change the overall dynamic structure of the liquid. Hydrogen bonding will be reinforced as those molecular dipoles that lie along the field gradient lines will be pinned. The population size of pinned molecules is relative to the local temperature and the magnitude

of the field gradient. These pinned molecules will anchor hindered rovibronic motions (i.e. librations) which retard the thermalization of absorbed vibrational energy to the hydrogen bond (HB) network or of surrounding molecules or bath. The spectral signature for such the OH librational mode of water at  $2560\text{cm}^{-1}$  has been observed in floating water bridges with an intensity above the thermal blackbody radiation distribution (§4.4.4). This type of non-equilibrium population will similarly alter the physical properties of the liquid and increase the enthalpy due to the retardation of energy dissipation in the network. The trapping of energy in local modes would increase the number of oscillators at  $3490\text{ cm}^{-1}$  and this is seen in the Raman spectra nearest the needle (§4.4.3). The observation that the temperature decreases slightly but the local energy increases now becomes understandable. Furthermore, the local entropy will also be affected in such a way as to promote local ordering which further reinforces the fine quantum coupling responsible for the collective mode further extending the coherence length of local vibrational states.

Ultrafast vibrational spectroscopy floating water bridges (§4.6 [31]) supports this view of an excited molecular population with enhanced collective modes. The vibrational lifetime for the OH stretch of HDO in the bridge at  $25^\circ\text{C}$  ( $630\pm 50\text{ fs}$ ) lies between the lifetimes found in bulk water at  $0^\circ\text{C}$  ( $630\pm 50\text{ fs}$ ) and ice Ih at  $0^\circ\text{C}$  ( $483\pm 16\text{ fs}$ ) [63] indicating that intermolecular coupling is enhanced. The dissipation of the absorbed energy to the bath however, is six fold slower in the bridge than bulk HDO:D<sub>2</sub>O. Taking these relaxation times with respect to the thermodynamic limit we find that the enthalpy of water in the floating water bridge is increased while the local entropy is decreased. This fits with the model discussed above and is further supported by the Raman spectra presented in §4.4.3.

In contrast with electrically driven equilibrium phase transitions reported and discussed elsewhere in the literature, [64]–[66] the behavior elucidated here is best understood as the emergence of metaproperties dependent upon an excited state. The inhomogeneous field gradient holds the liquid in a steady-state far from equilibrium with the environment. If the field is extinguished the population collapses as is expected for dissipative structures that obey non-equilibrium thermodynamics and exhibit non-reversible behavior [67], [68]. The generation of a vibronically coupled “pinned” molecular population is a non-adiabatic process; there is heat flow in order to balance entropy production; changing the bath entropy which will affect the flow of heat into or out of the region. This is essentially a thermoelectric effect governed by the Onsager reciprocal relations and which is responsible for establishing the electro-convective flow [47], [69] observed here interferometrically. Mass transport out of the locally polarized region, driven both by the gradients in density and chemical potential is further accelerated by electrokinetic forces arising at interfaces in the system [70]. In addition to the air-water interface an internal dynamical surface is also present. This surface is defined by how far the electric field gradient extends in the liquids with a magnitude greater than the dissipative energies of the bulk which are proportional to both the temperature and any shear forces present. The de-excitation of molecules is thus driven by electro-convective transport

which depletes the population and establishes an upper bound on the size. It is expected that this would be a materially dependent feature and different polar liquids should exhibit differences in this behavior.

## 5.6 Implications of an extended vibrational energy mode

From the observations we find evidence to suggest that in liquid water an electric field gradient which is sufficiently steep to polarize the molecular dipoles and to affect the electronic and protonic distributions is also sufficient to cause the decoupling of local and collective vibrational modes over length scales greater than immediate nearest neighbors. This finding shows an inherent ability of liquid water to support vibrational demixing at the mesoscale. [71] Such behavior has already been noted for the mechanism of ultrafast energy relaxation whereby the local excited intramolecular vibrational modes rapidly couple to intermolecular vibrational and bending modes.[53], [54] The energy transfer proceeds as the excitation traverses configurations with ever lower energy level until finally the absorbed perturbation becomes trapped in a strongly hydrogen bonded trap.[53] The important distinction is that the relaxation pathway in water is one which utilizes the strong interaction of the hydrogen bond, which in the case of the experiments presented here exhibit enhanced polarization [72], [73]. When one expands the number of molecules involved in the relaxation process a length scale emerges whereby the local and collective modes can effectively decouple from each other – the mesoscale [74]–[76]. In the presence of the field gradient this decoupling is enhanced and essentially results in transiently isolated molecular populations within the liquid. Given that such electric field gradients as those found here have also been observed in a number of natural systems, e.g. cells[77], clay particles[78], and cloud droplets[79], it is possible to consider that within a volume of physically continuous liquid isolated regions with unique properties can form. The interplay between the reactive force generated by the polarization of water dipoles and the driving field gradient establishes a stabilizing disequilibrium that is spatially defined by the magnitude of the applied field gradient and the dipole response dynamics of the molecules. The electric field gradients are thus sufficient to stabilize local regions whereby the chemical potential follows the gradient, and thus reactivity can be spatially confined without the need for a physical barrier such as a membrane. The high charge density, and well defined hydrophobic/hydrophilic profiles, of many biomolecules provides the ideal situation to maintain such mesoscale pockets of augmented water activity. The asymmetric transport of energy in liquid water can thus be effectively controlled by the presence of strong electric field gradients and likely plays a role in the water regulation of living cells.[80]

## 5.7 Enhanced local field heterogeneity drives quantum chaos

The overestimation of temperature by  $T_2$  relaxation measurements in glycerol (§4.5.1) indicates that in the water bridge there is a strong disruption of configurational entropy. Extrapolating from observations with water it is considered that deprotonated glycerol ions as well as quasi-free protons are present in a glycerol bridge. It is also expected that there will also be enhancement of both collective and local vibrational modes as glycerol and glycerol-water solutions behave similarly to the inhomogeneous electric field experiments illustrated in §4.4. The spatial distribution of these modes is expected to stochastically jump at the mesoscale and thus generate an instantaneous field value which is perturbed by the transient field generated as ions and molecules move through the external electric field gradient. The reciprocity of electric and magnetic currents establishes a strongly coupled reactive electromagnetic (near) field. The effect of this on heat flow will also change the configurational temperature of the molecules.

Vibrational spectroscopy provides a point of correlation to the rotational and translational dynamics of magnetic relaxation. It is not strictly possible to equate the spectral responses of water and glycerol due to the differences in the symmetry properties (point group) of the molecules. However, the requirement holds that with respect to fermionic hydrogen exchange the overall wavefunction must be anti-symmetric and further that this relationship links the nuclear spin symmetries with the rovibronic wavefunction. Thus a change in nuclear relaxation will couple to both rotational as well as vibrational modes and the correlation times must also scale accordingly. The faster OH stretch relaxation and the delayed thermalization of the absorbed energy can be understood as resulting from a structural rearrangement responsible for and associated with a partial collapse of the tetrahedral network of water. Such a collapse is supported by 2D neutron and Raman scattering results present evidence that in the water bridge the number of hydrogen bonds per water molecule is reduced and that the water molecules are partially aligned [6], [58]. A partial collapse of the hydrogen bond network will reduce the connectivity of the water molecules, which can thus explain the slowing down of the thermalization of the energy, as this process requires the equilibration of the energy over many water molecules.

A partial collapse of the network will also affect the modes that accept the energy of the excited OH stretch vibration. These modes are the HDO bending mode ( $\sim 1450 \text{ cm}^{-1}$ ), the librations ( $\sim 800 \text{ cm}^{-1}$ ), the hydrogen-bond stretch vibrations ( $\sim 200 \text{ cm}^{-1}$ ) and the hydrogen-bond bend vibrations ( $\sim 50 \text{ cm}^{-1}$ ). Especially the lower-energy accepting modes are quite susceptible to structural rearrangements, and changes in their frequency and coupling to the OH stretch vibration could explain the observed acceleration of the vibrational energy relaxation. In other words local modes lose connection with more distant neighbors and the

absorbed energy becomes stuck. This fits with the apparent rise in temperature as measured by  $T_2$  – whereby the trapped energy is now stored in the phase coherence of an isolated (small population) nuclear spin. This is but one possible interpretation of the observed response as more experimental and theoretical work is needed in order to fully redress the possible mechanisms underlying the observations presented in §4.5.1.

The molecular environment can be seen to develop spatial and temporal heterogeneities that will redistribute energy within the liquid chaotically. This differs from the random distribution (thermal) distribution assumed for an equilibrium system. The locally varying interaction field can be described as a hypersurface which in the case where a high field gradient is present develops local wells. The spacing, depth, and lifetime of these wells is related to the molecular dynamics. Thus it is expected that given the correct energy the well structure imposed by the excited population dynamics will overlap with the ground state fluctuations at least enough so that thermal perturbations now also become trapped. The emergence of non-adiabatic electronic-nuclear coupling dynamics is a hallmark of mesoscale (semi-quantal) physics [59].

The flow of energy in the electrically excited state is dependent upon the interaction of three principle field gradients: electric, thermal, and magnetic which are governed by the proportionality relationship:

$$\nabla^2 E \cdot \frac{1}{2} q v^2 \mathbf{p} \propto \nabla^2 B \cdot \mu k_B T \propto \nabla^2 T \cdot S \Psi \quad (\text{Eq.5.13})$$

Where  $q$  is the effective group charge,  $v$  the velocity of the charge,  $\mathbf{p}$  the polarization vector,  $\mu$  the magnetic dipole moment vector,  $k_B$  Boltzmann's constant,  $T$  temperature,  $S$  total entropy, and  $\Psi$  the chemical potential.

These forces couple into the local chemical potential of the system by exchange of energy between different forms. At the mesoscale the liquid develops a heterogeneous structure whereby different local molecular groups exhibit transient couplings between different fields as expressed in Eq. 5.13. The flow of energy proceeds in such a manner as to produce maximal configurational entropy [55] in the system. The hallmark of such a process is the emergence of a chaotic basin of stability whereby the different quantum mechanical oscillator classes exchange local and global mode couplings via the moderating fields. The explicit system of equations governing this type of behavior has yet to be formalized but will follow after the work of Tanaka [60] which builds upon mode-coupling theory by extending the ordering definition to the mesoscale and examining the exchange between density and orientational entropies.

## Bibliography

- [1] M. Sammer, A. Wexler, P. Kuntke, H. Wilsche, N. Stanulewicz, E. Lankmayr, J. Woissetschlaeger, and E. Fuchs, "Proton production, neutralisation and reduction in a floating water bridge," *J. Phys. D. Appl. Phys.*, 2015.
- [2] B. E. Conway and E. Gileadi, "Kinetic theory of pseudo-capacitance and electrode reactions at appreciable surface coverage," *Trans. Faraday Soc.*, vol. 58, p. 2493, Jan. 1962.
- [3] P. Atkins and J. De Paula, "Atkins Physical Chemistry (8th Edition)," pp. 682–683, 2006.
- [4] E. C. Fuchs, A. Cherukupally, A. H. Paulitsch-Fuchs, L. L. F. Agostinho, A. D. Wexler, J. Woissetschlaeger, and F. T. Freund, "Investigation of the mid-infrared emission of a floating water bridge," *J. Phys. D. Appl. Phys.*, vol. 45, no. 47, p. 475401, Nov. 2012.
- [5] E. C. Fuchs, B. Bitschnau, J. Woissetschlaeger, E. Maier, B. Beuneu, and J. Teixeira, "Neutron scattering of a floating heavy water bridge," *J. Phys. D. Appl. Phys.*, vol. 42, no. 6, p. 065502, Mar. 2009.
- [6] E. C. Fuchs, P. Baroni, B. Bitschnau, and L. Noirez, "Two-dimensional neutron scattering in a floating heavy water bridge," *J. Phys. D. Appl. Phys.*, vol. 43, no. 10, p. 105502, Mar. 2010.
- [7] L. B. Skinner, C. J. Benmore, B. Shyam, J. K. R. Weber, and J. B. Parise, "Structure of the floating water bridge and water in an electric field," *Proc. Natl. Acad. Sci. U. S. A.*, vol. 109, no. 41, pp. 16463–8, Oct. 2012.
- [8] D. Rai, A. D. Kulkarni, S. P. Gejji, and R. K. Pathak, "Water clusters (H<sub>2</sub>O)<sub>n</sub>, n=6–8, in external electric fields," *J. Chem. Phys.*, vol. 128, no. 3, p. 034310, Jan. 2008.
- [9] L. Glasser, "Proton conduction and injection in solids," *Chem. Rev.*, vol. 75, no. 1, pp. 21–65, Feb. 1975.
- [10] L. Onsager, "Physics of Ice," in *Proceedings of the International Symposium, Munich, 1968*, N. Riehl, B. Bullemer, and H. Engelhardt, Eds. New York: Plenum Press, 1969.
- [11] N. Bjerrum, "Structure and Properties of Ice," *Science*, vol. 115, no. 2989, pp. 385–90, Apr. 1952.
- [12] M. Freda, A. Piluso, A. Santucci, and P. Sassi, "Transmittance Fourier Transform Infrared Spectra of Liquid Water in the Whole Mid-infrared Region: Temperature Dependence and Structural Analysis," *Appl. Spectrosc.*, vol. 59, no. 9, pp. 1155–1159, Sep. 2005.
- [13] D. Kraemer, M. L. Cowan, a Paarmann, N. Huse, E. T. J. Nibbering, T. Elsaesser, and R. J. D. Miller, "Temperature dependence of the two-dimensional infrared spectrum of liquid H<sub>2</sub>O," *Proc. Natl. Acad. Sci. U. S. A.*, vol. 105, no. 2, pp. 437–442, 2008.
- [14] S. O. Diallo, E. Mamontov, W. Nobuo, S. Inagaki, and Y. Fukushima, "Enhanced translational diffusion of confined water under electric field," *Phys. Rev. E. Stat. Nonlin. Soft Matter Phys.*, vol. 86, no. 2 Pt 1, p. 021506, Aug. 2012.
- [15] M. Zahn and T. Takada, "High voltage electric field and space-charge distributions in highly purified water," *J. Appl. Phys.*, vol. 54, no. 9, pp. 4762–4775, 1983.
- [16] D. R. Lide, W. M. M. Haynes, G. Baysinger, L. I. Berger, D. L. Roth, D. Zwillinger, M. Frenkel, and R. N. Goldberg, "CRC Handbook of Chemistry and Physics," 2010.

- [17] D. B. Fenneman and R. J. Gripshover, "80 CH 1573-5ED," in *XIVth Pulsed Power Modulator Symposium*, 1980, pp. 150–153.
- [18] H. T. Wang and J. D. Cross, *Proceedings of the 3rd International Conference on Properties and Applications of Dielectric Materials*.
- [19] G. A. Ostroumov, *Zh. Tekh. Fiz.*, vol. 24, p. 1915, 1954.
- [20] O. M. Stuetzer, *Phys. Fluids*, vol. 5, p. 534, 1962.
- [21] N. J. Félici, *Rev. Gén. Electr.*, vol. 78, p. 730, 1969.
- [22] M. Tanaka, G. Girard, R. Davis, A. Peuto, and N. Bignell, "Recommended table for the density of water between 0 C and 40 C based on recent experimental reports," *Metrologia*, vol. 38, no. 4, pp. 301–309, Aug. 2001.
- [23] J. N. Murrell and A. D. Jenkins, *Properties of Liquids and Solutions*. Wiley, 1994.
- [24] J. Woissetschlaeger, A. D. Wexler, G. Holler, M. Eisenhut, K. Gatterer, and E. C. Fuchs, "Horizontal bridges in polar dielectric liquids," *Exp. Fluids*, vol. 52, no. 1, pp. 193–205, 2012.
- [25] J. Woissetschlaeger, K. Gatterer, and E. C. Fuchs, "Experiments in a floating water bridge," *Exp. Fluids*, vol. 48, no. 1, pp. 121–131, Jul. 2010.
- [26] P. Blanckenhagen, *Ber. Buns. Ges.*, vol. 79, pp. 891–903, 1972.
- [27] A. Hassanali, F. Giberti, J. Cuny, T. D. Kühne, and M. Parrinello, "Proton transfer through the water gossamer," *Proc. Natl. Acad. Sci. U. S. A.*, vol. 110, no. 34, pp. 13723–8, 2013.
- [28] R. Martens and F. Freund, "The potential energy curve of the proton and the dissociation energy of the OH<sup>-</sup> ion in Mg(OH)<sub>2</sub>," *Phys. Status Solidi*, vol. 37, no. 1, pp. 97–104, Sep. 1976.
- [29] H. Wengeler, R. Martens, and F. Freund, "Proton Conductivity of Simple Ionic Hydroxides Part II: In Situ Formation of Water Molecules Prior to Dehydration," *Berichte der Bunsengesellschaft für Phys. Chemie*, vol. 84, no. 9, pp. 873–880, Sep. 1980.
- [30] H. J. Bakker and H.-K. Nienhuys, "Delocalization of protons in liquid water," *Science*, vol. 297, no. 5581, pp. 587–590, 2002.
- [31] L. Piatkowski, A. D. Wexler, E. C. Fuchs, H. Schoenmaker, and H. J. Bakker, "Ultrafast vibrational energy relaxation of the water bridge," *Phys. Chem. Chem. Phys.*, vol. 14, no. 18, pp. 6160–4, May 2012.
- [32] C. J. T. de Grotthuss, "Sur la décomposition de l'eau et des corps qu'elle tient en dissolution à l'aide de l'électricité galvanique," *Ann. Chim.*, vol. 58, pp. 54–73, 1806.
- [33] P. Gosar, "On the mobility of the H<sub>3</sub>O<sup>+</sup> ion in ice crystals," *Nuovo Cim.*, vol. 30, no. 3, pp. 931–946, 1963.
- [34] A. K. Soper, "The Radial Distribution Functions of Water as Derived from Radiation Total Scattering Experiments: Is There Anything We Can Say for Sure?," *ISNR Phys. Chem.*, vol. 2013, p. 1, 2013.
- [35] J. Woissetschlaeger, A. D. Wexler, G. Holler, M. Eisenhut, K. Gatterer, and E. C. Fuchs, "Horizontal bridges in polar dielectric liquids," *Exp. Fluids*, vol. 52, no. 1, pp. 193–205, Oct. 2012.

- [36] E. L. Mertz, "Anomalous microscopic dielectric response of dipolar solvents and water," *J. Phys. Chem. A*, vol. 109, no. 1, pp. 44–56, 2005.
- [37] C. Zhang, F. Gygi, and G. Galli, "Strongly anisotropic dielectric relaxation of water at the nanoscale," *J. Phys. Chem. Lett.*, vol. 4, no. 15, pp. 2477–2481, 2013.
- [38] Y. P. Kalmykov, W. T. Coffey, and D. S. F. Crothers, "Microscopic models for dielectric relaxation in disordered systems," vol. 041103, 2004.
- [39] J. Ropp, L. C., T. C. Farrar, and J. L. Skinner, "Rotational motion in liquid water is anisotropic: a nuclear magnetic resonance and molecular dynamics simulation study," *J. Am. Chem. Soc.*, vol. 123, no. 1, pp. 8047–8052, 2001.
- [40] D. C. Elton and M.-V. Fernández-Serra, "Polar nanoregions in water: a study of the dielectric properties of TIP4P/2005, TIP4P/2005f and TTM3F," *J. Chem. Phys.*, vol. 140, no. 12, p. 124504, Mar. 2014.
- [41] A. K. Soper and C. J. Benmore, "Quantum differences between heavy and light water," *Phys. Rev. Lett.*, vol. 101, no. 6, pp. 1–4, 2008.
- [42] C. Vega, "Water: one molecule, two surfaces, one mistake," *Mol. Phys.*, vol. 113, no. 9–10, pp. 1145–1163, 2015.
- [43] J. L. Aragones, L. G. MacDowell, J. I. Siepmann, and C. Vega, "Phase diagram of water under an applied electric field," *Phys. Rev. Lett.*, vol. 107, no. 15, pp. 1–4, 2011.
- [44] L. Shi, Y. Ni, S. E. P. Drews, and J. L. Skinner, "Dielectric constant and low-frequency infrared spectra for liquid water and ice Ih within the E3B model," *J. Chem. Phys.*, vol. 141, no. 8, p. 084508, 2014.
- [45] B. M. Auer and J. L. Skinner, "IR and Raman spectra of liquid water: Theory and interpretation," *J. Chem. Phys.*, vol. 128, no. 22, p. 224511, 2008.
- [46] M. Yang and J. L. Skinner, "Signatures of coherent vibrational energy transfer in IR and Raman line shapes for liquid water," *Phys. Chem. Chem. Phys.*, vol. 12, pp. 982–991, 2010.
- [47] U. Kaatz, "The dielectric properties of water in its different states of interaction," *J. Solution Chem.*, vol. 26, no. 11, pp. 1049–1112, 1996.
- [48] K. Adamiak and P. Atten, "Simulation of corona discharge in point–plane configuration," *J. Electrostat.*, vol. 61, no. 2, pp. 85–98, 2004.
- [49] A. Kara, Ö. Kalenderli, and K. Mardikyan, "Effect of Dielectric Barriers To the Electric Field of Rod-Plane Air Gap," *COMSOL Conf. 2006*, 2006.
- [50] S. Sugai, "Effect of the charge-density-wave gap on the Raman spectra in orthorhombic TaS<sub>3</sub>," *Phys. Rev. B*, vol. 29, no. 2, pp. 953–965, 1984.
- [51] P. Goli, J. Khan, D. Wickramaratne, R. K. Lake, and A. a Balandin, "Charge Density Waves in Exfoliated Thin Films of Van der Waals Materials," *Cond-mat*, p. 1211.4486, 2012.
- [52] J. Skinner, B. Auer, and Y. Lin, "Vibrational line shapes, spectral diffusion, and hydrogen bonding in liquid water," *Adv. Chem. Phys.*, vol. 142, 2010.
- [53] K. Ramasesha, L. De Marco, A. Mandal, and A. Tokmakoff, "Water vibrations have strongly mixed intra- and intermolecular character," *Nat. Chem.*, vol. 5, no. 11, pp. 935–40, 2013.
- [54] H. J. Bakker and J. L. Skinner, "Vibrational spectroscopy as a probe of structure and dynamics in liquid water," *Chem. Rev.*, vol. 110, no. 3, pp. 1498–517, Mar. 2010.
- [55] Y. Maréchal, "The molecular structure of liquid water delivered by absorption spectroscopy in the whole IR region completed with thermodynamics data," *J. Mol. Struct.*, vol. 1004, no. 1–3, pp. 146–155, Oct. 2011.
- [56] R. Ludwig, "Water: From clusters to the bulk," *Angew. Chemie - Int. Ed.*, vol. 40, no. 10, pp. 1808–1827, 2001.
- [57] D. E. Moilanen, E. E. Fenn, Y. Lin, J. L. Skinner, B. Bagchi, and M. D. Fayer, "Water inertial reorientation : Hydrogen bond strength and the angular potential," vol. 105, no. 14, 2008.
- [58] D. Rai, "Ab Initio Investigations on Some Dipole-Bonded Molecular Clusters, Their Interaction with Water Molecules, and Externally Applied Electric Field," University of Pune, Pune, India, 2008.
- [59] E. Ayars, H. Hallen, and C. Jahncke, "Electric Field Gradient Effects in Raman Spectroscopy," *Phys. Rev. Lett.*, vol. 85, no. 19, pp. 4180–4183, 2000.
- [60] H. J. Bakker and H.-K. Nienhuys, "Delocalization of Protons in Liquid Water," *Science (80-. )*, vol. 297, no. 5581, pp. 587–590, 2015.
- [61] E. C. Fuchs, B. Bitschnau, A. D. Wexler, and F. Woisetschläger, Jakob Freund, "A Quasi-Elastic Neutron Scattering Study of the Dynamics of Electrically Constrained Water," *J. Phys. Chem. B*, 2015.
- [62] R. L. a Timmer, K. J. Tielrooij, and H. J. Bakker, "Vibrational Förster transfer to hydrated protons," *J. Chem. Phys.*, vol. 132, no. 19, p. 194504, May 2010.
- [63] S. Woutersen, U. Emmerichs, H.-K. Nienhuys, and H. Bakker, "Anomalous Temperature Dependence of Vibrational Lifetimes in Water and Ice," *Phys. Rev. Lett.*, vol. 81, pp. 1106–1109, 1998.
- [64] E.-M. Choi, Y.-H. Yoon, S. Lee, and H. Kang, "Freezing Transition of Interfacial Water at Room Temperature under Electric Fields," *Phys. Rev. Lett.*, vol. 95, no. 8, p. 085701, Aug. 2005.
- [65] J. Bartlett, A. van den Heuvel, and B. Mason, "The growth of ice crystals in an electric field," *Zeitschrift für Angew. Math. und Phys. ZAMP*, vol. 14, no. 5, pp. 599–610, 1963.
- [66] I. M. Svishchev and P. G. Kusalik, "Electrofreezing of Liquid Water: A Microscopic Perspective," *J. Am. Chem. Soc.*, vol. 118, no. 3, pp. 649–654, 1996.
- [67] I. Prigogine, "Time, Structure, and Fluctuations," *Science (80-. )*, vol. 201, no. 4358, pp. 1065–1071, 1978.
- [68] A. Kleidon and R. D. Lorenz, Eds., *Non-equilibrium Thermodynamics and the Production of Entropy*. Springer-Verlag Berlin Heidelberg, 2005.
- [69] J. B. Hubbard, L. Onsager, W. M. van Beek, and M. Mandel, "Kinetic polarization deficiency in electrolyte solutions," *Proc. Natl. Acad. Sci. U. S. A.*, vol. 74, no. 2, pp. 401–4, 1977.



- [70] J. R. Melcher and G. I. Taylor, "Electrohydrodynamics: A Review of the Role of Interfacial Shear Stresses," *Annu. Rev. Fluid Mech.*, vol. 1, no. 1, pp. 111–146, Jan. 1969.
- [71] R. E. Van Vliet, M. W. Dreischor, H. C. J. Hoefsloot, and P. D. Iedema, "Dynamics of liquid-liquid demixing: Mesoscopic simulations of polymer solutions," *Fluid Phase Equilib.*, vol. 201, no. 1, pp. 67–78, 2002.
- [72] S. Woutersen and H. J. Bakker, "Resonant intermolecular transfer of vibrational energy in liquid water," *Nature*, vol. 402, no. 6761, pp. 507–509, 1999.
- [73] E. T. J. Nibbering and T. Elsaesser, "Ultrafast Vibrational Dynamics of Hydrogen Bonds in the Condensed Phase," *Chem. Rev.*, vol. 104, pp. 1887–1914, 2004.
- [74] P. K. Gupta and M. Meuwly, "Dynamics and vibrational spectroscopy of water at hydroxylated silica surfaces," *Faraday Discuss.*, vol. 167, p. 329, 2013.
- [75] T. Yagasaki, M. Matsumoto, and H. Tanaka, "Spontaneous liquid-liquid phase separation of water," *Phys. Rev. E - Stat. Nonlinear, Soft Matter Phys.*, vol. 89, no. 2, pp. 1–5, 2014.
- [76] H. Tanaka, "Importance of many-body orientational correlations in the physical description of liquids," *Faraday Discuss.*, vol. 167, p. 9, 2013.
- [77] K. M. Tyner, R. Kopelman, and M. a Philbert, "'Nanosized voltmeter' enables cellular-wide electric field mapping," *Biophys. J.*, vol. 93, no. 4, pp. 1163–74, Aug. 2007.
- [78] S. Yariv and H. Cross, *Geochemistry of Colloid Systems: For Earth Scientists*. Springer Science & Business Media, 2012.
- [79] D. R. MacGorman and W. D. Rust, *The Electrical Nature of Storms*. 1998.
- [80] B. L. De Groot, T. Frigato, V. Helms, and H. Grubmüller, "The mechanism of proton exclusion in the aquaporin-1 water channel," *J. Mol. Biol.*, vol. 333, pp. 279–293, 2003.
- [81] R. C. Ponterio, M. Pochylski, F. Aliotta, C. Vasi, M. E. Fontanella, and F. Saija, "Raman scattering measurements on a floating water bridge," *J. Phys. D: Appl. Phys.*, vol. 43, no. 17, p. 175405, May 2010.
- [82] M. A. Porter, "Nonadiabatic dynamics in semiquantal physics," *Reports Prog. Phys.*, vol. 64, no. 9, pp. 1165–1189, 2001.



Photo credit chapter 5 overleaf: *Forest Lake, Plitvička jezera*, ©A.D. Wexler, 2013



# 6

## Much To Do About Water

### *Impact, Applications, Outlook*

*The main findings from this work are recapitulated by analogy in order to better appreciate the influence of extrinsic fields have on strongly interacting particles whose population is above a critical size. Our attention is then turned towards the possibility for a new era of human technology based on the uniquely programmable liquid state.*

## 6.1 Rethinking Water: A programmable material

The discrete water molecule  $\text{H}_2\text{O}$  is a physical entity which exists only in the gas phase where dynamics dominate and there is no intermolecular interaction beyond collisions due to the high kinetic energy of the molecules. Water molecules also possess a permanent electric dipole resulting from polarization of the electron distribution and due to the differences between the electron affinity of the two atomic species oxygen and hydrogen. The dipole has a rather simple shape that looks more like a potato than the typical molecular model images we are used to. In the condensed liquid and solid phases water molecules interact strongly via hydrogen bonds which are both electrostatic and covalent in nature. The ratio between these two contributions is dependent on the local intermolecular geometry (structure) as well as the amount of energy in the system. As a first approach to considering the energy and dynamics of water molecules it is useful to consider the simple case where only a few molecules are present. When the number of molecules in the system is less than or equal to five, the molecules will form planar ring like structures, however once the number increases to six the onset of three dimensional structures is observed. It is useful to keep these simple interaction shapes in mind when considering the complex interactions occurring in the bulk liquid. If we freeze the network and take a look at the arrangement and interactions of individual molecules (already a rather dubious prospect) we can find a wide variety of geometries similar to those found for only a few molecules. The well-known tetrahedral arrangement is at best considered an average conformation through which most molecules will pass given a long enough period of time. The local molecular geometry is constantly fluctuating – driven by thermal energy – and any given molecule can have between zero and six hydrogen bonded neighbors [1]. These neighbors will change on average once every picosecond as they translate from position to position diffusing along gradients of energy, responding to local voltage fluctuations, and encountering other molecules and in so doing exchanging states. An average water molecule will travel a distance of  $\sim 150,000$  molecules in one second. The dance is dizzyingly fast but it is a dance none the less and by analogy we can consider a dance club filled with dancers that we can observe but only they can hear the music and experience the interactions between each other.

To maintain a correct view of these interactions we must also keep in mind that quantum processes (such as spin coupling) dominate and in keeping with the Copenhagen convention for quantum mechanics means we will only ever know the odds of something happening on the dance floor. The music, the friendships and enmities, the attractive forces, the club lights, and the shape or layout of the club will influence the dancers: their dance steps and those of their nearest neighbors are well correlated even if they are vastly different. The addition of strong perturbations such as acidic ions will radically alter the local dynamics and can even

produce new long range dynamics (imagine Brad Pitt and Angelina Jolie walk into the club and go their separate ways moving through the crowded dancers and enticing them with their attractiveness – as word spreads you may even find that the dancers will segregate based upon their sexual preferences). The network of water molecules in the liquid state like the dancers in our thought experiment can be stimulated and in the water bridge the applied electric field, along with the electrolytically generated ions, does this. Upon examination of the bridge using elastic total radiation scattering we find that the static structure of water is largely the same with some small shifts. The oxygen lattice spacing remains unchanged while the position of the hydrogen nuclei within this lattice show an overall reduction in the intermolecular nearest neighbor distances (the dancers hands are closer together). We also can see that the electric field slightly changes where water molecules will be located in relationship to each other. The coordination number tells us how many nearest neighbors an average molecule will have and examining the probability distribution (back to the casino) as a function of distance from the origin gives an impression of where the allowed approaches are (the dancers won't step on each other's feet). This analysis of orientational correlation at a fixed probability level shows that the electric field "squishes" the distribution and disrupts previously continuous regions of approach. In other words, the electric field has polarized the material and enforces a subset of interaction geometries. The total orientational probability density reinforces the understanding that molecules are more likely to interact in the presence of the electric field than in the normal bulk (just as the dancers would interact more likely if the DJ was playing really good music).

This analysis is the result of taking the corrected scattering data from neutron and x-ray experiments, passing them to a molecular dynamics simulation (reverse Monte Carlo) and then analyzing the geometries and energies present in the system. It is expected that there is a difference between the two systems as the imposed electric field adds additional energy to the system however it is not possible to cause the two simulated molecular systems (1000 water TIP4P molecules) to converge in two important quantities – intermolecular energy and pressure. This indicates that the models used are insufficient to recover the actual experimental conditions and one must keep this in mind when considering the findings. It also indicates that there is an essential non-equivalence between the two systems which cannot be resolved using the imposed simulation constraints and a new model system needs to be developed.

The experimental evidence thus far gathered from the water bridge reminds us that with the application of the electric field there is a strong dynamic response. Ultrafast spectroscopy revealed the paradox whereby nearest neighbors exhibit increased coupling which results in a shorter OH stretch vibration lifetime but that the release of the absorbed heat is much slower than expected and indicates that the water network has developed local energy traps. The shift in dynamics is also observable as there is a change in the infrared emission of the water bridge when compared to bulk water. Infrared emission is a ubiquitous phenomenon since all materials emit infrared radiation according to the Planck radiation law, and so does the water

bridge. However, despite operating at elevated temperatures the water bridge spectrum is both blue shifted and shows a more narrow distribution of energy around 2160 wavenumbers. This energy is associated with the local energy traps and is typically assigned to hindered rotational freedom (overtone of librations). More recently it has been found that the jumps between energy levels of the OH stretch oscillator have a similar energy and that in addition to changing the translational dynamics of water this emission feature hints that within the local environment proton transfer kinetics will also change. A study of the proton mobility using quasi-elastic neutron scattering (QENS) hints at two kinds of protons in the system: one more strongly bound than in the bulk, and one more mobile with average jump lengths of 3 Å, indicating a proton delocalization and a change from the next-neighbor interaction in the bulk to a “next-to-next-neighbor” interaction in the bridge. An examination of the proton dynamics in a glycerol bridge using nuclear magnetic resonance (NMR) relaxation mapping further corroborates the idea of different proton transfer kinetics. The magnetic dipole of hydrogen nuclei is probed by successive radio frequency pulses. The relaxation of the excited nuclei in a strong magnetic field tells us something about the forces that are acting on the H-nuclei. By measuring the evolution of nuclear magnetic spins the dynamics of the local environment can be deduced. The longitudinal relaxation ( $T_1$ ) provides information about the coupling between the local nuclear spin and the bulk – this is similar to the ultrafast population relaxation, it also provides a measure of the systems enthalpy or how well does heat flow in the system. Transverse relaxation ( $T_2$ ) on the other hand provides a measure of the coupling between neighboring spins and is a measure of the local configurational entropy – this can be compared with the ultrafast anisotropy decay rate whereby the strength of this interaction which is hydrogen bond mediated is measured and found to be stronger than expected for liquid water. By calibrating  $T_1$  and  $T_2$  to sample temperature it is possible to compare the relaxation dynamics with each other on a common scale. In each of the nine bridges examined we found that where the electric field strength is greatest  $T_2$  always reports a higher temperature than  $T_1$ . In the bridge itself the relationship holds for most but not all bridges and this is due in part to the more dynamic environment in the bridge whereby large temperature swings, fluctuating electric field strength, and liquid flow obscure the signal. Regardless of the data spread in the bridge the NMR relaxation maps agree with the other measured quantities and again support a model view which shows local correlated structures immersed in a partially melted hydrogen bonding network. Going back to the dance floor model we can think of a high school dance where the dancers stay in their cliques – the cheerleaders won’t dance with the nerds!

Within water there are two types of spin isomers. The singlet state para-water and the triplet state ortho-water. While the precise mechanisms of exchange and interconversion between spin isomers is ongoing discussion in the literature the relative abundance in ordinary water is generally accepted to be 3:1 ortho/para. These two species of water have distinct properties that are determined by the constraints of quantum mechanics. For a molecule with two spin

$\frac{1}{2}$  nucleons (the hydrogen nuclei in this case) the Pauli symmetry principle requires that the total solution for the exchange of the two fermionic hydrogens be antisymmetric. In simple terms the spin symmetry determines the motion of the molecule. Thus ortho-water with symmetric spins and a magnetic moment will rotate because the rotation-vibration solution to the wave function (rovibronic Eigen states) is antisymmetric. It is easy to think of this by mechanical analogy. Imagine you are standing on a platform which can spin about a central axis. In each of your hands you hold a spinning bicycle wheel. If both wheels spin in the same direction (ortho-) you will also begin to rotate as the angular momentum in the wheels adds to together and is transferred to your position in an asymmetric way. To make sense of this last part – consider what would happen if the wheel were wet – droplets coming from a point on the wheel furthest from your centerline would fly in one direction on your right and the opposite on your left – the asymmetric force would push you and you would begin to rotate. If the wheels spin in opposite directions the transferred momentum cancels and you remain stationary. Thus ortho-water molecules will always rotate, while those in the para-configuration will remain stationary. Going back to the dance floor analogy we can begin to imagine how the dance will be affected if 75% of the dancers are always spinning around and the remaining 25% remain stationary. A spinning dancer will take a different kind of trajectory when translating across the floor compared to a dancer who is moving without rotation. It is not only the rotational states that are affected but the vibrational states as well – and ortho-water molecules have a net higher kinetic energy which will dissipate via vibrational states which in turn affect the chemical properties of the molecule. Because the magnetic properties of the two spin isomers differ it was first postulated and then recently demonstrated that the application of an external electric to a molecular beam of water molecules is able to separate the two spin isomers from each other. This is due to the DC Stark effect and is related to the splitting of energies in the presence of a forcing field – which has the same intensity as what is found in the water bridge.

In order to explore the role the pure inhomogeneous electric field has on the momentum distribution of water a simple experiment was constructed using a point-plane electrode pair with a cuvette of water placed between them. The plane electrode was energized with 20 kV and the point electrode (an acupuncture needle 300  $\mu\text{m}$  dia.) placed on ground potential. There was a small leakage of current through ionization of the air but this value was typically on the order of nano-amps. Modelling of the electric field in the designed experiment shows that the field gradient is sharply focused under the point electrode and that a weak return displacement current follows the outer walls of the cuvette on the liquid side. Raman imaging was then performed and measurements revealed that where the field is the strongest there is a depopulation of the center frequencies in the molecular vibrational bands which suggests that the once continuous momentum distribution is now separated into two discrete populations. In other words the DC Stark effect also works in the ambient liquid state and results in a splitting of the allowed energy levels. The application of an electric field at MV/m will distort



the hydrogen bonded network dynamics and our dancers will begin to move differently – the dance has changed and with the ease of flipping a switch. The electric field not only affects the type of motions that are allowed or disallowed but it also affects the probability that a water dissociation product (hydronium or hydroxide ion) will be able to jump from one local energy well to another. The once continuous equilibrium distributions of spin states, ionic mobilities, and molecular motions has shifted to an excited distribution – the dancers are jumping up and down, spinning around (or not – but in different groups!) and holding into tight little local groups. The local environments can be so vastly different that their relative population density will redefine the bulk averaged energy distribution. In the most simple of terms what was once a random network has become focused and directed. The emergence of quantum mechanically controlled energy channels now dominate the material and thus electrical stress provides a means to control the material beyond bulk level constraint. We can program water to perform different types of “tasks” at different locations.

Nature uses this fact and it is the principle reason why water is essential to life. If we examine some biochemical machinery such as photosystem II or aquaporins we find that the construction of the molecular machinery is such that there are well defined channels between hydrophobic and hydrophilic regions not to mention very strong electric field gradients. These biochemical constructions change the local molecular properties of water to efficiently support not only the general process but more critically to provide the exact conditions for one tiny segment of process. In one region the spin state equilibrium will change and support or retard ion diffusion, in another region free protons or electrons will be trapped in a well of tightly bound water molecules, in yet another region the viscosity will be optimal for the gliding of two protein subunits against each other, and further on still the heat capacity will be changed so that thermal fluctuations are focused to provide energy recovery to enhance efficiency or dissipated to protect labile products. All of this happening at a spatial resolution on the order of a few Ångströms and with processing speeds between femtoseconds and picoseconds! Such special conditions are not restricted to the intricacies of biological systems. Soil particles also provide the strong electric field gradients to alter the local chemistry and physical properties of water. Environmental chemistry that does not account for such local effects is hindered by an incomplete view of the natural world.

The possibility that we can learn to design technological systems capable of locally programming water's physical and chemical properties are very real. It is possible that some water treatment methods already take a step in this direction, however, without a fully developed theoretical framework the potential to exploit these technologies is limited. From the limited discussion presented here the reader can begin to consider the impacts of having control over properties such as viscosity, surface tension, diffusion, temperature and heat capacity, solubility, pH, and reactivity. Not only can we consider the development of whole process technology schemes but also new classes of materials which truly mimic one of nature's greatest secrets: programmable water.

## 6.2 A different approach to water technology

Water is currently processed in a manner consistent with how we experience it in nature. Springs, lakes, rivers and oceans have inspired us. We collect water in basins, withdraw it from underground reservoirs, and pump it through pipes, filters, and reactors of all kinds. Water is processed as a bulk commodity by the millions of cubic meters per day. It seems we are always trying to get rid of one thing while keeping another, and to this end we again look to nature for inspiration to develop filtering and processing technology. The trend in water technology is toward systems which integrate microbial communities with separation technologies.

One potential answer is revealed upon examining the role of water in living systems. The biochemical machinery of life is complex and precisely tuned by billions of years of evolution to operate at very high efficiencies. This is largely due to the intimate role that water molecules play in charge transfer (e.g. proton-coupled electron transport) and upon the way that the local water environment is shaped by the surrounding metabolic structure. Studies on the structure and dynamics of water in purified suspension of proteins and other high mass biomolecules confirms that this influence extends beyond the hydration shell [2]. Exactly how far out this change extends remains an ongoing controversy. The mechanism is in part related to strong electric field gradients ( $>10^{10}$  V/m<sup>2</sup>) generated by spatial variations in charge distribution over the macromolecules. Biological organisms are essentially made up of a highly folded surface with lots of water trapped in and between all the tiny folds. The short distances (sub-nm) together with rather small potentials (hundreds of mV) translate into very steep potential gradients inside organisms [3]. The influence of such gradients is only recently beginning to be understood and mostly in conjunction with *ab initio* calculations which reveals that they can enhance the cooperative modes of water.

There is growing awareness within the biophysical community that water is not a passive ground substance in which biological life occurs but lies at the very heart of and holds the fragile energetic ‘jewel’ that is the living state itself. There are extreme examples of organisms – i.e. many microorganisms, small animals (e.g. tardigrades), and lower plants (*S. lepidophylla*) – that can successfully dehydrate their metabolic machinery and upon rehydration restore function. Living systems are adept at withdrawing from the environment the essential necessities for life. Modern Humans on the other hand require a far greater reach with heavy impact on the natural world. Can we not take another step towards building technology that truly mimics nature? Forests purify large volumes of water using sunlight as the primary source and do a number of planet regulating tasks at the same time. Tree water is not fit for human consumption, it doesn't scale well with our population centers, and is incompatible with our technological ‘style’. Biomimetic technologies (not merely copy pasting biological molecules in massive monocultures on ‘dead’ substrates as this will never work because the entropically toxic environment will quickly destroy the functionality) present an opportunity to move past the sustainability barriers that we currently face.



There is the need for a revolution in our approach to water. Rather than approaching the material from the bulk or purely molecular perspective we need to redress our thinking to encompass the notion of fine control at the mesoscale. The mesoscale refers to the length scale whereby a large number of molecules are involved but the behavior of the system is still susceptible to quantum mechanical fluctuations. This drives the system in a chaotic manner which generates fluctuations in various physical quantities (such as electron density). The fluctuations are dependent upon the allowed energy transitions which are dependent on the size of the coupled molecular ensemble. The continuous density of states observed at the macroscale has degenerated to a state of quantum confinement. Local potential wells can develop which will dissipate in an irreversible manner.

The addition of an external forcing field gradient can further confine these fluctuations and result in directional gradients of chemical potential, or temperature for example. One can thus control the physical properties of water by shifting the distances over which molecules interact. By changing the balance between locally favored and extensible structures the flow of energy within the hydrogen bonding network can be controlled. Local states can trap energy whereas extensible states permit the rapid transfer of energetic modes over long distances. By deliberately engineering materials that favor different energetic states one can control the kinetics associated with that material surface. This work is also important for the engineering of self-assembling and self-healing materials.

## 6.3 An era of new human technology

### 6.3.1 Materials and medicines

The continued study of EHD liquid bridges can improve a number of EHD based technologies such as ink-jet printing, micro- and nano-materials processing, drug delivery, biomedical applications, and desalination. Within the water technology sector nearly all methods can benefit by reexamining where electric and thermal field gradients may exist and ways to take advantage of this. For instance several methods are now emerging which recover energy from chemical potential (e.g. salinity and carbonic acid gradients) the engineering of the membranes involved can be advanced by optimizing the local molecular solvent gradients to either enhance or retard local processes. Similar principles can be applied for directed meso-assembly using the computational processing power of water – biopolymers are a good starting point for custom materials that are also sustainable. The polymerization of these materials often proceeds via dehydration reactions – water is energetically linked to the precursor state and control of the water will influence the placement of the monomeric subunits. The directed excitation by structured EM fields might be used to write structures that are biologically derivable, biodegradable, and have the potential for very high efficiencies.

### 6.3.2 New lifeforms

We have discovered an essential “trick” of nature which can be used to generate an entirely new class of technologies. Biological life exists in a water based system, however, it is conceivable that novel “technical-life” forms could be produced which are based in polar liquids other than water. The capabilities of such systems are difficult to predict, but may prove useful in non-aqueous chemistry and the reclamation of harsh environment types of situations. However, the true outcome of such a development is unknown and might make our own species extinct (along with other water based biotechnologies) and should be considered with caution. On the other hand this awareness that other polar liquids could potentially support life forms very different from our own will fuel the search for extraterrestrial intelligence.

### 6.3.3 Computational capabilities

The idea of performing computations using molecular states is not new however the use of water for such tasks is currently absent from the literature. Water is uniquely suited for computational tasks and has the potential for self-optimization based on boundary gradients (which define the solution basin) and have massive parallel capability. In order to access such computational capabilities there is a technical need to develop tomographic levels of control using a number of forcing fields – a static electric field gradient is just one of these. In addition acoustic, magnetic, and higher frequency electromagnetic fields need to be applied to develop functional computational units. The ultimate goal is a fluid processor that will self-optimize both the structure and dynamics of the ‘logic circuit’ needed for the task. In other words the potential to construct an evolving computational engine exists. We can only speculate as to the performance characteristics, however, based upon the four energy conformations shared between a water dimer, and taking the average translational switching rate the raw processing power contained in a single droplet of water 1 mm diameter is approximately  $10^{15}$  times greater than the 20 petaFLOP Blue Gene/Q super computer.

### 6.3.4 Geoengineering

It has been suggested that an active solution is required to address and mitigate the impacts of climate change on the planet and with a particular focus on human life. Well perhaps well intentioned any attempts to engage in planetary climate engineering will certainly plunge us into a clear awareness of our ignorance of the natural world in which we live. Very little is known for instance regarding the precise dynamics which drive weather and ocean currents. While it is true that temperature and pressure gradients play a major role, the obvious electrical nature of both atmospheric and oceanic processes needs to be addressed. Not only from the large planetary convection scale but to the level of how different masses of water are interacting at the mesoscale, and how the developed electrical forces will in turn drive gradients of temperature and pressure.

## Bibliography

- [1] R. H. Henchman and S. J. Cockram, "Water's non-tetrahedral side," *Faraday Discuss.*, vol. 167, p. 529, 2013.
- [2] H. Frauenfelder, G. Chen, J. Berendzen, P.W. Fenimore, H. Jansson, B. H. McMahon, I. R. Stroe, J. Swenson, and R. D. Young, "A unified model of protein dynamics," *Proc. Natl. Acad. Sci. U. S. A.*, vol. 106, no. 13, pp. 5129–34, Mar. 2009.
- [3] K. M. Tyner, R. Kopelman, and M. a Philbert, "'Nanosized voltmeter' enables cellular-wide electric field mapping," *Biophys. J.*, vol. 93, no. 4, pp. 1163–74, Aug. 2007.

Photo credit chapter 6 overleaf: *Three Worlds*, Halberstadt, ©A.D. Wexler, 2013

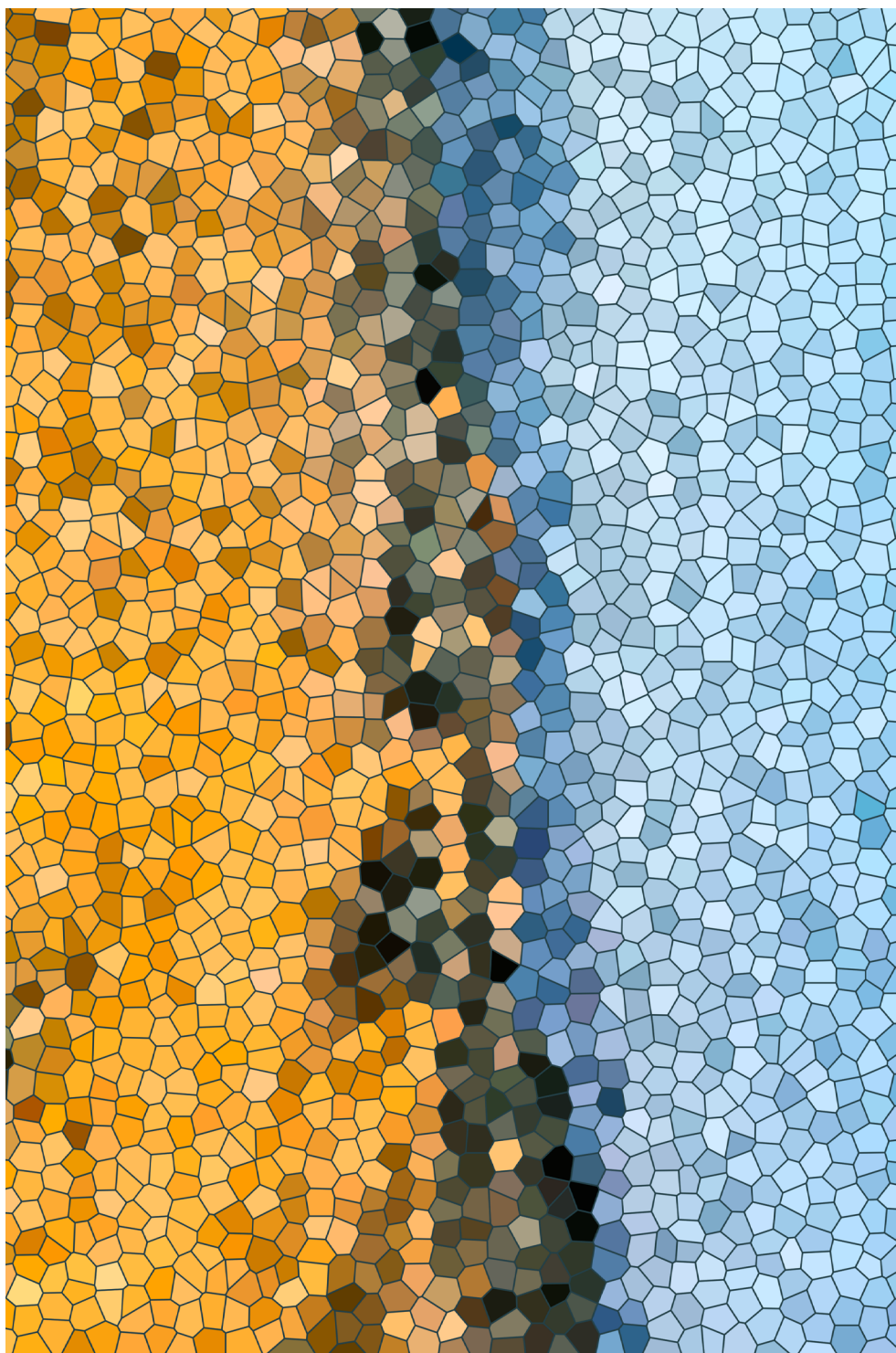


## Summary

Water is essential to a healthy and secure world. Developing new technologies which can take full advantage of the unique attributes of water is important for meeting the ever increasing global demand while reducing the production footprint. Water exhibits unexpected departures in more than 70 physical and chemical properties when compared to other molecular species of similar chemical composition. The principal cause for this behavior is ascribed to the large number of hydrogen bonds which form between neighboring water molecules. Hydrogen bonds are moderately strong in water and exhibit both electrostatic as well as covalent character. When examining the liquid state these interactions play a significant role in moderating the interchange between dynamics and structure. In disordered materials such as a liquid there are three length scales of importance: 1) at the microscopic molecular level interactions dominate, 2) the macroscopic level where classical forces act upon the statistically isotropic medium, and 3) the mesoscopic level where heterogeneous interactions manifest as evolving transient structures each with unique dynamical behaviors. The mesoscale is important to most environmental and biological processes and is even more poorly understood than the liquid state in general. The aim of this thesis is to explore the extended molecular behavior of liquid water excited by strong electric field gradients.

The floating water bridge belongs to a larger class of phenomena called electrohydrodynamic (EHD) liquid bridges. These self-suspending liquid catenaries can occur in a number of polar liquids provided the conductivity is low. They exhibit elevated temperatures and bidirectional flow patterns, as well as sub-Hz diameter oscillations. The flow behavior and dynamics of these bridges is complex but can be addressed by continuum level EHD theory. The polarizing effect of the electric field gradient accelerates the fluid tangentially along the surface resulting in a Taylor pump which supplies the bridge with liquid. The free hanging section is stable against gravity within a band of operational parameters; whereby, the electric field strength is sufficient to confine fluid elements within the bridge. A standardized protocol for operating stable EHD bridges in multiple configurations is developed and presented. This is the primary tool used throughout the thesis and provides a macroscopic object for the experimental examination of how forces, which typically only occur over a few nanometers in nature, affect the organization of polar liquids, notably water. In order to examine the role that the electric field gradient plays in the observed molecular changes found in EHD bridges a simple point-plane electrode system was also employed experimentally.

There are available a number of tools which provide complimentary information on chemical and physical processes occurring in the liquid state. A brief introduction is given on the interaction between electromagnetic waves and matter with respect to field theory and methods from atomic physics. The basis for interaction over different length scales is established. Electrochemical characterization includes the quantification and identification of the charge carrying species present, the relative proton concentration, and the complex



dielectric response. The vibrational and rotational motion of molecules is measured with a combination of infrared emission spectroscopy and imaging. This permits the detection of both the thermal bath and non-equilibrium molecular excited states. The local structure of the liquid matter contained in the bridge can be elucidated through the methods discussed here. X-rays provide information on the electron density; whereas, neutrons reveal nuclear positions. Together with isotope substitution a complete picture of the motionally averaged local structure of the liquid in the bridge can be recovered. Quasi-elastic neutron scattering provides a measure of the diffusion, relaxation, and other slow energy or mass transfer modes in materials. This data compliments the NMR methods which probe the strength of both intra- intermolecular coupling in the system. Very small perturbations in the optical properties of a liquid can be detected using interferometry and these ultimately reflect changes in the polarizability of the liquid which can arise from changes in physical properties. Raman scattering is an inelastic method which can probe changes to the polarizability of a liquid that reflect shifts in the local molecular environment and can be used to determine both local and non-local vibrational coupling.

Magnetic resonance imaging was used to track the flow field present in the bridge without the use of tracer particles; revealing that the bridge has a layered structure, with distinct flow regimes lying one on top of the other. Investigation of the electrochemistry in the water bridge found that protons account for 87% of the charge transport in the bridge. Impedance spectroscopy and pH measurement corroborate the finding that a proton gradient forms across the entire system.

The results from elastic neutron and X-ray scattering reveal that the static structure is unchanged within the given accuracy of the employed measurements. However, the systematic analysis of the data using a reverse Monte Carlo computer simulation revealed dynamical changes that are reliable above the limited instrument precision. The imposed electric field of an EHD bridge distorts the local Coulombic interactions between molecules altering the dielectric relaxation pathway so that it becomes more favorable for the absorbed energy to become trapped locally for a longer period of time.

The electric field in the bridge system is not uniform. Strong field gradients are present which stimulate changes in the molecular polarizability, generating gradients of physical properties, and restricting the allowed rotational-vibrational relaxation transitions. These trends are comparable to those from ultrafast relaxation measurements where the vibrational lifetime of the OH stretch, in a mixture of light and heavy water, was found to be significantly shorter in the bridge than in the neat liquid. The energy absorbed in the measurement, however, remained trapped in a local intermediate state longer in the bridge before being released as a thermal perturbation. The nuclear relaxation dynamics in a glycerol bridge showed similar behavior where the transverse and longitudinal magnetization lifetimes diverged from the expectation values given the systems temperature.

From the experimental observations several features of electrically excited liquid water appear. At the gross continuum level the operation of a floating water bridge results in the production of a charge imbalance between anolyte and catholyte. This is in part due to the enhanced proton mobility in the bridge. Protons no longer are confined to the hydrogen bond mediated Grotthuss mechanism but can travel even faster through a delocalized state. This means that charge can be pumped faster than it can be neutralized resulting in the observed electrochemical differences. The energy level of protons in the conduction channel is the difference between the ground and excited state levels observed as a non-thermal mid-infrared emission feature. The proton channel will be active over relatively short distances as it is disrupted by fluctuations in molecular position driven by local force gradients. These channels are localized and discontinuous providing the physical basis for the onset of mesoscale dynamic heterogeneity in the excited liquid. The picture begins to emerge whereby local trapping states and long-range cooperative coupling modes dynamically exchange energy. The energy exchange is far from equilibrium and supports multiple transfer mechanisms. At the mesoscale the excited state exhibits traits of a chaotic dynamical system and provides a varied energetic landscape whereby rotational-vibrational transition dipoles, nuclear spin states, and thermodynamic potentials, such as the configurational entropy, non-adiabatically – that is there is a pumping of heat in response to the induced fluctuating gradient fields. The transfer of perturbations from local to collective modes and vice versa requires that the chemical, thermal, and electromagnetic potentials present in the molecular milieu be linked to the entropy production. This clearly shows why when considering water one must use the full quantum mechanical description, especially where the transfer of protons is of concern. Proton motion in water is governed by quantum chaos and is as dependent upon the local wave-function as on the chaos stabilized quantum field through which the proton 'travels'.

This early foray into the non-equilibrium dynamics and mesoscale organization of electrically excited liquid water opens an opportunity to develop technologies which better mimic nature. Taking biological systems as the exemplary standard by which to compare it is necessary to develop soft matter based technical systems which take advantage of the link between electric, magnetic, and thermal fields to drive chemical and physical processes with higher efficiency. Water, as well as other polar liquids, can be locally controlled so as to induce spatial variation in the chemical potential whereby one can imagine a reactor where disparate physical or chemical process can occur in close proximity without the need for rigid segregating structures. Furthermore, this level of control is dynamical such that the organization of the partitioning in the liquid can be changed in time allowing the energy requirements of the intended process is optimized. It is thus conceivable that the size, complexity, costs, and footprint of many industrial and municipal processes can be reduced. Rather than treating liquids as mere bulk fluids to be pushed and pumped through a process the opportunity presents itself to use the internal structure and dynamics of liquids to build novel liquid state technologies that more closely mimic nature.

## Acknowledgements

This is the hardest part of the writing; who to thank, and for what? There are many more than those mentioned here who were essential to this thesis and my quasi-sanity leading up to and during its genesis. Please forgive my omission for whatever reason; I thank you for being part of this journey!

I don't think I will ever be able to express in words the gratitude I feel for the generosity and sacrifices my parents made to get me started off in the world. They have both continued to love and support me and for that I know I am lucky. Fred, Chris and the rest of the VT clan you gave me a second home in the woods and helped me feel that I was ok just as I am. Grandma you truly are a saint and I know you (and Grandpa!) had some secret hand in the wonder I feel for the world. Joey I would not have made it to this point without your blessing and love. Kaka, Evan, Mary, Russell, George, Patty, John, Jim, Anita, and all the rest I really wish I could see you more often; missing you is the hardest part of being "over here". Josh, Amy, Stokely, Carlton you four give me real hope for the future; you show me love can conquer all.

Vaughn, Chris, Suzie, & Portia thanks for making Miami a place I can always come home to. Frank you showed me that sometimes even the toughest of us need the love of friends. Danny we miss you. Mr. Alonso and Dr T. I this would not have happened without your early guidance. Estella you gave me the chance to fly on my own. Amy, Alan, & Sarah for showing me that there was more to life than academia and that I needed to go find myself first.

Nathan Beedle or showing me there is more to life than work. Myong you are missed but never forgotten. The Kelvis (and Sam!) for always opening your home to me even when that meant 4am karaoke AND putting up with whatever drama was in progress. Smohawk, where to start... I better not, this is public record. Todd we have been through so much and yet not enough, where to next? I promise I won't bring my recording gear this time. J-Rey for your heart support and wisdom. K&R May thank you for believing in me. Baym for searching the other side of Rumi's puzzle, Jinga awaits us! Dana for teaching me to be present. Jenni for finding and sharing so much beauty with me. Lopezians you were there at the dawn, right there with me, when the water was full of stars; our friendship has continued to carry me and I look forward to our reunion. To my BUSM brothers and sisters I miss you all, and couldn't have gotten this far without all the love we shared. Pat, Chewy, and Ben you taught me to think with my fingers. I wish to someday share my insights on the living organism with you. Timeh and Ron Don you guys are charlatans, and I love you both – the next one is on me. Kachi thanks for the earth medicine and the lovely, albeit too infrequent, chats. Mae fffffff. Whitey for the QM 8-bit retro! Shout out to Vance and Andy Detloff!

Forest and Owl you two are so lovely and were of the few who managed to make the trip to see me while deep down in the trenches, I wish I had been less preoccupied. Next time, we should find a beach. Tricia, Jackson, Bella, and Kari we found the beach!

Jerry you gave the spark of curiosity in me a safe place to conflagrate. Rainer your inventive genius inspires me, nobody can build scientific instruments from abandoned relics like you. Ronnie you are one of the few people I have ever met who is so much like me and at the same time not at all -- must be the birthday. Vanya, where's my vacuum pump? Katya you continue to amaze me. Hyok for playing it cool when things went pear shaped. To the Sagstadt Marina Crew thanks for making a slip a home, for Jeopardy, and more PBR than I care to recall. Doughbie for showing me the freedom of the sea.

Cézan thanks for the adventures whether by sea, roll, or chill. Let's go bro! Janke – you. Eloah & Flawoco what music! Rik & Baukje, Hilde & Uche, Bob & Rianne, Maarten, Tako, Joost & Rhoda -- PK is just a street, but with you it's more like *Utopia*. Daina, Andrea, Eszter, and KCFrie you made home a daily occurrence. Astrid it is difficult to put it into words how much you have helped my years here, you are more than a friend, you are my sister. Maxime & Claudia you were always there at just the right time. Phillip & Sandra you two have always been so kind to me even when my kitten accidentally caused the warp core to explode. Bernhard I cherish your brilliant enthusiasm. Slawik for that knowing look. Gerrit O. thanks you for the mind expanding discussions. Tom, Olivier, & Doekle I didn't want to get in that car, but I am thankful you made me go. Vytautas *fapas ritas*, binaural beats & COLA! Don & Doville for being the best ~~angels~~ devils a guy could have. Judita for reminding me that I have to take care of me first. Chrissie for bringing me to the pack. Taina for laughing so much that my lights burst. JJ and Marco for that trip we haven't taken yet! Lucy & Wout for your insightful wit! Jan & Claudia for really caring & extra beers. Albert for always being so dang nice! Joeri for being my friend when I needed one. Marianne your good nature rescued the Reservoir Dogs experiment! Mark for the rooftop sunrise and the good times. Janneke, Pau, Olivier, Gerwin, and Andrew thanks for the adventure. Matthias, Andrea, and Natalia for tackling the nitty gritty. Rienk I owe you a mix tape! Wim, Janneke, Jelmer, Ton, Agnieszka, Bianca de Virus, Meike, Piet, & Ernst thanks for keeping the engine running! To the Wetsus Secretaries for all the great help over the years. Special thanks to Roely for getting the reading copies ready and sent on time! Bert thank you for giving the chance to create something entirely new. Arie it is too bad you had to go and I will miss your keen observations on human behavior the most. Heleen your strength and professionalism are only outweighed by your kindness and good nature, you inspire me. To the rest of my Wetsus colleagues thank you for being – JOY!

A few of you really gave more than can ever be repaid as we reached for the stars. Foppe you had the magic to get it here when no one else could. Jan you are a true craftsman. Harm for giving that extra bit to get us over the top. Harrie for saying it like it is. Johannes 'Sticky Santa' for all the UV glue and the excellent circuitry. Tjesse Overdijk, one word -- Hydrazine! Sandra you took on every challenge and came back. I look forward to your dissertation. Thank you Jack and the crew at the ESTEC for supporting our very difficult mission and welcoming us back for a second try. For everyone else who brought food, lent a hand when no less than three would do, and cheered on *Volturnus* thank you for being there.



Cees and Johannes you have built something which is truly revolutionary. The world needs more places where multidisciplinary collaboration can succeed. I am grateful that you have entrusted so much in the vision of the people who gather around yours. Thank you for providing a unique environment where both scientific freedom and technical creativity are supported. Wetsus is a unique and special place.

Kees, Ruud, Gerrit, Georg, and Johannes you have struggled along side us in this work and you never gave up. The bedrock of your patronage and enthusiasm made this possible. Gert, Ursula, Susanne, Brigitte, Antonio, Nikola, Łukasz, thank you for your very real contributions to the work in this thesis and for sharing with me your excellent technical knowledge, experimental wisdom, and your parts in helping to write this book.

Mariana & Anna, my lovely paranymphs, thank you for sharing both the battles and triumphs. These years would have been empty without your friendship.

I thank Prof. Brecker, Prof. Musso, Prof. van Amerongen, Dr. Yoo, and Prof. Swain for your effort to examine this thesis. I hope it was fun to read but I know that this was not an easy subject. I hope someday to share with you the next iteration of this work.

Jakob how can I thank you for everything you have done? The patience you have shown me, the wisdom you have shared, all of the experimental work you have contributed, your mentorship, encouragement, and sweetly bizarre humor are rivers feeding into the ocean of gratitude I feel for your role in making this thesis and my promotion possible. Beyond that you have been a real friend to me and always made the most difficult steps passable. I wish that you may always be *home on the range...* “where seldom is heard a discouraging word, and the skies are not cloudy all day.”

Elmar if it wasn't for you this would never have happened. This work is as much yours as it is mine. These years have been a challenge to say the least and it takes a special partnership to make it through, we are lucky. Who would have thought that we could have taken a “party trick” and learned so much about water and ourselves in the process. Thank you for expanding the horizon, aiming for the impossible, and for believing in my abilities to get us closer. *Per aspera ad astra* my friend, my brother, someday we shall.

Sarah this book would not be if not for you, and yet it is not for you, the future is.

Adam D. Wexler  
24 March 2016  
Leeuwarden

## About the Author

Adam David Wexler is originally from New York City and has lived throughout the United States before moving to Leeuwarden to begin his doctoral research. He received his BSc. in Botany from the University of Washington in Seattle before taking a hiatus from academia to work in sustainable agriculture. Always curious, Adam has developed a diverse technical background stemming from his work as an engineer and fabricator in the glass, maritime, and optoelectronics industries. In addition to his technical skills he has also worked in healthcare as a craniosacral therapist using aspects of traditional chinese medicine and aquatic therapy to assist people suffering from chronic injury and trauma. Witnessing the recovery taking place in the clinic piqued his curiosity in water and he soon joined the research community again. He first worked on the problem of polyelectrolyte colloid interactions with the Pollack group at his alma mater – UW. This gave him direct experience with advanced optical instrumentation and nanofabrication techniques. It also taught him the pitfalls of water research and the exceptional care that must be exercised when working with the universal solvent. Adam holds an MSc from Wageningen University in Water Technology and has studied the floating water bridge since 2010. During this time he established and now heads the Arie Zwijnenburg Laboratory for Advanced Microscopy and Optical Metrology. He is co-inventor on two patents and was project leader for the development of an orbital research platform. For his contributions to furthering the science of measuring and understanding the interaction of water molecules Adam received the 2015 Professor Marcel Mulder Prize. He plans to continue his research efforts to make clear the underlying mechanism linking water and life.



## Author's Publications

### First author papers included in this thesis

- A. D. Wexler, M. López Sáenz, O. Schreer, J. Woissetschläger, and E. C. Fuchs, "The preparation of electrohydrodynamic bridges from polar dielectric liquids," *J. Vis. Exp.*, no. 91, p. e51819, Jan. 2014
- A. D. Wexler, S. Drusová, J. Woissetschläger, and E. C. Fuchs, "Raman and Interferometry Investigation of the Influence of an Inhomogeneous Electric Field on Water," *PCCP*, in review, pre-press version arXiv:1603.07902v1 [cond-mat.mes-hall].
- A. D. Wexler, S. Drusová, E. C. Fuchs, J. Woissetschläger, G. Reiter, M. Fuchsjäger, and U. Reiter, "Magnetic resonance imaging of flow and mass transfer in electrohydrodynamic liquid bridges," *Journal of Visualization*, in review, pre-press version arXiv:1603.07896 [physics.flu-dyn].
- A. D. Wexler, B. Bitschnau, A. Cervellino, N. Casati, A. K. Soper, J. Woissetschläger, and E. C. Fuchs, "The local structure of electrically stressed liquid water and implications for modelling of dielectric relaxation," *J. Phys. D*, in revision, pre-press version arXiv:1603.07537v1 [cond-mat.mes-hall].
- A. D. Wexler, E. C. Fuchs, J. Woissetschläger, S. Felsing, L. Brecker, U. Reiter, M. Fuchsjäger, and G. Reiter, "Imaging of proton cooperativity in electrically stressed glycerol bridges using combined MR thermography and relaxation mapping," in preparation.

### Non-first author papers included in thesis

- E. C. Fuchs, B. Bitschnau, A. D. Wexler, and F. Woissetschläger, Jakob Freund, "A Quasi-Elastic Neutron Scattering Study of the Dynamics of Electrically Constrained Water," *J. Phys. Chem. B*, 119 (52), 15892–15900, 2015.
- E. C. Fuchs, M. Sammer, A. D. Wexler, P. Kuntke, and J. Woissetschläger, "A floating water bridge produces water with excess charge," *J. Phys. D*, 49 (12), 125502, 2016.
- M. Sammer, A. D. Wexler, P. Kuntke, H. Wilsche, N. Stanulewicz, E. Lankmayr, J. Woissetschläger, and E. Fuchs, "Proton production, neutralisation and reduction in a floating water bridge," *J. Phys. D: Appl. Phys.*, 2015.
- E. C. Fuchs, A. D. Wexler, A. H. Paulitsch-Fuchs, L. L. F. Agostinho, D. Yntema, and J. Woissetschläger, "The Armstrong experiment revisited," *Eur. Phys. J. Spec. Top.*, vol. 223, no. 5, pp. 959–977, Aug. 2013.
- E. C. Fuchs, A. Cherukupally, A. H. Paulitsch-Fuchs, L. L. F. Agostinho, A. D. Wexler, J. Woissetschläger, and F. T. Freund, "Investigation of the mid-infrared emission of a floating water bridge," *J. Phys. D: Appl. Phys.*, vol. 45, no. 47, p. 475401, Nov. 2012.
- L. Piatkowski, A. D. Wexler, E. C. Fuchs, H. Schoenmaker, and H. J. Bakker, "Ultrafast vibrational energy relaxation of the water bridge," *Phys. Chem. Chem. Phys.*, vol. 14, p. 6160, 2012.
- J. Woissetschläger, A. D. Wexler, G. Holler, M. Eisenhut, K. Gatterer, and E. C. Fuchs, "Horizontal bridges in polar dielectric liquids," *Exp. Fluids*, vol. 52, no. 1, pp. 193–205, 2012.

A. H. Paulitsch-Fuchs, E. C. Fuchs, A. D. Wexler, F. T. Freund, L. J. Rothschild, A. Cherukupally, and G. J. W. Euverink, "Prokaryotic transport in electrohydrodynamic structures," *Phys. Biol.*, vol. 9, no. 2, p. 026006, Apr. 2012.

E. C. Fuchs, L. L. F. Agostinho, A. Wexler, R. M. Wagterveld, J. Tuinstra, and J. Woissetschläger, "The behaviour of a floating water bridge under reduced gravity conditions," *J. Phys. D: Appl. Phys.*, vol. 44, no. 2, p. 025501, Jan. 2011.

E. C. Fuchs, A. D. Wexler, L. L. F. Agostinho, M. Ramek, and J. Woissetschläger, "Methanol, Ethanol and Propanol in EHD liquid bridging," *J. Phys. Conf. Ser.*, vol. 329, p. 012003, Dec. 2011.

### Additional papers not covered in this thesis

- A. Paulitsch-Fuchs, A. Zsohár, A. D. Wexler, A. Zauner, C. Kittinger, J. de Valença, and E. C. Fuchs, "Living cells in a floating water bridge," *Phys. Biol.*, 2016, in review.
- M. Sammer, C. Kamp, A. H. Paulitsch-Fuchs, A. D. Wexler, C. J. N. Buisman, and E. C. Fuchs, "Strong Gradients in Weak Magnetic Fields Induce DOLLOP formations in Tap Water," *MDPI Water*, vol. 8, no. 3, 79, 2016.
- G. W. Steen, E. C. Fuchs, A. D. Wexler, H. L. Offerhaus, "Identification and quantification of 16 inorganic ions in water by Gaussian curve fitting of near-infrared difference absorbance spectra," *Appl. Opt.*, 54 (19), 5937–5942, 2015.
- R. Valladares Linares, A. D. Wexler, S. S. Bucs, C. Dreszer, A. Zwijnenburg, H.-C. Flemming, J. C. Kruithof, and J. S. Vrouwenvelder, "Compaction and relaxation of biofilms," *Desalin. Water Treat.*, no. June, pp. 1–13, 2015.
- C. Dreszer, A. D. Wexler, S. Drusová, T. Overdijk, A. Zwijnenburg, H.-C. Flemming, J. C. Kruithof, and J. S. Vrouwenvelder, "In-situ biofilm characterization in membrane systems using Optical Coherence Tomography: Formation, structure, detachment and impact of flux change," *Water Res.*, vol. 67, pp. 243–254, Sep. 2014.
- H. Yoo, E. Nagornyak, R. Das, A. D. Wexler, and G. H. Pollack, "Contraction-induced changes in hydrogen bonding of muscle hydration water," *J. Phys. Chem. Lett.*, vol. 5, no. 6, pp. 947–952, 2014.
- C. Dreszer, H.-C. Flemming, A. D. Wexler, A. Zwijnenburg, J. C. Kruithof, and J. S. Vrouwenvelder, "Development and testing of a transparent membrane biofouling monitor," *Desalin. Water Treat.*, vol. 52, no. 10–12, pp. 1807–1819, Mar. 2014.
- I. S. Klyuzhin, F. Ienna, B. Roeder, A. Wexler, and G. H. Pollack, "Persisting water droplets on water surfaces," *J. Phys. Chem. B*, vol. 114, no. 44, pp. 14020–7, Nov. 2010.
- J. Zheng, A. Wexler, and G. H. Pollack, "Effect of buffers on aqueous solute-exclusion zones around ion-exchange resins," *J. Colloid Interface Sci.*, vol. 332, no. 2, pp. 511–4, Apr. 2009.
- D. F. Mandoli, A. Wexler, J. Teschmacher, and A. Zukowski, "BRIEF INCUBATION OF GAMETANGIA-BEARING CAPS IN ANTIBIOTICS ELIMINATES BRANCHING IN PROGENY OF ACETABULARIA ACETABULUM (CHLOROPHYTA) I," *J. Phycol.*, vol. 31, no. 5, pp. 844–848, Oct. 1995.
- Photo credit summary overleaf: *Mosaic Dunes, Maspalomas*, ©A.D. Wexler, 2015



Netherlands Research School for the  
Socio-Economic and Natural Sciences of the Environment

# D I P L O M A

*For specialised PhD training*

The Netherlands Research School for the  
Socio-Economic and Natural Sciences of the Environment  
(SENSE) declares that

**Adam David Wexler**

born on 18 April 1974 in New York, United States of America

has successfully fulfilled all requirements of the  
Educational Programme of SENSE.

Leeuwarden, 19 March 2016

the Chairman of the SENSE board

Prof. dr. Huub Rijnaarts

the SENSE Director of Education

Dr. Ad van Dommelen

*The SENSE Research School has been accredited by the Royal Netherlands Academy of Arts and Sciences (KNAW)*



K O N I N K L I J K E N E D E R L A N D S E  
A K A D E M I E V A N W E T E N S C H A P P E N



The SENSE Research School declares that **Mr Adam D. Wexler** has successfully fulfilled all requirements of the Educational PhD Programme of SENSE with a work load of 60.6 EC, including the following activities:

#### SENSE PhD Courses

- o Environmental Research in Context (2012)
- o Research in Context Activity: 'Contributing to the implementation of an optical metrology laboratory (OML) and the development and testing of a hypergravity research demonstrator (which received the Professor Marcel Mulder Award)' (2012-2015)

#### Other PhD and Advanced MSc Courses

- o Lasers and Optics for Fluids Research, European centre of excellence for sustainable water technology (Wetsus) and Graz University of Technology (2010)
- o Our Future Leaders, The Recess College (2012)
- o European Water campus business challenge, European centre of excellence for sustainable water technology (Wetsus) (2014)
- o International Summer School '1D- and 2DNMR Spectroscopy in Liquids', Austrian Chemical Society (GÖCh) (2014)
- o MicroCOR winter school on Chemical Imaging by Coherent Raman and nonlinear microscopy, Les Houches Physics School, France (2014)

#### External training at a foreign research institute

- o Hypergravity experiments, ESA-ESTEC, The Netherlands (2012)
- o Wide-angle X-ray scattering, The Paul Scherrer Institut (PSI), Switzerland (2012)
- o Optical frequency comb theory and operation, Menlo Systems, Germany (2013)
- o Spin echo small angle neutron scattering, Technical University Delft, The Netherlands (2013)
- o Magnetic resonance imaging and velocimetry, Medical University of Graz, Austria (2013-2015)
- o NMR spectroscopy, University of Vienna, Austria (2014)
- o Optics Studio Software Training, Zemax, United Kingdom (2015)

#### Management and Didactic Skills Training

- o Supervising two MSc and one BSc student with theses (2012, 2014)
- o Teaching assistance in PhD course 'Lasers and Optics in Fluid Research' (2013-2014)

#### Selection of Oral Presentations

- o *Coherence, Chaos, and Liquid Bridges – an Experimentalist's Evaluation of Nanoscale Theories Applied to Liquid Water*. International Conference on Materials for Advanced Sensors and Transducers, Low Energy Coherent Systems Session, 24-28 May 2012, Budapest, Hungary
- o *Magnetic resonance imaging of electrohydrodynamic liquid bridges: measurement of relaxation times in electrically stressed polar liquids*. NMR mini-symposium, 16<sup>th</sup> Austrian Chemistry Days, 21-24 September 2015, Innsbruck, Austria

SENSE Coordinator PhD Education

Dr. ing. Monique Gulickx

This work was performed in the cooperation framework of Wetsus, European Center of Excellence for Sustainable Water Technology ([www.wetsus.nl](http://www.wetsus.nl)). Wetsus is co-funded by the Dutch Ministry of Economic Affairs and Ministry of Infrastructure and Environment, the European Union Regional Development Fund, the Province of Fryslân, and the Northern Netherlands Provinces. The author would like to thank the participants of the research theme "Applied Water Physics" for the fruitful discussions and their financial support.



Cover and Layout: A.D. Wexler

Special Thanks: Cézán van Slingerland and Ferdinand Schwörer

Printed by Gildeprint, Enschede (NL)

